Version 1.0
December 2007

Wide Field Camera 3 Instrument Handbook for Cycle 17

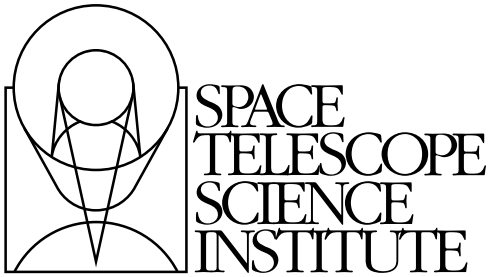

Space Telescope Science Institute
3700 San Martin Drive
Baltimore, Maryland 21218
help@stsci.edu

Operated by the Association of Universities for Research in Astronomy, Inc., for the National Aeronautics and Space Administration

User Support

For prompt answers to any question, please contact the STScI Help Desk.

- **E-mail:** help@stsci.edu
- **Phone:** (410) 338-1082
  (800) 544-8125 (U.S., toll free)

World Wide Web

Information and other resources are available on the WFC3 World Wide Web sites at STScI and GSFC:

- **URL:** http://www.stsci.edu/hst/wfc3
- **URL:** http://wfc3.gsfc.nasa.gov

WFC3 Instrument Handbook Revision History

Version	Date	Editors
1.0	December 2007	Howard E. Bond and Jessica Kim Quijano

Contributors:

Sylvia Baggett, Ray Boucarout, Tom Brown, Howard Bushouse, Nicholas Collins, Colin Cox, Ilana Dashevsky, Linda Dressel, Mauro Giavalisco, George Hartig, Bryan Hilbert, Robert J. Hill, Diane Karakla, Jessica Kim Quijano, Randy Kimble, Martin Kümmel, Harald Kuntschner, Matt Lallo, Olivia Lupie, Peter McCullough, John MacKenty, Eliot Malumuth, Andre' Martel, Larry Petro, Elizabeth Polidan, Manuel Quijada, Neill Reid, Massimo Robberto, Massimo Stiavelli, Randal Telfer, Nolan Walborn, Jeremy Walsh and Tom Wheeler.

Citation:

In publications, refer to this document as:
Bond, H. E., and Kim Quijano, J., et al. 2007, “Wide Field Camera 3 Instrument Handbook, Version 1.0” (Baltimore: STScI)

Send comments or corrections to:
Space Telescope Science Institute
3700 San Martin Drive
Baltimore, Maryland 21218
E-mail:help@stsci.edu

Table of Contents

Acknowledgments

The WFC3 Science Integrated Product Team (2007)

Sylvia Baggett
Howard Bond
Tom Brown
Howard Bushouse
Linda Dressel
George Hartig
Bryan Hilbert
Robert Hill (GSFC)
Jessica Kim Quijano
Randy Kimble (Instrument Scientist, GSFC)
John MacKenty (Deputy Instrument Scientist)
Andre' Martel
Peter McCullough
Larry Petro

Past Science IPT Members

Wayne Baggett
Laura Cawley
Ed Cheng (GSFC, now Conceptual Analytics)
Ilana Dashevsky
Don Figer
Mauro Giavalisco
Shireen Gonzaga
Christopher Hanley
Ron Henry
Pat Knezek
Ray Kutina
Casey Lisse
Olivia Lupie
Neill Reid
Massimo Robberto
Michael Robinson
Megan Sosey
Massimo Stiavelli

The WFC3 Scientific Oversight Committee

Bruce Balick, University of Washington
Howard E. Bond, Space Telescope Science Institute
Daniela Calzetti, Space Telescope Science Institute
C. Marcella Carollo, Institute of Astronomy, ETH, Zurich
Michael J. Disney, Cardiff University
Michael A. Dopita, Mt Stromlo and Siding Spring Observatories
Jay Frogel, AURA
Donald N. B. Hall, University of Hawaii
Jon A. Holtzman, New Mexico State University
Gerard Luppino, University of Hawaii
Patrick J. McCarthy, Carnegie Observatories
Robert W. O'Connell, University of Virginia (Chair)
Francesco Paresce, European Southern Observatory
Abhijit Saha, National Optical Astronomy Observatory
Joseph I. Silk, Oxford University
John T. Trauger, Jet Propulsion Laboratory
Alistair R. Walker, Cerro Tololo Interamerican Observatory
Bradley C. Whitmore, Space Telescope Science Institute
Rogier A. Windhorst, Arizona State University
Erick T. Young, University of Arizona

Thanks

The Editor thanks the authors who prepared first drafts of the chapters: Larry Petro (Chapters 4 and 10); Massimo Robberto (Chapters 5 and 7); Sylvia Baggett (Chapter 6); Howard Bushouse, Martin Kümmel, Harald Kuntschner, and Jeremy Walsh (Chapter 8); Tom Brown (Chapter 9 and Appendices A, C, and D); Bryan Hilbert (Appendix A); George Hartig (Appendix B); and Howard Bushouse (Appendix E).

We thank the Technical Editor, Susan Rose for her contributions to the editing and production of this *Instrument Handbook*.

CHAPTER 1:

Introduction to WFC3

In this chapter . . .

1.1 Overview

The **Wide Field Camera 3** (**WFC3**) is a fourth-generation imaging instrument that is designed to be installed in the *Hubble Space Telescope* (*HST*) during Servicing Mission 4 (SM4). At this writing in the autumn of 2007, SM4 is scheduled for August 2008. Cycle 17 of the *HST* observing program will begin following SM4, and is currently planned to cover the interval from the conclusion of SM4 and the ensuing orbital verification phase through December 2009. The Space Telescope Science Institute (STScI) will accept observing proposals for WFC3 in the review process for Cycle 17.

This *WFC3 Instrument Handbook* has been prepared by the WFC3 team at STScI. It is the basic technical reference manual for WFC3 observers. The information in this *Handbook* is intended to be useful for Cycle 17 Phase I proposers, for the subsequently selected General Observers (GOs) as they prepare their Phase II specifications, and for those analyzing WFC3 data.

It should be noted that WFC3 is, at this writing, still under development. Although this *Handbook* is as accurate as possible, the information herein is still subject to possible changes before SM4, and also as a consequence of experience gained after WFC3 is operating onboard *HST*.

The WFC3 instrument will occupy *HST*'s radial scientific-instrument bay, where it will obtain on-axis direct images. During SM4 the shuttle astronauts will install WFC3 in place of the current Wide Field Planetary Camera 2 (WFPC2). WFPC2, in turn, was

installed during SM1 in December 1993, to replace the original Wide Field/Planetary Camera (WF/PC1). WFC3, like WFPC2, contains optics that correct for the spherical aberration discovered in the *HST* primary mirror following launch of the telescope in April 1990.

WFC3 uses some components of the original WF/PC1, which will thus see service once again onboard *Hubble*. WFC3 is designed to ensure that *HST* maintains its unique imaging capabilities until the end of its mission, while at the same time advancing its survey and discovery capability through WFC3's combination of broad wavelength coverage, wide field of view, and high sensitivity. WFC3 will also provide a good degree of redundancy for the currently partially inoperative Advanced Camera for Surveys (ACS), planned for repair during SM4, as well as for the Near-Infrared Camera and Multi-Object Spectrometer (NICMOS) cameras.

A key feature of WFC3 is its panchromatic wavelength coverage. By combining two optical/ultraviolet CCDs with a near-infrared HgCdTe array, WFC3 will be capable of direct, high-resolution imaging over the entire wavelength range from 200 to 1700 nm. Equipped with a comprehensive range of wide-, intermediate-, and narrow-band filters, WFC3 will have broad applicability to a variety of new astrophysical investigations.

WFC3 is a facility instrument. It is being developed, constructed, characterized, and calibrated by an Integrated Product Team (IPT) led by NASA's Goddard Space Flight Center (GSFC), and composed of staff astronomers and engineers from GSFC, STScI, Ball Aerospace & Technologies Corp., the Jet Propulsion Laboratory (JPL), and other industrial contractors.

A Scientific Oversight Committee (SOC), selected by NASA from the international astronomical community and appointed in 1998, provides scientific advice for the design and development of WFC3. The SOC's activities have been in a range of areas, including: definition of the key scientific goals and success criteria for WFC3; participation in project reviews; recommending an optimum set of filters and grisms for the instrument and the pixel scale and field of view of the detectors; participation in the selection of flight detectors; and advice on technical trade-off decisions in the light of the scientific goals of the instrument. The SOC continues to provide oversight on all aspects of WFC3 development, with the aim of assuring that the camera will achieve its scientific goals.

1.2 Key Features of WFC3

The optical design of WFC3 features two independent channels, one sensitive at ultraviolet (UV) and optical wavelengths, approximately 200 to 1000 nm (the **UVIS channel**), and the other sensitive at near-infrared (near-IR) wavelengths, approximately 800 to 1700 nm (the **IR channel**). A channel-selection mirror will direct on-axis light from the *HST* optical telescope assembly (OTA) to the IR channel, or the mirror can be removed from the beam to allow light to enter the UVIS channel. This means that *simultaneous* observations with the UVIS and IR detectors are not

possible. However, both UVIS and IR observations can be made *sequentially*, even during the same *HST* orbit.

The extended wavelength range, combined with high sensitivity, high spatial resolution, large field of view, and a wide selection of spectral elements, makes WFC3 an extremely versatile instrument. Key features of WFC3 include:

- **UVIS channel:** two 2k×4k CCDs; pixel scale 0.04 arcsec/pix; field of view 162×162 arcsec; wavelength range 200-1000 nm; S/N=10 in a 10-hour exposure (F606W filter) for a point source with *V*=28.9.
- **IR channel:** 1k×1k HgCdTe array; pixel scale 0.13 arcsec/pix; field of view 123×136 arcsec; wavelength range 800-1700 nm; S/N=10 in a 10-hour exposure (F160W) for a point source with *H*=28.0.
- 62 wide-, medium-, and narrow-band filters in the UVIS channel.
- 15 wide-, medium-, and narrow-band filters in the IR channel.
- 1 grism in the UVIS channel, and 2 grisms in the IR channel.

A "White Paper," prepared by the SOC and the Science IPT, outlines some scientific areas that will especially benefit from the capabilities of WFC3. These include searches for galaxies at redshifts up to $z\sim10$; studies of the physics of star formation in distant and nearby galaxies; investigations of resolved stellar populations down to faint levels in the UV, optical, and near-IR; and high-resolution imaging of objects in the solar system. WFC3's panchromatic capabilities will allow investigations of the assembly and evolution of galaxies; star birth, evolution, and death and its relation to the interstellar medium; and meteorology of the outer planets. The White Paper (Stiavelli, M., & O'Connell, R.W., eds., 2000, "*Hubble Space Telescope* Wide Field Camera 3, Capabilities and Scientific Program") can be found at:

http://wfc3.gsfc.nasa.gov/white_paper.html

1.3 WFC3 Quick Reference Guide

The most important basic information about WFC3 can be found in this Handbook at the following locations:

- Table 5.1: Instrument Characteristics (field of view, pixel scale, detector parameters, etc.)
- Table 6.2: UVIS Channel Filters and Grism
- Figures 6.2-6.5: Plots of system throughput for UVIS Filters
- Table 7.2: IR Channel Filters and Grisms
- Figures 7.2-7.3: Plots of system throughput for IR Filters

1.4 Current Instrument Status

At present (autumn 2007), as the editing of this *Instrument Handbook* was being completed, WFC3 continues to be developed and tested.

We recently completed a system-level thermal-vacuum test of WFC3 at Goddard Space Flight Center. This test successfully demonstrated the overall operation and performance of the instrument, and test data provide much of the basis for the performance predictions in this *Handbook*.

At present, the main uncertainty associated with WFC3, and the motivation for another system-level thermal-vacuum test planned for early 2008, is the continuing testing of the flight detector assemblies. Information presented in this *Handbook* is based upon the performance of best available detectors, but their assemblies still require additional testing. Current plans call for the installation of these detectors into the instrument in December 2007, followed by their testing and calibration within the instrument in February-March 2008.

1.5 Special Considerations for Cycle 17

1.5.1 WFC3 is Still Under Development

It should be noted that SM4 has not yet occurred at this writing, and that the instrument is still undergoing testing as described in Section 1.4.

Thus the information provided in this *Handbook,* although as accurate as possible at the time of writing, will remain somewhat uncertain until post-SM4 testing and calibration has been accomplished.

Proposers and users of WFC3 should monitor the Cycle 17 Web site for the latest information:

http://www.stsci.edu/hst/proposing/docs/cycle17announce

1.5.2 Return to Three-Gyro Mode in Cycle 17

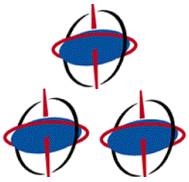

We anticipate that all HST observations in Cycle 17 will be undertaken in the Three-Gyro Science Mode, providing greater scheduling flexibility and greater sky coverage (at a given time) than in Cycles 14, 15 and 16.

Proposers should plan their observations accordingly, using the target availability table in the Primer (Table 6.1 in Section 3) at:

`http://www.stsci.edu/hst/proposing/documents/cp/primer_cover_.html`

and the visibility tools on the HST Phase 1 Proposal Roadmap Web site, step 12 at:

`http://apst.stsci.edu/apt/external/help/roadmap1.html`

1.6 Sources of Further Information

Table 1.1 provides a guide to online documents containing further information about *HST*, the proposal process, and data analysis.

Table 1.1: Useful documents.

Purpose	Document or resource
General observatory information	HST Primer http://www.stsci.edu/hst/proposing/docs/proposing/documents/cp/primer.pdf
Phase I proposals	Proposing Overview http://www.stsci.edu/hst/proposing/docs/proposingOverview Call for Proposals http://www.stsci.edu/hst/proposing/documents/cp/cp_cover.html
Phase II programs	Phase II Proposal Instructions http://www.stsci.edu/hst/programs/hst/proposing/docs/p2pi.html Astronomer's Proposal Tool (APT) for Phase I and II preparations http://apt.stsci.edu/
Data analysis and instrument characteristics	General WFC3 Information and Updates http://www.stsci.edu/hst/wfc3 WFC3 Data Handbook (Available late in Cycle 17) Dither Handbook http://www.stsci.edu/hst/wfpc2/documents/dither_handbook.html Space Telescope Analysis Newsletter http://www.stsci.edu/hst/acs/documents/isrs/hst/acs/documents/newsletters WFC3 Instrument Science Reports (ISRs) http://www.stsci.edu/hst/wfc3/documents/ISRs Calibration and Pipeline Information http://www.stsci.edu/hst/Post-observation

Proposers who desire more detailed information about WFC3 capabilities should refer to the WFC3 Instrument Science Reports (ISRs; see link in Table 1.1), which contain extensive details about all aspects of the instrument. Proposers may also seek further assistance as described in the next section.

1.7 The WFC3 Instrument Team at STScI

STScI supports a team of Instrument Scientists, Data Analysts, Engineers, and Scientific Programmers, who support the design, development, operation, calibration, and documentation of WFC3. STScI also maintains a "Help Desk" to provide answers quickly to any WFC3- and *HST*-related questions. Please refer all questions regarding WFC3 and *HST* to the Help Desk, as follows:

- E-mail: help@stsci.edu
- Phone: (410) 338-1082

CHAPTER 2:

WFC3 Instrument Description

In this chapter . . .

2.1 Optical Design and Detectors

The optical design of WFC3 was driven by the need to provide a large field of view and high sensitivity over a broad wavelength range, excellent spatial resolution, and stable and accurate photometric performance. WFC3 features two independent imaging cameras: the **UV/optical channel** (**UVIS**) and the **near-infrared channel** (**IR**). Figure 2.1 shows a schematic diagram of the instrument's optical and mechanical layout.

On-axis light coming from the *HST* optical telescope assembly (OTA) is intercepted by the flat 45° WFC3 pick-off mirror (POM) and directed into the instrument. A channel-select mechanism (CSM) inside WFC3 then diverts the light to the IR channel via a fold mirror, or the CSM mirror can be removed from the beam to allow light to enter the UVIS channel. Because of this design, only a single channel, either UVIS or IR, can be used at any one time, although it is possible to switch between them fairly quickly.

Optical elements in each channel (anamorphic aspherical correctors) correct separately for the ~1/2 wave spherical aberration of the *HST* primary mirror. Both channels also have internal flat-field illumination sources.

Two different types of detectors are used in the two channels. The UVIS channel uses two butted 4096×2051 thinned, back-illuminated e2v Ltd. (formerly Marconi) CCD detectors to support imaging between 200 and 1000 nm. The IR channel uses a

1024×1024 Teledyne (formerly Rockwell Scientific) HgCdTe detector array, with the central 1014×1014 pixels useful for imaging, and covering the near-infrared between 800 and 1700 nm.

The primary characteristics of the two channels are summarized in Table 2.1.

Table 2.1: Characteristics of the two WFC3 channels.

Channel	*f*-ratio	Detector type	Spectral range (nm)	Detector pixel format	Pixel scale (arcsec)	Field of view (arcsec)
UVIS	31	CCD	200-1000	2×2051×4096	0.0395×0.0395	162×162
IR	11	HgCdTe	800-1700	1014×1014	0.121×0.135	123×136

Figure 2.1: Schematic optical layout of the WFC3 instrument. Note that for schematic simplicity, the incoming OTA beam and POM have been rotated into the plane of the optical diagram. The actual incoming OTA beam direction is into the page and then reflected by the POM into the instrument. Yellow indicates light from the OTA, which is sent into the camera by the pick-off mirror. The Channel Select Mechanism then either allows light to pass into the UVIS channel (blue path), or directs light into the IR channel (red path). Mechanisms and optics in both channels allow for focus and alignment, and correct for the OTA spherical aberration. Filters and grisms are contained in the UVIS SOFA and the IR FSM. The UVIS channel has a mechanical shutter, while the IR channel is shuttered electronically by the detector. Light is detected by either the UVIS CCDs or the IR focal-plane array. A separate subsystem provides flat field illumination for both channels.

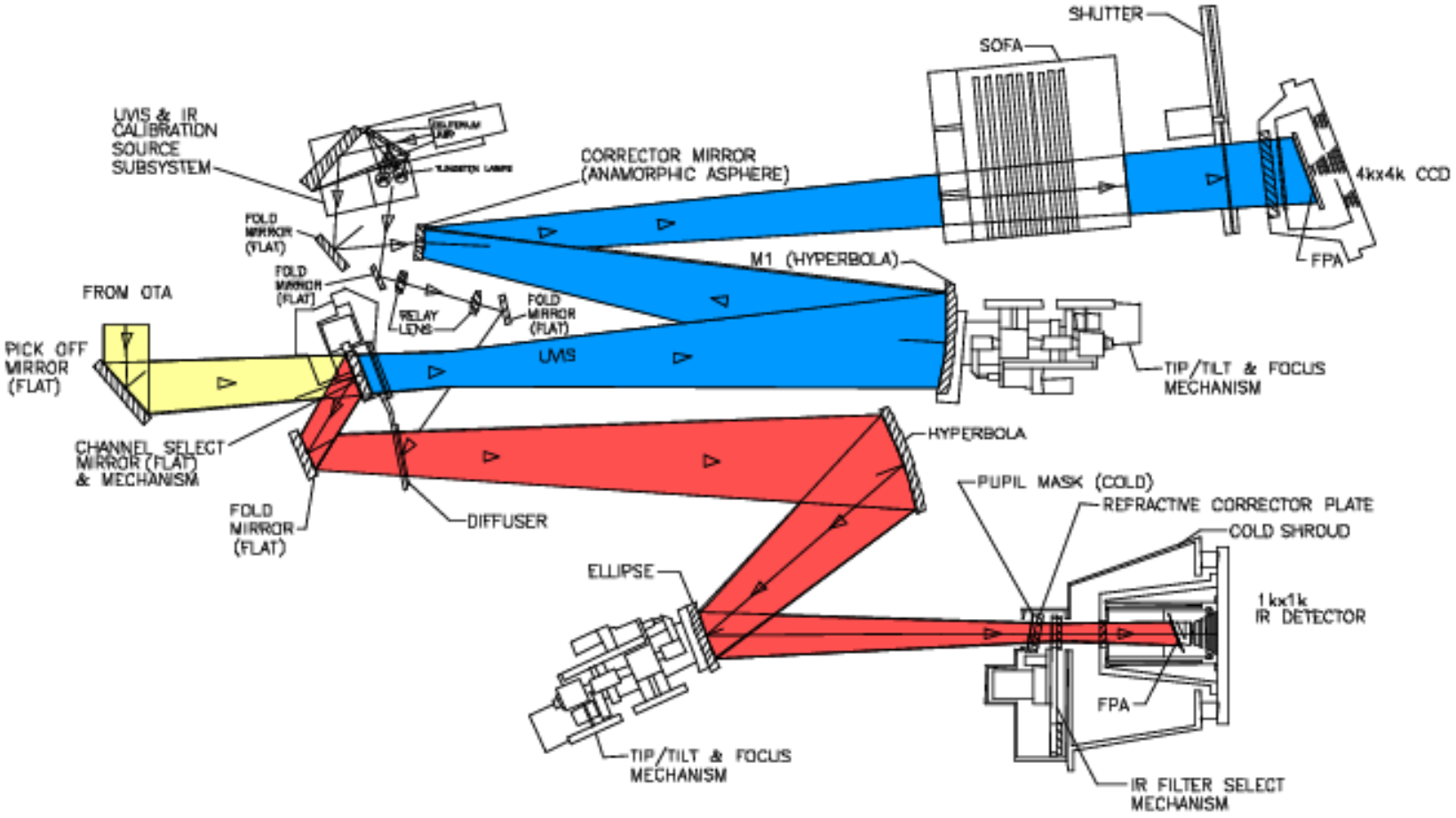

2.2 Field of View and Geometric Distortions

WFC3 replaces WFPC2, *Hubble*'s first large-area camera that included corrections for the spherical aberration of the *HST* primary mirror. The appearance of the *HST* focal plane following a fully successful SM4 is shown in Figure 2.2.

Figure 2.2: The *HST* focal-plane layout, showing the instrument complement following a successful SM4. The diameter of the outer black circle, projected onto the sky, is about 28 arcminutes.

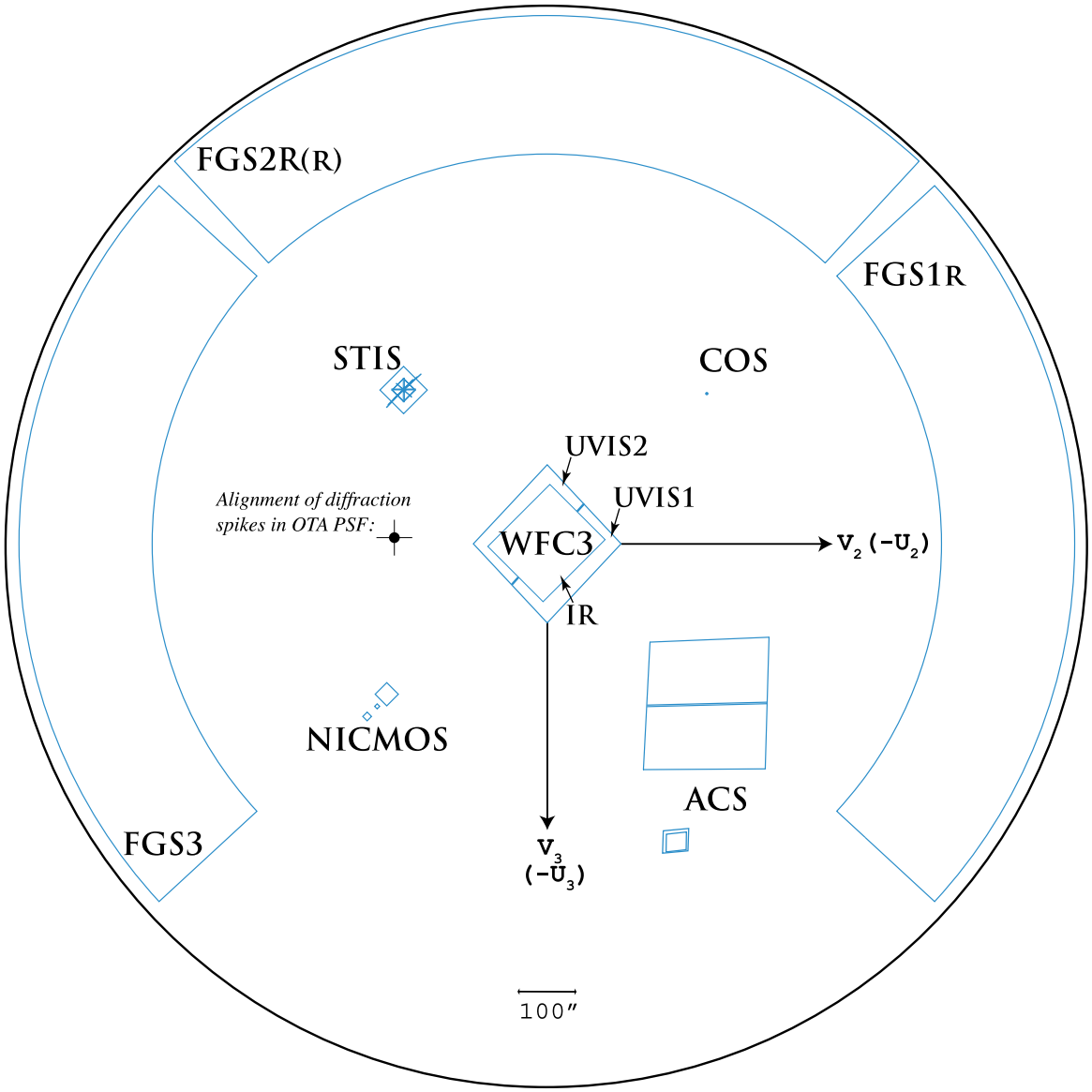

As is the case for ACS, WFC3 images are subject to significant geometric distortions. These result primarily from the tilt of the focal plane relative to the optical axis (required for constant focus across the detectors; see Figure 2.1), which leads to a modest elongation of the field of view in both channels. In the UVIS detector, most of

the distortion runs approximately parallel to the diagonal direction of the CCD, while in the IR channel the distortion is parallel to the sides of the detector. As a result, the UVIS field projected onto the sky is shaped like a rhombus, with an acute angle between the *x*- and *y*-axes of the detector of approximately 86.1°. The IR channel projected onto the sky is rectangular, with an aspect ratio of about 0.90. Individual pixels projected onto the sky will have the same geometry; thus the UVIS pixels are rhomboidal, measuring 0.0395 arcsec on each side, while the IR pixels are rectangular, measuring 0.121×0.135 arcsec.

For further discussion of geometric distortions in WFC3, see Appendix B.

2.3 Spectral Elements

2.3.1 The Filter Selection Process

Both WFC3 channels are equipped with a broad selection of spectral elements. These elements were chosen on recommendation of the WFC3 SOC, following a lengthy process with wide scientific and community input. Initial community suggestions and advice were considered at the WFC3 Filter Selection Workshop, held at STScI on July 14, 1999. Other input came from the WFC3 Science White Paper (see Section 1.2), from a suite of SOC-developed test proposals representing a broad range of current astronomical investigations, and from statistics of historical filter use in previous *HST* imaging instruments. The filter sets were chosen to fully cover the wavelength regimes of both WFC3 channels with a range of bandwidths, while complementing the filter sets available in ACS and NICMOS.

Based upon the SOC recommendations, the WFC3 IPT (see Section 1.1) developed detailed specifications for the vendors who designed and manufactured the filters. The final flight spectral elements were fully characterized, evaluated by the IPT and SOC, approved for flight, and installed into the filter wheels.

2.3.2 Filter and Grism Summaries

On the UVIS side, the selectable optical filter assembly (SOFA) contains a stack of 12 filter wheels housing a total of 48 elements: 42 full-frame filters, 5 quad filters, and 1 UV grism. Each wheel also has an open, or empty, slot. For UVIS observations, the appropriate wheel is rotated to place the chosen filter into the light path, and the other eleven wheels are rotated to place the open slot in the light path.

The IR channel has a single filter wheel housing 17 elements: 15 filters and 2 grisms; an 18th slot contains a blank, opaque blocker. For IR observations, the requested single element is rotated into the light beam.

The filter assortments in both channels include wide-, medium-, and narrow-band filters, as well as low-dispersion grisms (one in the UVIS channel, two in the IR channel) for slitless spectroscopy. The wide- and medium-band filters include most of

the popular passbands used in extragalactic, stellar, and solar-system astronomy, as well as passbands similar to those already used in other *HST* instruments for photometric consistency and continuity. The classical *UBVRIJH*, Strömgren, and Washington systems are reproduced, along with the filters of the Sloan Digital Sky Survey (SDSS). In addition, several extremely wide-band filters have been included in both channels, for ultra-deep imaging.

There is also a total of 36 different narrow-band passbands in the UVIS channel, consisting of 16 full-field filters and 5 quad filters. (Quad filters are 2×2 mosaics occupying a single filter slot; each one provides four different bandpasses, at the cost of each one covering only about 1/6 of the field of view.) The narrow-band filters provide the capability for high-resolution emission-line imaging in many of the astrophysically important transitions, as well as the methane absorption bands seen in planets, cool stars, and brown dwarfs.

In addition to the wide-band filters, the IR channel includes six narrow-band filters, which likewise sample the most important planetary, stellar, and nebular spectral features in the near-IR.

Finally, wide-band filters with similar wavelength coverages to those of the grism dispersers are available, allowing direct images of spectroscopic targets in the same spectral regions; such images allow accurate identification of the sources as well as providing wavelength calibration.

Unlike ACS or WFPC2, no ramp filters or polarizers are included in either WFC3 channel.

Table 6.2 and Table 7.2 provide a complete summary of the filters available for imaging with the UVIS and IR channels, respectively. Individual filter transmission curves as well as filter+WFC3+HST system throughput curves are presented in Appendix A. Figure 3.2 shows the overall integrated system throughputs of WFC3 compared to other instruments.

2.4 Detector Read-Out Modes and Dithering

The detectors in both channels offer readouts of subarrays, and the UVIS channel also allows on-chip binning. A variety of dithering schemes will be offered to observers by the Astronomer's Proposal Tool (APT) software, including specially designed "canned" patterns as well as user-defined ones. See Appendix C for details.

The post-observation pipeline software (see Appendix E) will carry out calibration of data taken in all of these configurations, and will offer the option of reconstructing dithered images with a drizzling algorithm. If the dither pattern incorporates non-integer pixel offsets, it effectively improves the sampling of the point-spread function (PSF). The software will also handle mosaicked images according to a set of rules or associations, and will rectify them onto a cartesian pixel coordinate system.

CHAPTER 3:

Choosing the Optimum *HST* Instrument

In this chapter . . .

3.1 Overview

This chapter addresses the general questions that arise when observers choose between proposing to use WFC3 or one or more of the other imaging instruments that are, or may be, available on *HST*.

For Cycle 17, the choice is complicated by uncertainties related to the upcoming SM4. Current plans for SM4 are not only to install WFC3 in place of WFPC2, but to repair both STIS and the ACS WFC and HRC channels (ACS/SBC remains operational at this writing). In this chapter, we have made the assumption that all of the SM4 installations and repairs will be successful.

In choosing between instruments for their particular projects, observers should carefully evaluate the capabilities of WFC3 and compare them to those of the other *HST* instruments, in the context of their own scientific goals. Observers should especially note that WFC3 intentionally provides some redundancy with the ACS and NICMOS instruments, in order to provide some protection against potential failures of either of those instruments. On the other hand, WFC3 also differs from those instruments (in fact, it largely complements them). Therefore, observers do need to give careful consideration to instrument capabilities in order to optimize their observations and should refer to the HST Call for Proposals for any policy issues.

3.2 Choosing Between Instruments

The primary factors to consider in choosing the best instrument are areal coverage, spatial resolution, wavelength coverage, sensitivity, and availability of specific spectral elements. Table 3.1 lists the primary characteristics of the imaging instruments that will be available on *HST* following a fully successful SM4.

For some research programs, the instrument choice may be dictated by the need for a particular spectral element. In this regard, WFC3 offers considerable capability because of its broad complement of wide-, medium-, and narrow-band filters both at UV/optical and near-IR wavelengths, as well as one UV grism and two near-IR grisms for slitless spectroscopy.

For studies at optical wavelengths, the trade-offs to consider when deciding between WFC3/UVIS and ACS/WFC include pixel size, field of view and, to some extent, throughput. WFC3 is generally preferable when angular resolution has higher priority than field of view, because of its finer pixel size. On the other hand, ACS/WFC has higher throughput than WFC3/UVIS at wavelengths longward of ~400 nm (see Figure 3.2), and hence it should be used if the highest possible sensitivity at such wavelengths is crucial. However, considerations of degraded charge-transfer efficiency (CTE) should also be kept in mind, since ACS will have been in the high-radiation space environment for more than six years at the time when WFC3 comes on line.

At UV wavelengths, WFC3/UVIS is the only imager on *HST* to offer a large field of view combined with high throughput. However, its spectral coverage does not extend shortward of 200 nm, whereas ACS/SBC and STIS/FUV-MAMA both reach down to 115 nm (STIS/NUV-MAMA reaches 160 nm), and also offer finer spatial sampling (see Table 3.1). Thus, WFC3 will be the choice whenever both large field of view and coverage down to 200 nm are required (e.g., multi-wavelength surveys). However, if observations at extreme far-UV wavelengths are necessary, or if the highest available spatial sampling is a primary requirement, then ACS/HRC, ACS/SBC, or the STIS UV channels should be considered.

At near-IR wavelengths WFC3/IR offers a much larger field of view and, generally, higher throughput than NICMOS. It also offers greatly improved sensitivity and ease of data reduction and calibration, due to the accurate bias subtraction made possible by the presence of reference pixels. However, WFC3 sensitivity is limited to wavelengths shortward of ~1700 nm, and WFC3 has coarser pixel sizes than NIC1 and NIC2, and does not offer a coronagraph or polarizers.

3.3 Comparison of WFC3 with Other *HST* Imaging Instruments

3.3.1 Wavelength Coverage

The WFC3 UVIS channel is similar in design to the Wide Field Channel (WFC) of the ACS. There are, however, a few differences. While ACS/WFC is blind at wavelengths shorter than about 370 nm (i.e., shortward of the *B* band), WFC3/UVIS has sensitivity extending down to 200 nm. The design trade-offs adopted to achieve this extended UV wavelength coverage (primarily the CCD coating and the use of aluminum coatings for the reflective optics) lead to a reduced sensitivity of WFC3 at longer optical wavelengths compared to that of ACS/WFC.

The ACS does have UV sensitivity in its High Resolution Channel (HRC). However, compared to ACS/HRC, WFC3/UVIS has a factor of 2 higher throughput at the *U* band (see Figure 3.2), and a field of view 35 times the area (but with spatial sampling that is 50% coarser). WFC3/UVIS has no sensitivity in the far-UV region below 200 nm. The far-UV is covered by the ACS Solar-Blind Channel (SBC) and by the Space Telescope Imaging Spectrograph (STIS) FUV-MAMA.

The WFC3 IR channel also provides nearly a factor of 2 improvement in sensitivity over NICMOS. However, its wavelength coverage is shorter, ending at about 1700 nm (compared with 2500 nm for NICMOS). The WFC3/IR cutoff at 1700 nm greatly reduces the instrument's sensitivity to the thermal background. Unlike NICMOS, the WFC3 IR channel does not have a cryogenic dewar for cooling of instrument components; instead, all optical components of the IR channel are actively cooled by a thermal-control subsystem. Although much simpler than the NICMOS cryocooler, this design allows the IR detector to be cooled only to ~145 K; also, the view of warmer components precludes suppression of the thermal background at wavelengths longer than ~1700 nm.

3.3.2 Field of View

Figure 3.1 schematically illustrates the fields of view, on the same scale, for all of the *HST* imaging instruments that will be available following a fully successful SM4.

Figure 3.1: Schematic diagram comparing relative sizes of the fields of view for all *HST* imaging instruments. Successive lines of text underneath each field of view give the field size in pixels, the pixel scale in arcseconds, and the field size in arcseconds. The diagram is schematic, and does not illustrate geometric distortions nor the relative locations in the *HST* focal plane.

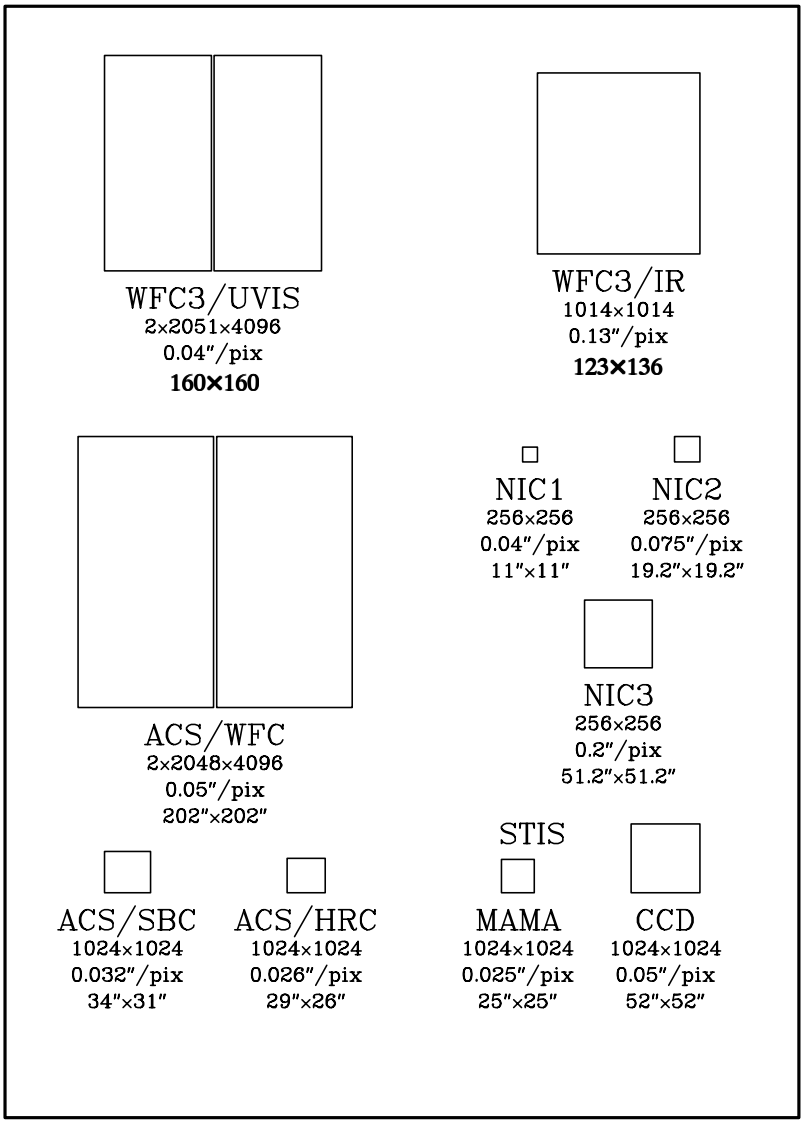

The WFC3 UVIS channel provides about 20% linearly finer pixels than ACS/WFC, obtained at the cost of covering only about 66% of the area of the latter's field of view.

The WFC3 IR channel covers about 6.4 times the area of the NICMOS NIC3 channel, with almost 2-times better spatial sampling, but it lacks the very high spatial samplings offered by the NICMOS/NIC1 and NIC2 channels. Further, the WFC3/IR channel covers 45 times the area of NICMOS/NIC2 channel with slightly coarser sampling, but arguable better photometric precision.

Table 3.1 presents a comparison of the wavelength coverage, pixel scale, and field of view of WFC3 and of the other *HST* imaging instruments that will be available following a successful SM4.

Table 3.1: Comparison of wavelength coverage, pixel scales, and fields of view of *HST*'s imaging instruments.

Instrument	Wavelength coverage (nm)	Pixel size (arcsec)	Field of View (arcsec)
WFC3 UVIS	**200 – 1000**	**0.04**	**162×162**
ACS WFC	370 – 1100	0.05	202×202
ACS HRC	200 – 1100	0.027	29×25
ACS SBC	115 – 170	0.032	34×31
STIS FUV-MAMA	115 – 170	0.024	25×25
STIS NUV-MAMA	165 – 310	0.024	25×25
STIS CCD	250 – 1100	0.05	52×52
WFC3 IR	**800 – 1700**	**0.13**	**123×136**
NICMOS NIC1	800 – 1900	0.043	11×11
NICMOS NIC2	800 – 2500	0.076	19×19
NICMOS NIC3	800 – 2500	0.20	51×51

3.3.3 Detector Performance

The UVIS and IR detectors are anticipated to have excellent performance in terms of read-out noise and dark current.

Table 3.2 summarizes our current estimates of these properties for the WFC3 flight detectors, and compares them with the parameters for other HST imaging detectors that will be available following a successful SM4.

Chapter 5 gives more detailed information about the detectors in both channels. Chapter 9 discusses sensitivities, limiting magnitudes, and exposure times.

Table 3.2: Characteristics of *HST* imaging detectors available after SM4. The WFC3/IR dark current includes the instrument thermal background.

Detector	Read-out noise (e^- rms)	Dark current (e^-/pix/s)
WFC3/UVIS	**3.1**	**<0.00014**
ACS/WFC	5.0	0.0038
ACS/HRC	4.7	0.0044
STIS/CCD	4.2 (gain=1), 7.6 (gain=4)	0.0025
WFC3/IR	**21**	**<0.05**
NICMOS/NIC2	26	0.110
NICMOS/NIC3	29	0.202

3.3.4 System Throughputs and Discovery Efficiencies

Figure 3.2 plots the expected system throughputs of the two WFC3 channels as functions of wavelength, compared to those of ACS, NICMOS, and WFPC2. These curves include the throughput of the OTA, all of the optical elements of the instruments themselves, and the sensitivities of the detectors. Throughputs were calculated at the central wavelength (the "pivot wavelength"; see footnote 3 to Table 6.2) of each wide-band filter of each instrument. The WFC3 throughputs are based on the currently selected flight detectors, and are still subject to change at this writing based on further laboratory measurements and the final IR detector choice.

As Figure 3.2 shows, WFC3 offers a unique combination of high sensitivity and wide spectral coverage ranging from the UV to the near-IR. WFC3 extends and complements, over a large field of view, the optical performance of ACS/WFC at wavelengths shorter than ~400 nm and longer than 1000 nm. The good degree of functional redundancy with ACS and NICMOS will help ensure that the unique scientific capabilities of *HST* will remain available until the end of its mission.

Another quantity that is useful when comparing different instruments, especially in the context of wide-angle surveys, is the "discovery efficiency," defined as system throughput times area of the field of view as projected onto the sky. In Figure 3.3 we plot the discovery efficiencies of the *HST* imaging instruments, again vs. wavelength. Note that the *y*-axis is now logarithmic. This figure dramatically illustrates the enormous gains that WFC3 will offer, compared to previous *HST* instruments, both in the optical/UV below 400 nm, and in the near-IR.

Figure 3.2: System throughputs of imaging instruments on *HST* as functions of wavelength. The plotted quantities are end-to-end throughputs, including filter transmissions, calculated at the pivot wavelength of each wide-band filter of each camera.

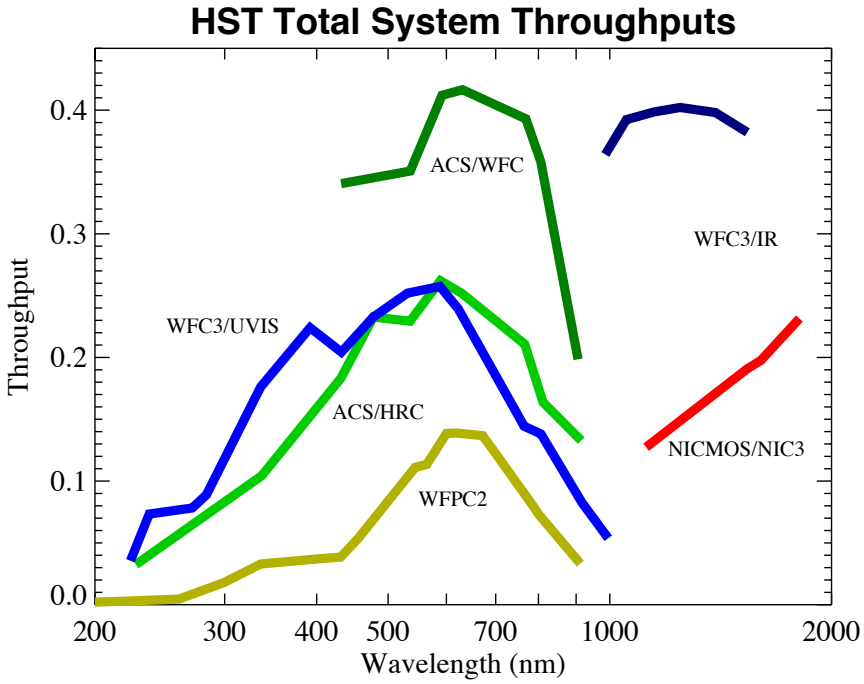

Figure 3.3: Discovery efficiencies of *HST* imaging instruments, including those expected for WFC3. Discovery efficiency is defined as the system throughput (plotted in Figure 3.2) multiplied by the area of the field of view. Note that the y-axis is now logarithmic.

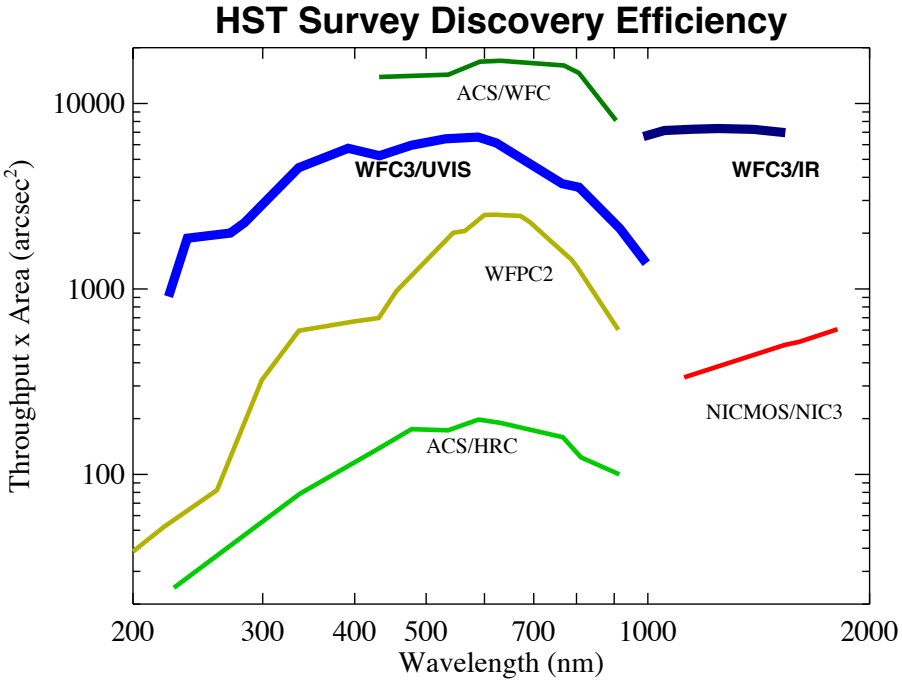

CHAPTER 4:

Designing a Phase I WFC3 Proposal

In this chapter . . .

4.1 Phase I and Phase II Proposals

In this Chapter we give an overview of the steps that are taken in preparing an HST observing proposal that involves WFC3 observations. "**Phase I**" refers to the initial proposal that is reviewed by the Telescope Allocation Committee (TAC). The Phase I proposal presents the scientific justification for the project, lists the targets to be observed and the instrument(s) to be used, and includes a request for a specific number of spacecraft orbits. (See the HST Call for Proposals for a full discussion of all policy issues.)

Only those proposals accepted by the TAC and approved by the STScI Director proceed to "**Phase II**," in which full details of the observations are specified.

The actual submission of proposals in both Phase I and Phase II is accomplished using the **Astronomer's Proposal Tool** (**APT**); see http://apt.stsci.edu.

This Chapter focuses on the steps for assembling the information needed to prepare a Phase I WFC3 proposal for submission using APT**.**

4.2 Preparing a Phase I Proposal

An HST program is a set of exposures specified so as to achieve one or more scientific objectives. We can break down the development of a WFC3 observing program, imaging and/or spectroscopic, into a six-step process. Often there is not a

unique way in which to achieve the scientific objectives, and you must assess their trade-offs and feasibilities. Furthermore, you will wish to use HST and WFC3 efficiently, in order to obtain as much science within as small an orbit allocation as possible. Therefore, you may need to iterate these steps in order to achieve a final feasible program that is also optimal.

In this chapter we introduce issues that you may need to consider in designing your observations. Later chapters in this *Handbook* will present detailed information for your use. These six steps, and the considerations they entail, are described in the following subsections.

4.2.1 Which WFC3 Channel(s) and Filter(s)?

First, from your science requirements, determine the desired wavelength(s) of observation. Those requirements may include considerations of the spectral energy distribution (SED) of the target, or the required angular resolution, which also varies as a function of wavelength. Typically, if the wavelength of observation is less than 1000 nm, then the WFC3 UVIS channel will be used; or if the wavelength is greater than 1000 nm, then the WFC3 IR channel will be used. Of course, if your program is panchromatic, it may involve use of both channels.

The angular resolution, field of view, and sensitivity of the two channels differ appreciably, and may also influence your selection of the WFC3 channel(s) to use (see Chapter 2 for an overview of the UVIS and IR channels). Features of interest in the target's SED can be matched to the spectral resolution of the observation by selecting appropriate filters (see Chapter 6 for the UVIS channel, Chapter 7 for the IR channel, and Appendix A.1 for detailed filter passbands), or grisms (see Chapter 8).

To match continuum features, wide-, medium-, and/or narrow-band filters may be selected, presenting the possibility of a trade-off between detector signal and spectral resolution. Note that the UVIS quad filters limit the field of view to one quadrant of the full field.

4.2.2 What Exposure Times?

Second, you should determine the exposure time and exposure sequences needed to achieve the required signal-to-noise (S/N) with the chosen filter(s) or grism(s). A full discussion of calculating the exposure time is presented in Chapter 9, but, as mentioned in that chapter, in most cases you will use the online Exposure Time Calculator (ETC). The S/N depends upon the target's incident flux and the noise from the background and detector sources. These sources include zodiacal light, detector dark current, and stray light from both Earth and bright targets in the field of view.

Having determined the basic exposure time necessary to achieve the required S/N, you will in most cases find it necessary to achieve that total exposure time through a sequence of shorter exposures. For instance, if the exposure time is greater than the maximum orbital target visibility, it will be necessary to obtain a sequence of

exposures. UVIS exposures exceeding 3,600 s require more than one exposure as do IR exposures greater than 2,800 s (see Chapter 6 and Chapter 7 for a fuller discussion).

Additional reasons to structure the total exposure time are described in the following paragraphs, as well as considerations peculiar to each of the two WFC3 channels.

Dithering and Mosaicking

A sequence of exposures obtained in a dither pattern of *HST* pointings will often be used to reduce the noise from flat-field calibration error. Including sub-pixel displacements in the dither pattern will allow better sampling of the point-spread function (PSF). You may design and specify a dither pattern, or use one of the pre-defined patterns already designed to sub-sample the PSF, to cover the UVIS inter-chip gap, or to mosaic a large field. The pre-defined sequences are presented in the Phase II Proposal Instructions, and information on designing your own patterns is presented in Appendix C of this *Handbook*.

Bright Targets

For bright targets, a sequence of shorter exposures may be needed to avoid entering the non-linear or saturation regimes of the detectors (see Chapters 5, 6, and 7).

Saturated images of bright targets may leave a persistent image of that target in subsequent images, which could degrade the quality of the image at the same position of a faint target, as described in Appendix D.

UVIS Exposures

For UVIS observations, it will almost always also be desirable to use a sequence of exposures, in order to remove cosmic-ray impacts. For observations with the UVIS channel of faint targets, the effects of charge-transfer efficiency (CTE) during readout of the detector must be considered (see Chapters 5 and 6). Charge injection for such images will mitigate the non-ideal CTE, but are not necessary at present and will only be offered after Cycle 17.

IR Exposures

For observations with the IR channel you must choose a readout method from the 16 available kinds of sample sequences, each of which may comprise from 1 to 15 non-destructive readouts. These include RAPID, up-the-ramp (SPARS and STEP), and Fowler (MIF) sequences (see Chapter 7). The exposure time is dictated by the sequence chosen. The ability to remove cosmic-ray impacts will depend upon the sequence chosen.

4.2.3 What Aperture or Subarray?

Next, from considerations of the target's angular size and structure, and of data volume, you should determine the WFC3 aperture or subarray you will use. The available UVIS apertures and subarrays are presented in Chapter 6, and those for the IR channel in Chapter 7.

In some cases, correct placement of an extended target within an aperture may require you to specify a special *HST* pointing and possibly the orientation of the field of view (which is determined by the spacecraft roll angle). Additional considerations may include detector imperfections such as the UVIS inter-chip gap (Chapter 5),

diffraction spikes (Chapters 6 & 7), filter ghost images (see Chapters 6 & 7), detector saturation (i.e., for bleeding in a UVIS image along a detector column; Chapter 5), detector charge transfer (Chapter 5), distortion of the image (Appendix B), or dispersion direction of the grism (see Chapter 8). However, most of these only need to be considered at the Phase II stage, unless they affect the number of orbits needed for the proposal.

Note that selection of a WFC3 aperture without specifying further constraints implicitly specifies: (1) the full image will be read out; (2) the target coordinates will be placed at a default location on the detector (see Chapters 6 & 7; generally the target will be placed at the center of the chosen field of view); and (3) the telescope roll angle will be unspecified, as it will depend on the date the exposure is executed. You may override any of these defaults, however.

You can reduce the size of the image read out and thus the volume of data obtained by selecting a subarray. For the UVIS detector, on-chip binning of the pixels will also reduce the data volume, but at the expense of angular resolution (see Chapters 5 & 6). Reducing the data volume will reduce the overhead to read out and transfer images, which may be desirable in order to allow more images of the target of interest to be obtained during an *HST* orbit. The location of the target can be specified with the POS TARG Special Requirement and the rotation of the image can be specified with the ORIENT Special Requirement (see Chapters 6 & 7).

4.2.4 What Overheads and How Many HST Orbits?

Fourth, determine the overhead times required, in addition to the exposure times, in order to operate the spacecraft and the camera (see Chapter 10).

The spacecraft overhead includes the time needed for guide-star acquisition or re-acquisition at the beginning of each orbit. The camera overheads include time needed to change filters, change between the UVIS and IR channels, read out the exposure to the WFC3 data buffer, and transfer the images from the buffer to the *HST* science data storage. Note that overheads are especially severe for sequences of short exposures, but these can sometimes be mitigated by using small subarrays.

Finally, you will add the overhead times to the exposure times to find the total time needed for your program, which is what you will request in your Phase I proposal.

This total time is expressed as the (integer) number of *HST* orbits required to obtain the observations.

4.2.5 Any Special Observations?

You may find that non-standard observations are necessary for your particular program. The available non-standard capabilities include user-defined UVIS subarrays (see Section 6.4.4).

It is also possible that your program may require calibration of WFC3 to greater accuracy than the standard calibrations (Appendix E) provide. If so, you may need to propose additional observations to better calibrate your science program. These

additional observations must be justified in your proposal submission, and you must request the number of additional orbits needed to accomplish them.

Unsupported modes of operating WFC3 should be discussed with the Help Desk.

4.2.6 What is the Total Orbit Request?

Having determined the content of the science and supporting observations necessary to achieve your scientific objectives, you must finally determine the total amount of *HST* time to carry out those activities by including the appropriate amount of time for spacecraft and instrument overheads.

Detailed procedures for determining the total amount of time to request in your Phase I proposal are presented in Chapter 10.

CHAPTER 5:

WFC3 Detector Characteristics and Performance

In this chapter . . .

5.1 Overview of this Chapter

This chapter describes the detectors used in the UVIS and IR channels of WFC3. All observers should have a basic understanding of how the detectors operate, and of their characteristics and limitations. For the most demanding observations, for example at very faint or extremely bright source levels, or for exposures using non-default parameters, a fuller understanding of the detectors may be needed. This chapter provides both basic and in-depth information on the detectors used in both WFC3 channels. Sections 5.2-5.4 discuss the CCD detectors used in the UVIS channel, and Sections 5.5-5.7 discuss the infrared detector used in the IR channel.

Table 5.1 summarizes the basic parameters of the CCD and IR detectors. For the CCDs the information is either an average for the two chips, or the range of values for both of them. The detectors listed in the table are the flight candidates at the time this is written (November 2007), but it is possible that other detectors could actually be flown, with similar but not necessarily identical characteristics.

Table 5.1: WFC3 Detector Characteristics

Characteristic	UVIS Channel CCDs	IR Channel Detector[1]
Architecture	e2v CCD detectors. Thinned, backside illuminated, UV optimized, multi-phase pinned, buried/mini-channel, charge injection capability.	Teledyne HgCdTe infrared detector. MBE-grown, substrate removed, on Si CMOS Hawaii-1R multiplexer.
Wavelength Range	200 to 1000 nm	800 to 1700 nm
Pixel Format	2 butted 2051 × 4096, 35 pixel gap	1024 × 1024 (1014 × 1014 active)
Pixel Size	15 μm × 15 μm	18 μm × 18 μm
Plate Scale	0.040 ”/pixel	0.13 "/pixel
Field of View on Sky	Rhomboidal, 162" × 162"	Rectangular, 123" × 136"
Quantum Efficiency	50-59% @ 250 nm 68-69% @ 600 nm 47-52% @ 800 nm	77% @ 1000 nm 79% @ 1400 nm 79% @ 1650 nm
Dark Count	0.16-0.41 e^-/hr/pixel (mean)	0.011 e^-/s/pixel (mode) 0.015 e^-/s/pixel (median)
Readout Noise	3.1 e^-	15.5 e^-(16-read linear fit)
Full Well[1]	75,000-80,000 e^-	93,000 e^-(95% linearity) 100,000 e^-(saturation)
Gain	1.5 e^-/DN	2.5 e^-/DN
ADC Maximum	65,535 DN	65,535 DN
Operating Temperature	–83°C	145 K

1. The full well value for the CCD, and all measured IR parameters, are based on laboratory measurements of the detectors alone, not installed in the instrument, and are thus preliminary.

5.2 The WFC3 UVIS Channel CCD Detectors

5.2.1 Basics of CCD Operation

A charge-coupled device (CCD) is a silicon-based detector containing a two-dimensional array of summing wells, called pixels (short for “picture elements”). Each pixel accumulates electric charge in proportion to the number of photons striking that location on the detector. Physically, the summing wells are created by electric fields established at the depletion (charge-free) regions of the Si-SiO_2 metal-oxide-semiconductor (MOS) capacitors. In a typical three-phase CCD, the size

of the depletion region is controlled by the voltage of three gates. The gates are arranged in parallel, with every third gate connected together.

At the end of an exposure, by changing the voltage of the gates with an appropriate clocking pattern, all packets of charge are sequentially transferred to the adjacent pixel, until they reach the readout circuitry at the detector's edge. It is important to distinguish between parallel and serial charge transfers: the transfer of charges between pixels occurs in parallel, row by row, whereas the extraction of the “zeroth” row at the edge occurs along an external serial register, where each packet is serially transferred to an output amplifier at the detector corner.

5.2.2 The WFC3 CCDs

The WFC3 UVIS channel uses two CCD detectors fabricated by e2v Ltd. (formerly Marconi Applied Technologies Ltd.). Both CCDs are 2051×4096 devices with 15×15 micron square pixels. There are 2051 rows by 4096 columns, where the row/columns definition follows the convention of having the parallel direction first and the serial direction second. Having the serial register along the long (4096 pixel) edge reduces the number of transfers needed on the photo-sensitive pixels, which are more sensitive to radiation damage events.

The WFC3 CCDs are three-phase devices, thinned and back-illuminated (“back-thinned”) to improve the sensitivity to UV light. “Back-illumination” means that the image is focused on the back side of the chip, without having to pass through the opaque gate structure implanted on the front side. “Thinning” refers to the removal of the thick substrate on which the chip was originally built, which is done because only those electrons generated in the vicinity of the gate structure can be collected efficiently.

The WFC3 CCDs also have buried channels and are operated in multi-pinned phase (MPP) mode. This buried channel, or mini-channel, has improved CTE for targets with relatively low signal levels (~10K e^- or less).

The buried channels also have the capability of injecting charges to fill in the traps and improve the CTE. Further details of these features are given in Section 5.4.8.

The two WFC3 CCDs are butted together along their long dimension to create a 2×1 mosaic. Figure 5.1 shows a picture of a CCD assembly similar to that to be flown. The butted configuration is equivalent to a 4102×4096 array, but with a ~35-pixel gap between the two chips (~1.4 arcsec on the sky).

The CCDs are cooled by a four-stage thermoelectric cooler (TEC) that allows them to operate at a nominal temperature of −83°C. The detectors are packaged inside a cold enclosure, which is nearly identical to the one used for ACS, itself a scaled-up version of the STIS design. The package includes a second cooled window to reduce the radiative heat load.

The CCD focal plane is assembled on a molybdenum (moly) base disk, which provides some shielding from cosmic rays and also serves as the thermal sink path from the hot side of the TEC stack to the heat pipes (which carry the heat to the external radiator). The "cover" with the external window is about 1 cm thick and is

made of "alloy 42" steel; it provides some protection from CRs incident on the front side of the CCDs.

The WFC3 CCDs are quite similar to those used in the ACS Wide Field Channel (WFC). They have the same pixel size, nearly the same format (2051×4096 in WFC3, compared to 2048×4096 in ACS), the same orientation of the serial and parallel registers, similar technology (buried-channel, MPP operation, mini-channel), and nearly identical mechanical interfaces. The main differences of the WFC3 chips compared to those in ACS/WFC are:

- UV optimization of the WFC3 wavelength response
- Significantly lower readout noise for the WFC3 chips (~3.1 e^- compared to ~5 e^-)
- 2051 rows instead of 2048
- Charge-injection capability
- ~35 pixel gap instead of 50

An overview of the WFC3 CCD performance was given above in Table 5.1.

Figure 5.1: Detector package similar to the WFC3/UVIS flight detector. The size of the 4kx4k array is approximately 6x6 cm, and it consists of two butted 2051x4096 CCDs with a 35-pixel gap between them.

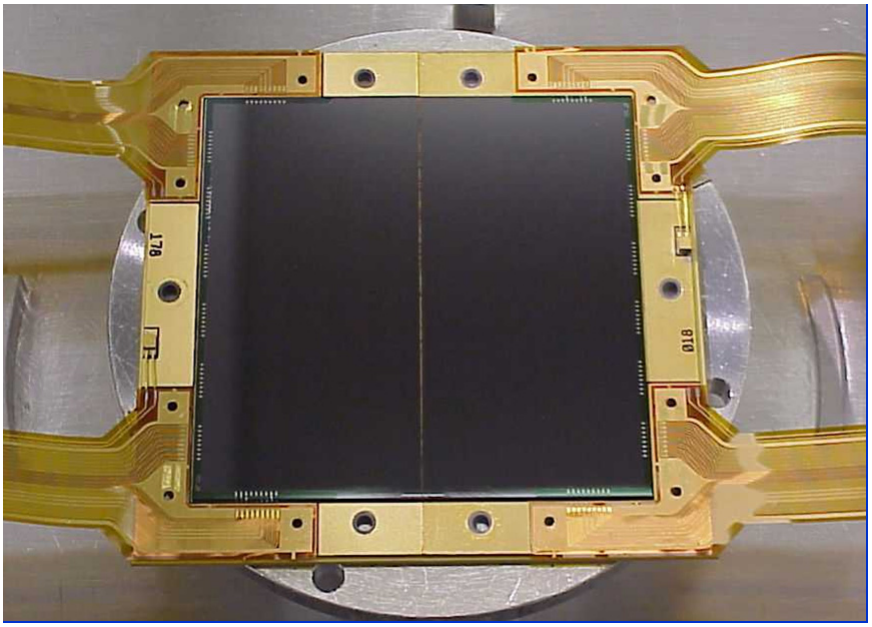

5.3 WFC3 CCD Readout Formats

5.3.1 Full-frame Readout

The WFC3 UVIS channel contains two CCD chips, each of which can be read out through two amplifiers. The amplifiers on Chip 1 are designated A and B, and those on Chip 2 as C and D. Although a chip may be read out through a single amplifier, the default and fastest readout mode employs all four amplifiers simultaneously, such that half of a chip is read out through each of the four amplifiers.

A single full-frame UVIS exposure produces a single FITS image file containing six extensions. The science image data from CCD Chip 2 are stored in extension [1] (sic) of the FITS file, and extensions [2] and [3] are used for data-quality flags and the error image. The science image data for CCD Chip 1 are stored in extension [4] (sic), and [5] and [6] are again used for data-quality flags and the error image for CCD Chip 1. Table 5.2 lists the chips, the associated amplifiers, and the FITS extensions of the science image data.

Whereas each CCD chip contains 2051x4096 pixels, the raw images returned by the WFC3 electronics contain a larger number of pixels. This is due to the detector overscan, a term which refers to portions of the detector which are not exposed to light. Overscan regions are useful for characterizing detector performance and efficiency.

Serial overscan corresponds to a fixed number of unexposed pixels at each end of each serial shift register. Conversely, parallel overscan is generated by additional parallel shifting before or after all of the exposed rows of the detector have been read out. Both serial and parallel overscan can be implemented either as physical overscan or virtual overscan. The physical overscan is a characteristic of the detector hardware, whereas virtual overscan is a software function, and the number of rows and columns of virtual overscan generated for an image is controllable via the readout timing pattern.

The overscan regions are described in more detail in Section 6.7.

Table 5.2: WFC3 CCD Naming Conventions.

CCD Chip	Amplifiers	Science Image FITS File Extension
1	A, B	[4]
2	C, D	[1]

5.3.2 Subarrays

The default mode is to read out all pixels of both CCD chips. However, it is possible to define rectangular subarrays. Only data from the area within the subarray are stored in buffer memory, and the rest of the image is discarded. The subarray size, in one or both detector axes, can be chosen from several pre-defined sizes, or specified by the observer.

UVIS subarray images contain no virtual overscan data, and serial physical overscan is present only if it is part of the defined subarray area.

Subarrays are discussed in detail in Section 6.4.4.

5.3.3 On-Chip Binning

The UVIS CCDs also provide an on-chip binning capability, in which several adjacent pixels may be read out as a single pixel. The available choices are 2x2 and 3x3 on-chip binning. If on-chip binning is used (again assuming four-amplifier readout), the overscan geometry is complicated by the need to truncate "odd" pixels, and each half of a row must be considered separately. With 2x2 binning, the first and last exposed pixels in each half of each row is combined with the adjacent overscan pixels. The last of the serial virtual overscan pixels in each half is not read out. There are 1051 binned pixels in each half: 12 physical overscan pixels, 1023 exposed pixels, two pixels consisting of combined overscan and exposed pixels, and 14 virtual overscan pixels. In the parallel direction, the physical row on each chip nearest the inter-detector gap will be combined with the adjacent overscan row. That leaves 1035 binned rows on each chip: 1025 exposed rows, one row consisting of combined overscan and exposed pixels, and 9 virtual overscan rows. The binned array size is 2070x2102.

With 3x3 binning, there are 701 binned pixels in each half of each row: 8 physical overscan pixels, one pixel combining the last physical overscan pixel with the first two exposed pixels, 682 exposed pixels, and 10 virtual overscan pixels (which should be adequate for bias subtraction). In the parallel direction, the two physical rows on each chip nearest the inter-detector gap will be combined with the adjacent virtual overscan row. That leaves 690 binned rows on each chip: 683 exposed rows, one row consisting of combined overscan and exposed pixels, and six virtual overscan rows. The binned array size is 1380x1402.

Two-amplifier readouts with on-chip binning proceed in a similar manner. With 2x2 binning, the first exposed pixel in each row will be combined with the last serial physical overscan pixel at the start of the row, and the last exposed pixel in each row will be combined with the first serial physical overscan pixel at the end of the row. Thus, each row will contain 12 binned serial physical overscan pixels, a single binned pixel from the addition of the last serial physical overscan pixel and the first exposed pixel, 2047 binned exposed pixels, a single binned pixel from the addition of the last exposed pixel and the first serial physical overscan pixel at the end of the row, 12 binned serial physical overscan pixels, and 29 binned serial virtual overscan pixels. In the parallel direction, the last exposed row (nearest the inter-chip gap) will be

combined with the first parallel virtual overscan row, leaving 1035 total rows from each chip. The final image size is 2070x2102.

With 3x3 binning, each binned row consists of 8 binned serial physical overscan pixels, one pixel from the addition of the last serial physical overscan pixel and the first two exposed pixels, 1364 binned exposed pixels, 1 binned pixel from the addition of the last two exposed pixels and the first serial physical overscan pixel, 8 binned serial physical overscan pixels, and 20 binned serial virtual overscan pixels. The parallel direction is treated identically to the four-amplifier readout with 3x3 binning, resulting, again, in a final image size of 1380x1402 pixels.

5.4 WFC3 CCD Characteristics and Performance

5.4.1 Quantum Efficiency

The quantum efficiencies (QEs) of the two WFC3 CCDs are plotted against wavelength in Figure 5.2. Here the QE is defined as electrons yielded per incident photon. The QEs were measured at the Detector Characterization Laboratory (DCL) at Goddard Space Flight Center. The plots demonstrate the high sensitivity of the CCDs in the UV down to 200 nm. On the other hand, the peak QE at ~600 nm is less than 70%, whereas the ACS/WFC detectors reach ~85% at their peaks.

The QE measurements were made with the detectors perpendicular to the incident light. As installed in WFC3, the CCDs are tilted by ~20 degrees with respect to the normal. The nominal change in thickness is ~6%, but the QE variations, as measured at the DCL on similar devices, turn out to be negligible.

5.4.2 Multiple-Electron Events at Short Wavelengths

In silicon, photons of energy higher than 3.1 eV (i.e., wavelength shorter than ~400 nm) can produce multiple electron-hole pairs when the energetic conduction-band electron collides with other valence-band electrons. At higher energies (energy above 3.65 eV, or wavelength below ~340 nm) the incident photons can directly extract more than one electron from the valence band. This effect (called “quantum yield”) of a single photon producing more than one electron must be taken into account properly when estimating the noise level for short-wavelength observations.

Since the generation of multiple electrons is a random phenomenon, an extra noise term must be added to account for an observed variance larger than that associated with the normal Poisson distribution of incoming photons. The QE curves presented in Figure 5.2 include the quantum-yield gain, which at 200 nm is about 1.7 e^-/photon. The algorithms in the WFC3 Exposure Time Calculator (ETC) take the quantum-yield effect into account and apply the proper reduction to the estimated S/N ratio.

Figure 5.2: Quantum efficiency of the WFC3/UVIS chips.

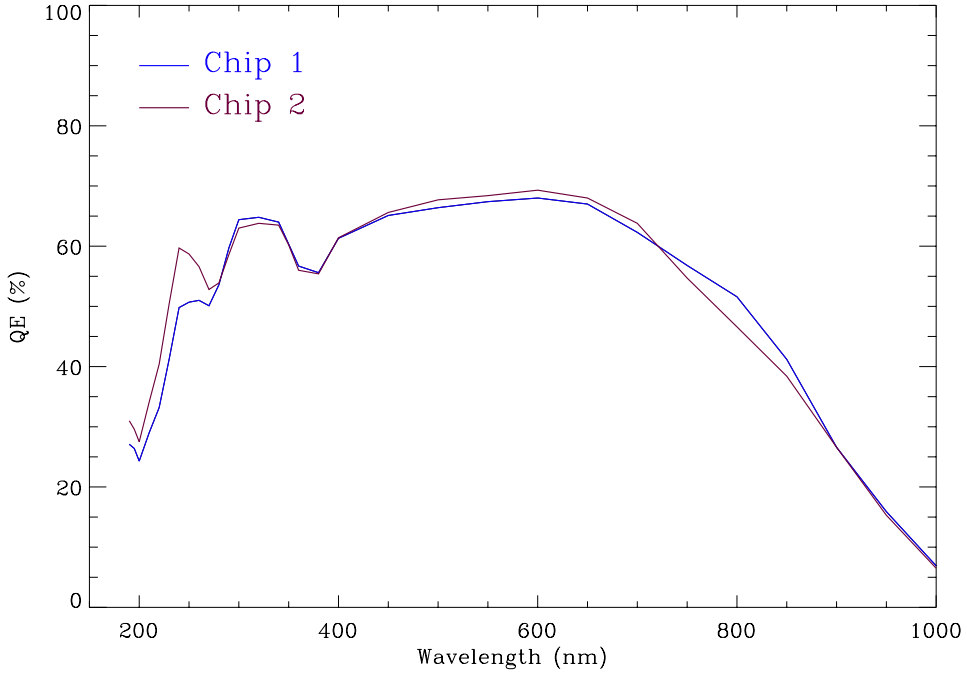

5.4.3 Flat Fields

The flat fields needed in the reduction of WFC3 images will combine information from two sources. Before launch, ground-based flats have been obtained for all filters at a S/N of ~200 per pixel. To refine the low-frequency domain of the ground flats, in-flight observations of a rich stellar field with large-scale dithers will be used. The resulting library of flat-field images will support photometry to ~1% accuracy over the full WFC3 CCD field of view.

Figure 5.3 shows examples of bias-corrected ground-based flats for two wide-band filters. Both are displayed with an inverse greyscale stretch chosen to highlight features; the vignetting in the upper-right corner is not instrument-related but an artifact of the optical stimulus. The crosshatch features in the UV flatfield (F336W) are normal, due to the detection-layer structure in the CCDs; the level is typically <5% peak-to-peak compared to the rest of the flat. The diamond-shaped pattern in the F555W flat field is caused by glints within the detector housing, an issue that has been resolved.

Figure 5.3: WFC3/UVIS ground-based flat fields at F336W (top) and F555W (bottom).

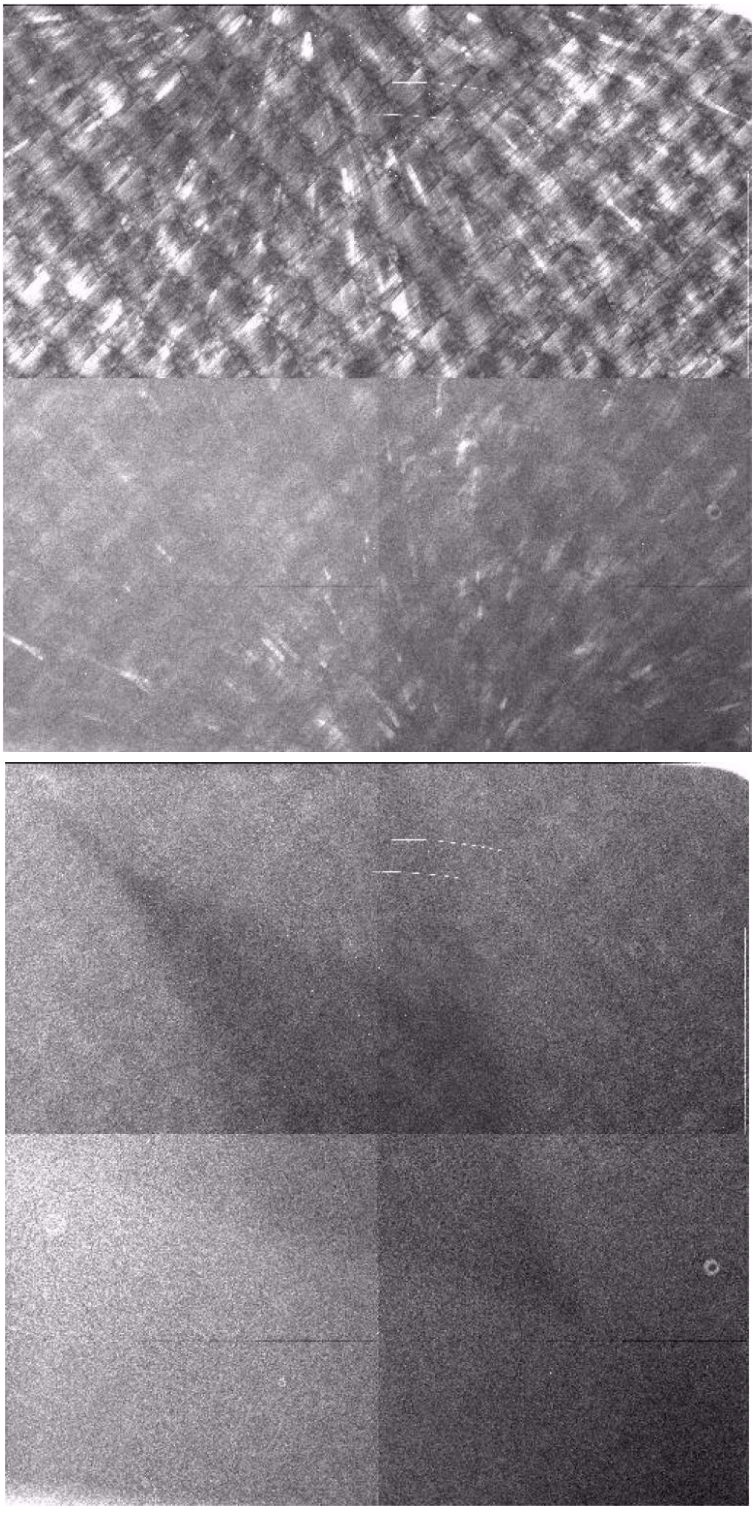

5.4.4 Long-Wavelength Fringing

Like most back-thinned CCDs, the WFC3 CCDs exhibit fringing at wavelengths longward of ~750 nm (see Figure 5.4). The peak-to-peak variation in the brightness of the flat-field signal for monochromatic input increases gradually with wavelength longward of the onset of fringing at 750 nm, and can reach levels of +/- 50% at the longest CCD wavelengths (see Figure 5.5).

Fringing results from interference due to multiple reflections between the front and back surfaces of the CCD. The amplitude of the fringes is a strong function of the detector thickness, wavelength, and spectral resolution. For broad-band illumination, the fringe pattern will depend on the spectrum of the incident light and on the bandwidth of the filter. The fringe pattern has been shown to be very stable, as long as the wavelength of light on a particular part of the CCD stays constant. Fringing can therefore be corrected if an appropriate flat field is available.

The fringe pattern can also be modeled, either by interpolating between or combining monochromatic patterns previously obtained in the laboratory, or from theoretical calculations.

For a detailed explanation of how to model the WFC3 fringe pattern, see Malumuth et al. (2003, Proceedings of SPIE, **4854**, Future EUV/UV and Visible Space Astrophysics Missions and Instrumentation, pp. 567-576).

Figure 5.4: Fringe pattern of CCD Chip 2 with monochromatic flat-field illumination at 976 nm.

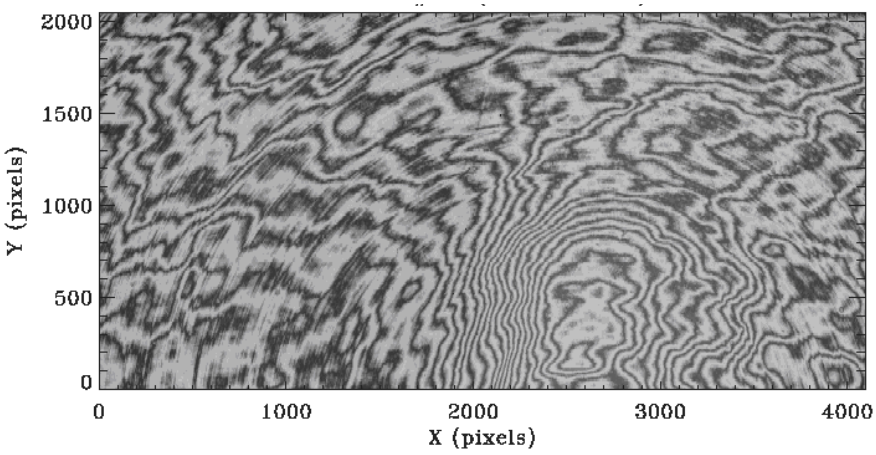

Figure 5.5: Normalized line plot of row=999 from the image shown in Figure 5.4.

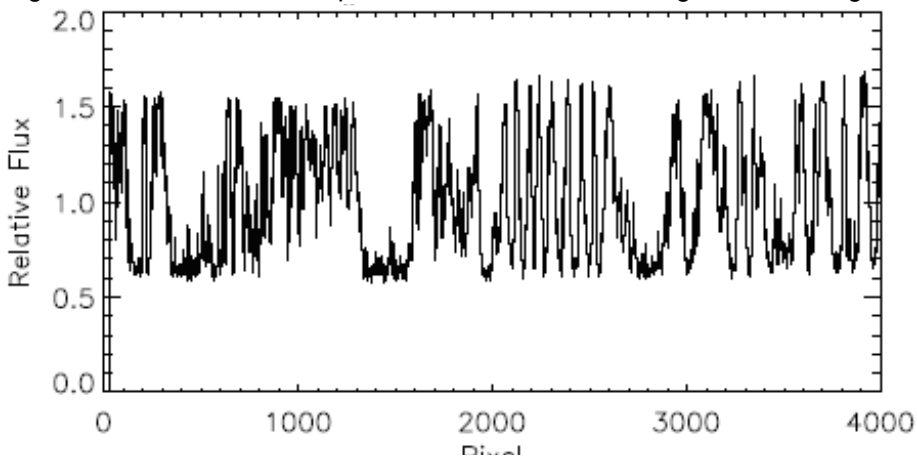

5.4.5 Linearity and Saturation

In general, the response of CCDs is intrinsically linear, with significant departures encountered only in the vicinity of full well. The departure from linearity of WFC3 CCDs remains well below 1% until ~80,000 electrons are accumulated on each pixel.

When CCDs become over-exposed, blooming occurs: if a pixel becomes full, the photo-generated excess charge spills into adjacent pixels along the column. Extreme overexposure is not believed to cause any long-term damage to the CCDs, so there are no bright-object limits for the WFC3 CCDs.

5.4.6 Gain

Electrons that accumulate in the CCD wells are read out and converted to data numbers (DNs), often called Analog-to-Digital Units (ADUs), by the analog-to-digital converter (ADC). The ADC output is a 16-bit number, producing a maximum of 65,535 DN for each pixel. A straightforward scheme in which one DN corresponded to one electron would make it impossible to measure signals larger than 65,535 electrons. Hence the conversion gain parameter provides a way of adjusting the scale so that multiple counts correspond to a single DN, allowing larger numbers of electrons to be measured. The conversion gain is defined as the number of electrons per DN.

Although it is possible to operate the WFC3 CCD detector at gains of 1, 1.5, 2, and 4 e^-/DN, only a gain of 1.5 e^-/DN will be supported. This gain permits sampling of the entire dynamic range of the detectors, with negligible impact on the readout noise.

The gains for the integrated WFC3 instrument were measured during the 2004 ground tests (WFC3 ISR 2005-08). The results are summarized in Table 5.3. The errors in the gain measurements are about +/-0.01 e^-/DN.

Table 5.3: WFC3/UVIS Gains.

CCD Chip	Amp	Gain (e^-/DN)
1	A	1.53
	B	1.52
2	C	1.56
	D	1.55

5.4.7 Read Noise

The readout noise level in the active areas and overscan regions for all of the amplifiers at the default gain setting was measured during the 2004 ground tests with a variety of methods (WFC3-ISR 2005-13). Table 5.4 shows the results obtained at the default gain setting of 1.5 e^-/DN.

Table 5.4: Readout noise (e^-) of WFC3 CCDs at gain =1.5 e^-/DN.

	CCD Chip 1				CCD Chip 2			
	Image area		Overscan		Image area		Overscan	
	Amp A	Amp B	Amp A	Amp B	Amp C	Amp D	Amp C	Amp D
Mean	3.12	3.23	2.99	3.05	3.11	3.24	2.95	3.07
Error	0.03	0.04	0.01	0.01	0.03	0.02	0.02	0.01

A preliminary analysis of the statistical behavior of the WFC3 ADCs shows some tendency for the least significant bit to be slightly biased at the readout speed adopted by the WFC3 electronics (see WFC3-ISR 2005-27). This minor effect should not degrade the photometric and noise characteristics of the WFC3/UVIS images.

5.4.8 Dark Current

The WFC3 CCDs, like most large-area scientific CCDs, operate with buried channels. Earlier generations of CCDs worked with surface channels, i.e., storing and transferring charges only along the surface of the semiconductor. In these earlier devices the Si-SiO_2 interface between the detector material Si (p-doped conductor) and the surface layer of SiO_2 (isolator) created significant charge traps, which limited both the charge-transfer efficiency and the dark current. In buried-channel devices, a shallow (~0.5 micron thick) n-type Si layer is implanted just below the surface between the p-doped Si and the SiO_2 surface, to store and transfer the collected signal charge away from the traps at the interface.

Dark current in WFC3 detectors is further reduced using MPP technology. The dark current generated at the Si-SiO_2 interface ultimately depends on two factors: the density of interface states and the density of free carriers (holes and electrons) that populate the interface. Electrons can thermally "hop" from the valence band to an interface state (sometimes referred to as a "mid-band state") and from there to the conduction band, producing a dark e-h pair. Free carriers also fill interface states and, if these states were completely populated, can suppress hopping and conduction, reducing the surface dark current at levels comparable to the bulk dark. Unfortunately, normal CCD operations deplete the interface of free carriers, maximizing dark current generation.

In MPP technology, the Si-SiO_2 interface is populated with holes that suppress the hopping conduction process. MPP mode is applied to the CCD by significantly biasing the array clocks negatively to invert (push electrons away from) the n-buried channel and "pin" the surface potential beneath each phase to substrate potential (hence the name multi-pinned phase). Biasing the array clocks in this manner causes holes from the p+ channel stops to migrate and populate the Si-SiO_2 interface, eliminating surface dark-current generation. Note that it is not possible to invert conventional CCDs in this way, as the sensor's full-well capacity would be annihilated since the potential wells

within a pixel all assume the same level. To circumvent this difficulty in MPP CCD technology an additional implant is included below one of the phases, allowing charge to accumulate in collecting sites when biased into inversion.

Besides eliminating surface dark current, MPP CCD technology offers additional advantages. For example, the charge-transfer efficiency of a CCD generally degrades with decreasing operating temperature. MPP technology assists in the charge-transfer process since it permits the use of higher operating temperatures.

The MPP CCD also eliminates residual image, a serious problem that has plagued low-signal-level CCD users for many years. Residual image, also known as quantum-efficiency hysteresis, results when the sensor is either overexposed or first powered up. Under these circumstances, electrons are found trapped at the Si-SiO_2 interface that slowly de-trap into the pixel's potential well. Residual charge may take hours or even days before its level falls below the read-noise floor. Inverting the CCD causes holes to recombine immediately with the trapped residual electrons, eliminating remnant image effects during integration as well as readout.

During pre-flight tests, the CCD dark current was measured both in the cryogenic environment at the DCL, and in the instrument during thermal vacuum testing. The dark currents in Table 5.5, in units of e^-/pix/hr, are from the 2004 thermal vacuum testing (see WFC3 ISR-2005-13).

Like all CCDs operated in a low-earth-orbit radiation environment, the WFC3 CCDs will be subject to radiation damage by energetic particles trapped in the radiation belts. Ionization damage and displacement damage are two types of damage caused by protons in silicon. The MPP mode is very effective in mitigating the damage due to ionization, such as the generation of surface dark current due to the creation of new trapping states in the Si-SiO_2 interface. Although protons lose only a minor fraction of their total energy via non-ionizing energy loss, lattice displacement damage can cause significant performance degradation in CCDs by decreasing the charge transfer efficiency (CTE), increasing the average dark current, and introducing pixels with very high dark current (hot pixels). Displacement damage to the silicon lattice occurs mostly due to the interaction between low-energy protons and silicon atoms. The generation of phosphorous-vacancy centers introduces an extra level of energy between the conduction band and the valence band of the silicon. As described above, new energy levels in the silicon bandgap increase the dark current as they allow thermally generated charges to reach the conduction band. As a consequence, the dark current of CCDs operated in a radiative environment is predicted to increase with time.

Table 5.5: WFC3/UVIS dark current, in e^-/pix/hr, as measured during ground tests.

	CCD Chip 1		CCD Chip 2	
	Amp A	**Amp B**	**Amp C**	**Amp D**
Dark	0.16	0.32	0.34	0.41
Error	0.09	0.10	0.10	0.11

5.4.9 Bad Pixels

Pre-flight tests of the WFC3 CCDs allowed classifying a number of pixels as either hot, dead, or QE outliers. The definitions of the relative thresholds are somewhat arbitrary, but the following are adopted: (1) hot pixels, identified using 1 hr long dark-current frames, are those that depart from the average dark current by more than 100 times the standard deviation of the main population; (2) dead pixels, measured with flat-field illumination of ~50% full well, are those that remain below 1000 electrons (the large majority being close to 0 electrons); and (3) outliers, also identified with flat-field illumination, are those that depart from the average by than 50 times the standard deviation of the main population.

Tables 5.6 and 5.7 summarize the results, providing both the total number of pixels and their fraction. With 0.25% and 0.40% flagged as bad, the cosmetic quality of the WFC3 CCD is excellent. Bad pixels are constantly monitored and the masks to be applied for their subtraction regularly updated in the standard data reduction pipeline.

Table 5.6: Summary of bad pixels for Chip 1.

Bad Pixel Type	Amp A	Amp B	Array Total	% of Array
Hot Pixels	458	718	1,176	0.03
Dead Pixels	1,110	16	1,126	0.03
QE Outliers	5,337	4,088	9,425	0.22
Total Non-functional*	5,794	4,806	10,600	0.25

*Note that the total may differ from the sum of the different types of pixels because some of the pixels are a combination of types (e.g., dead and QE outlier, etc.).

Table 5.7: Summary of bad pixels for Chip 2.

Bad Pixel Type	Amp C	Amp D	Array Total	% of Array
Hot Pixels	5,444	5,307	10,751	0.26
Dead Pixels	0	0	0	0
QE Outliers	2,716	3,443	6,159	0.15
Total Non-functional*	8,154	8,748	16,902	0.40

*Note that the total may differ from the sum of the different types of pixels because some of the pixels are a combination of types (e.g., dead and QE outlier, etc.).

5.4.10 Cosmic Rays

Pending on-orbit measures with WFC3, we can use ACS data to predict the effect of cosmic rays on the WFC3 CCDs. The fraction of ACS pixels affected by cosmic rays varies from 1.5% to 3% during a 1000-s exposure for both CCD cameras, similar to what was seen on WFPC2 and STIS. This number provides the basis for assessing the risk that the target(s) in any set of exposures will be compromised. The affected fraction is the same for the ACS WFC and HRC, despite their factor of two difference in pixel areas, because the census of affected pixels is dominated by charge diffusion, not direct impacts.

Observers seeking rare or serendipitous objects, as well as transients, may require that every single WFC3 pixel in at least one exposure among a set of exposures is free from cosmic-ray impacts. For the cosmic-ray fractions of 1.5% to 3% in 1000 s, a single ~2400 s orbit must be broken into 4 exposures (4 CR-SPLITs of 500 to 600 s each) to reduce the number of unrecoverable pixels to 1 or less. (We recommend that users dither these exposures to remove hot pixels as well.)

The flux deposited on the CCD from an individual cosmic ray does not depend on the energy of the cosmic ray but rather the distance it travels in the silicon substrate, and thus on its direction of incidence. The electron deposition due to individual cosmic rays has a well-defined cutoff, with negligible events of less than 500 e^- and a median of ~1000 e^- (see Figure 5.6).

Figure 5.6: Electron deposition by cosmic rays on ACS/WFC.

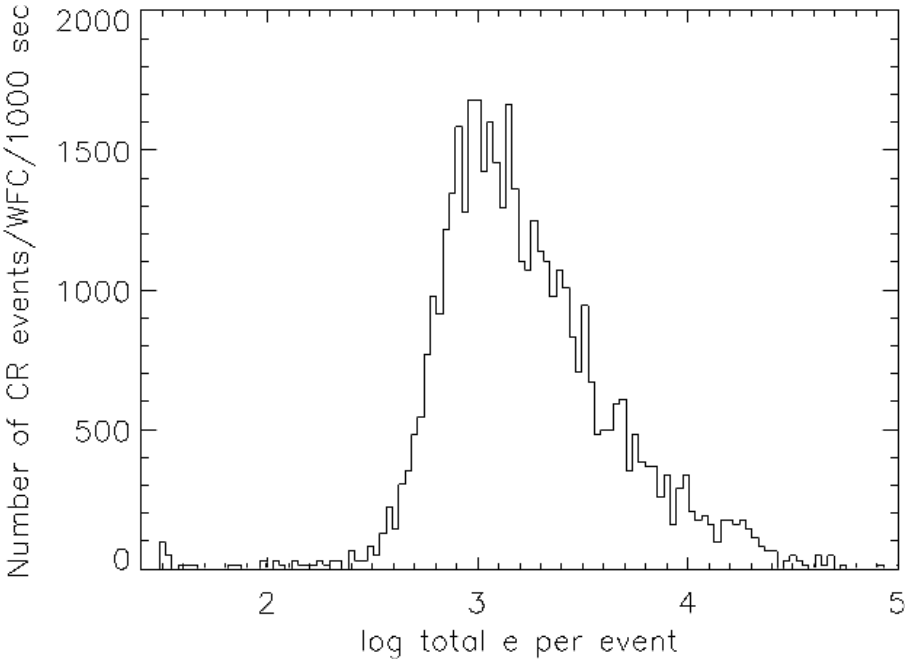

The distribution of the number of pixels affected by a single cosmic ray is strongly peaked at 4 to 5 pixels. Although a few events are seen which encompass only one pixel, examination of these events indicate that at least some, and maybe all of these sources are actually transient hot pixels or unstable pixels which can appear hot in one exposure (with no charge diffusion) and normal in the next. There is a long tail in the direction towards increasing numbers of compromised pixels.

Distributions of sizes and anisotropies can be useful for distinguishing cosmic rays from astrophysical sources in a single image. The size distribution for both chips peaks near 0.4 pixels as a standard deviation (or 0.9 pixels as a FWHM). This is much narrower than for a PSF and is thus a useful discriminant between real unresolved astronomical sources and cosmic rays.

5.4.11 Charge-Transfer Efficiency

Charge-transfer efficiency (CTE) is a measure of how effective the CCD is at moving charge from one pixel location to the next when reading out the chip. A perfect CCD would be able to transfer 100% of the charge as it is shunted across the chip and then out through the serial register. In practice, small traps in the silicon lattice compromise this process by retaining electrons, and then releasing them at a later time. (Depending on the trap type, the release time ranges from a few microseconds to several seconds.) For large charge packets (several thousand electrons), losing a few electrons along the way is not a serious problem, but for smaller (~100 e^- or less) signals, it can have a substantial effect.

CTE is typically measured as a pixel-transfer efficiency, and would be unity for a perfect CCD. The CTE numbers for the WFC3 CCDs were measured at the DCL using a ^{55}Fe source, and showed that charge loss is of the order of 3-5x10^{-7} e^-/transfer, an excellent value for pre-flight devices.

5.5 The WFC3 IR Channel Detector

5.5.1 Overview

The infrared channel of WFC3 employs a low-noise, high-QE, 1024×1024 pixel HgCdTe array manufactured by Teledyne Imaging Sensors (formerly Rockwell Science Center). The detector area sensitive to light is 1014×1014 pixels. Active cooling by a six-stage thermoelectric cooler (TEC) keeps the detector at a nominal operating temperature of 145 K. Although the IR detector is sensitive between 400 and 1700 nm, the detector coating is optimized for wavelengths longward of ~1000 nm, where the QE reaches its peak. The IR channel filter set is also limited to wavelengths above 800 nm, making the IR channel complementary to the UVIS channel.

Compared to CCD detectors, IR detectors like the one used in the WFC3 IR channel show higher read noise and dark current. Unlike CCDs, however, IR detectors allow the accumulated signal to be read out non-destructively multiple times, without affecting other pixels. The capability to sample the signal multiple times during the integration can be exploited to reduce the effective read-out noise significantly. IR detectors are also immune to the charge bleeding exhibited by CCDs at high signal levels; however, saturation may still be a problem because pixels subject to the highest signal levels show higher dark-current rates ("image persistence") in subsequent exposures.

The capability of multiple readouts and the absence of bleeding makes IR detectors capable of very high dynamic-range observations. Non-destructive readout also allows recovering pixels affected by cosmic rays (CRs), since CR hits may be recognized and removed between adjacent reads. Unlike CCDs, IR detectors do not show long-term on-orbit CTE degradation, since they do not employ the charge-transfer mechanism used in CCDs. IR detectors, however, are intrinsically non-linear. Nevertheless, at low and intermediate count levels, the departure from linearity is quite modest and can be well calibrated by a quadratic fit, whose parameters can be determined for each pixel.

5.5.2 IR Detector Basics

In this section, we briefly describe the operational principles of the WFC3/IR detector. Figure 5.7 (adapted from McLean 1997, Electronic Imaging in Astronomy: Detectors and Instrumentation) shows the basic physical structure of the photovoltaic HgCdTe detector used in WFC3.

Figure 5.7: Cross-section of a WFC3-IR detector (not to scale).

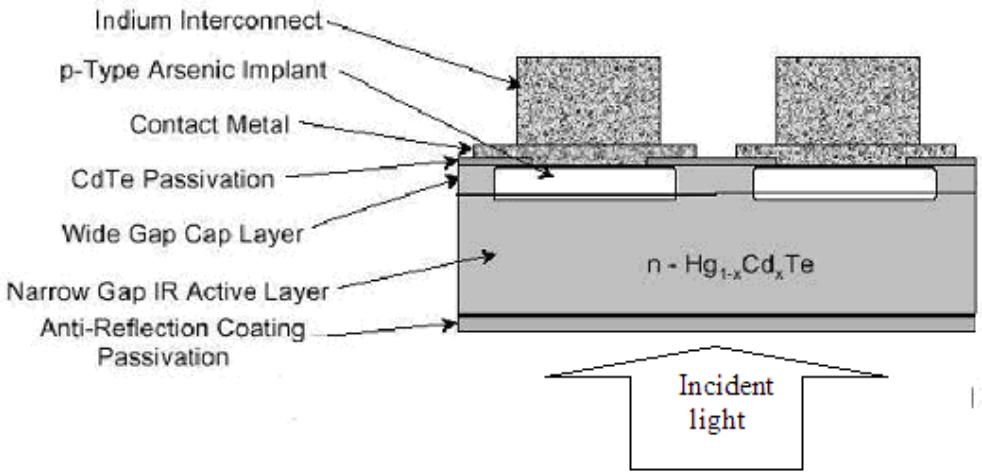

Infrared detectors used in astronomy today are basically two-dimensional arrays of p-n junctions working as photodetectors (photodiodes). In a p-n junction, negative charges migrate from the n-type doped material to saturate the unmatched covalent bonds of the adjacent p-type material. The displaced carriers establish an electric field across the junction, setting up an intermediate region depleted of free carriers. The depletion region is therefore both charged and highly resistive. The strength of the electric field and the size of the depletion region may be increased by applying an external electric field ("negative bias"). This biasing corresponds to the initial RESET applied at the beginning of the integration. When an incident IR photon is absorbed by the photosensitive material, it creates a free electron-hole pair. The two photo-generated charges drift in the material and would eventually recombine. However, if the mobility of the charge carrier (a hole in an n-type material) is high enough, it will reach the depletion region before recombining and be swept to the other side of the junction by the electric field. There, in the p-type region, it will recombine with one of the electrons of the ionized holes, causing a reduction of the voltage across the junction. This change of voltage can be measured and, being proportional to the number of photo-generated charges, provides a direct measure of the photons captured on each pixel.

In the case of the WFC3 IR detector, the photosensitive material is made of HgCdTe grown with a molecular beam epitaxial (MBE) process on a ZnCdTe substrate. The fraction (stoichiometric ratio) of Hg vs. Cd controls the long-wavelength cutoff of the material, whereas the doping material (As for the p-type, In for the n-type) creates the p-n junction. The MBE growth process is different from that used in the NICMOS detectors on HST, in which the HgCdTe was grown on sapphire in a liquid phase (PACE process). MBE growth on a ZnCdTe substrate is expected to provide a better lattice match to HgCdTe than sapphire, creating fewer defects and charge traps at the interface between the two materials. The

MBE growth process is followed by the processing phase, in which the implants and contacts of each pixel are manufactured.

As usual with IR arrays, the readout circuitry is made on a separated CMOS chip (multiplexer or MUX), which is eventually hybridized to the detector with an indium contact for each pixel (see Figure 5.8). After the two chips have been hybridized, the ZnCdTe substrate is removed to reduce the susceptibility of the device to cosmic-ray events and to increase the sensitivity at short wavelengths. The final chip therefore is a CMOS device connected through indium columns to a thin layer (a few microns thick) of HgCdTe photosensitive material.

Figure 5.8: Basic "hybrid" structure of infrared array detectors (not to scale).

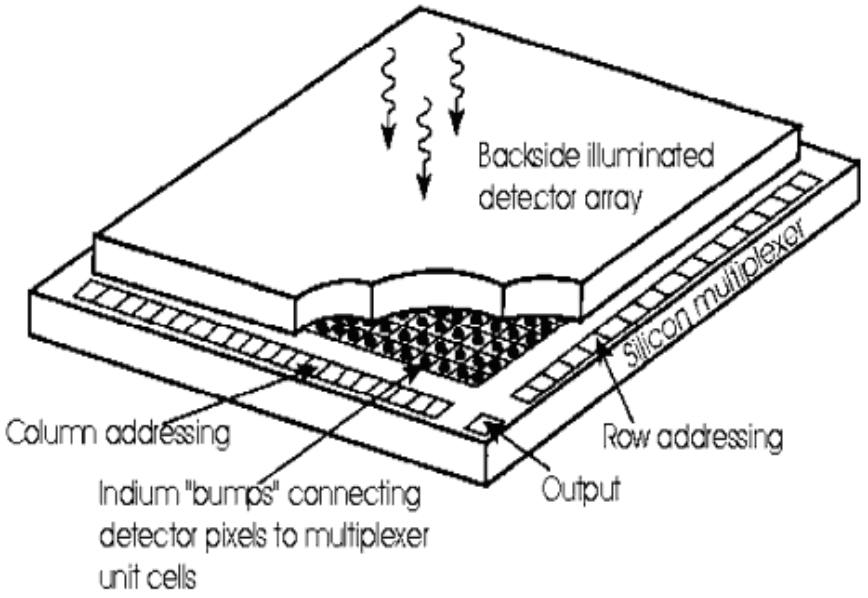

In the MUX, each pixel has its own dedicated readout circuitry (unit cell). In particular, the voltage change across the p-n junction is monitored by a field-effect transistor (FET) configured as a source-follower amplifier, which has gain of 1 and effectively decouples the detection process from the noisy readout circuitry. Two other FETs connect the pixel to the reset voltage and the output line. Figure 5.9 shows the equivalent circuit diagram for the WFC3 detector unit cell. Each WFC3 IR unit cell contains three transistors. For comparison, the NICMOS detectors have four transistors, whereas the latest generation of Hawaii-2RG detectors for JWST has seven transistors per unit cell. A higher number of transistors increases the versatility of the device. For example, on the NICMOS detectors it is possible to reset each individual cell, whereas on WFC3 detectors the reset is sent simultaneously to all cells on the same row. Note that since there are no potential barriers between pixels, pixels do not spill charges into nearby pixels when they reach a certain level (“blooming full well”) of accumulated charges, as in typical multiphase CCDs. Therefore, IR detectors do not show "bleeding" along columns. Moreover, due to individual readout, bad pixels do not block the rest of the column as they do in a CCD.

Figure 5.9: Equivalent circuit diagram of the WFC3/IR unit cell.

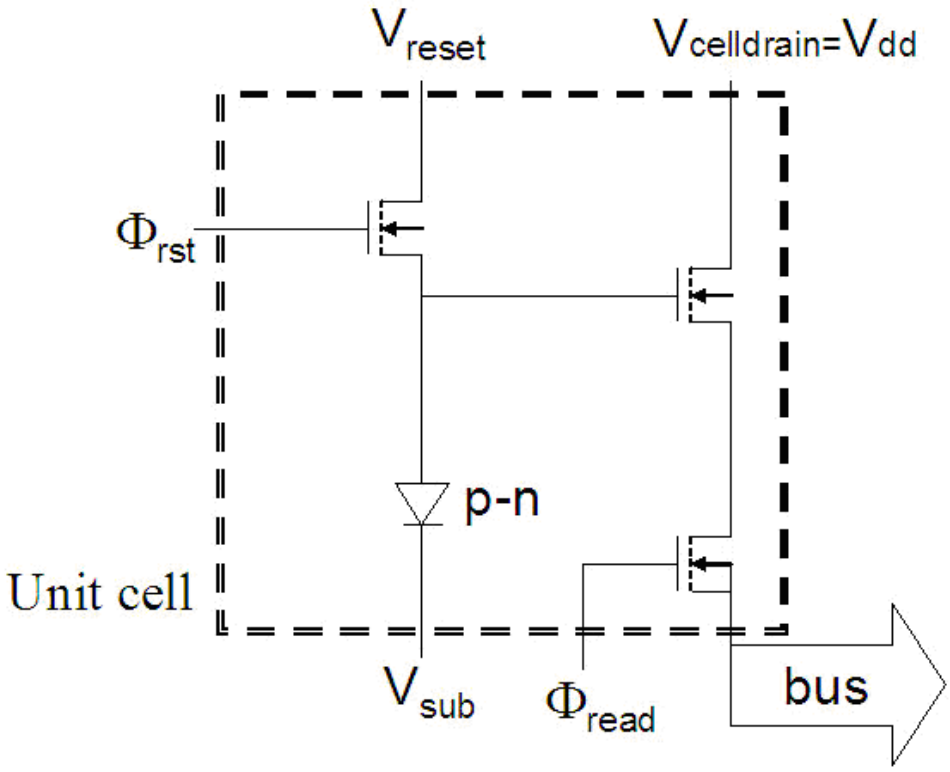

5.6 WFC3 IR Readout Formats and Reference Pixels

The WFC3 IR detector contains 1024×1024 square pixels of 18×18 micron physical size. The detector is divided into four quadrants of 512×512 pixels, each of which is read out independently from its outer corner, as illustrated in Figure 5.10.

Figure 5.10: Schematic layout of the WFC3 IR detector. The long (red) and short (blue) arrows indicate the direction of the fast and slow multiplexer clocking, respectively. In contrast to CCD "bucket-brigade" image-shifting to the output amplifier, the IR detector pixels are selected for readout in a raster pattern by multiplexer circuits.

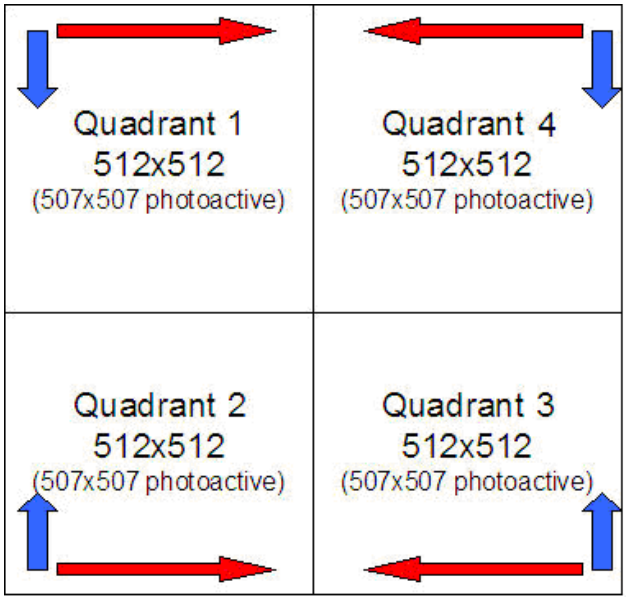

A major effort has been made to eliminate both the amplifier glow and bias jumps that have affected the NICMOS detectors.

To eliminate the amplifier glow entirely, WFC3 uses external amplifiers located in the immediate vicinity of the detector, rather than those directly on the multiplexer (which are also present, but are not activated in the WFC3 implementation).

In regard to bias jumps, the WFC3 IR class of detectors has been the first to use reference pixels, configured as follows (see Figure 5.11). Of the 1024×1024 pixels, only the inner 1014×1014 pixels are light-sensitive. The five outer rows and columns of pixels all around the array use fixed capacitances to provide constant-voltage reference values. There are actually two types of reference pixels: (1) the pixels on the outermost columns/rows are connected to capacitors located out of the unit-cells. Their values follow a 4x periodic pattern, providing 4 sequentially increasing voltage levels all within the range of the detector output signal; (2) the 4 inner rows/columns are instead connected to capacitors created within their cells. These on-board capacitors are identical by design and all provide nearly the same reference signal. The present version of the WFC3/IR data-reduction pipeline uses only the on-board reference pixels, as they provide a more robust statistical estimate of the variable detector pedestal.

The reference pixels track the low-frequency drift of the readout electronics and efficiently remove the “pedestal” variations that affected, for example, NICMOS. Pre-launch tests have also shown that the reference-pixel signal is sensitive to the detector temperature and may therefore be used to assess the expected level of dark current during the integration independently of the temperature.

Figure 5.11: Schematic layout of the active pixels (dark blue) and of the reference pixels at one of the corners of the WFC3/IR detector. The color coding represents different values of the reference pixel capacitances.

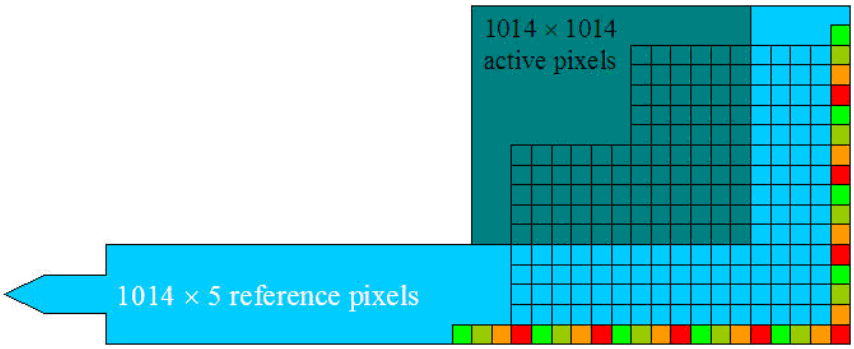

5.7 WFC3/IR Detector Characteristics and Performance

5.7.1 Quantum Efficiency

The quantum efficiency of the flight IR detector, as measured at the Goddard Detector Characterization Lab (DCL), is presented in Figure 5.12.

Figure 5.12: Quantum efficiency curve of WFC3/IR detector.

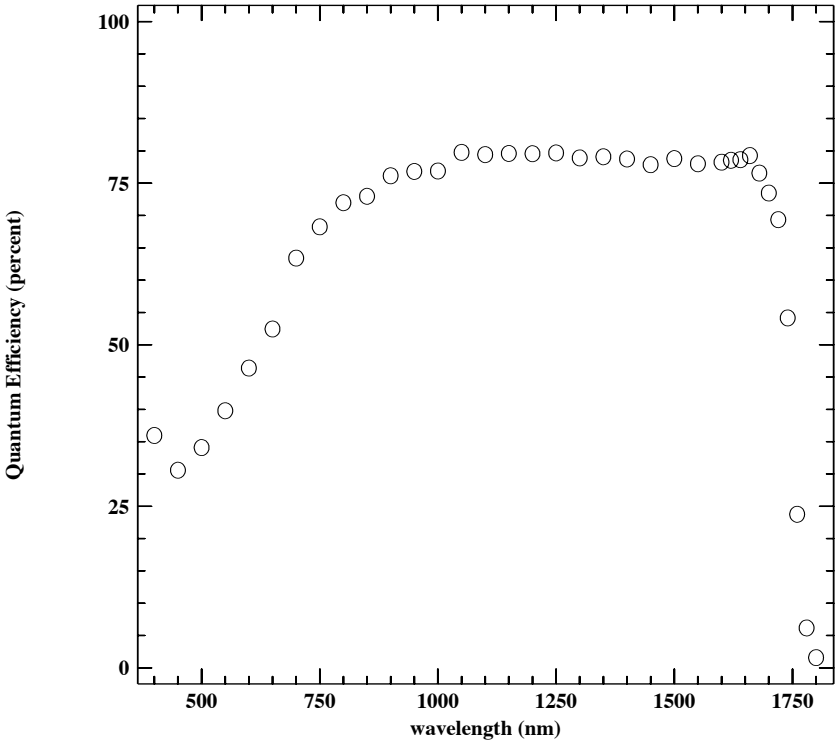

5.7.2 Dark Current

To avoid the complexity and limited lifetime of a stored-cryogen system, while at the same time providing the low operating temperatures required for dark-current and thermal-background reduction, the WFC3 IR detector is refrigerated with a six-stage TEC to a nominal operating temperature of 145 K. This is an unusually high temperature for near-IR detectors, and has required tailoring the composition of the HgCdTe material for a long-wavelength cutoff at ~1700 nm. The higher band-gap associated with the short cutoff wavelength effectively limits both the intrinsic detector dark current and its sensitivity to the internal thermal background.

WFC3 IR exposures taken with a blank filter in place provide a measure of the detector dark current. The dark current of the flight array has a skewed distribution, with different mean, median, and mode values (see Table 5.1). The difference between these two values is due to the asymmetry of the dark-current distribution among the pixels, which is characterized by a long tail of "hot pixels" randomly located across the detector. The cumulative dark-current distribution, i.e., the fraction of pixels with a dark current higher than a certain level, is shown in Figure 5.13.

A major effort has been made to operate the TEC in the most stable conditions. Tests made on similar detectors indicate that the dark-current variations can be largely calibrated and subtracted out using reference pixels.

Figure 5.13: Histogram of the dark current level of WFC3/IR detector.

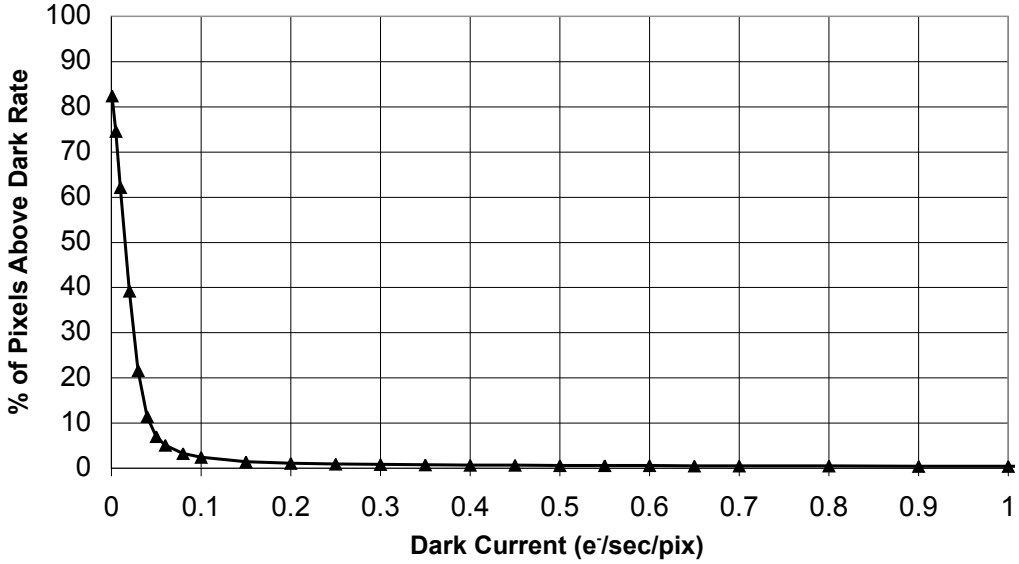

5.7.3 Read Noise

Each detector has four independent readout amplifiers, each of which reads a 512x512 quadrant. The four amplifiers generate very similar amounts of read noise. This is illustrated in Figure 5.14, which compares the pixel read noise distributions for the four quadrants of the detector. The histograms were derived from a stack of 40

16-read ramps in the following manner. For each pixel, a linear fit was made to the counts as a function of read (time), yielding a slope (count-rate) for that pixel; the standard deviation of the 40 count-rates for each pixel provides a measure of the noise for that pixel. Note that the noise computed in this way is total noise, no correction has been made for dark current (although the results in the figure are for 1 s ramps so the dark contribution should be small).

Figure 5.14: Histogram of the readout noise characteristics of the WFC3/IR detector.

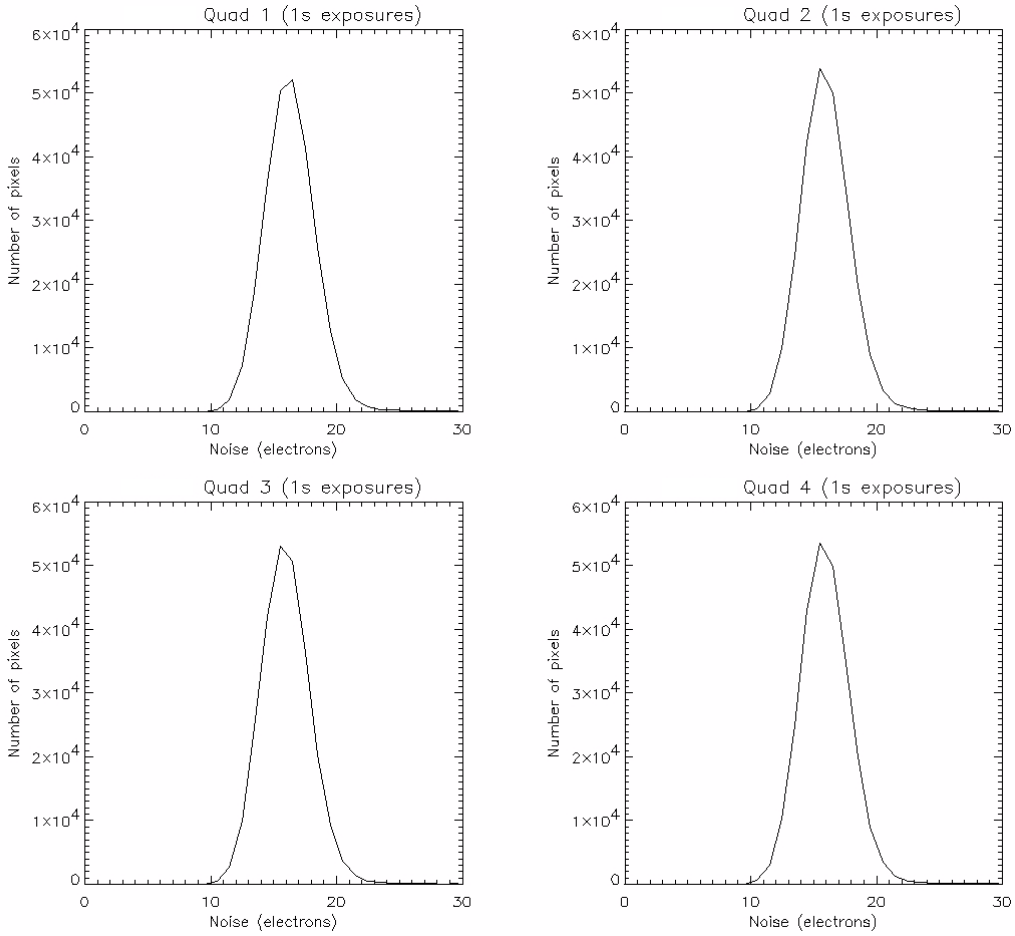

The data presented in Figure 5.14 represent the distribution of electronics-induced rms uncertainties, as measured from a series of difference images of short uniformly spaced ramps of dark images. The distributions for all quadrants are relatively narrow, with a FWHM of about 16 electrons, indicating that there are only few anomalously noisy pixels. The read noise is independent of temperature.

For some scientific programs, such as ultra-low-background observations, read noise becomes a non-negligible component of the noise floor. The contribution to the read noise in WFC3 IR data due to digitalization errors associated with the conversion from electrons to data numbers (DN) is negligible.

5.7.4 Flat Fields

Flat fields taken with the WFC3/IR array show response variations on both large and small scales. In Figure 5.15 we show the flat-field pattern at four wavelengths: 1000, 1300, 1600, and 1720 nm. This last measure, at the detector cutoff wavelength, shows significant non-uniformity due to variations in the stoichiometric composition of the HgCdTe photoactive material.

Figure 5.15: Flat-field exposures at 1000, 1300, 1600, and 1720 nm (from left to right).

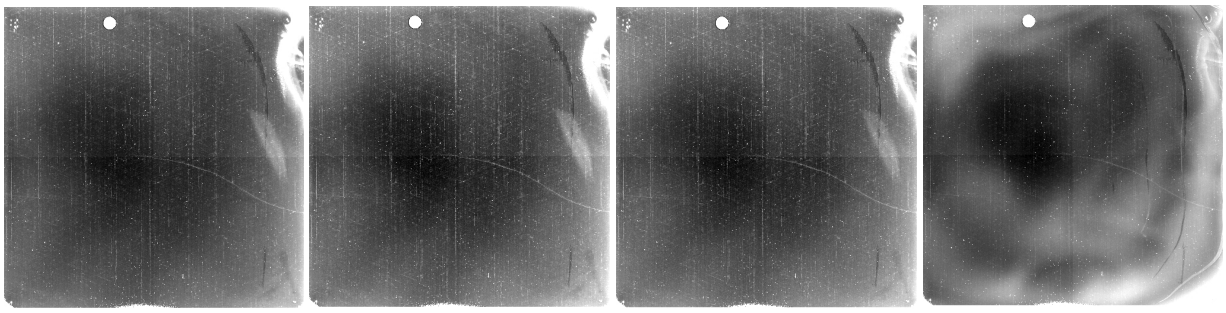

The high-frequency flat-field pattern contains a number of defects that are related to blemishes on the detector surface. Being on the focal plane, they show a very sharp profile. Defects in the optical path, especially particles on the cold enclosure window and filters, are out of focus and show a more diffuse, nearly circular pattern. Flat-field procedures are expected to remove these effects to better than 1%**.**

Note that the flat-field images were obtained in the laboratory with the detector only. When installed in the full instrument, the flat fields may be somewhat different.

Flat-field frames are normally generated using the internal calibration system from a pair of "lamp-off" and "lamp-on" exposures. Differencing these two exposures then leaves the true flat-field response. The count rate in such an image is a direct (albeit relative) measure of the QE uniformity modulated by the field dependency of the throughput of the optical system.

5.7.5 Linearity and Saturation

The WFC3 IR calibration program shows that the detector response is in fact (slightly) non-linear over the full dynamic range. This behavior is illustrated in Figure 5.16, which presents a plot of average counts as a function of read number within a sample sequence (reads are spaced evenly in time). The filled circles are the measured average signal; a linear fit has been made to the measurements up to ~70,000 electrons. The lower curve with the open squares shows the resulting residuals to the linear fit. The top horizontal line marks the level at which the counts deviates by more than 5% from linearity (about 95,000 electrons). The center horizontal line, labeled 'diode bias = 0', marks the location at which the diode voltage difference becomes zero, i.e., counts higher than this level can be suspect as the diode is positively biased. That is, an exposure begins with the reset diode voltage difference at about -0.25 volts. Incoming photons gradually add to this voltage such that eventually, it reaches zero (diode bias 0). At this point, the device experiences a strong dark current which

counter-acts the effect of incoming photons. Photons can still be collected above the 60,000 electron level but observers should be aware that the value read out in this regime will depend strongly on the incoming photon rate and the exposure time.

Figure 5.16: Average counts as a function of read number (time) for WFC3/IR detector.

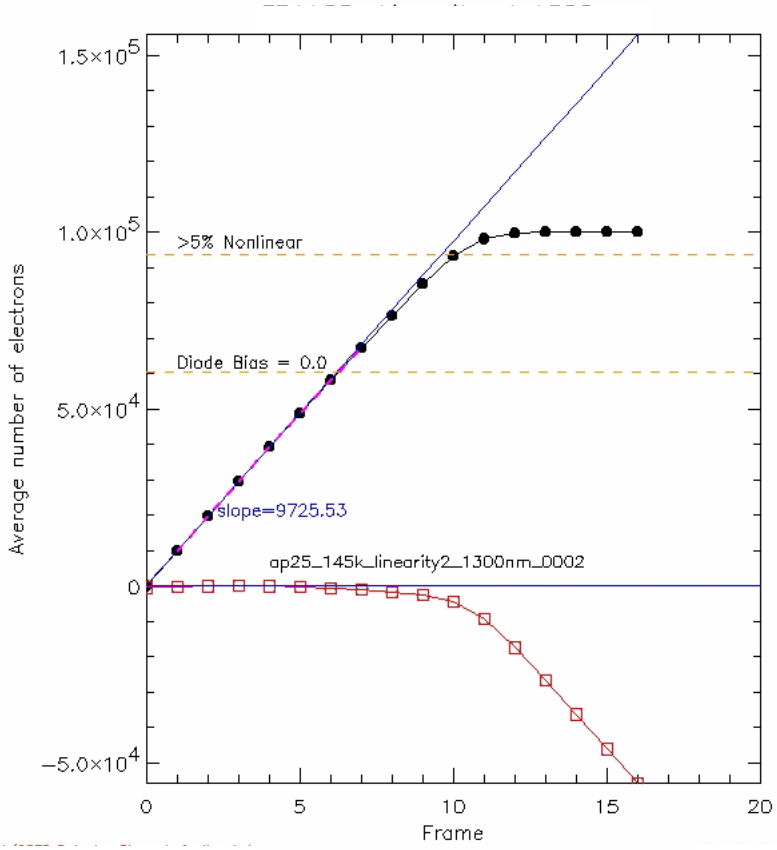

The linearity correction implemented in the WFC3/IR calibration pipeline corrects pixels over the entire dynamic range between zero and saturation. Once the pixel value exceeds the saturation threshold, the pixel is flagged as saturated in the data-quality array within the FITS file and no linearity correction is applied. Pixels driven heavily into saturation can begin to show decreasing readout values, such that their DN values fall back below the defined saturation threshold. This behavior can lead to a situation where a pixel is flagged as saturated in one or more readouts, but then not flagged in later readouts. To prevent this from happening, the calibration processing system flags saturated pixels in all subsequent readouts for pixels that are found to be above the saturation threshold in any given readout.

5.7.6 Detector Cosmetics

The WFC3/IR detector has a number of pixels that show an anomalous responsivity. Such "bad pixels" come in various flavors. So-called "hot" pixels have a more than 100 times the average dark current, and thus show excessive charge

compared to the surrounding pixels. On the other hand, "cold pixels" are much less sensitive to incident photons than the typical pixel and are defined as having a negative slope when measured up the ramp (i.e., pixel value is lower in last frame up the ramp compared to first frame). The anomalously low responsivity of a "cold" pixel could be due to a lower intrinsic QE of the pixel, or to surface defects. Some pixels do not respond at all ("dead pixels") to incoming light. Quantitative statistics of the hot/cold pixels in the WFC3/IR camera are given in Table 5.8. It is important to note that the impact of bad pixels on the quality of WFC3 IR images can be minimized by dithering the observations.

Table 5.8: Bad Pixels in WFC3/IR detector.

Pixel Type	Percentage
Cold[1]	0.05
Hot[2]	0.04

1. A cold pixel is defined as having a negative slope when measured up the ramp.
2. A hot pixel is defined as having more than 100 times the median dark current of the array.

CHAPTER 6:

UVIS Imaging with WFC3

In this chapter . . .

6.1 WFC3 UVIS Imaging

As described in Chapter 2, the optical design of WFC3 features two independent channels, each with its own separate optics, filters and grisms, and detectors. The **UVIS channel** is sensitive to UV and optical wavelengths (200-1000 nm), and the **IR channel** is sensitive to near-infrared wavelengths (800-1700 nm).

Only a single channel, either UVIS or IR, can be used at any one time. Thus they cannot be used in parallel, but they can be used sequentially.

A schematic diagram showing the locations of the fields of view of the UVIS and IR detectors in the HST focal plane is given in Figure 2.2.

This chapter describes the capabilities of the UVIS channel. The following chapter, Chapter 7, describes the IR channel. Detailed performance characteristics of the detectors used in both channels are given in Chapter 5 and summarized in Table 5.1.

6.2 Specifying a UVIS Observation

In the HST proposal system, it is relatively simple to specify the parameters for a UVIS observation. The parameters available to General Observers for the UVIS channel are the following:

1. **Configuration**: always **WFC3/UVIS**
2. **Mode**: always **ACCUM**
3. **Aperture:** must be specified; **UVIS** selects readout of the full area of both CCDs; other choices are discussed in Section 6.4.5
4. **Spectral Element:** must be specified for each exposure; see Section 6.5
5. **Optional Parameters:** the available options control splitting of the exposures for cosmic-ray removal (see the Phase II Instructions for the **CR-SPLIT** Optional Parameter), and the **BIN** Optional Parameter for on-chip binning (see Section 6.4.4)
6. **Special Requirements:** see the Phase II Instructions for details of Special Requirements related to the timing of observations and for dithering and mosaicking. Also available is the exposure-level Special Requirement **POS TARG** for offsetting the target position from the default center of the aperture (see Section 6.4.3 for a discussion of the UVIS channel coordinate system).
7. **Number of Iterations** and **Time per Exposure:** the exposure time for the UVIS channel must be a multiple of 0.1 s, ranging from 0.5 to 3600 s, except that 0.6 s is not allowed; see Section 6.7.1 for details).

6.3 UVIS Channel Characteristics

In concept and functionality, as well as in many design details, the WFC3 UVIS channel is patterned after the ACS/WFC channel. The UVIS channel contains an optical train providing focus and alignment adjustments as well as a correction for the OTA spherical aberration, a filter-selection mechanism, a shutter mechanism, and a CCD detector assembly (which uses the same camera-head design as ACS/WFC). These are supported by a thermal-control subsystem and also by control and data-handling electronics subsystems.

The UVIS channel was designed for highest performance in the 200-400 nm wavelength range. This optimization for the ultraviolet includes the use of aluminized mirrors with magnesium-fluoride coatings, and CCDs whose sensitivity extends down to 200 nm. In spite of the UV optimization, the UVIS channel remains sensitive well out into the visible, red, and near-IR part of the spectrum. Figure 3.2 provides a comparison of the WFC3 UVIS and ACS system throughputs.

The detectors in the WFC3 UVIS channel are two 4096×2051 pixel CCDs, butted together to yield a 4096×4102 array with a ~35 pixel (1.4 arcsec) gap. The gap can, of course, be filled in by using appropriate telescope dithering strategies (see Section 6.10.1 and Appendix C). The CCDs are thinned, back-illuminated Marconi Corporation (now e2v technologies Ltd.) devices with UV-optimized anti-reflection coatings and 15 micron pixels. The plate scale is approximately 0.04 arcsec per pixel, providing a good compromise between adequate sampling of the PSF and a wide field of view. Geometric distortions introduced by the WFC3 optics cause the nominally square detector to map onto the sky as a skewed rhombus, about 162×162 arcsec in size.

Uniform response within each pixel and excellent charge-transfer efficiency (CTE) are key to achieving accurate photometric performance. The anticipated CTE performance of the UVIS detectors over WFC3's lifetime is expected to be better than previous HST instruments due to several factors. First, shielding (similar to ACS/WFC and WFPC2) has been used to protect the CCDs from the high-radiation space environment, thereby slowing the production of charge traps. Second, the WFC3 CCDs have been designed with a mini-channel (improved over ACS/WFC), which will reduce the number of traps seen by small charge packets during read-out transfers. In addition, the WFC3 CCDs will have the option of charge injection, which, by filling traps, can mitigate the effects of CTE losses without an excessive increase in noise level. However, charge injection is not available in Cycle 17.

6.4 UVIS Field Geometry

6.4.1 Field of View and Pixel Size

As described above, the UVIS channel uses two 4096×2051 CCDs, butted together to yield a 4096×4102 array with a ~35 pixel (1.4 arcsec) gap. The field of view projected onto the sky is rhombus-shaped, 162 arcsec on a side, with an angle of 86.1° between the sides. The pixels projected onto the sky are also rhomboidal, ~0.0395 arcsec on a side.

6.4.2 Geometric Distortion

As just noted, distortions due to the WFC3 optics cause the nominally square field of view of the UVIS detector to map onto the sky as a skewed rhombus.

The distortion will affect both the photometric accuracy and the astrometric precision; nominal calibrations for these effects will be provided. For further discussion of WFC3 geometric distortion, see Appendix B.

6.4.3 Coordinate Systems

There are four different coordinate systems defined for use with the CCDs in the UVIS channel, each tailored to specific purposes. They are shown in Figure 6.1 and are as follows:

- Detector-based system (Xdet, Ydet)
- Image-based system (AXIS1, AXIS2)
- Proposal POS TARG system (X-POSTARG, Y-POSTARG)
- HST-based system (V2, V3 or U2, U3)

Figure 6.1: WFC3 CCD detector coordinates.

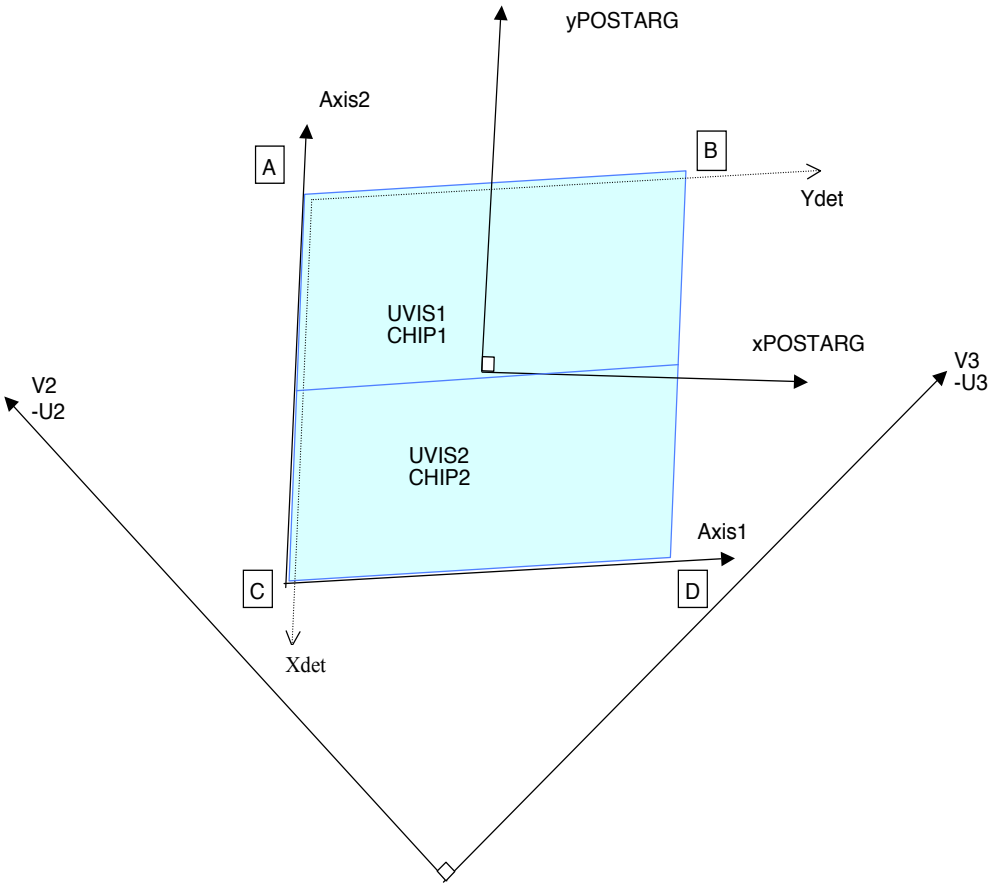

The **detector-based reference frame** (Xdet, Ydet, as shown in Figure 6.1) is used by the flight software for commanding the detectors. It is an orthogonal system, in pixel units, based upon the orientation of the CCD serial registers; its origin is at Amplifier A (the four amplifiers are in the outer corners of the detectors, as shown in Figure 6.1). The serial-readout direction is along the Ydet axis; this is also the nominal dispersion direction for the UVIS grism, G280. Parallel shifting is performed along constant Xdet, and serial shifting is done along the constant Ydet direction. Each of the two UVIS chips consists of 2051 physical pixels in the Xdet direction and 4096 pixels in the Ydet direction. The physical overscans at the end of each serial shift register are

included in the detector coordinate system; the virtual overscan pixels are not included (overscans are discussed in more detail in Section 6.7.2).

The **image-based coordinate system** (AXIS1, AXIS2, as shown in Figure 6.1) is defined for the ground system, and is used primarily by the calibration pipeline and other data-analysis software. Sometimes also referred to as the user or AXIS frame, when an image is displayed on a computer screen, this system has the X axis increasing to the right and the Y axis increasing to the top of the screen. For this coordinate system the origin is at Amplifier C. Note that for the WFC3 UVIS field of view, AXIS1 and AXIS2 map to +Ydet and −Xdet, respectively, in the detector-based coordinate system. The lengths of these axes, in pixels, are stored in the FITS image header keywords NAXIS1 and NAXIS2.

The **POS TARG reference frame**, sometimes referred to as the spacecraft system, is used for specifying the placement of an astronomical target relative to a physical aperture fiducial point in the instrument field of view. Its units are arcseconds. Some HST instruments have multiple physical apertures such as different slits; for the UVIS channel, which has only the two CCDs, the POS TARG system has been defined such that the Y-POSTARG axis is parallel to AXIS2 (note that the X-POSTARG axis will not be perfectly parallel to AXIS1 due to geometric distortion).

As is the case for other HST instruments, the POS TARG origin is defined to be at the center of the user-selected UVIS aperture (such as the geometric center of a particular chip, or the optimum center of a quadrant, etc.; see Table 6.1 below for the names of the various UVIS channel apertures). Figure 6.1 illustrates the POS TARG reference frame as centered on the aperture named “UVIS,” whose center is near the middle of the WFC3 UVIS field of view; the POS TARG directions are indicated by arrows labeled +X-pos and +Y-pos.

The **HST-based**, or vehicle (V2, V3), system is an orthogonal reference frame tied to the telescope and is used operationally for alignment, pointing, and slewing purposes. The V1 axis lies along the optical axis while V2,V3 run parallel and perpendicular, respectively, to the solar-array rotation axis (see Figure 2.2). Note that the (undistorted) diagonals of the WFC3 CCD detector run along the V2,V3 directions.

HST observers may be more familiar with the U2,U3 coordinate system than V2,V3; for example, the specification of the ORIENT angle Special Requirement uses the position angle of the U3 axis. The U2,U3 coordinates are defined as U2 = −V2 and U3 = −V3, and are marked in Figure 6.1 as well.

6.4.4 Subarrays and On-Chip Binning

While the default WFC3 UVIS readout mode is full-frame (both CCDs), **subarrays** may be employed to read out and store only a portion of the full field of view. Subarrays may be used, for example, in cases where the full-field data-volume and/or instrument-overhead requirements would constrain the observations unacceptably. There are also circumstances in which on-chip binning may be desirable.

The following paragraphs describe the predefined subarrays available for use with the WFC3 UVIS channel, as well as the capability for creating custom subarrays. These are followed by a discussion of on-chip binning.

Pre-Defined Subarrays

The WFC3 UVIS channel supports three pre-defined subarray sizes: two of them (2kx4k and 512x512 pixels) are suitable for use with any of the filters, and one (2kx2k pixels) is designed for use primarily with the quad filters.

The first two subarrays may be used with any filter element and are invoked via the appropriate Aperture parameter in the Phase II observing proposal; these apertures contain the string "2K4" or "512" in their names. The 2kx4k subarray will be centered at or near the center of one of the CCDs, while the 512x512 subarray can be placed at the center of either CCD, or in any one of the four outer chip corners (see Section 6.4.5 for more detail). These are fully supported modes when used with CCD chip 1; their use with CCD chip 2, while implemented in the observing system, is currently not available to observers.

For the special case of quad filters (which are optical elements that include four different bandpasses simultaneously, one bandpass per WFC3 UVIS quadrant), the observer must select one of the "QUAD" aperture values in the Phase II proposal, in conjunction with the desired quad filter via the filter parameter. This combination of quad aperture and quad filter will ensure that the target is placed in the correct quadrant for imaging with the requested quad bandpass. Furthermore, specification of the subarray quad aperture (UVIS-QUAD-SUB) instructs the ground system to read out only the 2kx2k quadrant of interest. If "-SUB" is omitted from the quad aperture name (i.e., UVIS-QUAD, UVIS-QUAD-FIX), the target will be positioned in the proper quadrant for the bandpass requested in the filter parameter, but the entire frame, both CCDs, will still be read out.

Use of any quad filter aperture, full-frame or subarray, is fully supported. However, if data volume and overhead time are not an issue, the observer is encouraged to allow full-frame readouts of quad-filter exposures, enabling serendipitous discoveries in the other quadrants of the image as well as enrichment of the HST data archive.

Note that the quad apertures may also be used with non-quad filters.

Custom Subarrays

If the pre-defined WFC3 UVIS subarray areas discussed above are insufficient for a science program, custom or observer-defined subarrays may be created through additional parameters in the Phase II proposal specifications, as described below. Note, however, that due to the large number of potential custom subarrays, although it is an allowed mode, the custom subarray is not a supported mode; this means that the observer is responsible for obtaining all necessary calibration data, along with the scientific data, and would have to request this additional time in the Phase I proposal.

Nearly any X,Y subarray dimension and centering in the field of view may be requested, though the resulting subarray must satisfy several requirements. First, the subarray must be read out through a single amplifier and thus must fall completely within a single CCD chip and, of course, fall on the same chip as the amplifier used for the readout. Furthermore, the subarray must be at least 1 pixel away from the edge of

the chip at all times, and finally, it must start on an even Y pixel (where 0 is the origin) and its size must be an even number of pixels in Y[1].

The APT proposal software tool will generate and report warnings to the observer, flagging any subarrays that violate these restrictions; the flight software will also verify that the requirements are satisfied.

Specifying the desired custom subarray size is done via the proposal parameters SIZEAXIS1 and SIZEAXIS2, which accept input in pixel units. By default, the STScI ground system centers the subarray at the aperture specified in the proposal. If a non-standard aperture position is desired, the location of the subarray center in the WFC3 field of view can be controlled via the CENTERAXIS1, CENTERAXIS2 parameters (again using pixel units). When constructing custom subarrays, keep in mind that, as discussed in the coordinate system section above, AXIS1 and AXIS2 map to +Y and −X in the detector system. If CENTERAXIS1, CENTERAXIS2 are not specified, the STScI ground system centers the subarray at the aperture specified in the proposal. If the target is repositioned within the aperture (e.g., via a POS TARG or PATTERN specification), *the subarray remains stationary on the detector, i.e., the target is moved with respect to the subarray.* This behavior can be overridden by setting the CENTERAXIS1, CENTERAXIS2 parameters to the string TARGET; this centers a subarray on the target coordinates regardless of the aperture reference point.

On-Chip Binning

For greater sensitivity when observing very faint targets, or for acquiring full-frame images as rapidly as possible, the BIN optional parameter in the observing proposal may be used to specify that the CCDs be read out in binned mode. Legal values for the parameter are NONE (the default), or 2 or 3, for 2x2 and 3x3 on-chip binning, respectively. On-chip binning is only allowed with full-frame readouts; it may not be used in conjunction with any subarray mode. To perform on-chip binning, multiple rows are parallel-shifted into the serial register, which is shifted multiple pixels at a time into a single output pixel, which is then read once. This type of binning improves the signal-to-noise in an image by minimizing readout noise: a 2x2 or 3x3 binned pixel will contain the same amount of read noise as a single pixel in an unbinned readout.

In addition to the S/N improvement, on-chip binning results in a significant reduction of readout overhead time, not only because of the shorter time needed to read out 1/4 or 1/9 of the usual full-frame number of pixels (~50 and ~23 sec, for 2x2 and 3x3 binning respectively, compared to 93 s for unbinned), but the image sizes will also be smaller, i.e., more images will fit into the instrument image buffer before it must be dumped to the SSR. However, binning will, of course, result in a loss of

1. The requirement for even pixel numbers is driven by the readout timing pattern used for subarrays, which employs a serial shift over the unwanted CCD pixels which is twice as fast as the normal slow serial shift used for reading out data. This is done to maintain synchronization with the WFC3 power supplies and minimize noise during the readout. This "fast" shifting past pixels outside the subarray area requires the subarray to be an even multiple of the time to "slow" serial shift a single pixel from the subarray

spatial resolution; the observer must weigh the benefit of binning against the cost of degraded resolution in the science images.

One final note regarding binning mode: it may also prove useful for CTE mitigation later in the WFC3 lifetime. Though the WFC3 CTE is expected to be excellent in the early years of operation, it will inevitably degrade due to the space environment. In existing HST detectors (and WFC3 is expected to be similar), a substantial amount of charge is lost into adjacent pixel(s), charge which binning would capture.

6.4.5 Apertures

The **APERTURE** parameter in the Phase II observing proposal controls the size and location of the field of view on the detector for the exposure, as well as the positioning of the target within that field of view. The default is to center the target within the chosen aperture, but a **POS TARG** Special Requirement may be added to offset the target relative to the center of the given aperture.

There are two types of predefined apertures: "**fixed**" and "**optimum**." The fixed positions refer to the geometric center of the aperture in question; as the name implies, their locations will remain fixed in aperture coordinates for the life of the instrument. The "optimum" apertures are placed near the geometric center of the region, but the precise location may be offset slightly from the geometric center so as to avoid any known CCD features (e.g., bad column) that might compromise the observation of a small target at that position. The locations of these "optimum" apertures may change over time as the characteristics of the CCD evolve.

The available WFC3 UVIS apertures are listed in Table 6.1. Note that there are both fixed and optimum versions for each of the primary locations: the center of the full two-chip detector (UVIS and UVIS-FIX), and the center of each chip (UVIS1 and UVIS2, and UVIS1-FIX and UVIS2-FIX). There are also fixed and optimum apertures for use with the quad filters only (UVIS-QUAD and UVIS-QUAD-FIX)[2].

There are also apertures for use with the two predefined generic UVIS subarray sizes (2kx4k and 512x512 pixels). The larger subarray can be placed at the center of CCD 1 (UVIS1-2K4-SUB); the smaller subarray can be placed in either the center of the CCD 1 field of view (UVIS1-M512-SUB) or in the corners (either near Amp A or near Amp B, using UVIS1-C512A-SUB or UVIS1-C512B-SUB). Similar predefined subarrays exist for CCD 2, and are listed for completeness in Table 6.1; however, due to limited resources, use of the CCD 2 subarrays is restricted.

All subarray apertures are placed at optimum positions on the CCD; there are no "fixed" subarray apertures. Finally, note that use of one of the predefined subarray apertures in the observing proposal simultaneously specifies *both* the size of the subarray *as well as* the positioning of that array within the WFC3 field of view; no further subarray parameters are required. If more flexibility is necessary for the

2. For the quad filters, the ground-system software determines the correct quadrant for target placement based upon the quad filter (FQ* filters listed in Table 6.2) requested by the observer. Note that for a quad-filter exposure, the full, two-CCD frame will be read out, unless the UVIS-QUAD-SUB aperture is selected, in which case only the single 2kx2k quadrant of interest is captured during readout.

subarray, a custom subarray may be defined. In this case, additional parameters beyond just aperture must be specified in the observing proposal to describe the desired subarray (e.g., SIZEAXIS1, SIZEAXIS2, and potentially CENTERAXIS1, CENTERAXIS2; see Section 6.4.4). This mode is, however, not supported and the observer is responsible for obtaining any necessary calibration data for non-standard apertures, and would have to request this additional time in the Phase I proposal.

Table 6.1: Predefined Apertures for WFC3/UVIS Channel

Aperture	Description
UVIS	Optimum center of full two-CCD field of view
UVIS-FIX	Geometric center of full two-CCD field of view
UVIS1	Optimum center of CCD Chip 1
UVIS1-FIX	Geometric center of CCD Chip 1
UVIS2	Optimum center of CCD Chip 2
UVIS2-FIX	Geometric center of CCD Chip 2
UVIS-QUAD	Optimum center of quadrant corresponding to selected quadrant filter
UVIS-QUAD-FIX	Geometric center of quadrant corresponding to selected quadrant filter
UVIS-QUAD-SUB	Optimum center of the quadrant corresponding to the selected quadrant filter, with a 2kx2k subarray to read out only that quadrant
UVIS1-2K4-SUB **UVIS2-2K4-SUB**	Optimum center of CCD Chip 1 or CCDChip 2 using a 2kx4k subarray[1]
UVIS1-M512-SUB **UVIS2-M512-SUB**	Optimum center of CCD Chip 1 or CCD Chip 2 using a 512x512 subarray[1]
UVIS1-C512A-SUB **UVIS1-C512B-SUB**	Optimum center of 512x512 subarray located in corner of CCD Chip 1 near either amp A or B
UVIS2-C512C-SUB **UVIS2-C512D-SUB**	Optimum center of 512x512 subarray located in corner of CCD Chip 2 near either amp C or D[1]
G280-REF	Grism reference aperture for undispersed exposures

1. The CCD Chip 2 subarrays, although listed here for completeness, are restricted and not currently offered to General Observers.

6.5 UVIS Spectral Elements

6.5.1 Filter and Grism Summary

An overview of the UVIS spectral elements, and of the process by which they were selected, was given in Section 2.3. This section gives further details of the UVIS filters and grism. Table 6.2 contains a complete listing of the available spectral elements in the UVIS channel. Figures 6.2 through 6.5 show the effective throughput curves, including the filter transmission convolved with the OTA, WFC3 optics, and detector response. All of the UVIS filters are contained in a multi-wheel package called the Selectable Optical Filter Assembly (SOFA).

More detailed information on the throughput curves of all of the filters is given in Appendix A. All measurements of the UVIS filters which involve wavelengths, as tabulated in Table 6.2 and plotted in Figures 6.2 through 6.5 and in Appendix A, were done in air. In evaluating critical cases (e.g., narrow-band imaging of redshifted galaxies), one should convert the air wavelengths to vacuum using, for example, the formula given by D. C. Morton (1991, *ApJS*, **77**, 119). It should also be noted that the laboratory measurements were done at a temperature of 20°C, whereas the UVIS filters will be operated on orbit at 0°C; this may lead to wavelength shifts which are expected to be small.

The UVIS filters have been chosen to cover a wide variety of scientific applications, ranging from color selection of distant galaxies to accurate photometry of stellar sources and narrow-band imaging of nebular gas. The set includes several very wide-band filters for extremely deep imaging, filters that match the most commonly used filters on WFPC2 and ACS (to provide continuity with previous observations), the SDSS filters, and filters that are optimized to provide maximum sensitivity to various stellar parameters (e.g., the Strömgren and Washington systems, and the F300X filter for high sensitivity to the stellar Balmer jump). There is a variety of narrow-band filters, which will allow investigations of a range of physical conditions in the interstellar medium, nebulae, and solar system. A few of the narrow-band filters are also provided with slightly redshifted wavelengths, for use in extragalactic applications. Finally, there is a UV grism that provides slitless spectra covering 200-400 nm.

Note that, in contrast to ACS, WFC3 does not have any polarizers or ramp filters.

Table 6.2: WFC3/UVIS Filters and Grism.

Name[1]	Description[2]	Pivot[3] λ (Å)	Width[4] (Å)	Peak Transmission
UVIS Long-Pass (LP) and Extremely Wide (X) Filters				
F200LP	Clear; grism reference	5686.9	(6500)	0.98
F300X	Extremely wide UV	2829.8	753.0	0.53
F350LP	Long pass	6812.0	(4500)	0.98
F475X	Extremely wide blue	4917.1	2199.6	0.94
F600LP	Long pass	8430.2	(4000)	0.99
F850LP	SDSS *z′*	9756.4	(1500)	0.96
UVIS Wide-Band (W) Filters				
F218W	ISM feature	2183.0	351.7	0.23
F225W	UV wide	2341.0	547.3	0.32
F275W	UV wide	2715.3	480.8	0.46
F336W	*U*, Strömgren *u*	3361.1	553.8	0.75
F390W	Washington *C*	3904.6	953.0	0.96
F438W	WFPC2 *B*	4318.7	676.8	0.84
F475W	SDSS *g′*	4760.6	1488.9	0.92
F555W	WFPC2 *V*	5309.8	1595.1	0.95
F606W	WFPC2 Wide *V*	5907.0	2304.2	0.99
F625W	SDSS *r′*	6254.0	1575.4	0.95
F775W	SDSS *i′*	7733.6	1486.0	0.85
F814W	WFPC2 Wide *I*	8304.7	2543.3	0.97
UVIS Medium-Band (M) Filters				
F390M	Ca II continuum	3893.8	210.5	0.88
F410M	Strömgren *v*	4107.0	182.8	0.98
FQ422M	Blue continuum	4217.7	113.3	0.69
F467M	Strömgren *b*	4680.7	218.0	0.98
F547M	Strömgren *y*	5447.0	714.0	0.88
F621M	11% passband	6216.7	631.0	0.99
F689M	11% passband	6886.0	708.6	0.94
F763M	11% passband	7636.3	798.6	0.97
F845M	11% passband	8468.9	886.7	0.96
UVIS Narrow-Band (N) Filters				
FQ232N	C II] 2326	2326.9	32.2	0.12
FQ243N	[Ne IV] 2425	2420.6	34.8	0.15
F280N	Mg II 2795/2802	2796.8	22.9	0.27
F343N	[Ne V] 3426	3438.0	140.0	0.78
F373N	[O II] 3726/3728	3729.6	39.2	0.78
FQ378N	*z* ([O II] 3726)	3790.9	89.2	0.83
FQ387N	[Ne III] 3868	3873.0	23.1	0.72
F395N	Ca II 3933/3968	3953.7	72.9	0.86
FQ436N	Hγ 4340 + [O III] 4363	4366.7	35.7	0.67
FQ437N	[O III] 4363	4370.6	24.6	0.70
F469N	He II 4686	4687.5	37.2	0.69
F487N	Hβ 4861	4870.7	48.4	0.85
FQ492N	*z* (Hβ)	4932.1	101.0	0.85

Name[1]	Description[2]	Pivot[3] λ (Å)	Width[4] (Å)	Peak Transmission
F502N	[O III] 5007	5009.0	57.8	0.87
FQ508N	*z* ([O III] 5007)	5089.7	117.9	0.87
FQ575N	[N II] 5754	5755.9	12.9	0.78
FQ619N	CH_4 6194	6197.5	61.6	0.89
F631N	[O I] 6300	6303.0	43.1	0.86
FQ634N	6194 continuum	6347.5	66.2	0.88
F645N	Continuum	6451.6	85.0	0.86
F656N	Hα 6562	6561.1	13.9	0.86
F657N	Wide Hα + [N II]	6565.1	96.3	0.90
F658N	[N II] 6583	6585.2	23.6	0.92
F665N	*z* (Hα + [N II])	6654.4	109.0	0.90
FQ672N	[S II] 6717	6716.1	14.9	0.89
F673N	[S II] 6717/6731	6764.5	100.5	0.91
FQ674N	[S II] 6731	6729.5	10.0	0.68
F680N	*z* (Hα + [N II])	6878.6	323.6	0.95
FQ727N	CH_4 7270	7274.7	64.8	0.89
FQ750N	7270 continuum	7500.6	68.8	0.85
FQ889N	CH_4 25 km-agt[5]	8891.8	93.7	0.90
FQ906N	CH_4 2.5 km-agt	9056.7	94.0	0.92
FQ924N	CH_4 0.25 km-agt	9246.3	89.2	0.94
FQ937N	CH_4 0.025 km-agt	9371.1	91.9	0.91
F953N	[S III] 9532	9529.7	84.6	0.90
	UVIS Grism (G)			
G280	UV grism	(2775)	1850	0.4

1. The spectral-element naming convention is as follows for both the UVIS and IR channels. All filter names begin with F, and grisms with G; if the filter is part of a four-element quad mosaic, a Q follows F. Then there is a three-digit number giving the nominal effective wavelength of the bandpass, in nm (UVIS channel) or nm/10 (IR channel). (For long-pass filters, the number is instead the nominal blue cut-off wavelength in nm.) Finally, for the filters, one or two letters indicate the bandpass width: X (extremely wide), LP (long pass), W (wide), M (medium), or N (narrow).
2. Filters intended for imaging in a red-shifted bandpass are given descriptions similar to the following: "*z* (Hα + [N II])".
3. "Pivot wavelength" is a measure of the effective wavelength of a filter (see A. Tokunaga & W. Vacca 2006, PASP, **117**, 421). It is calculated here based only on the filter transmission. Values are approximate for the long-pass filters. All wavelength measurements in this table were made in air.
4. Full width at 50% of peak transmission for wide and medium bands, and at 10% of peak transmission for narrow bands. For long-pass filters, the widths are approximate and include convolution with the detector QE.
5. km-agt (km-amagat) is a unit of vertical column density, equal to 2.69×10^{24} molecules/cm^2.

Most of the UVIS filters, as well as the UVIS grism, are full-sized elements that cover the entire UVIS field of view. However, in order to provide a larger number of bandpasses, there are five “quad” filters, identified with "FQ" in the filter name, where each bandpass covers ~1/4 of the WFC3 UVIS field of view (i.e., each bandpass covers half of a single CCD chip). The quad filters are discussed in more detail below.

The UVIS channel is designed to be used with a single filter or grism in the light path. Although possible in principle, unfiltered imaging, or imaging through a combination of two filters (from two different SOFA wheels), would lead to significantly degraded image quality and has not been tested; thus these options are not permitted.

While the red blocking in the WFC3 UV filters is generally very good, resulting in negligible red leaks for hot objects (typically <<1% for targets with effective temperature $T_{\rm eff}$ > 10,000 K), the red leak can become significant in some filters for cooler targets (e.g., ~10% in F225W for a star with $T_{\rm eff}$ = 5000 K). More details are available in “Filter Red Leaks” on page 74; Table 6.3 in that section tabulates red-leak values as a function of stellar effective temperature.

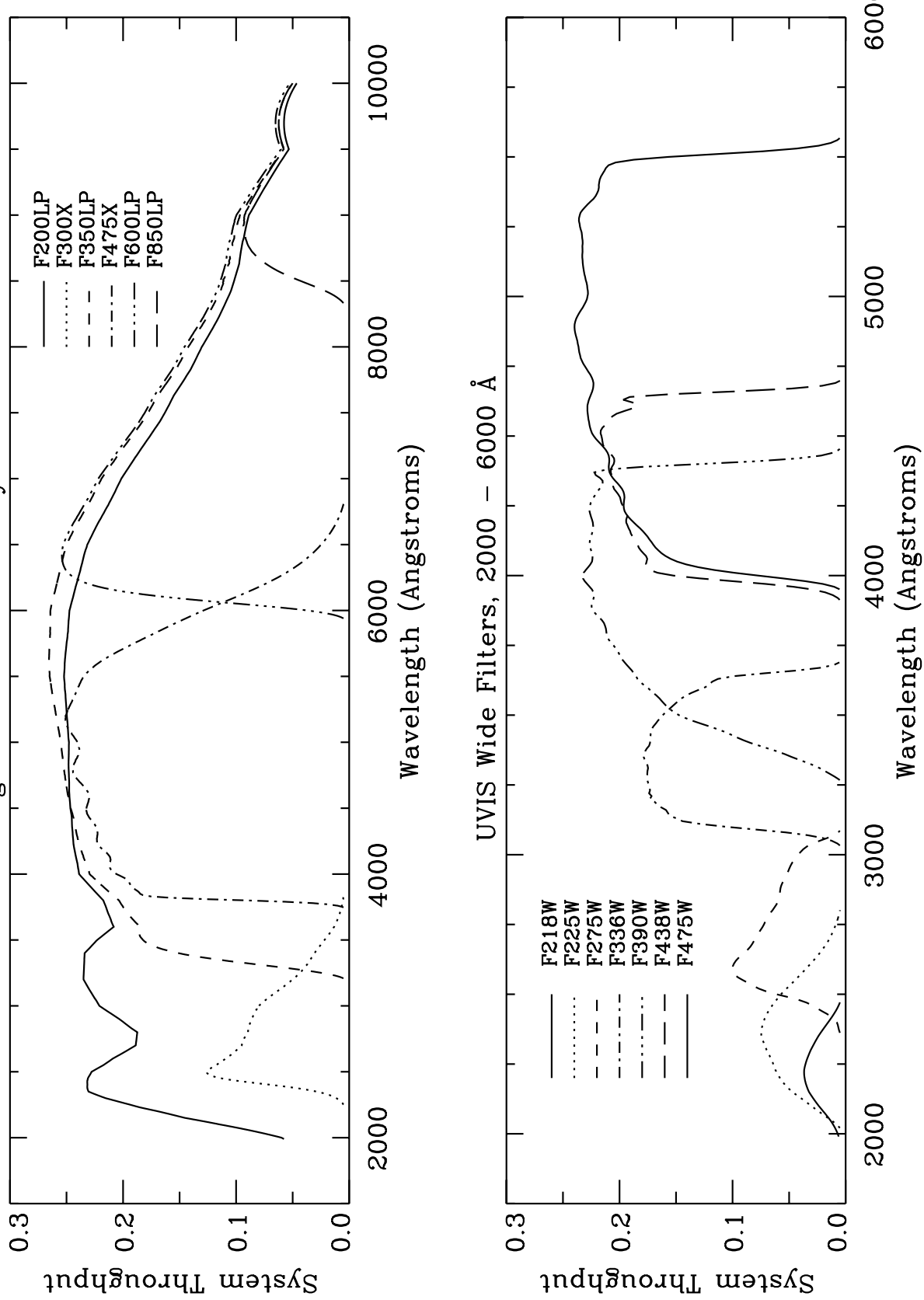

Figure 6.2: Integrated system throughput of the WFC3 UVIS long-pass and extremely wide filters (top panel) and of the wide-band filters covering 2000-6000 A (bottom panel). The throughput calculations include the *HST* OTA, WFC3 UVIS-channel internal throughput, filter transmittance, and the QE of the UVIS flight detector. Throughputs in all plots below ~3200 A include correction for quantum yield. Instrument throughput is not yet well-characterized below 2000 A and above 10,000 A.

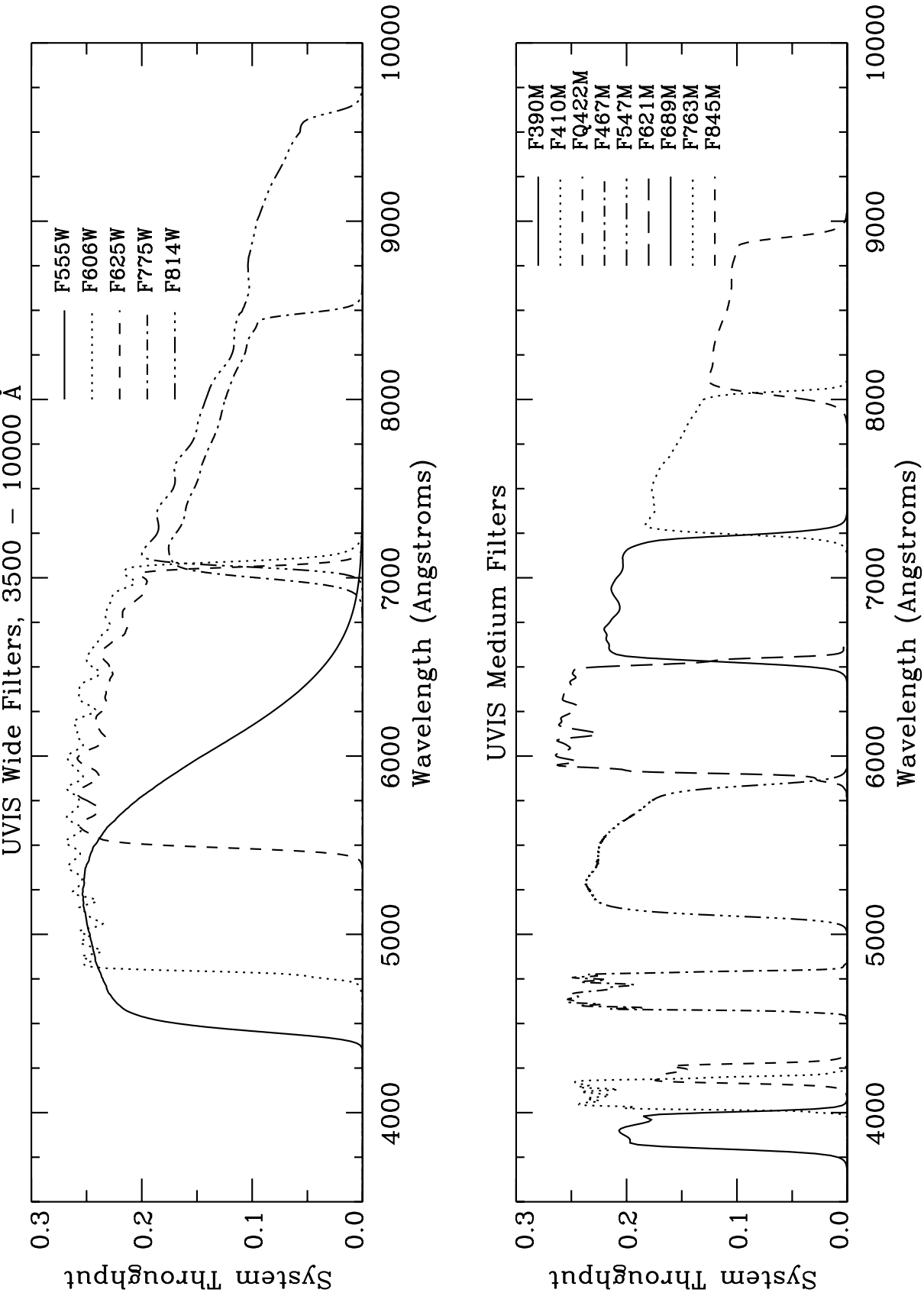

Figure 6.3: Integrated system throughput of the WFC3 UVIS wide-band filters covering 4000-10,000 A (top panel) and the medium-band filters (bottom panel). The throughput calculations include the *HST* OTA, WFC3 UVIS-channel internal throughput, filter transmittance, and the QE of the UVIS flight detector.

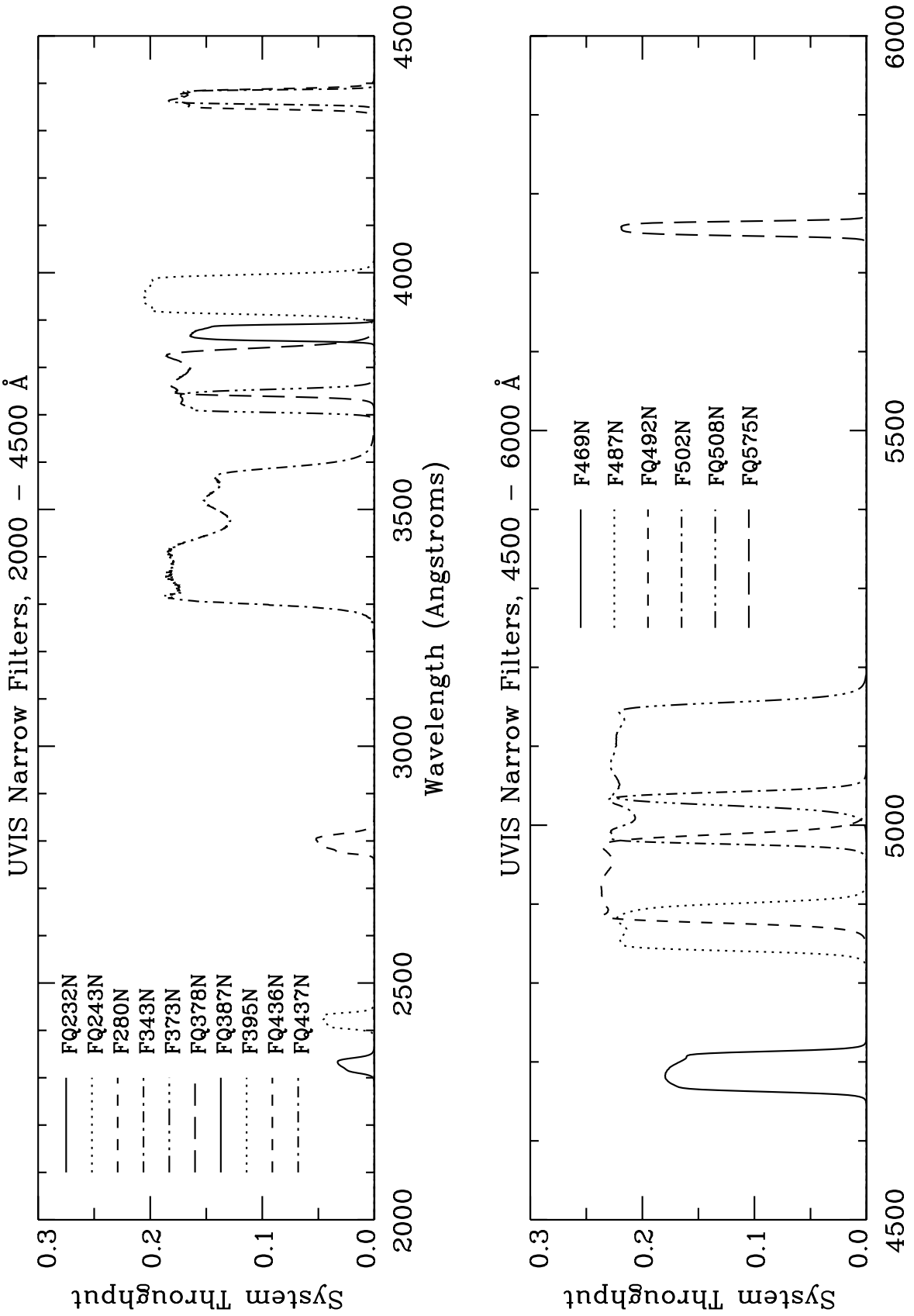

Figure 6.4: Integrated system throughput of the WFC3 UVIS narrow-band filters covering 2000-4500 A (top panel) and the narrow-band filters covering 4500-6000 A (bottom panel). The throughput calculations include the *HST* OTA, WFC3 UVIS-channel internal throughput, filter transmittance, and the QE of the UVIS flight detector.

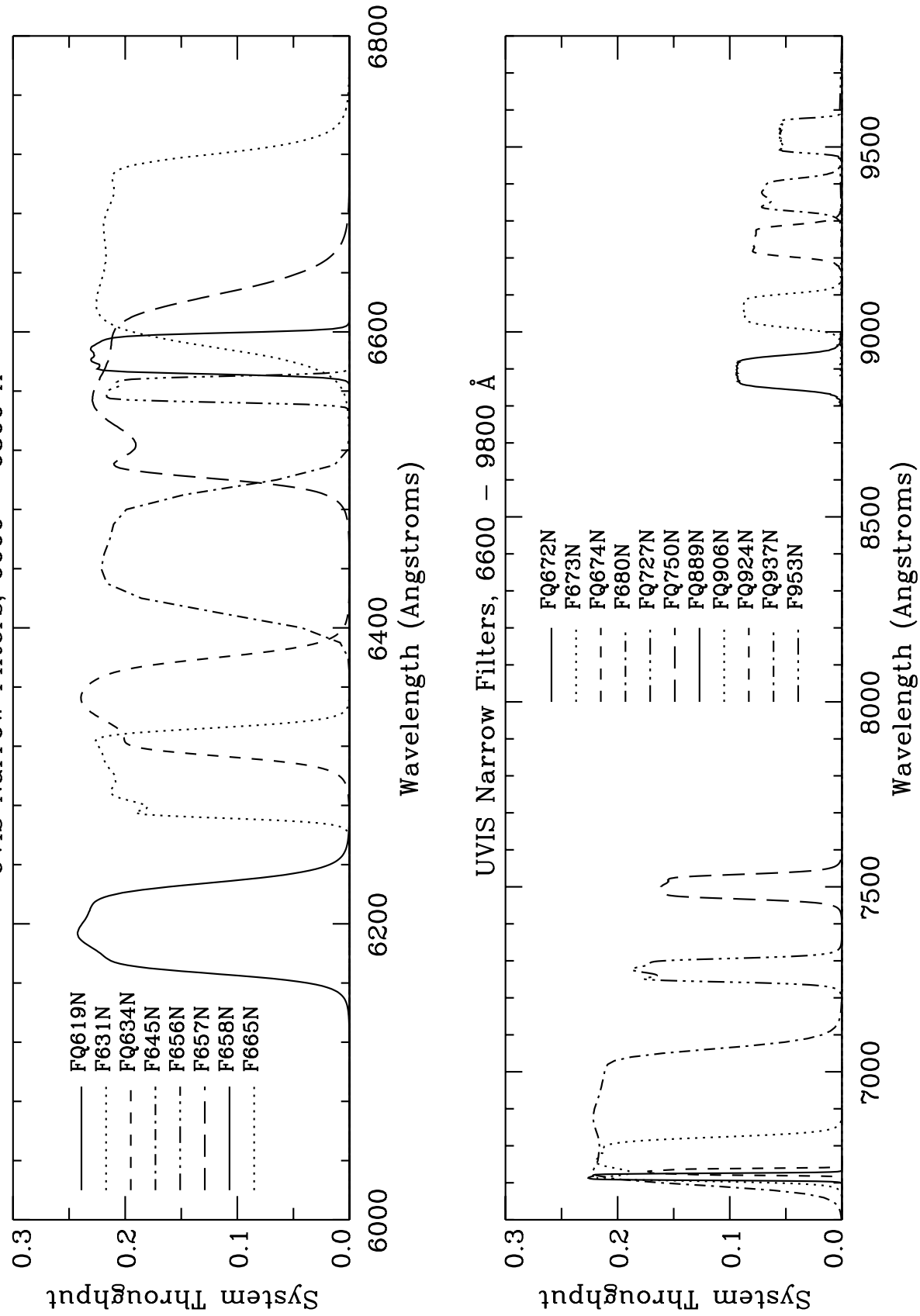

Figure 6.5: Integrated system throughput of the WFC3 UVIS narrow-band filters covering 6000-6800 A (top panel) and the narrow-band filters covering 6600-9600 A (bottom panel). The throughput calculations include the *HST* OTA, WFC3 UVIS-channel internal throughput, filter transmittance, and the QE of the UVIS flight detector.

UV Filters

As mentioned earlier, the WFC3 UVIS optics and CCDs have been optimized for UV imaging. As such, the UV filters play a key role and considerable effort has been made to procure filters with the best possible characteristics, including maximum throughput, maximum out-of-band blocking, and minimal ghosts.

The UV filters include the shortest-wavelength F218W, intended for studies of the ISM absorption feature; the wide F225W and F275W for broad-band UV imaging; the Strömgren *u* (F336W) and Washington C (F390W) for stellar astrophysics; the extremely wide F300X for very deep imaging; and narrow bands such as F280N (Mg II) and the quad filters FQ232N and FQ243N (C II] and [Ne IV]).

There is also an ultra-wide F200LP filter; it is simply a fused-silica element with a UV-optimized anti-reflection coating which covers the UVIS channel's entire spectral range (200-1000 nm). The F200LP filter is analogous to the clear filter on STIS.

WFC3's maximum sensitivity to hot sources can be obtained by subtracting an F350LP image from an F200LP, thereby creating a very broad ultraviolet bandpass. In Figure 6.6, the gray curve shows the filter transmission for the F200LP filter, and the black curve shows the effective transmission for a F200LP minus F350LP difference image. For redder targets, some additional calibration may be necessary to account for differences in the transmission of the two filters longward of ~450 nm.

Figure 6.6: Sensitivity of F200LP-F350LP compared to other UV filters (F225W, F275W and F300X). Dashed curves show blackbody functions for 20,000 and 50,000 K.

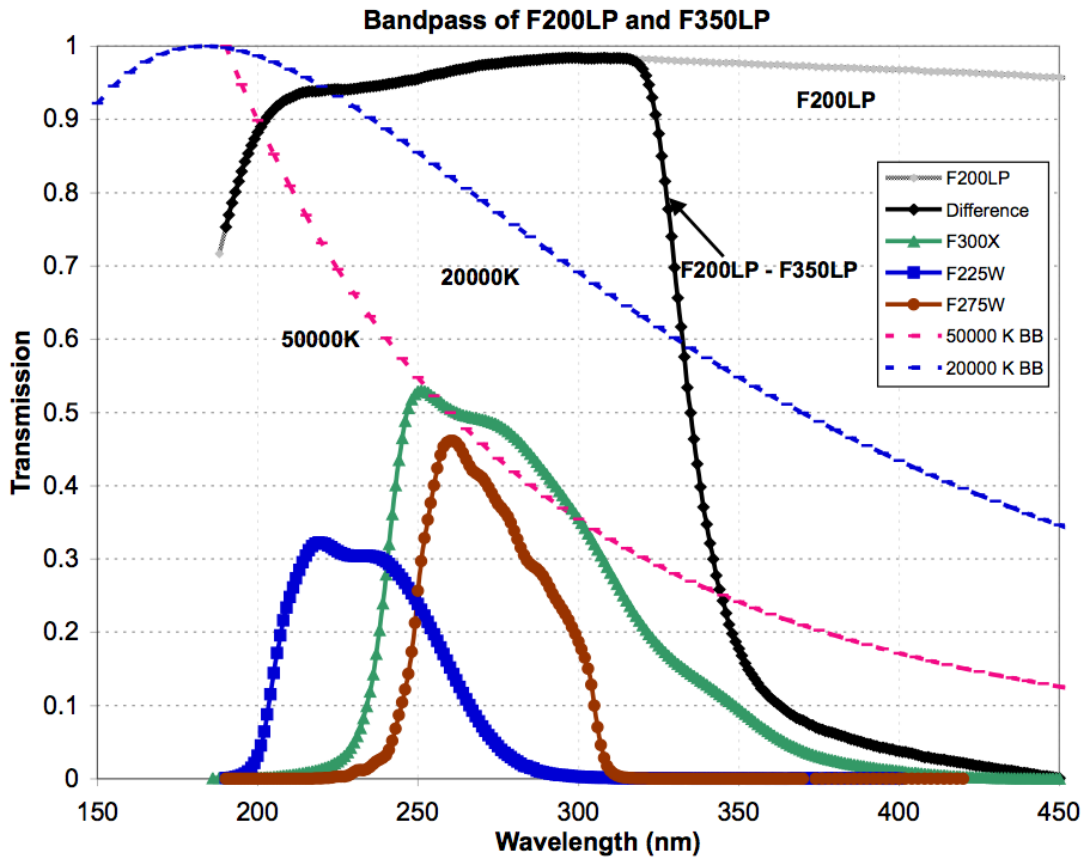

Wide-band Filters

The most commonly used WFPC2 and ACS wide filters are also included in the WFC3 filter set. In addition to a wide *V*-band filter (F606W), there is the Johnson-Cousins *BVI* set (F438W, F555W, F814W).

The Sloan Digital Sky Survey (SDSS) *griz* filter set (F475W, F625W, F775W, F850LP) is designed to provide high throughput for the wavelengths of interest and excellent rejection of out-of-band wavelengths. These filters will provide wide, non-overlapping filter bands that cover the entire range of CCD sensitivity from blue to near-IR wavelengths.

Medium-band Filters

The medium-band filters include the Strömgren set (*u*, *v*, *b*, and *y*), as well as some continuum bands needed for use with narrow-band imaging (F390M, FQ422M). The four 11% passband filters were added to the WFC3 UVIS set in order to cover the ~600-900 nm wavelength region with equal-energy filters. The "11%" refers to the filter bandwidths, which are ~11% of the central wavelength.

Narrow-band Filters

The WFC3 UVIS channel contains 36 different narrow-band filters, covering a variety of species and most of the astrophysically interesting transitions, including Hα, Hβ, Hγ, He II, C II], [N II], [O I], [O II], [O III}, [Ne IV], [Ne V], [S II], and Ca II. The methane absorption bands seen in planets, cool stars, and brown dwarfs are also covered.

Quad Filters

The WFC3 UVIS channel contains five quad filters: each is a 2×2 mosaic of filter elements occupying a single filter slot, with each quadrant providing a different bandpass (typically narrow-band, although there are also several bandpasses intended for continuum measurements).

A quadrant nominally covers only 1/4 of the WFC3 total field of view or about 80"×80", although edge effects will result in an unvignetted field somewhat smaller than 1/4 of the field of view. The five quad filters on WFC3 significantly increase the number of available narrow-band filters. The WFC3 quad filters are identified by the prefix "FQ" in the filter name in Table 6.2.

Grism

The UVIS channel has a UV grism (G280), a spare from WF/PC-1. It provides slitless spectra with a dispersion of about 1.4 nm/pix and a spectral resolution of about 70, over the 200-400 nm wavelength range. Typically, a grism observation will be accompanied by a direct image, for source identification and wavelength calibration; an ideal filter for the identification image would be the F200LP discussed above. Chapter 8 discusses WFC3 slitless spectroscopy in detail.

6.5.2 Filter Red Leaks

The design and manufacture of the UV filters was based on a careful balance of the in- and out-of-band transmissions: in general, higher in-band transmission results in poorer suppression of out-of-band transmission, and vice versa. The WFC3 filters represent an attempt to achieve an optimum result, maximizing the in-band transmission while keeping the out-of-band transmission as low as possible in order to minimize red leaks.

Table 6.3 below summarizes the red-leak levels for the WFC3 UV filters. The table lists the fraction of the total signal that is due to flux longward of 400 nm, as a function of stellar effective temperature. As can be seen from the table, red leaks should not be an issue for observations of any target taken with F275W or F336W. The other UV filters will have some red leak, whose importance depends on stellar temperature. The red leak in F218W, for example, will exceed ~1% for objects cooler than ~7000 K, while in F300X the red leak reaches ~1% for objects as hot as 10,000 K. The most extreme red leaks will arise from F218W and F225W observations of objects with $T_{\rm eff}$ of ~5000 K or cooler, necessitating appropriate corrections.

Table 6.3: Fraction of flux longward of 400 nm as a function of effective temperature.

$T_{\rm eff}$ (K)	F218W	F225W	F275W	F300X	F336W
2000	1.0E+00	1.0E+00	1.0E+00	9.3E-01	6.9E-02
3000	9.8E-01	9.9E-01	8.2E-01	2.8E-01	2.9E-03
4000	9.2E-01	7.4E-01	1.3E-01	1.6E-01	1.0E-03
5000	5.9E-01	1.0E-01	9.5E-03	5.8E-02	1.7E-04
6000	5.0E-02	7.2E-03	1.4E-03	2.4E-02	5.4E-05
7000	1.3E-02	1.8E-03	7.1E-04	1.7E-02	3.3E-05
8000	7.1E-03	9.2E-04	5.0E-04	1.5E-02	2.8E-05
9000	4.5E-03	5.3E-04	3.7E-04	1.3E-02	2.3E-05
10000	3.4E-03	3.8E-04	3.0E-04	1.1E-02	2.0E-05
11000	2.4E-03	2.6E-04	2.2E-04	9.0E-03	1.5E-05
12000	1.9E-03	2.0E-04	1.7E-04	7.4E-03	1.2E-05
13000	1.5E-03	1.6E-04	1.4E-04	6.2E-03	1.0E-05
14000	1.3E-03	1.3E-04	1.2E-04	5.3E-03	8.6E-06
15000	1.1E-03	1.1E-04	1.0E-04	4.6E-03	7.6E-06
20000	6.3E-04	6.1E-05	6.4E-05	3.1E-03	5.2E-06
30000	3.5E-04	3.3E-05	4.0E-05	2.0E-03	3.5E-06
40000	2.8E-04	2.5E-05	3.2E-05	1.6E-03	2.8E-06
50000	2.7E-04	2.5E-05	3.2E-05	1.6E-03	2.8E-06

6.5.3 Ghosts

The WFC3 UVIS channel exhibits three different types of optical ghosts: a) those due to reflections between the CCD front surface and the two detector package windows; b) those due to reflections between the window surfaces; and c) those due to reflections between the surfaces of the particular filter in use.

Window Ghosts

When a point source is positioned at the lower right of the field of view, reflections between the CCD and windows appear along the diagonal from the center of the field of view towards the upper left; these ghosts gradually move outside the field of view as the target source moves out of the lower right corner. Smaller ghosts appear closer to the target source: they are due to reflections between the window surfaces (see Figure 6.10 for an image showing these ghosts).

Filter Ghosts

Filter ghosts, however, can occasionally fail to satisfy the specification. During initial instrument-level ground tests, while most of the WFC3 UVIS filters performed consistently with, or exceeding, expectations, a few of the filters were found to have filter ghosts. The highest-priority filters affected by ghosts were re-manufactured and re-installed into the SOFA.

The levels of filter ghosts in the majority of the final flight filter set are now <0.1%, well within the specified requirements. However, a subset of the final flight filters still have ghosts exceeding the specification, which calls for <0.2% of the total flux to reside in the ghost. These filters are listed in Table 6.4. They have been retained in the flight instrument either because they were of lower scientific priority, or because the ghost level was deemed acceptable in light of the otherwise excellent performance characteristics of the filters (e.g., in- and out-of-band transmission, sharpness of bandpass edges). While some scientific programs (e.g., stellar photometry) may be unaffected by filter ghosts, others (e.g., observations of extended targets or faint objects adjacent to bright ones) could be adversely affected. In such cases, extra planning and/or data-analysis efforts may be needed, e.g., combining images taken at different dither positions and/or roll angles, or applying a deconvolution algorithm.

Table 6.4: Filters exceeding the filter ghost requirement, measured during ground testing of the integrated instrument (see WFC3 ISR 2007-09).

Filter	Description	Ghost Level (% of total PSF flux)
F200LP	Clear, grism reference	0.35[1]
F218W	ISM feature	1.3
F225W	UV wide	0.4
FQ232N	CII] 2326	7.0
FQ243N	[Ne IV] 2425	5.0
F280N	Mg II 2795/2802	0.6
F300X	Extremely wide UV	0.3
F656N	Hα 6562	0.4
F658N	[N II] 6583	0.4
F665N	z(Hα + [N II])	0.1
F673N	[S II] 6717/6731	0.3
F680N	z(Hα + [NII])	0.3

1. Laboratory measurement of stand-alone filter.

6.6 UVIS Optical Performance

At this writing, we do not have direct observations of the sky using WFC3 installed in HST. However, extensive laboratory measurements have been made during WFC3 ground testing, and these indicate that excellent optical performance will be achieved.

Many of these measurements have been made in conjunction with a separate optical stimulus, which provides external light sources to WFC3. Adapted from the stimulus used for WF/PC-1 and WFPC2, it simulates the *HST* OTA as seen by WFC3, including the major optical aberrations. It supplies flux-calibrated point-sources as well as flat-field illumination via an integrating sphere.

The following subsections summarize the expected flight optical performance for the UVIS channel.

6.6.1 Model PSF and FWHM

In the UVIS channel, ground-based point-source measurements of artificial sources from the optical stimulus have been taken at 16 positions across the field of view and at four different wavelengths. These show excellent imaging performance over the

entire field of view that satisfies the required specifications. Results obtained from ground data taken with the optical stimulus do, however, require corrections in order to estimate the on-orbit performance, e.g., by taking into account the differences in the central obscuration ratios and the spider widths and including the mid-frequency figure error of the OTA mirrors.

Figure 6.7 plots the azimuthally-averaged model OTA+WFC3 PSF at three different UVIS wavelengths, indicating the fractional PSF flux per pixel at radii from 1 pixel to 5 arcsec. Table 6.5 lists the full width at half maximum of the model PSF core in units of pixel and arcsec for 10 wavelengths.

Table 6.5: WFC3/UVIS PSF FWHM (pixels and arcseconds) vs. wavelength.

Wavelength (nm)	FWHM (pix)	FWHM (arcsec)
200	2.294	0.096
300	1.990	0.083
400	1.812	0.076
500	1.691	0.070
600	1.622	0.068
700	1.629	0.068
800	1.720	0.072
900	1.880	0.078
1000	2.109	0.088
1100	2.321	0.097

Figure 6.7: Azimuthally averaged WFC3/UVIS PSF.

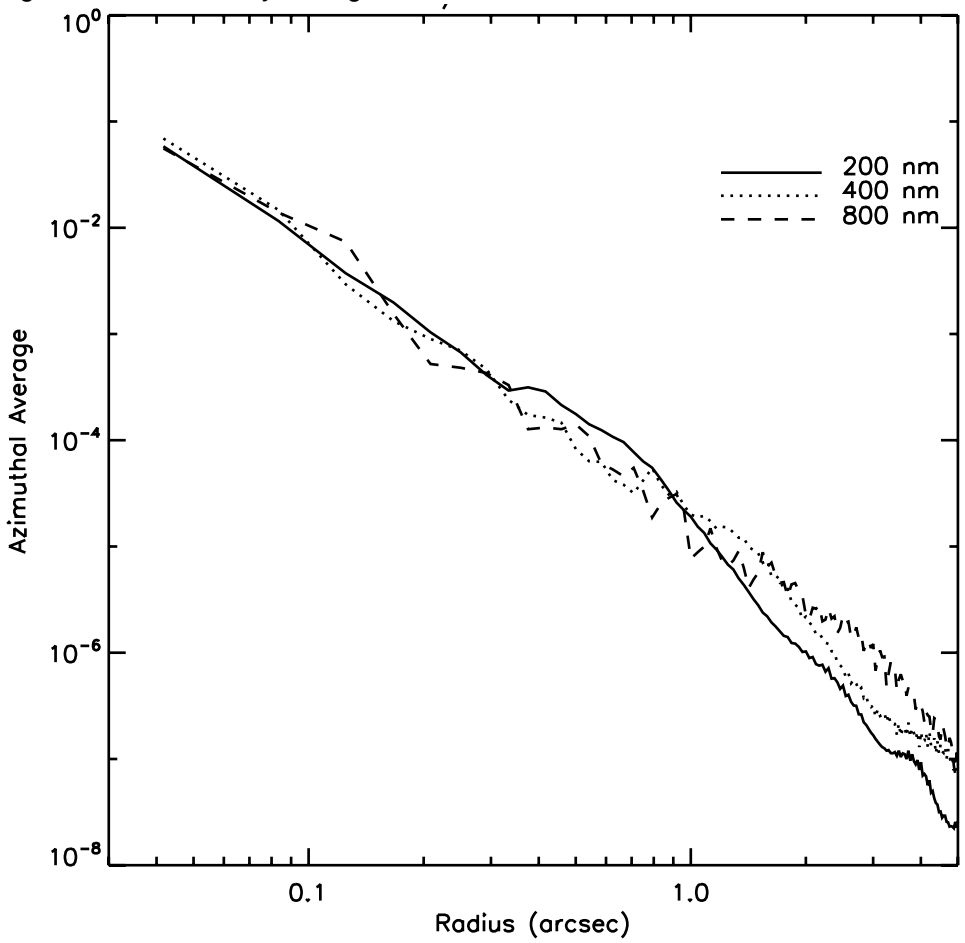

6.6.2 Encircled and Ensquared Energy

The **encircled energy** is the fraction of the total light from a point source that is contained within a circular aperture of a given radius. Like the FWHM, it is useful for comparison of well-behaved PSFs, such as WFC3's in the infrared. Since modern detectors have nominally square pixels, it is often more convenient to evaluate the energy falling within a certain number of pixels ("**ensquared energy**") instead of the encircled energy, which requires interpolation to account for the fractional pixels intercepted by a circular aperture.

Extrapolation of the encircled energy results from ground-based to on-orbit yields the encircled and ensquared energy values presented in Tables 6.6 and 6.7 and plotted in Figure 6.8 for 200, 400, and 800 nm.

Figure 6.8: Encircled Energy for the WFC3/UVIS channel.

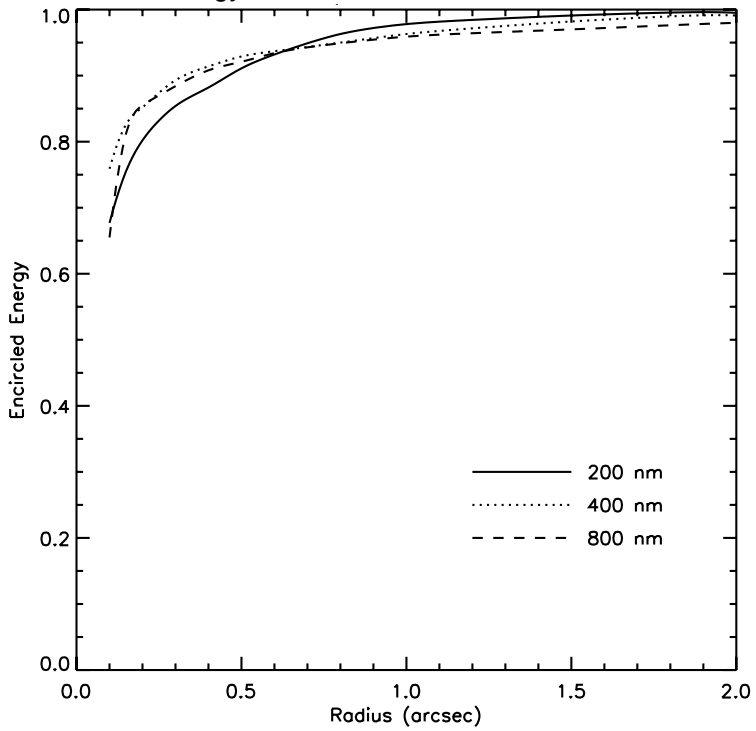

Table 6.6: WFC3/UVIS PSF Encircled Energy Fraction vs. Aperture radius (arcsec).

Aperture radius (arcsec)	Wavelength (nm)									
	200	**300**	**400**	**500**	**600**	**700**	**800**	**900**	**1000**	**1100**
0.10	0.677	0.743	0.759	0.751	0.727	0.693	0.655	0.626	0.614	0.609
0.15	0.755	0.804	0.826	0.836	0.835	0.827	0.812	0.783	0.745	0.699
0.20	0.802	0.840	0.852	0.861	0.860	0.858	0.855	0.850	0.848	0.834
0.25	0.832	0.867	0.874	0.879	0.878	0.874	0.870	0.867	0.869	0.865
0.30	0.854	0.884	0.893	0.894	0.893	0.891	0.884	0.879	0.879	0.876
0.40	0.882	0.907	0.914	0.920	0.915	0.910	0.908	0.905	0.900	0.894
0.50	0.911	0.920	0.929	0.932	0.931	0.928	0.921	0.916	0.919	0.917
0.60	0.932	0.931	0.937	0.943	0.941	0.938	0.934	0.929	0.928	0.924
0.80	0.963	0.953	0.950	0.954	0.954	0.951	0.949	0.945	0.946	0.944
1.00	0.978	0.968	0.963	0.962	0.961	0.960	0.959	0.955	0.957	0.954
1.50	0.991	0.988	0.982	0.979	0.977	0.974	0.970	0.969	0.972	0.970
2.00	0.995	0.994	0.991	0.990	0.986	0.982	0.980	0.978	0.979	0.977

Table 6.7: WFC3/UVIS PSF Ensquared Energy Fraction vs. Aperture size (pixels), where the target is centered on the aperture and falls on the central pixel.

Aperture size (pixels)	Wavelength (nm)									
	200	300	400	500	600	700	800	900	1000	1100
1×1	0.127	0.165	0.187	0.198	0.196	0.184	0.166	0.147	0.129	0.112
2×2[1]	0.368	0.432	0.454	0.461	0.461	0.456	0.439	0.414	0.384	0.350
3×3	0.554	0.620	0.627	0.613	0.589	0.574	0.568	0.563	0.554	0.534
5×5	0.708	0.769	0.790	0.793	0.779	0.751	0.710	0.668	0.641	0.626
7×7	0.770	0.815	0.833	0.842	0.843	0.838	0.830	0.814	0.788	0.748
9×9	0.809	0.847	0.858	0.865	0.863	0.862	0.859	0.854	0.854	0.846
11×11	0.836	0.870	0.878	0.883	0.881	0.876	0.872	0.871	0.871	0.866
13×13	0.855	0.885	0.894	0.897	0.895	0.891	0.884	0.879	0.881	0.879
15×15	0.869	0.896	0.906	0.909	0.905	0.903	0.898	0.891	0.889	0.885
17×17	0.883	0.906	0.915	0.919	0.915	0.911	0.908	0.903	0.900	0.893
19×19	0.896	0.914	0.921	0.926	0.923	0.919	0.915	0.912	0.911	0.903
21×21	0.909	0.920	0.927	0.932	0.930	0.925	0.921	0.917	0.919	0.913
23×23	0.920	0.925	0.933	0.937	0.935	0.932	0.927	0.923	0.923	0.921
25×25	0.929	0.930	0.937	0.941	0.940	0.937	0.932	0.928	0.928	0.924
51×51	0.986	0.980	0.973	0.972	0.969	0.967	0.965	0.963	0.964	0.963
101×101	0.996	0.995	0.994	0.994	0.991	0.988	0.986	0.984	0.985	0.983

1. For the 2×2 aperture, the target is located at the center of the array.

6.6.3 Other PSF Behavior and Characteristics

Temporal Dependence of the PSF: HST Breathing

Short-term focus variations are usually referred to as "OTA breathing," "HST breathing," "focus breathing," or simply "breathing." Breathing affects all data obtained with all instruments onboard HST. The WFC3 UVIS PSF will likewise suffer from small temporal variations induced by the HST breathing. The focus changes are attributed to the contraction/expansion of the OTA due to thermal variations during an orbital period. Thermally induced HST focus variations also depend on the thermal history of the telescope. For example, after a telescope slew, the telescope temperature variation exhibits the regular orbital component plus a component associated with the change in telescope attitude. The focus changes due to telescope attitude are complicated functions of Sun angle and telescope roll. More information and models can be found on the "HST Thermal Focus Modeling" Web site at:

http://www.stsci.edu/hst/observatory/focus/thermal.html

Breathing is expected to produce variations of the UVIS PSF FWHM by as much as 8% at 200 nm, 3% at 400 nm and 0.3% at 800 nm, on typical timescales of one orbit. Some variation over the field of the PSF response to breathing is also expected,

since the detector surface is not perfectly matched to the focal surface, and the optical design includes some field-dependent aberration.

Pixel Response Function

The point-spread function (PSF) is the distribution of light from a point source as spread over a number of pixels. Even with a very small optical PSF, however, charge diffusion, or migration of charge from one pixel into adjacent neighbor pixels, can degrade the sharpness of a CCD PSF. The effect, a type of pixel-to-pixel crosstalk, is usually described in terms of the pixel-response function (PRF), which maps the response of the detector to light from a hypothetical very sharp PSF whose light all falls within an individual pixel. Observations using the integrated WFC3 instrument along with optical stimulus point-sources provided empirical PSFs, for comparison with, and to provide constraints for, the models. Those models, which included an independent assessment of the low-order wavefront error, the pupil mask, and a reasonable estimate of the detector Modulation Transfer Function (MTF), yield good agreement with the observed instrumental encircled-energy curves. The resulting best empirical fit to the pixel response convolution kernel is shown in Figure 6.9. (The flux at 250 nm shown in Figure 6.9 does not add to 1 because there is a small amount of flux outside the 3×3 pixel box.)

Figure 6.9: CCD Pixel Response functions at 250 nm (top) and 810 nm (bottom).

$$\begin{bmatrix} 0.027 & 0.111 & 0.027 \\ 0.111 & 0.432 & 0.111 \\ 0.027 & 0.111 & 0.027 \end{bmatrix}$$

$$\begin{bmatrix} 0.002 & 0.037 & 0.002 \\ 0.037 & 0.844 & 0.037 \\ 0.002 & 0.037 & 0.002 \end{bmatrix}$$

PSF Characteristics

To allow for a more extensive assessment of the UVIS PSF, unsaturated data (highlighting the bright PSF core) were combined with highly saturated data (emphasizing the faint PSF wings), producing the high-dynamic-range composite images shown in Figure 6.10. As noted in the figure caption, the streaks to the right of the 250 and 350 nm images are artifacts due to the optical stimulus; there is also a slightly warm column near the left edge of the 250 nm image and a blocked column just to the left of the 350 nm PSF.

Figure 6.10: High dynamic range composite UVIS PSFs at 250 and 350 nm (top) and 633 and 810 nm (bottom); stretch is logarithmic. Streaks to the right in the top images are due to the optical stimulus; there is a slightly warm column at the left edge of the top left image and a blocked column to the left of the PSF in the top right image.

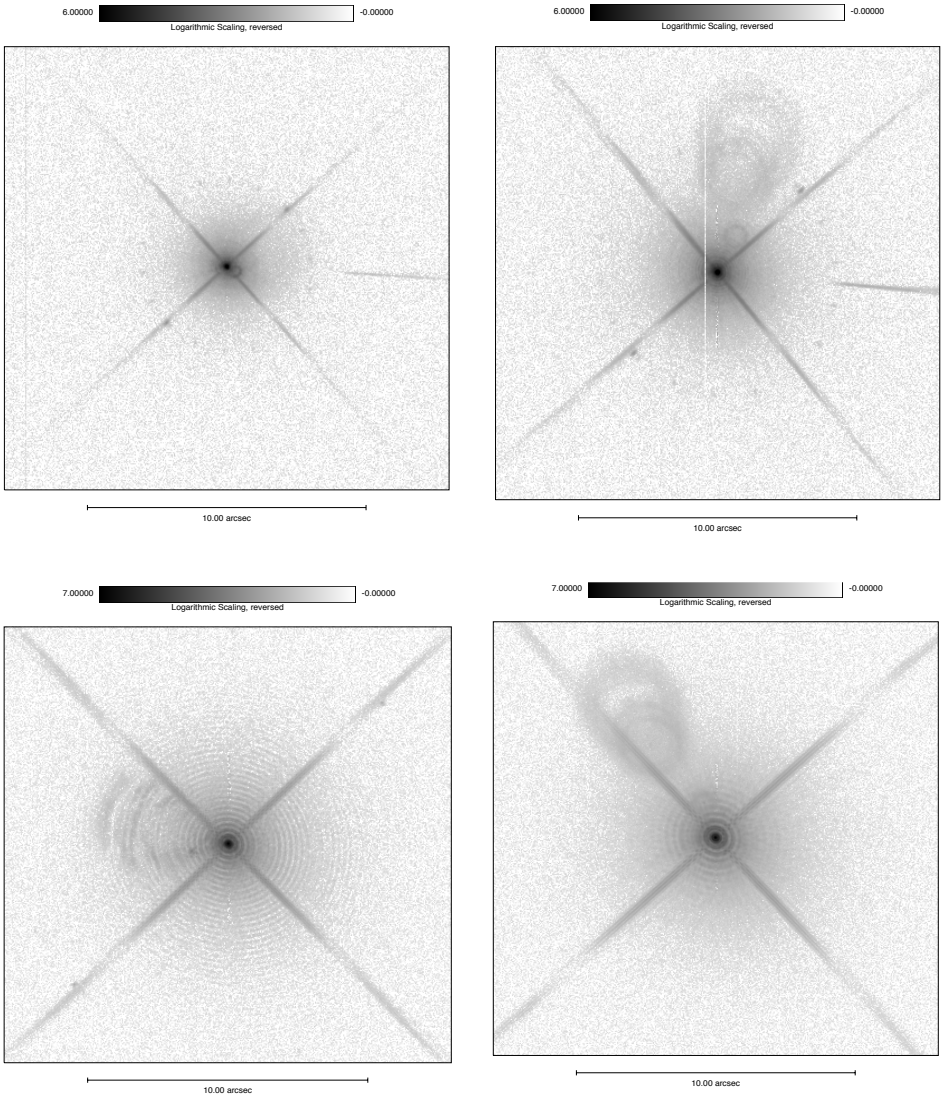

Different types of ghosts are visible in the images. As expected from the UVIS channel design, there are low-level ghosts due to reflections between the four surfaces of the two anti-reflection-coated detector windows: these are the sets of relatively large diameter, ring-shaped ghosts seen in all but the 250 nm images. Ghosts due to reflections from the CCD to the windows, as discussed above in Section 6.5.3, fall further from the PSF, along the diagonal from lower right to upper left of the field of view, and are not visible in these frames which image only a subsection of the WFC3 field of view.

Also evident are filter ghosts, due to reflections between the surfaces of a given filter. In single-substrate or air-gap filters (the latter consisting of two substrates joined via thin spacers), filter ghosts appear as small extended shapes, closer to the PSF

centers than the window ghosts, e.g., the ring-shaped features in the 250 and 350 nm images (F275W and F336W filters, respectively). In multi-substrate filters (a stack of two or more substrates bonded or laminated together with a layer of optical adhesive) filter ghosts appear as faint, point-like features, such as the ghost in the 633 nm (F625W) image. Note: the F275W filter, used for the 250 nm image in Figure 6.10, has since been replaced with an improved filter, reducing the filter ghost level from 0.7% to <0.1%. The filter ghosts are low level (<0.05% in 350 nm image and <0.1% in the 633 nm image). A small number of filters exhibit brighter ghosts and are discussed in detail in Section 6.5.3 and are tabulated in Table 6.4.

Finally, a ring of very faint spots centered on the point-source images appear in the image in Figure 6.10; their origin is unknown. The spots may be a diffraction effect, as the radius is proportional to the wavelength. Two slightly brighter spots may be related to the ring spots: they appear at the same distance from the PSF as the ring spots, just off the lower left and upper right spider features.

6.7 UVIS Exposure and Readout

6.7.1 Exposure Time

Integration times in the UVIS channel are controlled via a mechanical shutter blade similar in design to the ACS/WFC shutter. The original intent was to reuse the JPL WFPC2 shutter design (where the shutter is mounted directly on the SOFA), but the WFC3 optical packaging constraints prohibited this. Sitting directly behind the SOFA, the WFC3 UVIS shutter is a rotating disk about 12 inches in diameter; it is divided into four 90° quadrants, with alternating quadrants providing the blocking (i.e., there are two open and two closed positions). The aperture of the shutter is at the outer edge of the disk, placed such that it does not vignette any light rays. When the shutter is in the closed position initially, a commanded move of 90° places it into an open configuration; at the end of the exposure, another move of 90° places the shutter back into a closed position. Although the shutter can be operated in either a clockwise or counterclockwise direction, the current flight software always moves the blade in the same direction.

The time per UVIS exposure must be between 0.5 s and 3600 s, excluding 0.6 s, in steps of 0.1 s.[3] Pre-flight testing has verified that shutter exposure times deviate by less than 1% for exposure times of 0.5 s, as well as those greater than or equal to 1 s. For example, typical variations of 4 ms were measured in a set of 1 s exposures. For

3. Under normal shutter operations, the 0.5 s exposure would not provide a sufficiently uniform exposure level. However, it has been implemented through a special "continuous sweep" operation, where the shutter disk moves smoothly through 180°, from one closed position to the next, thus meeting the uniformity requirement. All exposures longer than 0.5 s are obtained via pairs of closed-to-open and open-to-closed commands.

exposure times between 0.7 s and 0.9 s (inclusive), exposure-time deviations were measured to be 2.6% (see WFC3 ISR 2004-14).

The shutter uniformity requirement specifies that any differences in exposure time across the field of view must be <0.01 s. Comparisons of long (30 s) and short (0.5 s) exposures taken during instrument-level ground tests have shown that the shutter provides a uniform exposure time across the field of view to ~0.004 s, easily meeting the requirement.

To allow for cosmic-ray removal during post-observation data processing, UVIS exposures can be split into multiple exposures. The Optional Parameter CR-SPLIT in the Phase II observing proposal can be used to equally divide the original exposure time into the specified number of subexposures (the default is 2, maximum of 8, subexposures). The exposure-splitting function may also be disabled by setting the CR-SPLIT parameter value to NO.

If CR-SPLIT is requested, the exposure time is first divided by the requested number of subexposures and the subexposure times are rounded down to the nearest multiple of 0.1 s. At the end of this process, if the resulting subexposure times are not legal values, the proposal software adjusts them so that they are allowed and reports those changes to the observer. Specifically, if the subexposure time is less than the minimum allowable exposure time, it is set to the minimum (0.5 s); if it exceeds the allowable maximum, it is set to the maximum (3600 s). And finally, if the subexposure time should be 0.6 s (which, as discussed above, is not a legal value), it is rounded down to 0.5 s.

6.7.2 ACCUM Mode

"**ACCUM**" is the only observing mode for the UVIS channel. In ACCUM mode, the shutter is opened and photons strike the CCDs and generate charge, which is accumulated until the shutter is closed at the end of the requested exposure time and the charge is read out. During the readout, the analog-to-digital (A-to-D) converter translates the charge into data numbers (DN) via the gain setting. There are four gains (1.0, 1.5, 2.0, and 4.0 e^-/DN) that are possible in principle. However, the only gain setting offered to observers is the default value of 1.5 e^-/DN.

A full detector readout of both UVIS chips takes 96 s; the image will contain all the exposed pixels from each CCD (2 times 2051x4096), as well as a variety of overscan pixels, described in more detail later in this section. Shorter readout times are possible by using smaller subarray readout sizes, as discussed in more detail in Section 6.4.4.

Each of the two CCD chips contains two on-chip amplifiers used for reading out, i.e., there is a total of four amplifiers available to read out the entire two-chip detector. The fastest--and default--way to read out the entire detector, at full spatial resolution, is to use all four amplifiers simultaneously; in this case, half of each CCD is read out through one of the four amplifiers. By default, four-amplifier, full-frame exposures read both CCDs (all four amps) simultaneously, rather than serially, reducing readout overhead time as well as minimizing the number of charge-transfer shifts. This capability will become increasingly important in later years of WFC3 operation, when charge-transfer inefficiency may become noticeable.

Readouts using other combinations of amplifiers are possible in principle, but are not offered to General Observers. Non-default combinations cause longer overhead times: for example, two-amplifier full-frame readout would take more than twice as long as a four-amplifier readout (~193 s vs. 96 s).

However, subarray readouts are all done through one amplifier only; by default, the amplifier closest to the subarray center is used.

Overscan Regions

The UVIS CCD detectors each have 4096x2051 pixels that are exposed to light. In addition, both chips have 25 extra columns at both ends that are not exposed to light; these 25 columns are *physical* overscan pixels. Moreover, during readout of the chips, extra pixels can be clocked in order to create *virtual* overscan pixels.

The location of the overscan regions in a raw image will vary, depending upon the type of readout that is performed. The overscan regions are used to monitor the instrument, and are needed to measure the bias level. The bias level is subtracted from the raw image, normally through the BLEVCORR step in the WFC3 calibration pipeline.

Figure 6.11 shows the format of a raw image obtained with full-chip unbinned four-amplifier readout. The raw image has 25 columns of physical overscan pixels located along the edge of each CCD chip in the serial direction only. In addition, there are two areas of virtual overscan: 60 columns of serial overscan in the center of each row and 38 rows (19 per chip) of parallel overscan next to the inter-chip gap. The serial physical overscan pixels are also known as the serial prescan, or leading-edge, overscan; the serial virtual overscan pixels are also called the trailing-edge pixels.

Figure 6.11: Format of a Raw Full-Chip WFC3 UVIS Image.

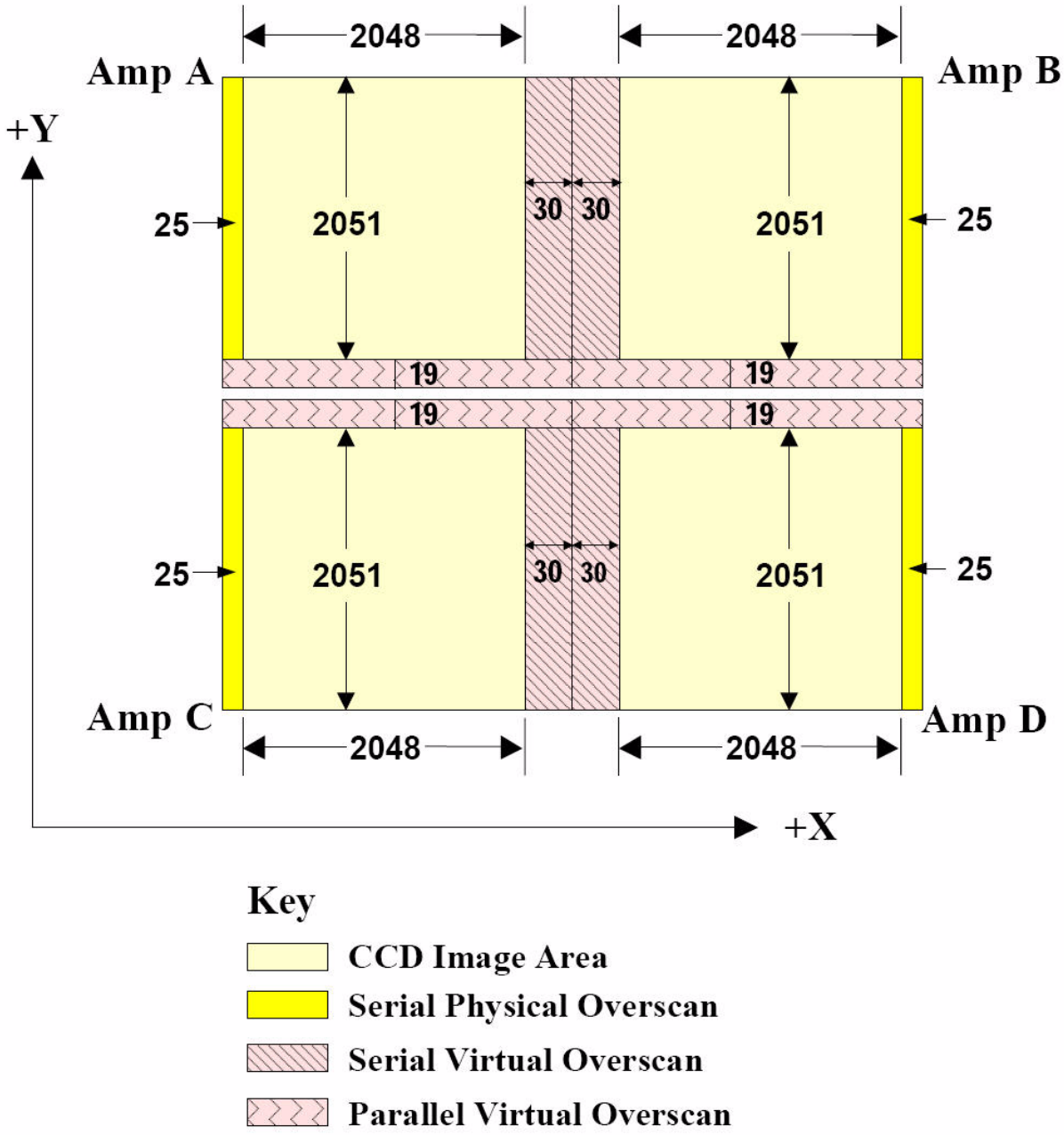

As Figure 6.11 illustrates, a raw image resulting from a default full-frame, four-amplifier readout of the UVIS channel will contain 110 columns of serial overscan (25x2 physical and 30x2 virtual) plus 38 rows of parallel virtual overscan, which combined with the 4096x2051 science pixels, result in a raw image size of 4140x4206 pixels (by convention, the parallel direction is listed first). Other types of readouts will have differing amounts and/or locations of overscan. Two-amplifier readouts of the full detector, for example, will contain the same number of rows and columns as the four-amplifier readouts, but all 60 of the serial virtual overscan will be at the end of each row. Subarrays will contain no virtual overscan of either type (serial

or parallel), although they *can* contain physical overscan if the subarray is defined such that it overlaps the physical overscan region. In general, it would be highly desirable to include some physical overscan in observations using subarrays.

Exposures taken with on-chip binning are complicated by the need to truncate "odd" pixels and to treat each half of the chip's row separately. Also, due to the odd number of some overscan pixels, the boundary between the data and overscan pixels of a binned exposure can contain binned pixels resulting from a combination of both data and overscan pixels. A 2x2 binned frame readout, for example, contains 2070 rows x 2102 columns. That is, each binned chip readout has 1035 rows (9 binned virtual overscan + 1 combined data/virtual parallel overscan + 1025 data) and each binned chip readout contains 2102 columns (12 physical overscan + 1 combined data/overscan + 1023 columns of data + 1 combined data/virtual overscan column + 14 virtual overscan pixels for each of the two amps in a chip). A 3x3 binned image will contain 1402x1380 pixels (8 overscan + 1 combined overscan/data + 682 data + 10 overscan columns in each amplifier of each chip and 6 overscan + 1 combined overscan/data + 688 data rows in each chip).

For completeness, we mention here that WFC3 can also be commanded to take EPER (extended pixel edge response) readouts, although this capability is intended for calibration/engineering purposes only. The EPER images are a way to measure and monitor charge-transfer inefficiency (CTI) effects using internal images, rather than external, pointed observations that would take HST observing time away from science observations. The EPER frame starts with an internal tungsten lamp flat field; any CTI present will cause a fraction of charge from that flat field to be captured temporarily in traps. As the frame is read out, the trapped charge escapes and can appear in the overscan regions as an exponential tail of deferred charge. The EPER readout includes significantly larger areas of overscan so that the full extent of the exponential tail can be measured, ideally down to where it becomes indistinguishable from the nominal noise level of the detector. That is, the EPER image allows direct measurement of the charge losses during the readout since nearly all the lost electrons are expected to appear in the exponential tail.

6.8 UVIS Sensitivity

6.8.1 Limiting Magnitudes

Table 6.8 presents the predicted limiting-magnitude performance of WFC3 and compares it with that of the ACS camera. The calculations are based on optimal extraction of a point source. The limiting ABMAG at a S/N of 10 was calculated for a 1-hour and a 10-hour exposure. The WFC3 filters used are listed in column 2; for ACS, the most comparable wide-band filter was used and its name is given in column 3. The ACS/HRC camera was assumed for the NUV and *U*-band comparison, and ACS/WFC was assumed for *B*, *V*, and *I*.

Table 6.8: Anticipated limiting-magnitude performance of WFC3 compared with that of ACS. The table provides limiting ABMAGs at a S/N of 10 for the indicated WFC3 filters and for ACS with its most similar filters. WFC3 UVIS comparisons are with the ACS HRC channel (NUV and *U*) and the ACS WFC channel (*B*,*V*,*I*).

Band	Filter		Limiting magnitude in 1 hr		Limiting magnitude in 10 hrs	
	WFC3	ACS	WFC3	ACS	WFC3	ACS
NUV	F225W	F220W	26.2	25.3	27.6	26.7
U	F336W	F330W	27.1	26.3	28.5	27.7
B	F438W	F435W	27.2	27.6	28.6	28.9
V	F606W	F606W	27.9	28.0	29.2	29.2
I	F814W	F814W	27.1	27.4	28.4	28.7

Chapter 9 gives further details on estimation of exposure times. More accurate estimates will require use of the WFC3 Exposure Time Calculator (ETC), available online.

6.9 Other Considerations for UVIS Imaging

6.9.1 Gain and Full-well Saturation

The dynamic range of a detector is determined not only by the full-well capacity of the device but also by the A-to-D converter (ADC) and gain setting that are used during readout to convert the accumulated charge into data numbers (DN). The WFC3 UVIS channel detectors use 16-bit ADCs (16 bits per pixel), so that the maximum DN that can be read out is $2^{16} - 1$ or 65,535. If the charge accumulated in a given pixel exceeds the ADC maximum, any additional charge will not result in any further increase in the DN and may, in cases of extreme saturation, result in values of zero.

The gain setting provides a mechanism for extending the scale to a larger maximum number of electrons by assigning a single DN to more than 1 electron; for the 1.5 e^-/DN chosen for the UVIS channel, the maximum DN of 65,535 corresponds to 98,302 electrons.

The full-well level of the CCD pixels (the amount of charge that they can physically store) has been measured on the ground at around 75,000-80,000 electrons, although each individual pixel has a slightly different level. The 1.5 e^-/DN setting thus fully samples the pixels up to their full-well levels, since the corresponding DN values are 50,000-53,000 DN.

If the charge accumulated in a given pixel exceeds the ADC maximum, any additional charge will not result in any further increase in the DN.

In addition, once the charge exceeds the pixel full-well level, it can escape that pixel and spread into adjacent vertical pixels; as the signal continues to accumulate, these adjacent pixels themselves can accumulate charge up through the ADC/gain level to full-well and leak into further adjacent vertical pixels, and so forth, resulting in the "blooming" effect. The MPP (multi-pin phasing) operation of the detectors, used to minimize surface dark current, constrains the "blooming," or charge overflow, along the detector columns (i.e., the blooming is only vertical and not horizontal).

Whenever the pixel full-well capacity is exceeded, the linearity and dark current can be adversely affected (the large number of photoelectrons effectively fill all trap states) and there can be after-effects such as the "blooming" discussed in the previous paragraph, as well as residual or persistence artifacts. However, WFC3 ground-test data have been taken to search for residual images following highly saturated images, and no persistence has been observed, at least on relatively short timescales (5-6 min after the saturated image). Long-timescale residual images, such as those seen occasionally in WFPC2 images, are not expected in WFC3, since the WFC3 chips are backside-illuminated and have had the substrate layer (which can cause bulk residual images) removed.

6.9.2 Cosmic Rays and Hot Pixels

The cosmic-ray fluxes for WFC3 UVIS are expected to be comparable to the levels seen in ACS, STIS CCD, and WFPC2. As with these previous HST instruments, typical WFC3 imaging observations will need to be split or dithered to obtain adequate cosmic-ray removal.

The WFC3 CCDs detectors can be expected to degrade over time due to exposure to the space environment. This damage manifests itself in two ways: as an overall higher dark current, and as an increased number of individual “hot pixels,” i.e., pixels with a higher-than-normal dark current. The Detector Characterization Laboratory (DCL) at Goddard Space Flight Center (GSFC) performed a variety of radiation tests on flight-like WFC3 detectors, in which the expected space environment was simulated in order to examine the effects on both dark-current and hot-pixel development and annealing. The devices were irradiated under flight-like conditions, at levels simulating an exposure equivalent to a final total of 27 months in orbit. Radiation doses were applied in stages (in 1-month equivalent steps), with the intervals between exposures used to anneal, or warm, the detector.

Not unexpectedly, the average dark current was found to rise during each "month" of testing, to about 0.5 e^-/pix/hour, with anneals bringing this value back down to around the pre-radiation rate of about 0.1 e^-/pix/hour. At the 2.5-year mark, the dark rate was found to jump to >5 e^-/pix/hour (still well below the 20 e^-/pix/hour dark-current specification for the CCDs at −83°C); subsequent anneals brought the level down to <2 e^-/pix/hour.

The radiation doses increased the number of new hot pixels by about 1200-2400 pixels/month/cm^2 (which is about 22,000-25,000 pixels/month/chip, or <0.5% of the total number of pixels in one chip; the exact numbers depend upon the dark-current level chosen to define a hot pixel). The anneal procedures repaired 80-97% of these

hot pixels. Extrapolation to end of life of the instrument predicts that the number of permanent hot pixels will cover 0.5-5% of the entire chip (the latter value assumes a hot pixel defined conservatively as >40 e^-/pix/hour, just twice the launch dark-current requirement). As with previous HST instruments, small dithers between separate exposures will be useful in identifying and removing residual hot pixels.

6.9.3 Charge-Transfer Efficiency

The charge-transfer efficiency (CTE) of the WFC3 CCDs, while expected to be excellent early in the mission (better than 0.999995), will inevitably decline over time as on-orbit radiation damage creates charge traps in the detectors. The UVIS CCDs are large-format devices, similar in size to those in the ACS WFC, and thus require significantly more charge-shifting steps during readout compared to smaller devices like the STIS and WFPC2 CCDs. As a result, effects due to radiation-induced charge-transfer inefficiencies will be encountered earlier than for the smaller-format detectors.

CTE losses can be mitigated by filling the charge traps; in WFC3, this can be done using a charge-injection capability, which inserts the charge electronically. Charge injection is preferable to the traditional pre- or post-flash techniques that use light, because the associated noise is lower. In laboratory tests of flight-like WFC3 CCDs, the noise due to charge-injection levels of ~10,000 e^- was measured to be only 10-15 e^- rms, much lower than the ~100 e^- Poissonian noise that would characterize a similar signal level achieved by exposure to light.

Early in the mission, charge injection will not be needed, and thus will not be available to observers. In later years, observers will be provided the option to activate the charge-injection capability via an Optional Parameter in the Phase II observing proposal.

6.9.4 Image Persistence

No significant image-persistence effects following over-exposure have been observed in preliminary instrument-level ground test data using the UVIS CCDs, as expected for back-illuminated devices.

6.9.5 Quantum Yield

Like the ACS HRC and STIS CCDs (and unlike WFPC2), the WFC3 UVIS CCDs are directly sensitive to UV photons. There is a critical wavelength, 339.68 nm, above which photons cannot produce more than one electron/hole pair in silicon (the corresponding energy is 3.65 eV). For wavelengths shorter than this critical wavelength, there is a finite probability that a single photon will produce two electrons on the detector.

This “quantum-yield” effect must be taken into account when estimating the detector QE and noise level of a UV observation, since the multiple electrons cause a

distortion in the Poisson distributions of electrons. The correction is about 1.7 e^-/photon at 200 nm. The S/N algorithms incorporated in the WFC3 Exposure Time Calculator (ETC) include the quantum-yield effect. See also Section 9.2.

6.10 UVIS Observing Strategies

6.10.1 Dithering Strategies

For imaging programs, STScI generally recommends that observers employ dithering patterns. Dithering refers to the procedure of moving the telescope by pre-determined amounts between individual exposures on a target; the resulting images are subsequently combined via post-observation processing techniques using software such as ***MultiDrizzle*** (see the HST Drizzle Web page).

Use of dithering can provide improved sampling of the PSF and better correction of undesirable artifacts in the images (e.g., hot pixels, cosmic rays, and the UVIS channel's inter-chip gap). Offsets on the scale of integer pixels, for example, allow for correction of hot pixels, while sub-integer pixel shifts allow for improved spatial resolution in the final combined image.

Larger offsets, on the scale of the detector's field of view, can also be used, typically to create mosaics. Dithers larger than a few pixels will be adversely impacted by the geometric distortion in the CCDs (a ~2% effect from corner to corner); in addition, large mosaics can sometimes require more than one set of guide stars for each pointing, resulting in a reduction in pointing accuracy (guide-star accuracy is about 1").

The set of Pattern Parameters in the observing proposal provides a convenient means for specifying the desired dither pattern. Parameters exist for full control of all aspects of dithering, including the pattern type (e.g., line, box, or user-defined), the number of points in a pattern, the number of images to be taken at each point, the spacing between dither points, and the orientation of the pattern, down to the spacing between parallel sides and angle between adjacent sides of a box pattern. See Appendix C for further discussion of dithering, mosaicking, and patterns.

For optimum cosmic-ray removal, at least two images are recommended at each point in a pattern; in particular, long integrations (>1000 s) will benefit from multiple images per point as they reduce the chance that a given pixel will be affected by a cosmic ray in all images taken at that pattern point. Observers may choose to employ one of the pre-defined dither patterns which have been developed to optimize WFC3 observations in one or more areas (e.g., to allow for simultaneous removal of hot pixels as well as cosmic rays, to cover the inter-chip gap, to minimize scale variation effects across the detector, to optimize mosaics without requiring the use of more than one guide star, etc.). The intent is that most small- and medium-sized imaging programs should be able to use (and benefit from) one of the pre-defined dither patterns. Alternatively, observers are welcome to construct a custom dither pattern, in

order to tailor it to the amount of allocated observing time and the desired science goals of the program. Finally, for very simple dither patterns, the POS TARG and ORIENT requirements can be used instead of the Pattern Parameters. A POS TARG positions the target off the aperture center by the specified X,Y offset (see Section 6.4.3 for discussion of this coordinate system), while ORIENT specifies the roll angle of the telescope.

In addition to Appendix C the HST Phase II Proposal Instructions contain details on the available library of pre-defined WFC3 dither patterns, parameters for designing custom patterns, as well as the use of the POS TARG and ORIENT requirements.

6.10.2 Parallel Observations

While the design of WFC3 precludes the simultaneous use of both the UVIS and IR channel, it is possible to use one or more of the other HST instruments in parallel with WFC3. Since each instrument covers a different location in the HST focal plane (see Figure 2.2), parallel observations typically sample an area of sky several arcminutes away from the WFC3 target. For extended targets such as nearby galaxies, parallel observations may be able to sample adjacent regions of the primary target. In other cases, the parallel observations will be looking at essentially random areas of sky; such images are typically used for survey purposes.

For processing and scheduling purposes, HST parallel observations are divided into two groups: coordinated and pure.

A **coordinated parallel** is an observation directly related to (i.e., coordinated with) a specific primary observation, such as in the extended galaxy example above. A **pure parallel** is an observation typically unrelated to the primary observation, for example, parallel imaging scheduled during long spectroscopic observations. The primary restriction on parallel observations, both coordinated and pure, is that they must not interfere with the primary observations: they may not cause the primary observations to be shortened; and they must not cause the stored-command capacity and data-volume limits to be exceeded. The proposal software (APT) enforces these rules and will notify the observer when a specified parallel is not permitted.

In order to prolong the life of the HST transmitters, the number of parallels acquired during each proposal cycle is limited. Proposers must provide clear and strong justification in order to be granted parallel observing time. Please refer to the HST Call for Proposals for current policies and procedures concerning parallels.

CHAPTER 7:

IR Imaging with WFC3

In this chapter . . .

7.1 WFC3 IR Imaging

As described in Chapter 2, the optical design of WFC3 features two independent channels, each with its own separate optics, filters and grisms, and detectors. The **UVIS channel** is sensitive to UV and optical wavelengths (200-1000 nm), and the **IR channel** is sensitive to near-infrared wavelengths (800-1700 nm).

Only a single channel, either UVIS or IR, can be used at any one time. Thus they cannot be used in parallel, but they can be used sequentially.

A schematic diagram showing the locations of the fields of view of the UVIS and IR detectors in the HST focal plane is given in Figure 2.2.

This chapter describes the capabilities of the IR channel. The previous chapter, Chapter 6, describes the UVIS channel. Detailed characteristics of the detectors used in both channels are given in Chapter 5 and summarized in Table 5.1.

7.2 Specifying an IR Observation

In the HST proposal system, the parameters for an IR observation available to General Observers are:

1. **Configuration**: always **WFC3/IR.**
2. **Mode**: always **MULTIACCUM.**
3. **Aperture**: must be specified; **IR** selects the full detector area; for others see Section 7.4.5.
4. **Spectral Element**: must be specified for each exposure; see Section 7.5.
5. **Optional Parameters**: in the IR channel **SAMPSEQ** specifies a predefined sequence of times at which the detector is read out, and **NSAMP** specifies the total number of readouts (and thus the total exposure time); see Section 7.7. **SAMPSEQ** and **NSAMP** are required for IR observations.
6. **Special Requirements**: see the Phase II Proposal Instructions for details of Special Requirements related to the timing of observations and for dithering and mosaicking. Also available is the exposure-level Special Requirement **POS TARG** for offsetting the target position from the default center of the aperture (see Section 7.4.3 for a discussion of the IR channel coordinate system).
7. **Number of Iterations and Time per Exposure**: in cases where two or more identical exposures are desired, the Number of Iterations may be set to 2 or more. In the IR channel, the Time per Exposure is fixed by the combination of **SAMPSEQ** and **NSAMP** (see item 5 above) and thus is not specified separately. Through various combinations it is possible to select times per exposure ranging from 2.93 to 2800 s (for readouts of the full detector array; shorter exposures are possible using subarrays).

7.3 IR Channel Characteristics

The WFC3 IR channel has been optimized for observing over the wavelength range 800-1700 nm. All the IR reflective optics (except for the WFC3 pick-off mirror, which intercepts on-axis light from the HST OTA and is shared with the UVIS channel) are coated with a silver layer for maximum IR throughput.

A schematic mechanical diagram showing both channels of WFC3 is given in Figure 2.1. Components of the IR channel include: the Channel Select Mechanism (CSM), which directs on-axis light from the HST OTA to the IR channel; a flat folding mirror; a two-mirror mechanism for providing focus and alignment adjustments; the Refractive Corrector Plate (RCP), which applies the spherical-aberration correction; the IR filter wheel (FSM or Filter Selection Mechanism); and finally the HgCdTe IR

detector package sealed inside a vacuum enclosure. There is no mechanical shutter in the IR channel; instead, the detector provides electronic shuttering. Dark-current measurements are obtained by using the BLANK, an opaque blocker in the filter wheel, which also is used to prevent the detector from viewing the Earth during occultations.

The WFC3 IR detector is a HgCdTe 1024×1024 array, with 18 micron pixels, bonded to a silicon multiplexer, with 1014×1014 pixels sensitive to incoming light. It is a direct descendant of the NICMOS 256×256 and Hawaii-1 1024×1024 arrays (more details on the detector are given in Chapter 5).

7.4 IR Field Geometry

7.4.1 Field of View and Pixel Size

The inner 1014×1014 pixels of the IR detector are exposed to incoming light. There are no gaps in the field (such as the gap between the two CCDs in the UVIS channel), or mechanical occultations (such as the coronagraphic spots on NICMOS-2).

The IR focal plane is tilted by ~22° with respect to the incoming beam. Thus the field of view as projected onto the sky is rectangular, with an aspect ratio of ~0.90. The pixels projected onto the sky are also rectangular, covering approximately 0.121×0.135 arcsec, with the shape varying slightly across the field. The field of view on the sky is 123×136 arcsec, or 4.65 arcmin^2.

7.4.2 Geometric Distortion

In addition to the rectangular field shape described above, the optical design of the IR channel also produces appreciable geometric distortion. Geometric distortions in both channels are discussed in more detail in Appendix B.

Distortion affects appropriate techniques for flat-fielding, photometric calibration, and astrometry, especially when complicated by resampling in order to combine dithered image sets. Plans are in place to update the ***MultiDrizzle*** software with the necessary corrections for WFC3 data. An introduction to ***MultiDrizzle*** is available online at:

http://www.stsci.edu/hst/acs/analysis/multidrizzle

7.4.3 Coordinate Systems

Like the CCD, the IR channel requires multiple coordinate reference frames, each relevant for a specific goal. Readers may also wish to refer to Section 6.4.3, which describes the coordinate systems for the UVIS channel. The coordinate systems used for the IR channel are illustrated in Figure 7.1 and are the following:

- **Image-based system** (AXIS1, AXIS2)
- **Proposal POS TARG system** (X-POSTARG, Y-POSTARG)
- **HST-based system** (V2, V3) or (U2, U3)

Figure 7.1: WFC3 IR detector coordinates.

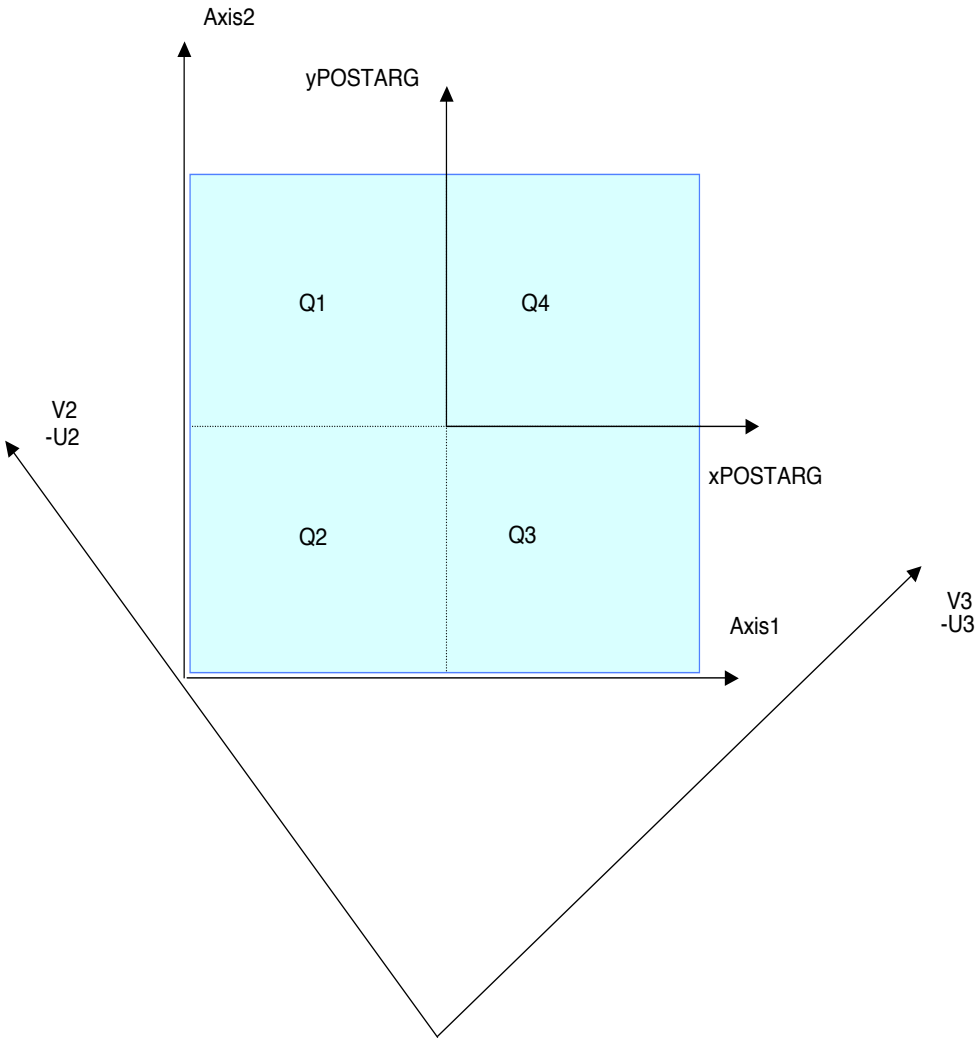

The **image-based coordinate system,** (AXIS1, AXIS2) in Figure 7.1, is a generic system used when an image is displayed on a computer screen. Here the origin of coordinates is at the lower left of the screen, the X axis increases to the right, and the Y axis to the top of the screen. Coordinates are expressed in pixel units. This system is used primarily by the generic conversion pipeline software, which creates science FITS files from the data telemetry coming from the telescope.

The **POS TARG reference frame**, (X-POSTARG, Y-POSTARG), is orthogonal on the sky, in units of arcseconds. It can be used to specify target placement at an offset location within the field of view, or for dithering or mosaicking purposes. In the IR channel, the POS TARG reference frame is designed to be co-linear with the AXIS reference frame, and it has its center located at the center of the chosen IR aperture. The transformation between the undistorted POS TARG (arcsec) frame and AXIS frame (pixels) contains non-linear distortion coefficients. For the IR detector, the POS TARG axes are parallel to the detector edges. Note, however, that the IR X,Y POS TARG axes are not parallel to the UVIS X,Y POS TARG axes; the former are rotated a few degrees counterclockwise with respect to the latter.

The **HST-based system** (V2, V3) is related to the main HST focal plane (U2, U3) by a simple translation and rotation. It is used as the slewing reference frame. Note that the edges of the IR detector are rotated by approximately 45∞ with respect to the V2, V3 axes.

7.4.4 Subarrays

In addition to obtaining standard full-field images, users can choose to read out smaller portions of the detector, called subarrays. Subarrays are useful to achieve reduced data volume, and/or to allow shorter exposure times. Shorter exposure times are especially important for the IR channel, because there is no physical shutter and the minimum integration time is limited by the time to read out the detector (2.9 s for full-frame readout). Very bright sources--including some of the primary "faint" IR photometric standards--may easily exceed the detector full-well of ~100,000 electrons in only a fraction of a second. Since the readout time is nearly proportional to the number of pixels read, subarrays can be used to reduce the effective integration time and make such observations feasible. This has been implemented in the IR channel with the RAPID readout mode, which in subarray mode runs at a speed nearly inversely proportional to the area of the subarray.

All of the IR subarrays are centered on the detector field of view. Four subarray sizes are supported, with pixel dimensions of 512×512, 256×256, 128×128, and 64×64. Note that the sizes of the subarrays refer to the actual active pixels, i.e., they do not include the reference pixels. (Of the 1024×1024 pixels of the WFC3 IR detector, only the inner 1014×1014 pixels are light-sensitive. The 5 rows and columns of pixels around the edge of the array use fixed capacitances to provide constant-voltage reference values.) The reference pixels, however, are still included in the output images, resulting in final images of 522×522, 266×266, 138×138, and 74×74 pixels. For subarray images, the reference pixels come from the same rows and columns of the subarray, with the 5×5 pixels at the subarray corners filled with the reference pixels

at the corresponding corner of the detector (see Section 5.5 for details on reference pixels).

The actual selection of a subarray is accomplished by requesting one of the IR channel's apertures, as described in the next subsection.

7.4.5 Apertures

The available IR apertures are listed in Table 7.1. As with other HST instruments, there are apertures centered at the geometric center of the array (or subarray), and apertures centered at "optimum" positions, defined on the basis of best image quality and detector cosmetics. In the former case, the aperture name has "-FIX" appended. In the latter case (without "-FIX" appended), the centering of the aperture on the detector may be optimized from time to time by STScI as circumstances warrant. Currently, without any in-flight information, the fixed and optimal apertures are identical.

Observers may wish to use a POS-TARG offset (or other method) to prevent an important target (especially if it is a single star) from being positioned exactly at the IR focal plane's center, where the four corners of the four amplifier's quadrants meet (and will divide the source if it is positioned there).

The available set of IR apertures is given in Table 7.1.

Table 7.1: WFC3 IR Apertures.

Aperture Name	Description
IR	Optimum center of IR detector
IR-FIX	Geometric center of IR detector
IRSUB64	Optimum center of 64×64 subarray
IRSUB64-FIX	Geometric center of 64×64 subarray
IRSUB128	Optimum center of 128×128 subarray
IRSUB128-FIX	Geometric center of 128×128 subarray
IRSUB256	Optimum center of 256×256 subarray
IRSUB256-FIX	Geometric center of 256×256 subarray
IRSUB512	Optimum center of 512×512 subarray
IRSUB512-FIX	Geometric center of 512×512 subarray
G102-REF	G102 reference aperture for undispersed exposures
G141-REF	G141 reference aperture for undispersed exposures

7.5 IR Spectral Elements

7.5.1 Filter and Grism Summary

An overview of the IR spectral elements, and of the process by which they were selected, was given in Section 2.3. This section gives details of the IR filters and grisms. Table 7.2 lists the IR channel's filters, with a general description and fundamental parameters of each. Figures 7.2 and 7.3 show the effective throughput curves, including the filter transmission multiplied by the throughput of the OTA, WFC3 optics, and detector response.

More detailed information on the throughput curves of all of the filters is given in Appendix A. All measurements of the IR filters which involve wavelengths, as tabulated in Table 7.2 and plotted in Figures 7.2 and 7.3 and in Appendix A, were done in air. It should be noted that the laboratory measurements were done at a temperature of -30°C, whereas the filters will be operated on orbit at -35°C; this may lead to wavelength shifts which are expected to be very small.

The IR channel is equipped with a single filter wheel with 18 slots, containing 15 passband filters, two grisms, and an opaque mask for dark-current measurements. The filter complement samples the spectral region between 800 and 1700 nm. All of the IR filter elements are full-sized, covering the entire field of view of the IR detector. Since all of the elements are mounted in a single wheel, only one element can be used at a given time.

The 900-1700 nm wavelength range is covered by a series of wide- and medium-band filters, with little wavelength overlap. Additional medium-band filters are centered on molecular bands and nearby continua, and several narrow-band filters are available for probing interstellar and nebular recombination lines.

The filter set is designed to include the most popular passbands used in extragalactic, stellar, and solar-system astronomy, as well as passbands similar to those already used in previous HST instruments.

Table 7.2: WFC3 IR Channel Filters and Grisms.

Name[1]	Description	Pivot[2] λ (nm)	Width[3] (nm)	Peak Transmission
	IR Wide-Band (W) Filters			
F105W	Wide *Y*	1048.95	292.30	0.98
F110W	Wide *YJ*	1141.40	503.40	0.99
F125W	Wide *J*	1245.90	301.50	0.98
F140W	Wide *JH* gap; red grism reference	1392.10	399.00	0.99
F160W	WFC3 *H*	1540.52	287.88	0.98
	IR Medium-Band (M) Filters			
F098M	Blue grism reference	982.93	169.48	0.97
F127M	H_2O/CH_4 continuum	1273.64	68.79	0.98
F139M	H_2O/CH_4 line	1383.80	64.58	0.98
F153M	H_2O and NH_3	1533.31	68.78	0.98
	IR Narrow-Band (N) Filters			
F126N	[Fe II]	1258.26	11.83	0.90
F128N	Paschen β	1283.30	13.54	0.94
F130N	Paschen β continuum	1300.62	13.28	0.96
F132N	Paschen β (redshifted)	1319.04	13.07	0.91
F164N	[Fe II]	1645.13	17.48	0.93
F167N	[Fe II] continuum	1667.26	17.16	0.93
	IR Grisms (G)			
G102	"Blue" high-resolution grism	(1025)	250	
G141	"Red" low-resolution grism	(1410)	600	

1. See Footnote 1 of Table 6.2 for naming conventions.
2. "Pivot wavelength" is defined as in Table 6.2. All wavelength measurements in this table were made in air.
3. Full width at 50% of peak transmission.

Wide-band Filters

The IR channel's versions of the ground-based *J* and *H* filters are F125W and F160W, respectively. The F125W filter has a width somewhat wider than that of a typical *J* passband used in ground-based cameras. The F160W filter's bandpass has been modified relative to ground-based *H* in order to give a better fit to the QE curve of the IR detector. Specifically, the WFC3 *H* filter's bandpass has been narrowed to approximately 1400-1700 nm, in order to limit thermal background and to have the

filter define the bandpass on the red side rather than the detector sensitivity cutoff. By contrast, NICMOS *H* filter (NICMOS F160W) covers about 1400-1800 nm. This narrowing for WFC3 reduces photometric errors due to spatial variations in the detector's QE cutoff.

The wide F140W filter covers the gap between the *J* and *H* bands that is inaccessible from the ground. F105W has a central wavelength similar to ground-based *Y*, but is considerably wider. The IR channel also includes a very wide filter, F110W, spanning the ground-based *Y* and *J* bands. This filter can be used for deep imaging, with a bandpass fairly similar to that of the corresponding wide-band filter in NICMOS (also called F110W).

Narrow-band Filters

The IR channel includes six narrow-band filters which sample some of the most astrophysically important planetary, stellar, and nebular spectral features in the near-IR (e.g., [Fe II] and Paschen-β).

Grisms

The IR channel has two grisms which provide slitless spectra (see Chapter 8 for more details). The "blue" G102 grism provides a dispersion of 2.5 nm/pix (or a resolution of ~210) over the 800-1150 nm wavelength range. The "red" G141 grism has a dispersion of 4.7 nm/pix (resolution of ~130) over the 1100-1700 nm range. In most cases, a grism observation will be accompanied by a direct image, for source identification and wavelength calibration. Recommended filters for this purpose are F098M for the G102 grism, and F140W for G141.

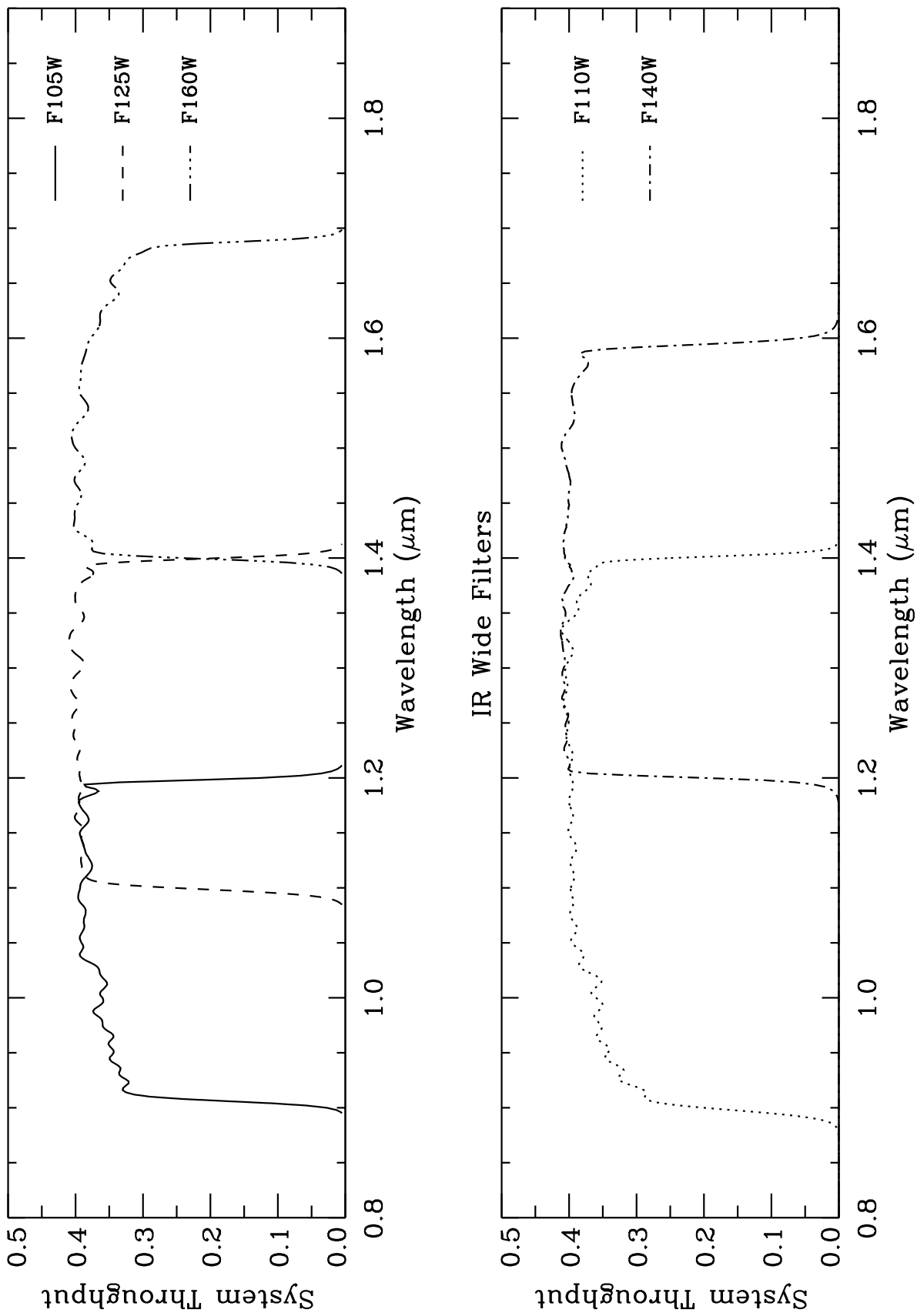

Figure 7.2: Integrated system throughput of the WFC3 IR wide-band filters, presented in two panels for clarity. The throughput calculations include the *HST* OTA, WFC3 IR-channel internal throughput, filter transmittance, and the QE of the IR detector. (Figured updated on Jan. 7, 2008)

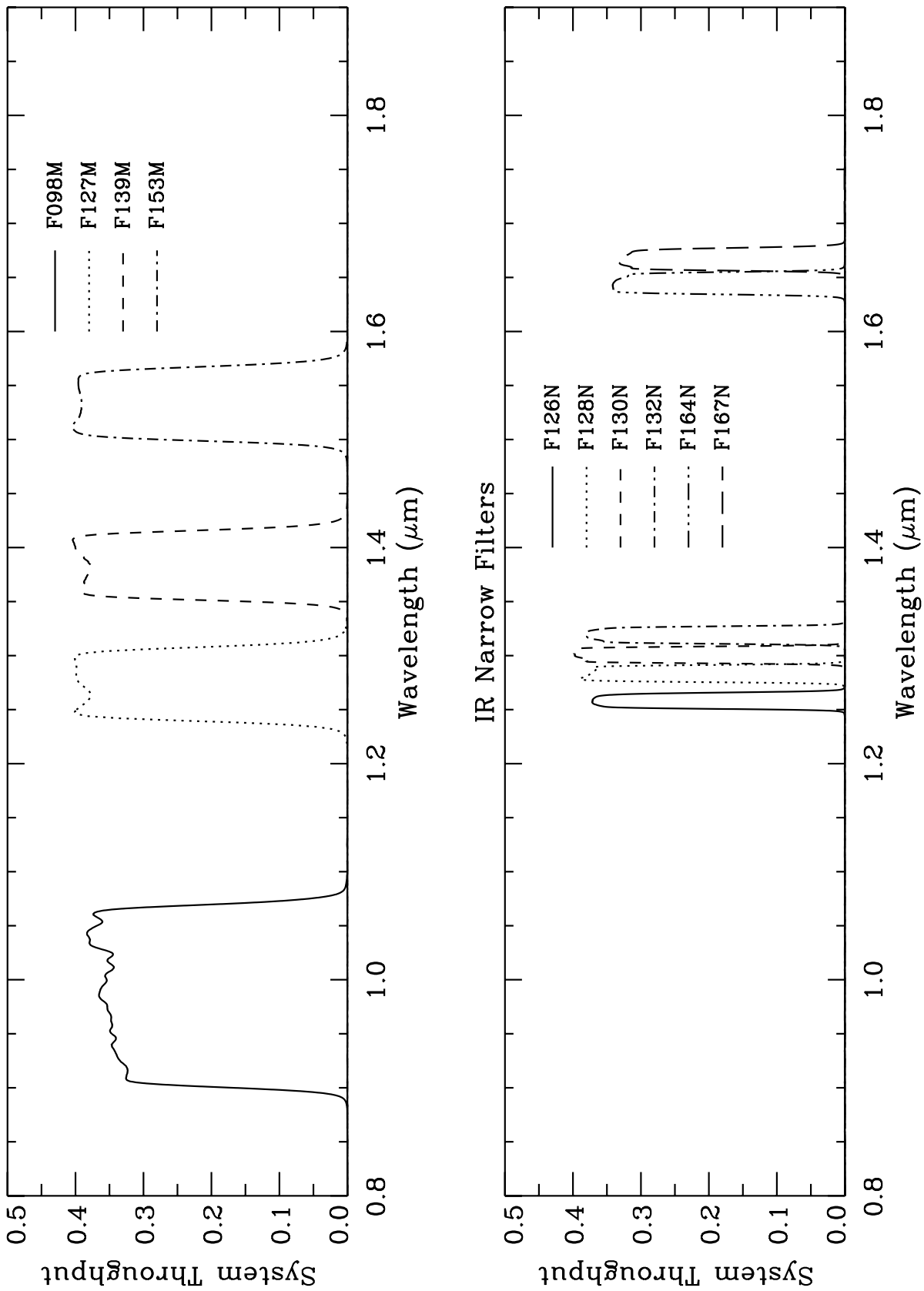

Figure 7.3: Integrated system throughput of the WFC3 IR medium-band filters (top panel) and narrow-band filters (bottom panel). The throughput calculations include the *HST* OTA, WFC3 IR-channel internal throughput, filter transmittance, and the QE of the IR detector. (Figured updated on Jan. 7, 2008)

7.5.2 Filter Blue Leaks

All of the IR filters have been constructed using IR-transmitting colored glass with thin-film coatings to achieve the desired bandpasses. As with the UVIS filter designs, better in-band transmission generally means somewhat less suppression of out-of-band transmission. While the final IR filters have excellent in-band transmission (>90%), a few also have a small, narrow peak of transmission between 750-800 nm. After the filters were manufactured, a new IR detector was chosen which has appreciable sensitivity well down into the optical wavelength range see Figure 5.12). Some of the IR filters will thus have a small amount of blue leak (i.e., a small amount of short-wavelength out-of-band light will be detected). None of the IR filters have significant red leaks.

Table 7.3 presents estimates of the blue-leak effect, listing the fraction of detected count rate expected from 710 to 830 nm for each filter. The throughput calculation includes transmission of the filter, the throughputs of the *HST* OTA and the IR optics, and the QE of the IR detector.

As can be seen from the table, blue leaks in all the wide-band and some of the narrow- and medium-band filters are minimal; however, several filters, notably F126N, F128N, and F153M, will have some blue leak (e.g., ~1% for objects with effective temperatures of 5000 K. Plans are being made to quantify and calibrate the effect as thoroughly as possible before launch. In programs that may suffer adverse effects due to the blue leaks, it may be useful to obtain UVIS images in the F763M filter, which covers the problematic wavelength region (750-800 nm).

Table 7.3: Fraction of detected count rate arising between wavelengths 710 to 830 nm as a function of effective temperature.

Filter	T_{eff} (K)										
	3500	5000	10000	15000	20000	25000	30000	35000	40000	45000	50000
F098M	3.8E-05	6.1E-05	8.4E-05	9.3E-05	9.8E-05	1.0E-04	1.0E-04	1.1E-04	1.1E-04	1.1E-04	1.1E-04
F105W	1.5E-05	2.2E-05	3.2E-05	3.5E-05	3.7E-05	3.9E-05	4.0E-05	4.1E-05	4.1E-05	4.1E-05	4.1E-05
F110W	8.8E-08	1.4E-07	2.4E-07	2.7E-07	2.9E-07	3.0E-07	3.1E-07	3.2E-07	3.2E-07	3.2E-07	3.2E-07
F125W	1.5E-07	2.4E-07	4.6E-07	5.3E-07	5.7E-07	6.1E-07	6.3E-07	6.5E-07	6.5E-07	6.5E-07	6.5E-07
F126N	6.4E-03	1.3E-02	2.6E-02	3.0E-02	3.3E-02	3.5E-02	3.6E-02	3.7E-02	3.8E-02	3.8E-02	3.8E-02
F127M	1.6E-03	3.2E-03	6.9E-03	8.0E-03	8.7E-03	9.2E-03	9.6E-03	9.8E-03	9.9E-03	1.0E-02	1.0E-02
F128N	5.7E-03	1.2E-02	2.7E-02	3.1E-02	3.3E-02	3.5E-02	3.6E-02	3.7E-02	3.7E-02	3.7E-02	3.7E-02
F130N	3.8E-04	6.7E-04	1.4E-03	1.6E-03	1.8E-03	1.9E-03	2.0E-03	2.0E-03	2.1E-03	2.1E-03	2.1E-03
F132N	3.7E-04	6.6E-04	1.4E-03	1.7E-03	1.8E-03	1.9E-03	2.0E-03	2.1E-03	2.1E-03	2.1E-03	2.1E-03
F139M	2.2E-03	3.9E-03	9.0E-03	1.1E-02	1.2E-02	1.3E-02	1.3E-02	1.4E-02	1.4E-02	1.4E-02	1.4E-02
F140W	6.3E-05	1.0E-04	2.4E-04	2.9E-04	3.2E-04	3.4E-04	3.5E-04	3.7E-04	3.7E-04	3.7E-04	3.7E-04
F153M	5.6E-03	9.9E-03	2.8E-02	3.3E-02	3.6E-02	3.9E-02	4.1E-02	4.2E-02	4.3E-02	4.3E-02	4.3E-02
F160W	9.4E-05	1.7E-04	4.8E-04	5.7E-04	6.3E-04	6.8E-04	7.1E-04	7.4E-04	7.4E-04	7.5E-04	7.5E-04
F164N	3.8E-03	8.0E-03	2.6E-02	3.1E-02	3.4E-02	3.7E-02	3.9E-02	4.0E-02	4.0E-02	4.1E-02	4.1E-02
F167N	3.3E-03	7.0E-03	2.2E-02	2.7E-02	3.0E-02	3.2E-02	3.4E-02	3.6E-02	3.6E-02	3.6E-02	3.6E-02

7.5.3 Ghosts

No significant optical ghosts are present in the IR channel.

7.6 IR Optical Performance

The following subsections summarize the expected flight optical performance for the IR channel. At this writing we do not have any direct observations of the sky using WFC3 installed in HST. However, extensive modelling as well as measurements made during ground testing provide a good basis for predicting the performance.

The performance of an imaging system is described by its point-spread function (PSF), i.e., the spatial distribution of the flux in an image of an extremely small point source. The PSF can be tabulated in various forms, and it can also be characterized by metrics such as the full width at half maximum (FWHM) and the encircled energy (EE) and ensquared energy.

7.6.1 Model PSF and FWHM

A theoretical PSF model for the IR channel is available; it includes residual aberration, the mid-frequency wavefront error of the OTA, the effect of the detector inter-pixel capacitive cross-talk, and first-order geometric distortion. The model reproduces with high accuracy the PSFs actually observed during ground testing of WFC3. The **FWHM** for IR channel images at ~1000 nm is approximately equal to 1 pixel of the IR detector, and it increases gradually with wavelength (see Table 7.4).

Table 7.4: WFC3/IR PSF FWHM (pixels and arcseconds) vs. wavelength.

Wavelength (nm	FWHM (pix)	FWHM (arcsec)
800	0.997	0.128
900	0.999	0.128
1000	1.009	0.129
1100	1.026	0.131
1200	1.049	0.134
1300	1.079	0.138
1400	1.115	0.143
1500	1.154	0.148
1600	1.199	0.153
1700	1.248	0.160

The model PSF at 1000 nm is illustrated in Figure 7.4. It assumes the source to be located at the center of a pixel. Table 7.5 presents the model PSF at 1000 nm in tabular form. Here the total flux from the source has been set to 1, and the pixel response over a 7×7 pixel square is tabulated. For example, the table shows that 36.1% of the total flux resides in the central pixel of the PSF.

Figure 7.5 plots the azimuthally-averaged model OTA+WFC3 PSF at three different IR wavelengths., indicating the fractional PSF flux per pixel at radii from 1 pixel to 5 arcsec.

Figure 7.4: Model of the WFC3/IR PSF at 1000 nm.

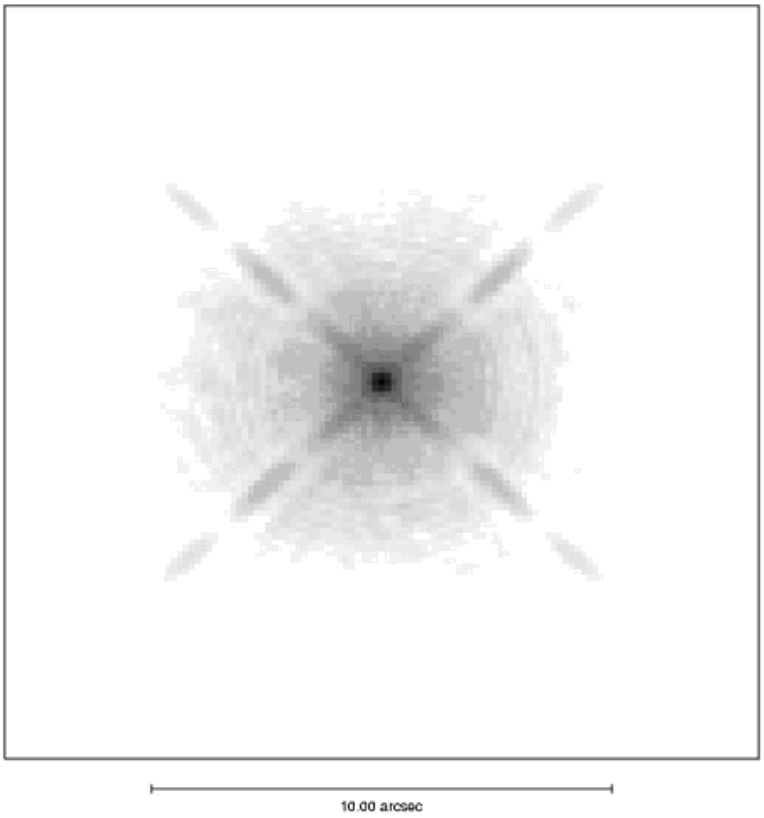

Table 7.5: Model PSF of WFC3/IR at 1000 nm, tabulated per pixel in a 7x7 pixel box.

0.001	0.001	0.002	0.001	0.001	0.002	0.001
0.002	0.002	0.004	0.006	0.003	0.002	0.002
0.002	0.004	0.033	0.071	0.033	0.004	0.002
0.002	0.008	0.075	0.361	0.075	0.008	0.002
0.002	0.005	0.037	0.075	0.035	0.004	0.002
0.002	0.002	0.004	0.007	0.004	0.002	0.002
0.001	0.002	0.002	0.002	0.002	0.002	0.001

Figure 7.5: Azimuthally averaged WFC3/IR PSF.

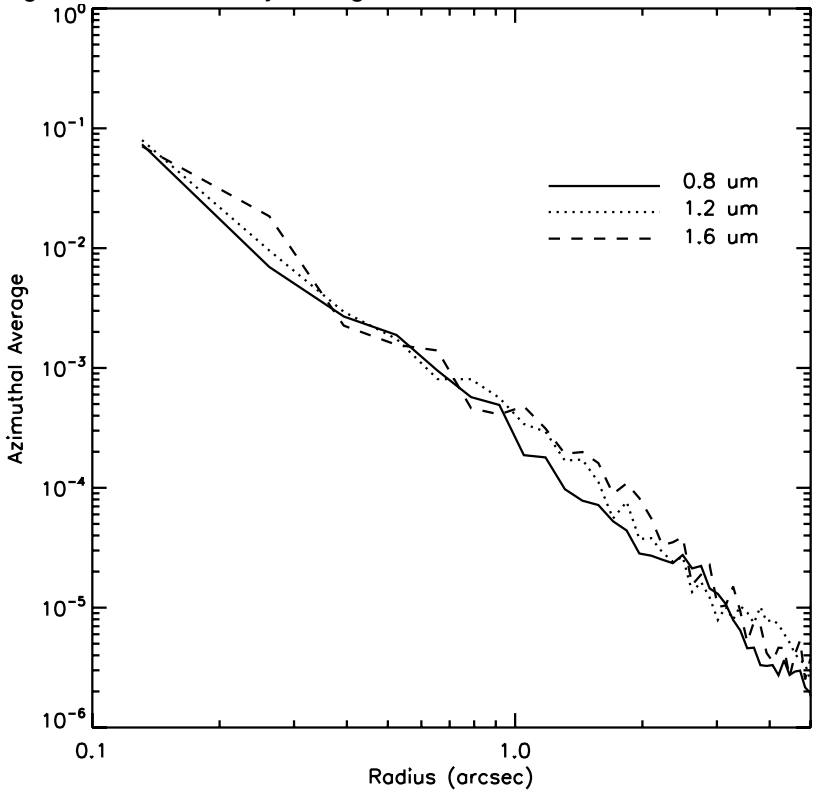

7.6.2 Encircled and Ensquared Energy

The **encircled energy** is the fraction of the total light from a point source that is contained within a circular aperture of a given radius. Like the FWHM, it is useful for comparison of well-behaved PSFs, such as WFC3's in the infrared. Since modern detectors have nominally square pixels, it is often more convenient to evaluate the energy falling within a certain number of pixels ("**ensquared energy**") instead of the encircled energy, which requires interpolation to account for the fractional pixels intercepted by a circular aperture.

Encircled-energy profiles for the IR channel at three representative wavelengths are plotted in Figure 7.6. The corresponding numerical values are presented in Table 7.6.

The ensquared energy, which provides the flux per pixel, is presented in Table 7.7.

Figure 7.6: Encircled Energy for the WFC3/IR channel.

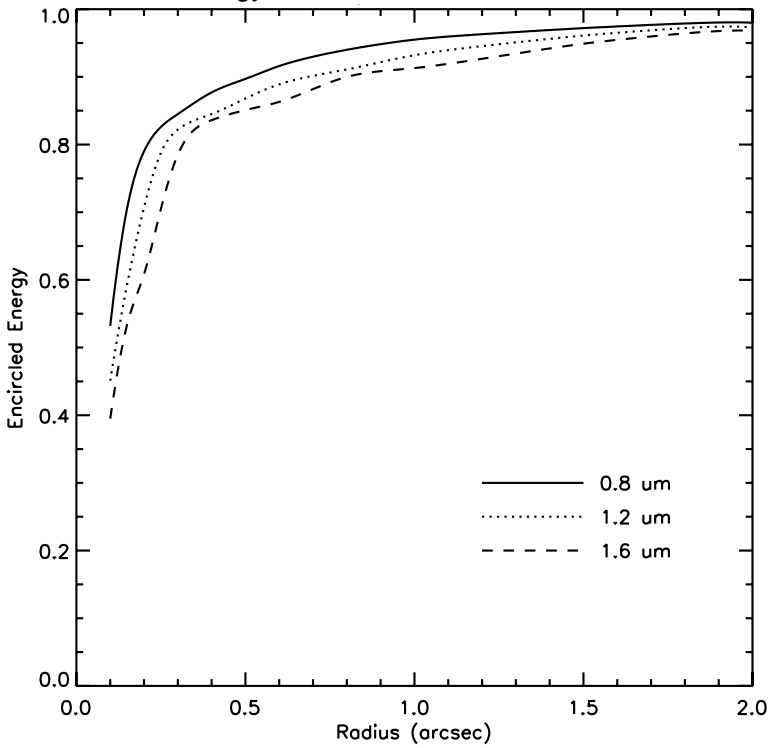

Table 7.6: WFC3/IR PSF Encircled Energy Fraction vs. Aperture radius (arcsec).

Aperture radius (arcsec)	Wavelength (nm)										
	700	800	900	1000	1100	1200	1300	1400	1500	1600	1700
0.10	0.557	0.532	0.508	0.486	0.468	0.451	0.436	0.422	0.410	0.395	0.379
0.15	0.727	0.706	0.677	0.648	0.619	0.593	0.572	0.555	0.545	0.534	0.524
0.20	0.799	0.790	0.775	0.757	0.734	0.707	0.679	0.651	0.630	0.608	0.591
0.25	0.830	0.826	0.819	0.811	0.801	0.788	0.772	0.751	0.731	0.705	0.678
0.30	0.851	0.845	0.838	0.833	0.828	0.822	0.815	0.806	0.800	0.785	0.766
0.40	0.881	0.877	0.869	0.859	0.851	0.845	0.841	0.838	0.840	0.836	0.832
0.50	0.903	0.897	0.890	0.885	0.877	0.868	0.858	0.852	0.854	0.851	0.848
0.60	0.921	0.916	0.906	0.899	0.894	0.889	0.883	0.874	0.870	0.863	0.859
0.80	0.943	0.940	0.933	0.926	0.919	0.911	0.905	0.901	0.904	0.900	0.896
1.00	0.956	0.955	0.949	0.944	0.937	0.932	0.927	0.920	0.918	0.913	0.910
1.50	0.972	0.972	0.970	0.967	0.965	0.961	0.956	0.952	0.953	0.949	0.944
2.00	0.979	0.980	0.979	0.977	0.975	0.973	0.971	0.968	0.972	0.968	0.964

Table 7.7: WFC3/IR PSF Ensquared Energy Fraction vs. Aperture size (pixels), where the target is centered on the aperture and falls on the central pixel.

Aperture size (pixels)	Wavelength (nm)										
	700	800	900	1000	1100	1200	1300	1400	1500	1600	1700
1×1	0.410	0.392	0.374	0.358	0.342	0.327	0.312	0.297	0.284	0.269	0.254
2×2[1]	0.719	0.697	0.670	0.641	0.613	0.588	0.567	0.550	0.539	0.527	0.516
3×3	0.814	0.809	0.799	0.786	0.771	0.751	0.728	0.702	0.680	0.654	0.631
5×5	0.874	0.869	0.858	0.850	0.844	0.840	0.835	0.830	0.830	0.825	0.820
7×7	0.909	0.903	0.895	0.889	0.882	0.872	0.862	0.855	0.857	0.854	0.852
9×9	0.932	0.928	0.919	0.911	0.905	0.899	0.894	0.888	0.886	0.876	0.868
11×11	0.947	0.944	0.937	0.930	0.923	0.915	0.911	0.906	0.906	0.902	0.897
13×13	0.956	0.955	0.950	0.943	0.938	0.932	0.925	0.918	0.920	0.916	0.911
15×15	0.962	0.963	0.958	0.954	0.948	0.943	0.938	0.932	0.932	0.926	0.922
17×17	0.966	0.967	0.965	0.961	0.957	0.952	0.947	0.943	0.943	0.939	0.933
19×19	0.969	0.970	0.969	0.967	0.963	0.959	0.955	0.950	0.952	0.948	0.943
21×21	0.972	0.973	0.972	0.970	0.968	0.965	0.961	0.958	0.959	0.954	0.951
23×23	0.975	0.975	0.974	0.972	0.971	0.969	0.966	0.963	0.965	0.961	0.957
25×25	0.978	0.978	0.976	0.975	0.973	0.972	0.970	0.967	0.969	0.966	0.963
51×51	0.993	0.994	0.992	0.991	0.990	0.989	0.987	0.986	0.989	0.988	0.987
101×101	0.998	0.999	0.998	0.998	0.997	0.997	0.996	0.996	0.998	0.998	0.997

1. For the 2×2 aperture, the target is located at the center of the array.

7.6.3 Other PSF Behavior and Characteristics

Temporal Dependence of the PSF: HST Breathing

Short-term focus variations are usually referred to as "OTA breathing," "HST breathing," "focus breathing," or simply "breathing." Breathing affects all data obtained with all instruments onboard HST. The WFC3 IR PSF will likewise suffer from small temporal variations induced by the HST breathing. The focus changes are attributed to the contraction/expansion of the OTA due to thermal variations during an orbital period.

Thermally induced HST focus variations also depend on the thermal history of the telescope. For example, after a telescope slew, the telescope temperature variation exhibits the regular orbital component plus a component associated with the change in telescope attitude. The focus changes due to telescope attitude are complicated functions of Sun angle and telescope roll. More information and models can be found on the "HST Thermal Focus Modeling" Web site at:

http://www.stsci.edu/hst/observatory/focus/thermal.html

Breathing is expected to produce variations of ~0.3% and less than 0.1% in the FWHM of the PSF of WFC3/IR at 700 nm and at wavelengths longer than 1100 nm, respectively, on typical timescales of one orbit.

Intra-pixel Response

The response of a pixel of an IR detector to light from an unresolved source varies with the positioning of the source within the pixel due to low sensitivity at the pixel's edges and dead zones between pixels. For NICMOS, the intra-pixel sensitivity was found to be an important effect: it varies by as much as 30%. This effect has an impact on point sources which depends on the sampling, and therefore, for a given pixel scale, on the wavelength of the diffraction-limited images. Well-dithered exposures will average out this effect, but photometric accuracy for stellar sources with few dither positions can be limited by uncertainties related to intra-pixel response.

For WFC3/IR, the intra-pixel response is expected to be significantly better (more uniform) than NICMOS, likely due to the much higher detector temperature which increases the electron mobility.

Inter-pixel Capacitance

The small pixel size, relative to that in NICMOS, increases the relevance of capacitive coupling between nearby pixels (see Brown et. al., 2006, *PASP*, **118**, 1443; Moore et. al., 2006, Opt. Eng., 076402). It affects the gain measurements and the PSF. The easiest method of estimating the inter-pixel capacitance is to measure the ratio of DNs in pixels adjacent to a "hot" (high-dark-current) pixel to the DNs in the hot pixel. The observer should be aware that such cross-talk occurs for all pixels, but is most noticeable around hot pixels.

7.7 IR Exposure and Readout

The general operating modes of IR detectors have been described in Chapter 5. In this section we will detail the readout modes implemented in WFC3.

7.7.1 Exposure Time

Unlike the UVIS channel, the IR channel does not have a mechanical shutter. Integration times are thus determined purely electronically, by resetting the charge on the detector to zero, and then accumulating signal until the exposure is completed. A second major difference from the UVIS channel is that the IR detector can be read out non-destructively as the exposure accumulates, as opposed to the single destructive readout at the end of a CCD exposure.

There is a set of pre-defined accumulation and readout sequences available to IR observers, which are used to set the total exposure time as described in the next subsection.

7.7.2 MULTIACCUM Mode

In IR observing it is possible, and desirable, to sample the signal multiple times as an exposure accumulates, and the MULTIACCUM mode accomplishes this. MULTIACCUM is the only observing mode available for the IR channel.

Multiple readouts offer three major advantages. First, the multiple reads provide a way to record a signal in a pixel before it saturates, thus effectively increasing the dynamic range of the final image. Second, the multiple reads can be analyzed to isolate and remove cosmic-ray events. Third, fitting to multiple reads provides a means for reducing the net effective read noise, which is relatively high for the IR detector.

The disadvantage of multiple readouts is that they are data-intensive. The HgCdTe detector array is 1024×1024 pixels, which is only about 1/16 by pixel number of the 4096×4102 UVIS array. However, since typically 16 IR readouts are used, the total data volume of a single IR exposure is generally the same as that of a single UVIS frame. A maximum of 32 IR readouts can be stored in the instrument buffer, after which the content of the buffer must be dumped to the HST Solid State Recorder (SSR). A buffer dump of 16 reads takes about 5.8 minutes.

MULTIACCUM readout consists of the following sequence of events:

1. **Array reset:** After a fast calibration of the Analog to Digital Converters, all pixels are set to a zero signal (i.e., to the detector bias level), with two rapid reset cycles of the entire chip.
2. **Array read:** The charge in each pixel is measured and stored in the on-board computer's memory. This is done as soon as practical after the second array reset in step 1. In effect, given the short delay and the time needed to read the array, a very short-exposure image is stored in memory.
3. **Multiple integration-read cycles:** The detector integrates for a certain amount of time and then the charge in each pixel is read out. This step can be repeated up to a total of 15 times during the exposure. All frames are individually stored in the on-board computer memory. Note that it takes a finite time (2.93 sec) to read the array, so there is a time delay between reading the first and last pixel. Since this delay is constant for each read, it cancels out in difference images.
4. **Return to idle mode:** the detector returns to idle mode, where it is continuously flushed in order to prevent charge build-up.

All sequences start with the same “reset, read, read” sequence, where the two reads are done as quickly as possible. This “double reset read” was originally implemented because the very first read after the reset may show a shading pattern that does not reproduce in the following reads.

The difference between two reads (“double-correlated sampling”) is required for capturing the *kTC* noise, which is defined as the uncertainty on the charge effectively loaded on a capacitance *C* at a temperature *T*. The *kTC* noise is a random offset present after the reset operation. Subtracting the first reset read from all subsequent reads is the standard way of removing the *kTC* noise. It is the so-called correlated double sampling (CDS).

7.7.3 MULTIACCUM Timing Sequences

There are 15 pre-defined timing sequences, optimized to cover a wide range of observing situations, available for the IR channel.

As noted in step 3 of the observing sequence described in Section 7.7.1, the maximum number of reads during an exposure is 15, which are collected as the signal ramps up. It is possible to select less than 15 reads, thus cutting short the ramp and reducing the total exposure time. However, the timing of the individual reads within any of the 15 sequences cannot be adjusted by the user. This approach has been adopted because of experience with NICMOS, which indicates that optimal calibration of IR detectors requires a dedicated set of reference files (e.g., dark frames) for each timing pattern.

In summary, a WFC3/IR exposure is fully specified by choosing:

- one of the 15 pre-defined timing sequences, and
- the total number of samples (NSAMP, which must be no more than 15), which effectively determines the total exposure time

The 15 pre-defined timing sequences for the IR channel are the following:

- One **RAPID** sequence: the detector is sampled with the shortest possible time interval.
- Five linear (**SPARS**) sequences: the detector is sampled with uniform time intervals between reads, a so-called "linear sample up the ramp." ("SPARS" is a contraction of the word "sparse.")
- Five log-linear (**STEP**) sequences: the detector is initially sampled with reads spaced logarithmically in time. After a specified time, the sampling then becomes uniform until the last sample;
- Four pseudo-Fowler (**MIF**) sequences, in which the signal is mostly sampled at the beginning and at the end of the ramp (see Fowler & Gatley, 1990, *ApJ*, **353**, L33). Six readouts each are made at the beginning and end of the ramp, with the remaining three uniformly spaced in between. ("MIF" stands for "Multiple Initial and Final.")

All 15 of the sequences above refer to readouts of the full 1024×1024 detector array. See Section 7.7.4 below for the timing sequences available for subarrays.

Details of the sequences are in the following paragraphs. The timings of the individual reads are given in Table 7.8.

RAPID Sequence

The RAPID sequence provides linear sampling at the fastest possible speed. For the full array, this means one frame every 2.9 s, and the entire set of 16 reads completed in less than 44 s. The RAPID mode is mainly intended for the brightest targets. Due to the overheads imposed by buffer dumps (see Chapter 10), observations in this mode done continuously would have low observing efficiency.

SPARS Sequences

The SPARS sequences use evenly spaced time intervals. The five available SPARS sequences are designated SPARS10, SPARS25, SPARS50, SPARS100 and

SPARS200, corresponding to sampling intervals of approximately 10, 25, 50, 100, and 200 s, respectively.

The SPARS modes can be regarded as the most basic readout modes, and they are applicable to a wide range of target fluxes. They provide flexibility in integration time and are well suited to fill an orbital visibility period with several exposures.

STEP Sequences

The five available logarithmic/linear sequences are STEP25, STEP50, STEP100, STEP200, and STEP400. They begin with logarithmic spacing up to the given number of seconds (e.g., 50 s for STEP50), and then continue with linear spacing for the remainder of the sequence.

The STEP mode is intended to provide a more uniform sampling across a wide range of stellar magnitudes, which is especially important for imaging fields containing both faint and bright targets. The faint targets require a long, linearly sampled integration, while the bright targets need to be sampled several times early in the exposure, before they saturate. Thus, the dynamic range of the final image is increased.

Fowler (MIF) Sequences

The four pseudo-Fowler sampling sequences perform six rapid reads at both the beginning and end of each exposure, plus three reads uniformly spaced through the middle of the exposure. The MIF sequences are MIF600, MIF900, MIF1200, and MIF1500. The numbers refer to the delays (in seconds) between the first and second groups of reads.

The MIF sequences allow the user to form an average of the initial and final reads (Fowler sampling), forming an image from the difference of these two images. The middle readouts allow for recovery of sources that would saturate at the end of the exposure, and for cosmic-ray removal. Note that these sequences are not useful unless all 16 reads are executed. Fowler sampling, in an idealized case, allows reduction of the readout noise by 1/sqrt(n), where n is the number of reads. In practice, the maximum improvement in effective read noise over a single initial and final read may be limited by other source of noise (e.g., 1/f noise) and overheads.

Figure 7.7: Example of STEP sequence with NSAMP=4. NSAMP+1 images are stored in the observer's FITS image.

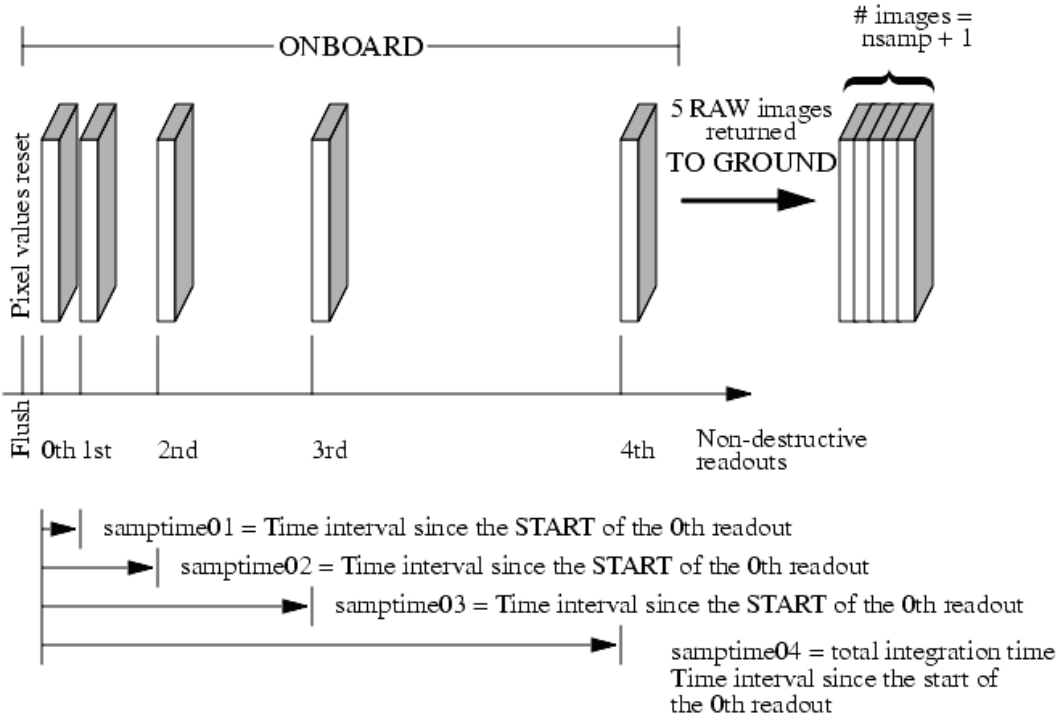

Table 7.8: Sample times of 1024x1024 MULTIACCUM readouts in seconds. The information in this table can also be found in Table 15.5 of the Phase II Proposal Instructions.

NSAMP	RAPID (sec)	SPARS (sec)					STEP (sec)					MIF (sec)			
		SPARS10	SPARS25	SPARS50	SPARS100	SPARS200	STEP25	STEP50	STEP100	STEP200	STEP400	MIF600	MIF900	MIF1200	MIF1500
1	2.932	2.932	2.932	2.932	2.932	2.932	2.932	2.932	2.932	2.932	2.932	2.932	2.932	2.932	2.932
2	5.865	12.933	27.933	52.933	102.933	202.932	5.865	5.865	5.865	5.865	5.865	5.865	5.865	5.865	5.865
3	8.797	22.934	52.933	102.933	202.933	402.932	8.797	8.797	8.797	8.797	8.797	8.797	8.797	8.797	8.797
4	11.729	32.935	77.934	152.934	302.933	602.932	11.729	11.729	11.729	11.729	11.729	11.729	11.729	11.729	11.729
5	14.661	42.936	102.934	202.934	402.934	802.933	24.230	24.230	24.230	24.230	24.230	14.661	14.661	14.661	14.661
6	17.594	52.937	127.935	252.935	502.934	1002.933	49.230	49.230	49.230	49.230	49.230	17.594	17.594	17.594	17.594
7	20.526	62.938	152.935	302.935	602.934	1202.933	74.231	99.231	99.231	99.231	99.231	159.531	234.531	309.531	384.530
8	23.458	72.939	177.936	352.935	702.935	1402.933	99.231	149.231	199.231	199.231	199.231	301.468	451.468	601.467	751.467
9	26.391	82.940	202.936	402.936	802.935	1602.933	124.232	199.232	299.231	399.231	399.231	443.405	668.405	893.404	1118.404
10	29.323	92.941	227.937	452.936	902.935	1802.933	149.232	249.232	399.232	599.231	799.232	585.343	885.342	1185.341	1485.340
11	32.255	102.942	252.937	502.937	1002.936	2002.933	174.233	299.232	499.232	799.231	1199.232	588.275	888.274	1188.273	1488.273
12	35.187	112.943	277.938	552.937	1102.936	2202.933	199.233	349.233	599.232	999.231	1599.233	591.207	891.206	1191.206	1491.205
13	38.120	122.944	302.938	602.938	1202.936	2402.933	224.234	399.233	699.233	1199.231	1999.233	594.139	894.139	1194.138	1494.137
14	41.052	132.945	327.939	652.938	1302.936	2602.933	249.234	449.234	799.233	1399.231	2399.234	597.072	897.071	1197.070	1497.069
15	43.984	142.946	352.940	702.939	1402.937	2802.933	274.235	499.234	899.233	1599.231	2799.235	600.004	900.003	1200.003	1500.002

7.7.4 Subarray Timing Sequences

As described in Section 7.4.4, subarrays are available in order to reduce data volume and enable short exposure times. Table 7.9 lists the sample times for subarrays of the IR channel of WFC3. Only the RAPID and SPARS10 sequences are tabulated, because only those will be calibrated by STScI. Other MULTIACCUM sequences can be used in principle but are not supported, and additional calibration observations would have to be made by the observer.

Observers interested in short exposures may wish to compare NICMOS to WFC3, because NICMOS subarrays may have less overhead than subarrays of WFC3/IR for certain applications, notably time-series photometry.

Table 7.9: Sample times in seconds for the RAPID and SPARS10 sequences for each subarray. The information in this table can also be found in Table 15.5 of the Phase II Proposal Instructions.

NSAMP	RAPID (sec)				SPARS (sec)			
	512x512	256x256	128x128	64x64	512x512	256x256	128x128	64x64
1	0.853	0.278	0.113	0.061	0.853	0.278	0.113	0.061
2	1.706	0.556	0.225	0.122	8.775	7.624	7.294	7.190
3	2.559	0.833	0.338	0.182	16.696	14.971	14.475	14.320
4	3.412	1.111	0.451	0.243	24.618	22.317	21.657	21.449
5	4.265	1.389	0.564	0.304	32.540	29.664	28.838	28.579
6	5.118	1.667	0.676	0.365	40.462	37.010	36.020	35.708
7	5.971	1.945	0.789	0.425	48.383	44.357	43.201	42.837
8	6.824	2.223	0.902	0.486	56.305	51.703	50.382	49.967
9	7.677	2.500	1.014	0.547	64.227	59.050	57.564	57.096
10	8.530	2.778	1.127	0.608	72.148	66.396	64.745	64.226
11	9.383	3.056	1.240	0.669	80.070	73.743	71.926	71.355
12	10.236	3.334	1.352	0.729	87.992	81.089	79.108	78.485
13	11.089	3.612	1.465	0.790	95.913	88.436	86.289	85.614
14	11.942	3.889	1.578	0.851	103.835	95.782	93.471	92.744
15	12.795	4.167	1.691	0.912	111.757	103.129	100.652	99.873

7.8 IR Sensitivity

7.8.1 Limiting Magnitudes

Table 7.10 presents the predicted limiting-magnitude performance of the WFC3 IR channel and compares it with that of the NIC3 camera. The calculations are based on a optimal extraction of a point source. The limiting ABMAG at a S/N of 10 was calculated for a 1-hour and a 10-hour exposure. The throughput curves for the WFC3 filters listed in column 2 were used; for NIC3, the most similar wide-band filter was used, and its name is given in column 3.

An Exposure Time Calculator (ETC) is available online. See Section 9.2.

Table 7.10: Anticipated limiting-magnitude performance of WFC3 compared with that of NIC3. The table provides limiting ABMAGs at a S/N of 10 for the indicated WFC3 filters and for NIC3 with its most similar filters.

Band	Filter		Limiting magnitude in 1 hr		Limiting magnitude in 10 hrs	
	WFC3	NIC3	WFC3	NIC3	WFC3	NIC3
J	F110W	F110W	27.1	26.1	28.4	27.3
H	F160W	F160W	26.3	25.9	27.6	27.1

7.9 Other Considerations for IR Imaging

7.9.1 Gain and Full-well Saturation

Like the UVIS channel, the IR channel uses 16-bit Analog to Digital Converters (ADCs), providing a digital output signal in the range between 0 and 65,535 data numbers (DNs). The default gain setting for the IR channel is 2.5 electrons/DN and is the only one offered to observers.

The default gain is compatible with the full-well saturation level of the IR channel, which is about 100,000 electrons (~40,000 DN at the default gain), and with the detector readout noise, of order 20-22 electrons per correlated double sampling.

7.9.2 Cosmic Rays and Hot Pixels

Cosmic rays affect the image quality. On-orbit measurement of the distribution of cosmic rays on NICMOS shows 1.2 to 1.6 events/second/camera for 5σ events. Taking into account the 3.4 times larger physical area of the WFC3 IR detector (3.39 cm^2 vs.

1.04 cm^2 for NICMOS), we estimate ~5 events/s/camera for WFC3 IR. Pending on-orbit observations with WFC3, we anticipate that the cosmic-ray event rate for WFC3 IR will be similar to NICMOS per unit area, but the fraction of pixels contaminated by cosmic rays will be less for WFC3 than NICMOS because WFC3's pixels are smaller (18 μm vs. 40 μm size).

As in NICMOS, the use of MULTIACCUM mode makes it possible to filter out cosmic rays since it provides a series of intermediate non-destructive reads. The intermediate reads are used by the WFC3 data pipeline to identify cosmic ray hits, similarly to what is normally done with the CR-SPLITs in CCD observations.

Passages though the South Atlantic Anomaly cause the highest number of cosmic ray hits. The NICMOS operations have been adjusted to minimize the effect of the SAA on instrument performance, and we plan to adopt similar strategies (e.g., continuous flushing the IR detector during the passage) for WFC3/IR.

7.9.3 On-orbit Degradation

Unlike the CCDs, minimal cosmic-ray damage to the IR detectors is anticipated. During ground testing using a particle accelerator, the WFC3/IR arrays have been subjected to radiation doses much higher than expected in their entire orbital lifetime, without sustaining any long-term damage or measurable degradation in QE.

7.9.4 Image Persistence

The IR detector is likely to exhibit some image persistence, particularly following observations of targets that saturate the detector by much more than (e.g., 100 times) each pixel's full well. The specific behavior is detector dependent; illustrative measurements have been made of four IR detectors similar to WFC3's. Flat-field exposures, intentionally over-exposed to 100 times full well, indicate that saturating an extended source results in excess dark current in the over-exposed pixels of less than or equal to 1 e^-/sec/pixel, three minutes after the over-exposure. The excess dark current due to persistence decays approximately exponentially with time, with an e-folding time of ~3 minutes. Hence, charge current due to persistence from an over-exposure is expected to decay asymptotically to very low levels after ~15 minutes.

Persistence due to an exposure that fills wells to less than approximately half capacity is expected to be negligible, for all subsequent exposures, even the one immediately thereafter. Observers with very demanding requirements for persistence are advised that the actual behavior of WFC3's detector has not been demonstrated under the variety of circumstances that will be experienced on HST. Also, the exponential model described above breaks down after many e-folding times; in particular, a very long tail (in time) of very-low-level persistence is seen commonly in laboratory measurements.

7.9.5 The IR Background

In space, the dominant sources of background radiation are zodiacal light and earthshine at shorter IR wavelengths, and the telescope thermal emission at longer wavelengths. For HST, the sum of these two background components has a minimum at about 1600 nm (roughly lying in the H band).

The surface brightness of zodiacal light is a function of the ecliptic latitude and longitude, and reaches a minimum ~120 degrees from the sun, i.e., near, but not at, the ecliptic poles increasing again to 180 degrees (anti-solar direction).

Table 7.11 gives low, high, and average values of the zodiacal background as seen by HST (see Stiavelli 2002, WFC3 ISR 2002-02). Table 7.11 itemizes components of the IR background and estimates their total and the minimum integration time required to reach background-limited performance.

Table 7.11: Zodiacal backgrounds from Stiavelli 2002 (WFC3 ISR 2002-02). Flux units have been converted to photon counts incident upon HST's aperture. Table 7.12 converts the average values from this table to e^-/s/pixel on the IR detector, including throughputs.

Background	erg $cm^{-2}s^{-1}Å^{-1}arcsec^{-2}$		photons (HST area)$^{-1}s^{-1}Å^{-1}arcsec^{-2}$	
	1.2 μm	1.6 μm	1.2 μm	1.6 μm
Minimum	4.90×10^{-19}	2.20×10^{-19}	0.013	0.008
Typical	7.35×10^{-19}	3.31×10^{-19}	0.020	0.012
Average	8.32×10^{-19}	3.86×10^{-19}	0.023	0.014
Maximum	2.15×10^{-18}	9.64×10^{-19}	0.059	0.035

For pointings very close to the bright Earth limb, the zodiacal background may be exceeded by earth-shine. The brightness of the earth-shine falls very rapidly with increasing angle from the Earth's limb, and for most observations only a few minutes at the beginning and end of the target visibility period will be significantly affected. The major exception to this behavior is a target in the continuous viewing zone (CVZ). Such targets will always be rather close to the Earth's limb, and so can sometimes see an elevated background for part of the orbit, even at shorter wavelengths where zodiacal emission ordinarily dominates.

For targets faint enough that the background level is expected to be much brighter than the target, the observer has these options when crafting the Phase II proposal: (1) specify a non-standard Bright Earth Avoidance (BEA) angle, which increases the angle from the Earth's limb from 20° to 25° (note that this is an available mode and must be specially requested through a Contact Scientist), or (2) specify the LOW-SKY option, which restricts observations to targets more than 40° away from the Earth's limb and restricts scheduling to times when the zodiacal background is no greater than 30% above the minimum achievable level. The second option decreases the available observing (visibility) time during each orbit and implies scheduling constraints.

7.10 IR Observing Strategies

7.10.1 Dithering Strategies

Dithering is used to improve image quality and resolution. By acquiring multiple images of a target at slightly different positions on the detector, one can compensate for detector artifacts (blemishes, hot pixels, and plate-scale irregularities), remove cosmic-ray events, and improve the effective resolution. When improved resolution is the goal, dithering is usually accomplished with sub-pixel offsets; this is especially important for WFC3-IR, because the PSF is undersampled by a factor of 2 (see Table 7.4). Integral-pixel steps are more appropriate when dithering is aimed solely at removing detector artifacts.

Larger dithers are used for mosaicking, used to cover a region of sky larger than the detector field of view. (Large dithers can also be used for "chopping," e.g., as used by NICMOS for background sampling; however, no chopping has been implemented for WFC3/IR.) Mosaicking maneuvers are usually much larger than dithering, but mosaicking and dithering are often combined, i.e., using large mosaic shifts to increase the sky coverage, accompanied by a number of small dithers to increase resolution and remove artifacts.

In WFC3, all these maneuvers must be accomplished by moving the telescope (whereas in NICMOS it is also possible to move the Field Offset Mirror). Dithers using the same guide stars must be contained within a ~130 arcsec diameter.

Mechanisms for dithering, via pre-defined patterns or manually (POS TARG special requirement), are described in detail in the Phase II Proposal Instructions.

7.10.2 Parallel Observations

Parallel observations, i.e., the simultaneous use of WFC3 with one or more other HST instruments, are the same for the IR channel as for the UVIS channel, previously described in Section 6.10.2.

7.10.3 Exposure Strategies

Given the variety of requirements of the scientific programs that will be executed with WFC3/IR, it is impossible to establish a single optimum observing strategy. In this section we will therefore guide the reader through the main constraints that should be taken into account when designing an observation, and provide a few examples.

Let us first summarize the constraints. To attain the ultimate sensitivity one has to:

- integrate long enough to be limited by background emission and not read noise.

- dither enough so that resolution can be restored to the diffraction limit and bad pixels and cosmic-ray impacts can be removed, while maintaining a homogeneous S/N ratio across the field.
- split the MULTIACCUM ramps into as many reads as possible for readout noise suppression.

These constraints put contradictory requirements on the ideal observing strategy. It is clear that, given a certain amount of total observing time, the requirement of long integrations for background limited performance is incompatible with a large number of dithering positions. Also, to split ramps for readout noise suppression decreases the observing efficiency, with a negative impact on the signal to noise ratio. Since the background seen by each pixel depends on the filter (Section 7.9.5), the optimal compromise must be determined on a case-by-case basis.

In this regard, it is useful to consider Table 7.12, which summarizes the total background seen by a pixel, including sky, telescope, and nominal dark current, and the time needed to reach 400 e^-/pixel of accumulated signal, corresponding to 20 e^-/pixel of background noise. This last value, higher than the expected readout noise of ~15 electrons after 16 reads, is used here to set the threshold for background-limited performance. The passage from readout-limited performance to background-limited performance can be regarded as the optimal exposure time for that given filter, in the sense that it allows for the largest number of dithered images without significant loss of S/N ratio (for a given total exposure time, i.e., neglecting overheads). For faint sources, the optimal integration time strongly depends on the background (zodiacal, thermal, and dark current) in each filter, ranging from just 360 s for the F110W filter to 2400 s for some of the narrow-band filters.

The optimal integration time shown in Table 7.12 can be compared with the integration times of the sampling sequences from Table 7.8. Table 7.13 synthesizes the results, showing for each filter which of the different ramps (SPARS, STEP, MIF) most closely matches the optimal integration times.

Table 7.12: Background (e^-/pix/s) levels at the WFC3/IR detector. The columns show, from left to right: a) filter name; b) thermal background from the telescope and instrument; c) zodiacal background; d) earth-shine background; e) dark current; f) total background; g) integration time needed to reach background-limited performance, set at an equivalent readout noise of 20 electrons.

Filter	Thermal	Zodiacal	Earth-shine	Dark Current	Total	Optimal Integration Time (sec)
F105W	0.051	0.639	0.196	0.020	0.905	441
F110W	0.051	1.053	0.314	0.020	1.438	278
F125W	0.051	0.613	0.176	0.020	0.860	465
F140W	0.024	0.739	0.203	0.020	0.985	405
F160W	0.101	0.455	0.121	0.020	0.697	574
F098M	0.051	0.372	0.117	0.020	0.560	714
F127M	0.051	0.140	0.040	0.020	0.251	1595
F139M	0.051	0.122	0.033	0.020	0.226	1769
F153M	0.058	0.117	0.031	0.020	0.226	1770
F126N	0.051	0.029	0.008	0.020	0.108	3712
F128N	0.051	0.031	0.009	0.020	0.110	3641
F130N	0.051	0.031	0.009	0.020	0.110	3622
F132N	0.051	0.030	0.008	0.020	0.109	3673
F164N	0.063	0.027	0.007	0.020	0.118	3401
F167N	0.069	0.027	0.007	0.020	0.123	3264

The selection of which sample sequence type (SPARS, STEP, MIF) to be used must take into account the science goals. There are three basic types of ramp sequences, each suited for different purposes:

- SPARS ramps, with their uniform sampling, maintain the detector in the most steady thermal condition, provide the most robust rejection of cosmic-ray events, and can be trimmed by removing a few of the final reads to fine-tune the integration time with little degradation of the achieved readout noise. Thus they are considered the standard sampling mode.
- STEP ramps are preferable for a high-dynamic-range scene, e.g., for photometry of a stellar clusters. The STEP sequences consist of four rapid reads followed by read with exposure time spaced logarithmically and ending with reads spaced linearly. This design provides for correction of any non-linearities early in the exposure and allows for increased dynamic range for both bright and faint targets.

- MIF ramps have the multiple reads clustered at the extremes of the integration time with three widely spaced reads in the middle to facilitate cosmic ray corrections and allow for saturation detection. These ramps provide for the ultimate reduction of the readout noise through multiple sampling, and are therefore ideal for faint targets. On the other hand, they cannot be effectively trimmed to adjust the integration time. In addition, cosmic ray corrections can be less optimal than with the STEP and SPARS sequences since the linear fit to the accumulated MIF signal before and after cosmic-ray impact depends upon only a small number of reads taken in the middle of the exposure. Therefore, MIF ramps are well-suited for programs with multiple exposures and several dithered pointings, like deep surveys of extragalactic fields.

(The RAPID sequence is not appropriate for background-limited performance.)

Table 7.13: Optimal exposure time for each WFC3/IR filter, along with the NSAMP=15 sequences that provide the closest match. The benefits and disadvantages of each sequence type are discussed in the accompanying text.

Filter	Optimal exposure time (sec)	SPARS	STEP	MIF
F105W	568	SPARS50	STEP50	MIF600
F110W	362	SPARS25	STEP25	MIF600
F125W	552	SPARS50	STEP50	MIF600
F140W	465	SPARS25	STEP50	MIF600
F160W	576	SPARS50	STEP50	MIF600
F098M	879	SPARS50	STEP100	MIF900
F127M	1471	SPARS100	STEP200	MIF1500
F139M	1569	SPARS100	STEP200	MIF1500
F153M	1521	SPARS100	STEP200	MIF1500
F126N	2439	SPARS200	STEP400	MIF1500
F128N	2410	SPARS200	STEP400	MIF1500
F130N	2410	SPARS200	STEP400	MIF1500
F132N	2410	SPARS200	STEP400	MIF1500
F164N	2174	SPARS200	STEP200	MIF1500
F167N	2105	SPARS200	STEP200	MIF1500

CHAPTER 8:

Slitless Spectroscopy with WFC3

In this chapter . . .

8.1 Grism Overview

WFC3 provides a capability for slitless spectroscopy in both of its channels. The UVIS channel has a single grism and the IR channel two grisms, enabling low-resolution slitless spectroscopy over the entire field of view of both detectors.

In the UVIS channel, the G280 grism allows spectroscopy over a useful wavelength range of 200-400 nm, at a dispersion of about 1.4 nm per pixel in the first-order. Above 400 nm the sensitivity is lower, and there can be overlap from second- order light from above 200 nm.

The two grisms for the IR channel cover the wavelength ranges 800-1150 nm (G102), and 1100 nm to the detector sensitivity cutoff at 1700 nm (G141). The dispersions are 2.5 and 4.7 nm per pixel, respectively.

Table 8.1 summarizes the capabilities of the three WFC3 grisms in first-order mode. The resolving power is listed for each grism at a wavelength near the center of its range of coverage. The dispersion differs slightly between the two chips of the UVIS channel, and the mean value is listed. The tilt of the dispersion direction relative to the detector *x*-axis is also listed.

Table 8.1: WFC3 UVIS and IR Grisms.

Grism	Channel	Wavelength range (nm)	Resolving power[1]	Dispersion (nm/pixel)	Tilt (deg)[2]
G280	UVIS	200-400	70 @ 300 nm	1.4	–3
G102	IR	800-1150	210 @ 1000 nm	2.5	+1
G141	IR	1100-1700	130 @ 1400 nm	4.7	0

1. Resolving power is based on FWHM of Gaussian image core in direction perpendicular to dispersion.
2. Tilt of dispersion direction with respect to the positive *x*-axis of the data frame.

8.2 Slitless Spectroscopy with the UVIS G280 Grism

The G280 grism is a WF/PC1 spare. Figure 8.1 shows a spectrum of a continuum lamp taken during ground testing of WFC3. The circled spot shows the location of a direct image of the source obtained with a separate (undispersed) F300X filter exposure, but superposed on the grism image for illustrative purposes only. The prominent star-like feature near the center of the picture is the zeroth-order grism image, and the positive and negative higher orders extend towards the left and right of the zeroth order, respectively. The +1st order is defined to be the order with the higher throughput (due to the grating blaze), even though it falls at lower *x*-pixels than the position of the zeroth order. The +1st order extends to about 1/4 of the size of the image to the left of the zeroth order; further left there is heavy overlap with higher orders.

Figure 8.1: Appearance of the G280 spectral orders on the detector. The circled source is the position of the direct image formed by summing an F300X image with the grism image. The stronger first-order is to the left and the zeroth-order is in the center.

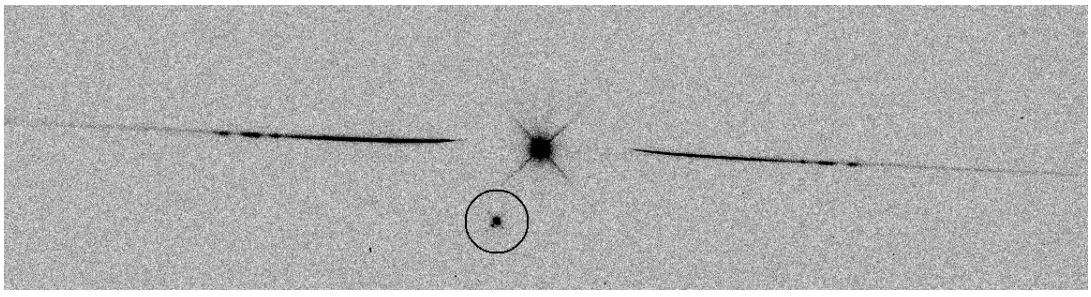

There are several features of this grism which differ, for example, from the G800L grism on ACS. There is an offset of about 170 pixels in the *y*-direction between the direct image and the spectra, the zeroth-order is relatively bright due to a lower grating efficiency, and there is curvature of the spectra at the blue ends of the first orders (nearest the zeroth order). The curvature of the spectra can be fitted well by a

fourth-order polynomial, and the amplitude of the distortion is about four pixels in the detector *y*-direction.

The dispersion has been measured during ground calibration and can be fitted by a fourth-order polynomial with an average dispersion of 1.4 and 1.5 nm/pixel in the +1st and −1st orders, respectively. The dispersion per pixel in the higher orders is higher by the approximate ratio of the orders; for example, in +3rd order it is 0.48 nm per pixel. These values were determined for UVIS Chip 1, and slight differences can be expected for Chip 2.

Figure 8.2 shows the absolute efficiency (including the instrument and CCD detector but not the telescope) for orders −2 through +3 as a function of wavelength. The +1st order is more sensitive than the zeroth-order at wavelengths less than 320 nm, but longward of this wavelength the zeroth-order dominates. On deep exposures, orders out to at least −8 and +8 have been detected. The distortion of the spectral traces and the dispersion solution for at least the first few positive and negative orders will be calibrated to allow determination of absolute wavelengths to better than one pixel. The G280 grism will also be calibrated in sensitivity, allowing the determination of absolute fluxes to better than about 10% accuracy.

Figure 8.2: The absolute throughput of the G280 grism as a function of wavelength for the first few orders.

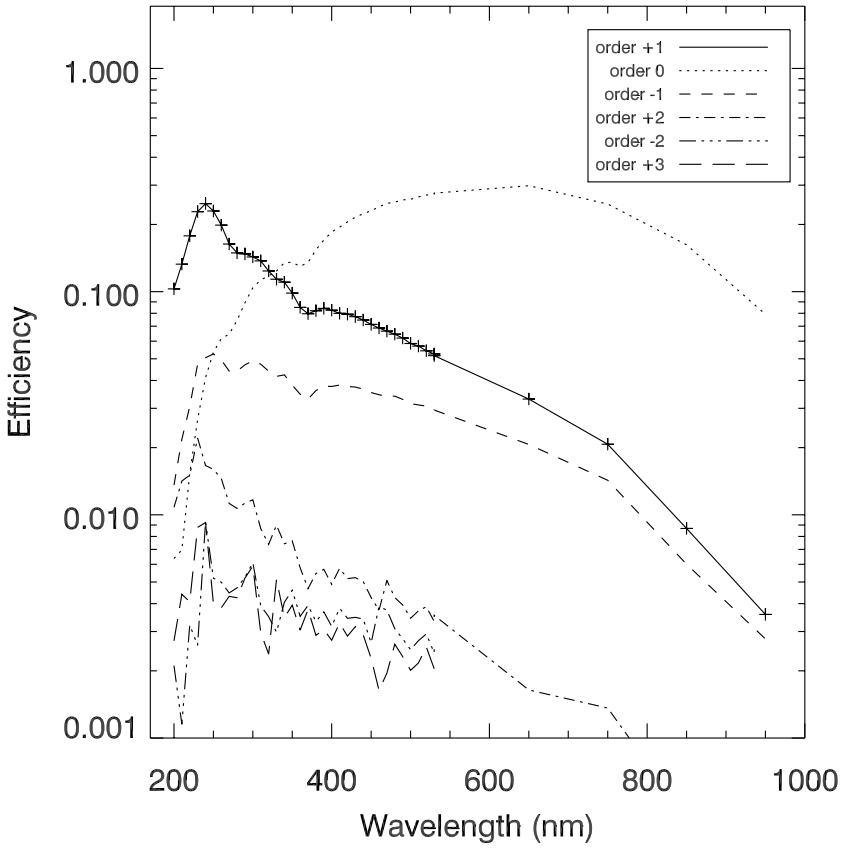

First-order spectra longward of 400 nm are likely to be overlapped by second-order light longward of 200 nm, for sufficiently hot sources.

Operationally, a grism exposure should always be accompanied by a direct image taken at the same guide-star pointing. This direct image allows the zero-point of the wavelength scale, and the size of the dispersed target, to be determined; the latter enables the size of the software extraction slit to be tuned to the object size. For slitless spectra, since the object takes the place of the slit in a conventional spectrograph, the spectral resolution is dependent on the object size, being lower for larger objects. The "natural" choice of a direct-imaging filter to provide the reference image for a grism exposure is F300X, since its response matches most closely the +1st-order grism response. However for fainter objects, or those with an unknown spectrum, the broader F200LP filter may be preferable.

For sufficiently bright objects, the multiple spectral orders may extend across the full field of view of the camera. This will lead to overlapping of fainter spectra in the vicinity of the bright-object spectrum. Therefore, a careful determination of the optimum telescope roll angle is required if one wants to obtain non-overlapped spectra of faint objects in the vicinity of much brighter objects.

8.3 Slitless Spectroscopy with the IR G102 and G141 Grisms

8.3.1 IR G102

The G102 grating provides first-order spectra over the wavelength range from the grism short-wavelength cutoff at about 800 nm up to 1150 nm. The dispersion is high enough that only the positive and negative first-order spectra, as well as the zeroth-order image, are visible on the detector when the target is centered in the field of view.

Figure 8.3 shows the disposition of the zeroth-order image and +1st-order spectrum (which has much higher sensitivity than the -1st order due to the grating blaze) for the G102 grism. The location of the direct image (superposed from an F105W undispersed exposure) is indicated in the figure.

Figure 8.3: G102 grism image with an F105W direct image superposed to illustrate the relative positions. Spectral orders 0, +1, and +2 are seen. Defects in image are on spare detector, not on current flight detector.

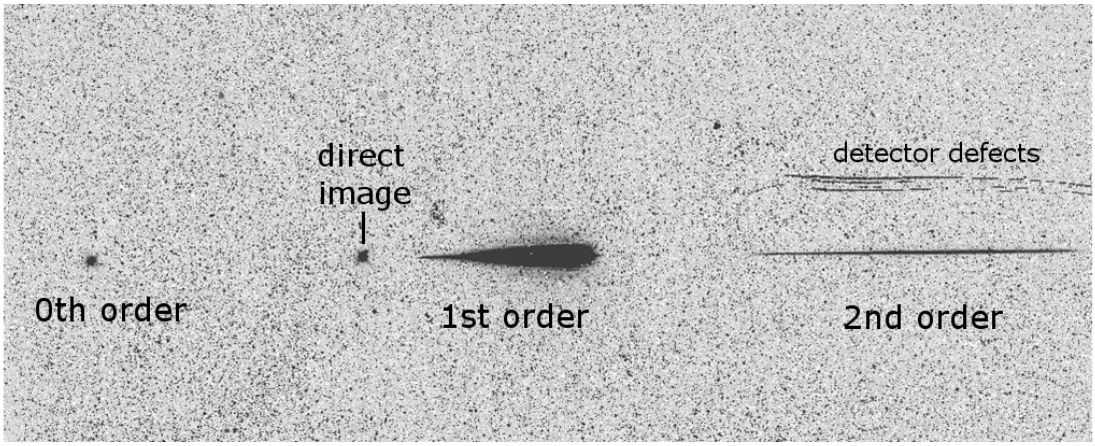

The trace of the first-order spectra is well described by a first-order polynomial. The tilt of the spectrum is 0.6° with respect to the detector *x*-axis.

The sensitivity in the zeroth order is much lower than for the +1, +2 orders. The dispersion in +1st order varies over the field from 2.38 to 2.56 nm/pixel; this variation will be calibrated from ground and on-orbit data to allow absolute wavelength calibration to better than one pixel. The absolute throughput of the G102 orders 0 to +2, including the instrument and the detector, is shown in Figure 8.4.

Suitable filters for the accompanying direct images for source selection and wavelength zero-point determination are F098M or F105W.

Figure 8.4: The absolute throughput of the G102 +1st order as a function of wavelength.

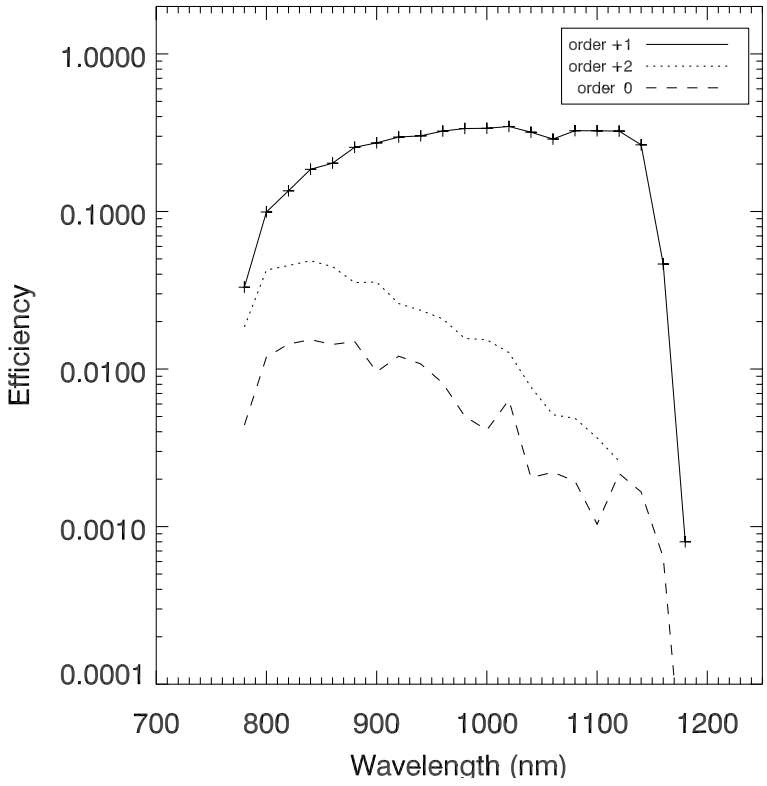

8.3.2 IR G141

For the lower-dispersion G141 grism, the zeroth-, first-, second-, and third-order spectra all lie within the field of view when the target is centered. Figure 8.5 shows the appearance of the spectra on the detector, with the superposed direct image, for the G141 grism. The measured spectral range is from 980 nm to the detector's long-wavelength cutoff at about 1700 nm. Over most of the spectral range, more than 80% of the throughput is in the +1st-order spectrum. The dispersion in +1st-order varies over the field from 4.55 to 4.80 nm/pixel; this variation will be calibrated from ground and on-orbit data to allow absolute wavelength calibration to better than one pixel. The absolute throughput of the G141 orders 0 to +3, including the instrument and the detector, is shown in Figure 8.6.

Figure 8.5: G141 grism image superposed with an undispersed F139M image. Zeroth-order is on the far left and the +3rd-order can be seen on the far right. Defects in image are on spare detector, not on current flight detector.

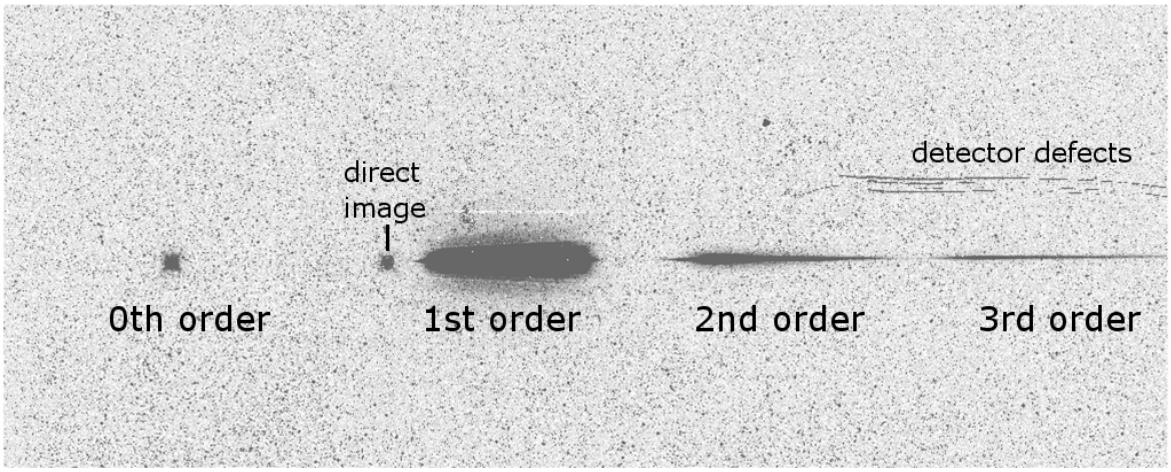

Figure 8.6: The absolute throughput of the G141 +1st order as a function of wavelength.

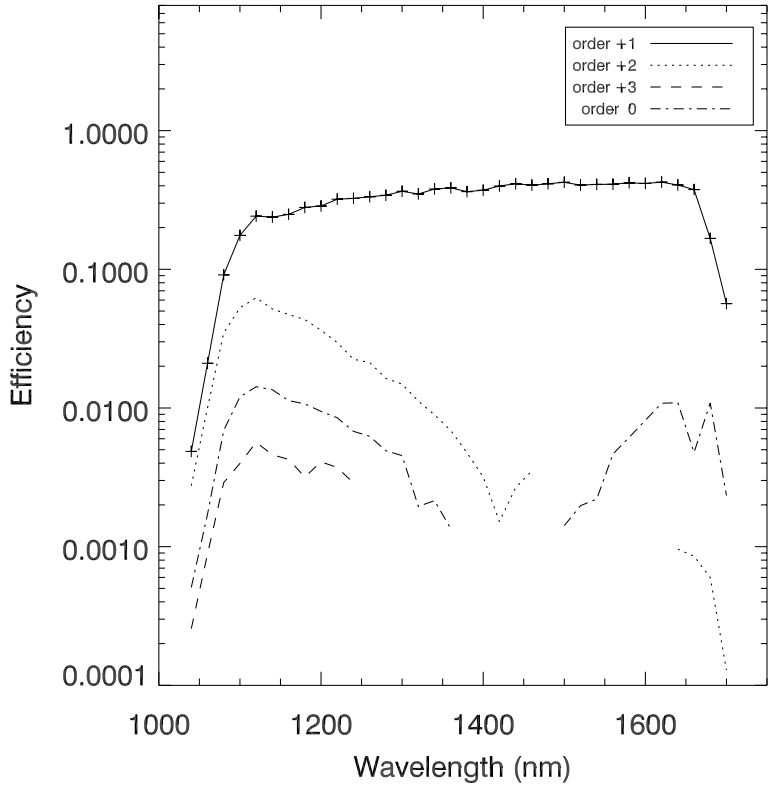

The usual filter recommended for the accompanying direct image is F140W, although F160W could be used for extremely red sources.

8.4 Sensitivities and Exposure-Time Estimation

Table 8.2 lists current estimates of the detection limits for slitless spectroscopy with the UVIS and IR modes. The numbers in the table are the *V* magnitudes of sources for which a 1-hour exposure will yield a spectrum with a S/N of 5 with extraction boxes of 1×5 and 1×3 pixels for the UVIS and IR, respectively. *V* magnitudes are given for three different assumed source spectral types.

Table 8.2: *V*-band detection limits for the WFC3 grism modes for 1-hour exposure and 5σ detection.

Mode	Spectral Type			Wavelength (nm)
	O2 V	A0 V (Vega)	G2 V	
UVIS/G280	23.6	20.7	17.4	250
IR/G102	20.6	21.3	22.2	1050
IR/G141	19.8	20.6	22.0	1550

For more accurate estimations of exposure times, observers should use the WFC3 Exposure Time Calculator (ETC). The ETC supports all three spectroscopic modes.

For more detailed simulations of WFC3 slitless data, a simulator will also be available which can generate 2D images (dispersed as well as direct) of synthetic target fields. The simulator package will be available via a Web interface (reduced functionality) and as a stand-alone IRAF package (full functionality). For further information, consult http://www.stecf.org/.

8.5 Extraction and Calibration of Spectra

Since there is no slit in the WFC3 grism mode, the PSF of the target determines the spectral resolution. In the case of non-stellar sources, it is the extension of the target in the direction of dispersion that limits the spectral resolution. Based on the extent of the direct image, the size of the software extraction slit can be set.

The dispersion of the grisms will be well characterized, but in order to set the wavelength zero-point, it is necessary to know the position of the target in the direct image. The zeroth-order will generally be too weak in a dispersed image to allow the wavelength zero-point to be set reliably. Given the typical spacecraft jitter, wavelength zero-points to +/−1 pixel should be routinely achievable using a direct image taken just before or after the grism image.

An extraction software package, called **aXe**, is available to extract, flat-field, wavelength- and flux-calibrate WFC3 grism spectra. Full details can be found at: http://www.stecf.org/instruments/ACSgrism/axe/. The package is also available in STSDAS.

CHAPTER 9:

WFC3 Exposure-Time Calculation

In this chapter . . .

9.1 Overview

Chapter 4 of this *Handbook* describes the procedures for designing a Phase I WFC3 observing proposal. Two of the steps involved in this process are estimating the exposure times needed to achieve your scientific goals, and then combining these individual exposures with their associated overheads to derive the number of spacecraft orbits that you will request in your Phase I proposal.

This chapter gives guidance on estimating exposure times. The following chapter, Chapter 10, then describes how to include the various overheads so as to determine the total number of spacecraft orbits needed for your program.

You should also refer to the *Call for Proposals*, which includes information on policies and practices with respect to orbit-time requests. The *HST Primer* provides specific advice on orbit determination. Below, we provide a summary of the WFC3 sensitivities and give several examples that illustrate how to calculate your exposure times for Phase I Proposals.

9.2 The WFC3 Exposure Time Calculator (ETC)

In most cases, you will find it convenient to use the online WFC3 Exposure Time Calculator (ETC) to make estimates of the required exposure times for your project. The ETC is available from the WFC3 Web site at:

`http://www.stsci.edu/hst/wfc3/tools/etc/`

The ETC calculates count rates for given source and background parameters. Once these are entered, the ETC then outputs signal-to-noise (S/N) ratios achieved for a given exposure time, or the exposure times required to achieve a given S/N ratio. The ETC supports both direct-imaging and spectroscopic (grism) observations. A variety of extraction apertures may be assumed, both circular and square, allowing the user to select either a radius in arcseconds or a size in pixels. It is also possible to input a calibrated spectral-energy distribution (SED) of your source directly into the ETC. The ETC also outputs peak per-pixel count rates and total count rates, to aid in feasibility assessment. Warnings will appear if the source will saturate the detector, which would not only compromise CCD and IR observations, but might even affect subsequent exposures with the IR channel (see Appendix D for further information). The ETC has extensive online help for its execution and interpretation of results.

It is also possible to use ***synphot*** in STSDAS to calculate count rates and the wavelength distribution of detected counts.

The remaining sections of this chapter give detailed information on the sensitivities of the UVIS and IR channels when combined with the various spectral elements, and the use of this information in the determination of count rates, for those who wish to understand the subject in depth.

9.3 Sensitivity Data

In this section, formulae appropriate for WFC3's imaging and spectroscopic modes are provided, from which one can calculate the expected count rates and the S/N ratio achieved in a given exposure time, based on the spectral energy distribution of a source. The formulae are given in terms of sensitivities, but we also provide transformation equations between throughput (QT) and sensitivity (S) for imaging and spectroscopic modes.

Throughputs are presented in graphical form as a function of wavelength for each of the imaging filters and grisms in Appendix A. Given the source characteristics and the sensitivity of the WFC3 configuration, calculating the expected count rate over a given number of pixels is straightforward. The additional information required is the encircled energy fraction (ε_f) in the peak pixel, the plate scale, and (for the spectroscopic modes) the dispersions of the grisms.

The sensitivity information is summarized in Tables 9.1 and 9.2. In these two tables, and in the following discussion, the filter transmission functions are denoted $T(\lambda)$, and the overall system response function (apart from the filter transmission) is denoted $Q(\lambda)$. The terms "counts" and "count rates" always refer to the number of detected *electrons* (which is converted to data numbers, or DNs, according to the gain

factors for the detectors; the gain is always 1.5 e^-/DN for the UVIS channel and 2.5 e^-/DN for the IR channel).

In Tables 9.1 and 9.2, the following quantities are listed:

1. The filter or grism designation.
2. The "pivot wavelength" for that filter or grism, λp. Pivot wavelength is a source-independent measure of the characteristic wavelength of a bandpass, defined such that it is the same if the input spectrum is given in units of F_λ or F_ν (see A. Tokunaga & W. Vacca 2006, PASP, 117, 421):

$$\lambda_p = \sqrt{\frac{\int Q(\lambda)T(\lambda)\lambda d\lambda}{\int Q(\lambda)T(\lambda)d\lambda/\lambda}}$$

3. The integral $\int Q_\lambda T_\lambda \, d\lambda/\lambda$, used to determine the count rate when given the astronomical magnitude of the source.
4. The ABmag zero-point, defined as the AB magnitude of a source with a flat F_ν that yields 1 count s^{-1} with the specified configuration.
5. The sensitivity integral, $\int S_\lambda \, d\lambda$, defined (see Section 9.4) as the count rate that would be detected from a flat F_λ source with a flux of 1 erg cm^{-2} s^{-1} $Å^{-1}$.
6. The encircled energy, defined as the fraction of PSF flux enclosed in the default photometry aperture (5×5 pixels for the UVIS and 3×3 pixels for the IR).
7. The fraction of the total PSF flux in the central pixel for a centered stellar source, useful for determining the peak count rate to check for saturation (see also Appendix D).
8. The sky background count rate (electrons s^{-1}), which is the count rate that would be measured with average zodiacal background and average earth-shine. For the IR channel, this quantity also includes the thermal background from *HST* and the instrument. It does not include the contribution from the detectors themselves (i.e., dark current and read noise).

The next two sections describe how to calculate two quantities:

- The count rate in counts s^{-1}, C, from your source over some selected area on the detector containing $N_{\rm pix}$ pixels.
- The peak count rate in counts s^{-1} pixel $^{-1}$, P_{cr}, from your source, which is useful for avoiding saturated exposures.

We consider the cases of point sources and diffuse sources separately in each of the following imaging and spectroscopy sections.

Table 9.1: Sensitivity Data for WFC3/UVIS Channel.

Spectral Element	Pivot λ (Å)	$\int Q_\lambda T_\lambda d\lambda/\lambda$	ABMAG zero-point	$\int S_\lambda d\lambda$	Encircled energy	Energy in central pixel	Background (sky) rate
F200LP	5159.3	0.2978	27.17	1.81E+19	0.76	0.18	0.0976
F218W	2239.3	0.0037	22.41	4.22E+16	0.72	0.14	0.0001
F225W	2383.4	0.0111	23.60	1.43E+17	0.73	0.14	0.0007
F275W	2716.7	0.0132	23.79	2.22E+17	0.75	0.15	0.0005
F280N	2844.1	0.0007	20.62	1.31E+16	0.76	0.16	0.0000
F300X	2848.1	0.0279	24.60	5.15E+17	0.76	0.16	0.0019
F336W	3357.4	0.0243	24.45	6.24E+17	0.78	0.17	0.0015
F343N	3435.1	0.0123	23.71	3.31E+17	0.78	0.17	0.0009
F350LP	5915.5	0.2203	26.84	1.76E+19	0.77	0.19	0.0990
F373N	3729.8	0.0021	21.80	6.69E+16	0.78	0.18	0.0002
F390M	3896.3	0.0102	23.51	3.53E+17	0.79	0.18	0.0015
F390W	3927.7	0.0498	25.23	1.75E+18	0.79	0.18	0.0087
F395N	3954.1	0.0042	22.54	1.50E+17	0.79	0.19	0.0007
F410M	4107.8	0.0100	23.48	3.84E+17	0.79	0.19	0.0025
F438W	4324.7	0.0307	24.70	1.31E+18	0.79	0.19	0.0088
F467M	4681.3	0.0108	23.57	5.40E+17	0.79	0.19	0.0040
F469N	4687.4	0.0019	21.68	9.48E+16	0.79	0.19	0.0007
F475W	4777.1	0.0683	25.57	3.55E+18	0.79	0.19	0.0249
F475X	4953.9	0.1061	26.05	5.93E+18	0.79	0.19	0.0404
F487N	4870.6	0.0028	22.09	1.49E+17	0.79	0.20	0.0010
F502N	5008.9	0.0030	22.18	1.72E+17	0.79	0.20	0.0012
F547M	5449.9	0.0290	24.64	1.96E+18	0.79	0.20	0.0138
F555W	5317.4	0.0761	25.69	4.90E+18	0.79	0.20	0.0345
F600LP	7506.6	0.0826	25.78	1.06E+19	0.73	0.17	0.0534
F606W	5879.7	0.0992	25.98	7.81E+18	0.78	0.19	0.0518
F621M	6209.8	0.0258	24.52	2.27E+18	0.77	0.19	0.0150
F625W	6224.2	0.0597	25.42	5.26E+18	0.77	0.19	0.0342
F631N	6303.1	0.0021	21.79	1.89E+17	0.77	0.19	0.0012
F645N	6451.7	0.0028	22.11	2.68E+17	0.77	0.19	0.0017
F656N	6561.0	0.0006	20.37	5.58E+16	0.76	0.19	0.0003

Spectral Element	Pivot λ (Å)	$\int Q_\lambda T_\lambda d\lambda/\lambda$	ABMAG zero-point	$\int S_\lambda d\lambda$	Encircled energy	Energy in central pixel	Background (sky) rate
F657N	6564.9	0.0041	22.53	4.06E+17	0.76	0.19	0.0025
F658N	6583.9	0.0009	20.93	9.37E+16	0.76	0.19	0.0006
F665N	6654.1	0.0044	22.59	4.42E+17	0.76	0.19	0.0027
F673N	6764.1	0.0038	22.44	3.96E+17	0.76	0.19	0.0024
F680N	6876.2	0.0120	23.68	1.29E+18	0.75	0.19	0.0076
F689M	6876.5	0.0219	24.34	2.36E+18	0.75	0.19	0.0137
F763M	7612.3	0.0177	24.11	2.33E+18	0.73	0.17	0.0118
F775W	7659.7	0.0283	24.62	3.79E+18	0.72	0.17	0.0189
F814W	8069.8	0.0419	25.04	6.22E+18	0.71	0.16	0.0284
F845M	8443.3	0.0131	23.78	2.13E+18	0.69	0.16	0.0091
F850LP	9164.2	0.0130	23.77	2.49E+18	0.67	0.14	0.0091
F953N	9530.6	0.0006	20.51	1.33E+17	0.65	0.14	0.0005
FQ232N	2464.7	0.0003	19.69	4.19E+15	0.73	0.14	0.0000
FQ243N	2495.8	0.0004	20.07	6.08E+15	0.74	0.14	0.0000
FQ378N	3791.4	0.0046	22.64	1.51E+17	0.79	0.18	0.0006
FQ387N	3873.2	0.0014	21.32	4.63E+16	0.79	0.18	0.0002
FQ422M	4218.0	0.0044	22.60	1.79E+17	0.79	0.19	0.0011
FQ436N	4366.5	0.0017	21.54	7.24E+16	0.79	0.19	0.0005
FQ437N	4370.4	0.0012	21.19	5.24E+16	0.79	0.19	0.0003
FQ492N	4932.1	0.0052	22.77	2.86E+17	0.79	0.20	0.0021
FQ508N	5089.8	0.0059	22.91	3.48E+17	0.79	0.20	0.0025
FQ575N	5756.7	0.0007	20.59	5.24E+16	0.78	0.20	0.0004
FQ619N	6197.5	0.0023	21.91	2.04E+17	0.77	0.19	0.0014
FQ634N	6347.4	0.0023	21.90	2.12E+17	0.77	0.19	0.0014
FQ672N	6715.4	0.0006	20.46	6.35E+16	0.76	0.19	0.0004
FQ674N	6729.7	0.0004	20.07	4.43E+16	0.76	0.19	0.0003
FQ727N	7274.1	0.0016	21.52	1.98E+17	0.74	0.18	0.0011
FQ750N	7500.5	0.0016	21.46	1.99E+17	0.73	0.17	0.0010
FQ889N	8889.6	0.0011	21.06	1.92E+17	0.67	0.15	0.0007
FQ906N	9055.4	0.0010	20.93	1.78E+17	0.67	0.15	0.0007
FQ924N	9245.3	0.0008	20.72	1.52E+17	0.66	0.14	0.0005
FQ937N	9370.5	0.0007	20.59	1.39E+17	0.66	0.14	0.0005
G280	5215.3	0.2679	25.59	2.45E+18	0.81	0.26	0.0892

Table 9.2: Sensitivity Data for WFC3/IR Channel.

Spectral Element	Pivot λ (Å)	$\int Q_\lambda T_\lambda d\lambda/\lambda$	ABMAG zero-point	$\int S_\lambda d\lambda$	Encircled energy	Energy in central pixel	Background (sky + thermal) rate
F098M	9860.2	0.0613	25.45	1.36E+19	0.79	0.36	0.5062
F105W	10531.3	0.1039	26.03	2.62E+19	0.78	0.35	0.8234
F110W	11477.0	0.1684	26.55	5.05E+19	0.76	0.34	1.3060
F125W	12462.9	0.0961	25.94	3.40E+19	0.74	0.32	0.7683
F126N	12579.8	0.0045	22.62	1.62E+18	0.74	0.32	0.0844
F127M	12735.3	0.0218	24.33	8.06E+18	0.73	0.32	0.2140
F128N	12826.6	0.0048	22.69	1.81E+18	0.73	0.31	0.0862
F130N	13001.1	0.0048	22.69	1.85E+18	0.73	0.31	0.0866
F132N	13182.6	0.0046	22.65	1.83E+18	0.72	0.31	0.0852
F139M	13833.9	0.0187	24.17	8.17E+18	0.71	0.30	0.1906
F140W	13912.4	0.1147	26.14	5.06E+19	0.71	0.30	0.8720
F153M	15318.1	0.0182	24.13	9.72E+18	0.67	0.28	0.1899
F160W	15368.0	0.0714	25.62	3.84E+19	0.67	0.28	0.6154
F164N	16395.1	0.0044	22.58	2.66E+18	0.65	0.26	0.0936
F167N	16635.7	0.0043	22.56	2.70E+18	0.64	0.26	0.0987
G102	9972.5	0.0891	25.86	2.02E+19	0.79	0.42	0.9736
G141	13830.3	0.1342	26.31	5.85E+19	0.73	0.34	1.4254

9.4 Count Rates (Imaging)

9.4.1 Point Source

For a point source, the count rate, *C*, can be expressed as the following integral over the bandpass of the filter:

$$C = A\int F_\lambda \frac{\lambda}{hc} Q_\lambda T_\lambda \varepsilon_f d\lambda = \int F_\lambda S_\lambda \varepsilon_f d\lambda$$

where:

- *A* is the area of an unobstructed 2.4-m telescope (i.e., 45,239 cm^2)

- F_λ is the flux from the astronomical source in erg cm^{-2} s^{-1} $Å^{-1}$.
- The factor λ/hc (where h is Planck's constant and c is the speed of light) converts ergs to photons.
- $Q_\lambda T_\lambda$ is the system fractional throughput, i.e., the probability of detecting a count per incident photon, including losses due to obstructions of the full 2.4-m OTA aperture. It is specified this way to separate out the instrument sensitivity Q_λ and the filter transmission T_λ.
- ε_f is the fraction of the point-source energy encircled within N_{pix} pixels.
- S_λ is the total imaging point-source sensitivity in units of counts s^{-1} $Å^{-1}$ per incident erg cm^{-2} s^{-1} $Å^{-1}$.

The peak counts s^{-1} $pixel^{-1}$ from the point source, C_{peak}, is given by the following integral over the bandpass:

$$C_{peak} = \int F_\lambda S_\lambda \varepsilon_f(1) d\lambda$$

where:

- F_λ, and S_λ are as above.
- $\varepsilon_f(1)$ is the fraction of energy contained within the peak pixel.

If the flux from the source can be approximated by a flat continuum (F_λ = constant) and ε_f is roughly constant over the bandpass, then:

$$C = F_\lambda \varepsilon_f \int S_\lambda d\lambda$$

We can now define an equivalent bandpass of the filter, B_λ, such that:

$$\int S_\lambda d\lambda = S_{peak} B_\lambda$$

where:

- S_{peak} is the peak sensitivity.
- B_λ is the effective bandpass of the filter.

The count rate from the source can now be written as:

$$C = F_\lambda \varepsilon_f S_{peak} B_\lambda$$

In Tables 9.1 and 9.2 above, we give the value of $\int S_\lambda d\lambda$ for each of the filters. Alternatively, we can write the count-rate equation in terms of V magnitudes:

$$C = 2.5 \times 10^{11} \varepsilon_f (\int QT d\lambda/\lambda) \times 10^{-0.4(V + AB_v)}$$

where V is the visual magnitude of the source, the quantity under the integral is the mean sensitivity of the detector+filter combination (also tabulated in Tables 9.1 and 9.2), and AB_v is the filter-dependent correction for the deviation of the source

spectrum from a constant F_ν spectrum. This latter quantity is tabulated for some representative astronomical spectra in Appendix A.

9.4.2 Diffuse Sources

For a diffuse source, the count rate, C, which is now per pixel, due to the astronomical source can be expressed as:

$$C = \int I_\lambda S_\lambda m_x m_y d\lambda$$

where:

- I_λ is the surface brightness of the astronomical source, in erg cm^{-2} s^{-1} Å^{-1} arcsec^{-2}.
- S_λ is as above.
- m_x and m_y are the plate scales in arcsec pixel^{-1} along orthogonal axes.

9.4.3 Emission-Line Sources

For a source where the flux is dominated by a single emission line, the count rate can be calculated from the equation

$$C = 2.28 \times 10^{12} \cdot (QT)_\lambda \cdot F(\lambda) \cdot \lambda$$

where C is the observed count rate in counts s^{-1}, (QT) is the system throughput at the wavelength of the emission line, $F(\lambda)$ is the emission-line flux in units of erg cm^{-2} s^{-1}, and λ is the wavelength of the emission line in angstroms. $(QT)_\lambda$ can be determined by inspection of the plots in Appendix A. See Section 9.9 for an example of count-rate estimation for an emission-line source.

9.5 Count Rates (Slitless Spectroscopy)

We now turn to estimation of count rates for slitless spectroscopy using the WFC3 grisms. In this case we are dealing with a dispersed image of the source.

For a point source with a continuous spectrum, the count rate, C, is calculated per pixel in the dispersion direction, and is integrated over a fixed extraction height N_{spix} in the spatial direction perpendicular to the dispersion. The count rate is:

$$C = F_\lambda S'_\lambda \varepsilon'_{Nspix} = F_\lambda A \frac{\lambda}{hc} Q_\lambda T_\lambda \varepsilon'_{Nspix} d$$

where:

- S_λ is the total point source sensitivity in units of counts s^{-1} per incident erg cm^{-2} s^{-1} $Å^{-1}$; and $S'_\lambda = S_\lambda \cdot d$.
- d is the spectral dispersion in Å $pixel^{-1}$.
- ε'_{Nspix} is the fraction of the point-source energy within N_{spix} in the spatial direction.
- the other quantities are as defined in the previous section.

For a source with an unresolved emission line with a flux of F in units of erg cm^{-2} s^{-1}, the total count rate recorded over the N_{spix} extraction height is:

$$C = FS_\lambda \varepsilon'_{Nspix}$$

These counts will be distributed over pixels in the dispersion direction according to the instrumental line-spread function.

In contrast to the case of imaging sensitivity S_λ, the spectroscopic point source sensitivity calibration ($S'_\lambda \times \varepsilon'_{Nspix}$) for a default extraction height of N_{spix} will be measured directly from observations of stellar flux standards after installation of WFC3 into *HST*. Therefore, the accuracy in laboratory determinations of T_λ for the WFC3 grisms will not be crucial to the final accuracy of their sensitivity calibrations, but at the current time the throughputs for these grisms are still somewhat uncertain.

The peak counts s^{-1} $pixel^{-1}$ from the point source is given by:

$$P_{cr} = \varepsilon'_f(1) F_\lambda S'_\lambda$$

where:

- $\varepsilon'_f(1)$ is the fraction of energy contained within the peak pixel.
- the other quantities are as above.

9.6 Estimating Exposure Times

9.6.1 S/N Reached in a Given Exposure Time

To derive the exposure time to achieve a given S/N ratio, or to derive the S/N ratio achieved in a given exposure time, there are four principal ingredients:

- Expected count rate C from your source over some area.
- The area (in pixels) over which those counts are received (N_{pix}).
- Sky background (B_{sky}) in counts s^{-1} $pixel^{-1}$.

- The detector background, or dark, (B_{det}) in counts s^{-1} $pixel^{-1}$ and the read-noise (R) in counts. (Section 9.7 provides information for determining the sky-plus-detector background.)

The S/N ratio achieved in exposure time t seconds, is given by:

$$S/N = \frac{Ct}{\sqrt{Ct + N_{pix}(B_{sky} + B_{det})t + \frac{N_{pix}}{N_{bin}} N_{read} R^2}}$$

where:

- C = the signal from the astronomical source in counts s^{-1}. (Note that the actual output image uses DN, which will be equal to Ct/G, where G is the gain.)
- N_{pix} = the total number of detector pixels integrated over to achieve C.
- N_{bin} = the number of detector pixels binned to one read-out pixel when on-chip binning is used.
- B_{sky} = the sky background in counts s^{-1} $pixel^{-1}$.
- B_{det} = the detector dark current in counts s^{-1} $pixel^{-1}$.
- R = the read noise in electrons; 3 e^- for the UVIS channel and 14 e^- for the IR channel (this is the effective read noise achieved by fitting the ramp of IR readouts, if close to the full sequence of 16 readouts is used).
- N_{read} = the number of detector readouts.

The above equation assumes the optimistic (but often realistic) condition that the background zero-point level under the object that is subtracted could be well known (from integrating over many pixels) but is still noisy in N_{pix} and does not significantly contribute to the error budget; in crowded fields this may not be true.In general, C in the numerator should be the signal in N_{pix} from the component to be measured (e.g., the point source in an image or the line emission in a spectrum), while C in the denominator is the total astronomical signal in N_{pix} (e.g., including light from the underlying galaxy in the image or from the continuum in the spectrum).

9.6.2 Exposure Time to Reach a Given S/N

Observers normally take sufficiently long integrations that the read noise is not important. This condition is met when:

$$Ct + N_{pix}(B_{sky} + B_{det})t > 2\frac{N_{pix}}{N_{bin}} N_{read} R^2$$

In the regime where read noise is unimportant, and virtually all of the astronomical signal in N_{pix} comes from the component being measured, the integration time to reach a given signal-to-noise ratio Σ is:

$$t = \frac{\Sigma^2[C + N_{pix}(B_{sky} + B_{det})]}{C^2}$$

If the source count rate is much higher than that of the sky plus detector backgrounds, then this expression reduces further to:

$$t = \frac{\Sigma^2}{C}$$

i.e., the usual result for Poisson statistics of $\Sigma = \sqrt{totalcounts}$.

More generally, the required integration time to reach a given S/N ratio is:

$$t = \frac{\Sigma^2[C + N_{pix}(B_{sky} + B_{det})] + \sqrt{\Sigma^4[C + N_{pix}(B_{sky} + B_{det})]^2 + 4\Sigma^2C^2\left[\frac{N_{pix}}{N_{bin}}N_{read}R^2\right]}}{2C^2}$$

9.6.3 Exposure Time Estimates for Red Targets in F850LP

At long wavelengths, ACS CCD observations are affected by a red halo due to light scattered off the CCD substrate. An increasing fraction of the light as a function of wavelength is scattered from the center of the PSF into the wings. This problem affects particularly the very broad z-band F850LP filter, for which the encircled energy depends on the underlying spectral energy distribution the most. At the current time, it is thought that this problem has been fixed for WFC3, and so this should not be a concern for those planning WFC3 observations.

9.7 Sky Background

As noted in the previous section, the backgrounds from the sky and from the detector must be taken into account when calculating expected S/N ratios or exposure times.

Detector backgrounds (as well as read-out noise) for the CCDs and IR detector are discussed in Chapter 5. This section deals with the sky backgrounds that can affect WFC3 observations.

The most important sources of sky background are:

- Earthshine (ES).
- Zodiacal light (ZL).

- Geocoronal emission (GC).

The background in counts s^{-1} $pixel^{-1}$ for imaging observations can be computed as:

$$B_{sky} = \int I_\lambda S_\lambda m_x m_y d\lambda$$

where:

- I_λ is the surface brightness of the sky background, in erg cm^{-2} s^{-1} $Å^{-1}$ $arcsec^{-2}$.
- S_λ is the point-source sensitivity for the imaging mode.
- m_x and m_y are the plate scales in arcsec $pixel^{-1}$ along orthogonal axes.

In the case of slitless spectroscopy, the image of the sky through a disperser is not uniform, because some wavelengths fall off the detector for regions of sky near the edge of the field of view. The regions of lower sky background will be strips at the long- and short-wavelength edges of the field of view; a UVIS grism spectrum is roughly 270 pixels long, while an IR grism spectrum is roughly 170 pixels long. The maximum width of the strips from where the signal starts to decline to the edge, where the signal is down by roughly a factor of 2, will be about half the total length of a spectrum of a point source, i.e., roughly 135 pixels (UVIS) or 85 pixels (IR), in the case of a sky background with a continuum of wavelengths. These small strips of lower sky background are ignored in the following formulae. Furthermore, since the spectra do not lie along the direction of the anamorphic distortion, the plate scales of m_x and m_y above must be replaced by the plate scales m_s and m_λ in the orthogonal spatial and dispersion directions, respectively. Interior to the strips, a point on the detector sees a region of sky over the full wavelength coverage of the disperser. Thus, for **spectroscopic observations**:

$$B^{\lambda}_{sky} = \int I_\lambda S'_\lambda m_s m_\lambda d\lambda$$

For a **monochromatic** sky emission line at $\lambda = L$ like [O II] 2471, which will dominate the background through the UVIS/G280 grism:

$$B^{L}_{sky} = I_L S'_\lambda m_s m_\lambda / d$$

where

- I_L is the monochromatic intensity of a line at wavelength L in erg cm^{-2} s^{-1} $arcsec^{-2}$.

The total sky background is:

$$B_{sky} = B^{\lambda}_{sky} + B^{L}_{sky}$$

Figure 9.1 and Table 9.3 show "high" sky background intensity as a function of wavelength, identifying the separate components which contribute to the background.

The "shadow" and "average" values of the earth-shine contribution in the WFC3 Exposure Time Calculator (ETC) correspond, respectively, to 0% and 50% of the "high" values in Figure 9.1 and Table 9.3. For the zodiacal sky background, the values in Figure 9.1 and Table 9.3 correspond to the high value of *V*-band surface brightness of 22.1 mag arcsec^{-2} from Table 9.4, while the "low" and "average" zodiacal light is scaled to *V* surface brightnesses of 23.3 and 22.7 mag arcsec^{-2}, respectively.

In Table 9.3 we present the "high" sky-background numbers, which are plotted in Figure 9.1. See the text and the caption of Figure 9.1 for more details. These high sky values are defined as the earth-shine at 38° from the limb and the high zodiacal light of $V = 22.1$ mag arcsec^{-2}.

Table 9.3: High sky backgrounds.

Wavelength (Å)	Earth-shine	Zodiacal light	Total background
		(erg cm^{-2} s^{-1} Å^{-1} arcsec^{-2})	
2000	7.69E-22	7.94E-20	8.02E-20
2500	1.53E-21	3.83E-19	3.84E-19
3000	1.43E-19	1.63E-18	1.77E-18
3500	8.33E-19	2.72E-18	3.55E-18
4000	1.66E-18	3.12E-18	4.78E-18
4500	2.59E-18	4.97E-18	7.57E-18
5000	2.63E-18	5.07E-18	7.70E-18
5500	2.55E-18	5.17E-18	7.72E-18
6000	2.42E-18	5.14E-18	7.56E-18
7000	1.95E-18	4.48E-18	6.42E-18
8000	1.56E-18	3.82E-18	5.38E-18
9000	1.23E-18	3.18E-18	4.40E-18
10000	9.97E-19	2.70E-18	3.70E-18
11000	8.02E-19	2.26E-18	3.06E-18
12000	6.65E-19	1.94E-18	2.61E-18
13000	5.58E-19	1.68E-18	2.24E-18
14000	4.70E-19	1.46E-18	1.93E-18
15000	3.97E-19	1.26E-18	1.66E-18
16000	3.35E-19	1.09E-18	1.43E-18
17000	2.79E-19	9.27E-19	1.21E-18

Figure 9.1: Sky background intensity as a function of wavelength.The total sky spectrum (black) for the "high-background" case adopted in the WFC3 ETC, along with the individual contributions from zodiacal light and earth-shine. These data correspond to a *V*-band surface brightness of 22.1 mag arcsec^{-2}. The only significant geocoronal emission line in the WFC3 spectral range is [O II] 2471 Å, shown as a line; it has a flux of 1.5×10^{-15} erg cm^{-2} s^{-1} arcsec^{-2}, extending beyond the upper limit of the plot.

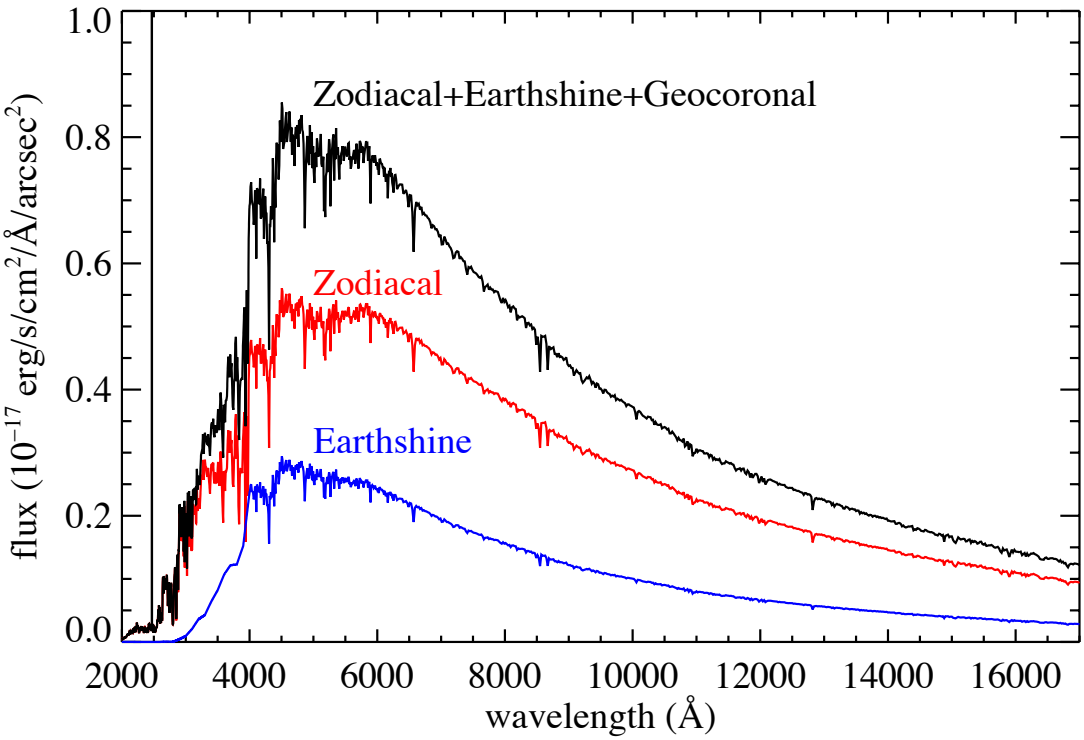

9.7.1 Background Variations and LOW-SKY

In the ultraviolet, the background contains a bright airglow line at 2471 Å, which varies in intensity from day to night and as a function of *HST* orbital position. The airglow line may be the dominant sky contribution in the UV both for imaging and spectroscopic observations. Away from the airglow line, at wavelengths shortward of ~3000 Å, the background is dominated by zodiacal light, where the small area of sky that corresponds to a pixel of the high-resolution *HST* instrumentation usually produces a signal that is much lower than the intrinsic detector background. The contribution of zodiacal light does not vary dramatically with time, but does vary by about a factor of about three throughout most of the sky as a function of distance from the Sun and ecliptic. Table 9.4 gives the variation of the zodiacal background as a function of ecliptic latitude and longitude relative to the Sun. For a target near ecliptic coordinates (50,0) or (–50,0), the zodiacal light is relatively bright at 20.9 mag arcsec^{-2}, i.e., about 9 times the faintest value of 23.3 mag arcsec^{-2}. Thus if you are considering deep imaging applications, you must carefully consider expected sky values.

On the other hand, earth-shine varies strongly depending on the angle between the target and the bright Earth limb. The variation of the earth-shine as a function of limb angle from the sunlit Earth is shown in Figure 9.2. The figure also shows the contribution of the moon, which is typically much smaller than the zodiacal contribution, for which the upper and lower limits are shown. For reference, the limb angle is approximately 24° when the *HST* is aligned toward its orbit pole (i.e., the center of the CVZ). The earth-shine contribution shown in Figure 9.1 and Table 9.3 corresponds to this position.

Figure 9.2: Background contributions in V magnitude per arcsec^2 due to the zodiacal light, Moon, and sunlit Earth, as a function of angle between the target and the limb of the Earth or Moon. The two zodiacal light lines show the extremes of possible values.

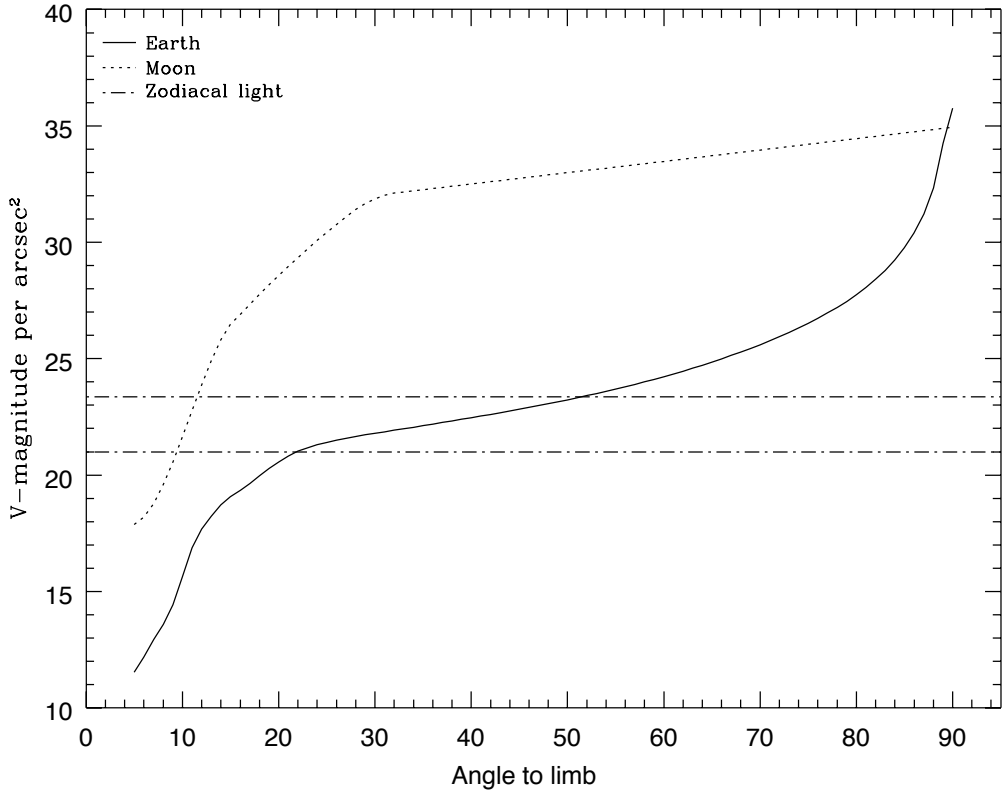

For observations taken longward of 3500 Å, earth-shine dominates the background at small (< 22°) limb angles. In fact, the background increases exponentially for limb angles < 22°. The background near the bright limb can also vary by a factor of ~2 on timescales as short as two minutes, which suggests that the background from earth-shine also depends upon the reflectivity of the terrain over which *HST* passes during the course of an exposure.

Table 9.4: Approximate zodiacal sky background as a function of ecliptic latitude and ecliptic longitude (in *V*-mag per arcsec^2). SA stands for Solar Avoidance zone, in which HST observations may not be made.

Ecliptic longitude (degrees)	Ecliptic latitude (degrees)						
	0	15	30	45	60	75	90
0	SA	SA	SA	SA	22.6	23.0	23.3
15	SA	SA	SA	SA	22.6	23.1	23.3
30	SA	SA	SA	22.3	22.7	23.1	23.3
45	SA	SA	22.1	22.5	22.9	23.1	23.3
60	21.3	21.9	22.4	22.7	23.0	23.2	23.3
75	21.7	22.2	22.6	22.9	23.1	23.2	23.3
90	22.0	22.3	22.7	23.0	23.2	23.3	23.3
105	22.2	22.5	22.9	23.1	23.3	23.3	23.3
120	22.4	22.6	22.9	23.2	23.3	23.3	23.3
135	22.4	22.6	22.9	23.2	23.3	23.4	23.3
150	22.4	22.6	22.9	23.1	23.3	23.4	23.3
165	22.3	22.5	22.8	23.0	23.2	23.4	23.3
180	22.1	22.4	22.7	23.0	23.2	23.4	23.3

Observations of the faintest objects may need the Special Requirement `LOW-SKY` in the Phase II observing program. `LOW-SKY` observations are scheduled during the part of the year when the zodiacal background light is no more than 30% greater than the minimum possible zodiacal light for the given sky position. `LOW-SKY` in the Phase II scheduling also invokes the restriction that exposures will be taken only at angles greater than 40° from the bright Earth limb to minimize earth-shine and the UV airglow lines. The `LOW-SKY` special requirement limits the times at which targets within 60° of the ecliptic plane will schedule, and limits visibility to about 48 minutes per orbit. The use of `LOW-SKY` must be requested and justified in the Phase I proposal.

The ETC provides the user with the flexibility to adjust separately both the zodiacal (low, average, high) and earth-shine (shadow, average, high) sky background components in order to determine if planning for use of `LOW-SKY` is advisable for a given program. However, the absolute sky levels that can be specified in the ETC may not be achievable for a given target; e.g., as shown in Table 9.4, the brightest zodiacal background for an ecliptic target is 21.3 V mag/arcsec^2, which is still brighter than both the low and average options with the ETC. By contrast, a target near the ecliptic pole would always have a zodiacal = low background in the ETC. The user is cautioned to carefully consider sky levels as the backgrounds obtained in *HST* observations can cover significant ranges.

9.7.2 Geocoronal Emission and SHADOW

Background due to geocoronal emission originates mainly from hydrogen and oxygen atoms in the exosphere of the Earth. In the far-UV spectral region, the strongest geocoronal emission lines are Lyman–α at 1216 Å, O I at 1304 Å, and O I] at 1356 Å, but WFC3 is of course not sensitive at these wavelengths. The only significant geocoronal emission line to which WFC3 is sensitive is [O II] 2471 Å, shown in Figure 9.1. In sunlight this line can be as bright as ~1.5×10^{-15} erg cm^{-2} s^{-1} arcsec^{-2}, while in Earth shadow it is much fainter, typically ~7.5×10^{-18} erg cm^{-2} s^{-1} arcsec^{-2}.

To minimize geocoronal emission the Special Requirement `SHADOW` can be requested. Exposures using this special requirement are limited to roughly 25 minutes per orbit, exclusive of the guide-star acquisition (or re-acquisition), and can be scheduled only during a small percentage of the year. `SHADOW` reduces the contribution from the geocoronal emission lines by roughly a factor of ten while the continuum earth-shine is set to zero. `SHADOW` requirements must be included and justified in your Phase I proposal (see the *Call for Proposals*).

9.8 Interstellar Extinction

Interstellar extinction can dramatically reduce the count rate detected from your source, particularly if you are working in the ultraviolet range made available for wide-field imaging by WFC3 but are inferring source brightnesses from optical data. Conversely, optically obscured objects may be much brighter in the IR than in the optical.

The Exposure Time Calculator includes the ability to correct exposure-time estimates for interstellar extinction based on the color excess $E(B-V)$. It may also be useful to refer to the standard references on interstellar extinction and its variations with location and metallicity, e.g., Fitzpatrick (1999, *PASP*, **111**, 63) and references therein.

9.9 Exposure-Time Calculation Examples

In the following sections you will find a set of examples for the two different channels and for different types of sources. The examples were chosen in order to present typical objects for the two channels and also to present interesting cases as they may arise with the use of WFC3.

9.9.1 Example 1: UVIS Imaging of a Faint Point Source

What is the exposure time needed to obtain a signal-to-noise of 10 for a point source of spectral type F0 V, normalized to $V = 27.5$, when using the UVIS F555W filter? Assume a photometry box size of 5x5 pixels, and average sky values.

The WFC3 Exposure Time Calculator (ETC) gives a total exposure time of 4996 s to obtain this S/N in a single exposure. Since such an exposure would be riddled with cosmic rays and essentially useless, it is necessary to specify how many exposures to split the observation into. WFC3/UVIS observations generally should be split if the exposure time is longer than about 5 minutes, but for multi-orbit observations, splitting into two exposures per orbit is generally sufficient.

For a typical object visibility of 53 minutes, after applying the requisite overheads, there is time for two exposures of approximately 1200 s per orbit. The required exposure time can thus be reached in 4 exposures, but re-running the ETC using `CR-SPLIT=4` raises the required exposure time to 5564 s (because of the extra noise introduced by the three extra readouts). To achieve the required exposure time would require `CR-SPLIT=5`, or three orbits; iterating the ETC one more time shows a total exposure time of 5737 s with this number of reads.

Using the pencil-and-paper method, Table 9.1 gives the integral $\int QTd\lambda/\lambda$ as 0.0761. An F0 V star has an effective temperature of 7,240 K; looking in Table A.1 the AB_v correction term for an effective temperature of 7,500 K is 0.03. According to Table 9.1, a 5x5 pixel square aperture encloses about 79% of the light from a star. The count rate can then be calculated from the equation

$$C = 2.5 \times 10^{11} \varepsilon_f \left(\int QTd\lambda/\lambda\right) \times 10^{-0.4(V + AB_v)}$$

or $2.5\text{x}10^{11}*0.0761*0.79*10^{-0.4(27.5+0.03)} = 0.146$ counts s^{-1}, which agrees with the ETC-returned value of 0.143. The exposure time can then be found by using the equation

$$t = \frac{\Sigma^2[C + N_{pix}(B_{sky} + B_{det})] + \sqrt{\Sigma^4[C + N_{pix}(B_{sky} + B_{det})]^2 + 4\Sigma^2 C^2\left[\frac{N_{pix}}{N_{bin}} N_{read} R^2\right]}}{2C^2}$$

to give $t = 5870$ s, which is close to the ETC-derived value of 5732 s. We have inserted the background rates of $B_{sky} = 0.0335$ (Table 9.1), $B_{det} = 0.0005$ (Chapter 5), a read noise of 3 e^- per read (Chapter 5), and 5 reads.

9.9.2 Example 2: IR Imaging of a Faint Extended Source

What is the exposure time needed to obtain a signal-to-noise of 10 for an elliptical galaxy that subtends an area of 1 $arcsec^2$ with an integrated *V*-magnitude of 26.7, when using the IR F140W filter? Assume a photometry box size of 9×9 pixels, and average sky values. Note that a 9×9 pixel box subtends 1.32 $arcsec^2$, so the equivalent

calculation would assume a surface brightness of 27.0 mag/arcsec^2 that uniformly fills this box. Also note that for simplicity we will assume a redshift of 0.

The WFC3 Exposure Time Calculator (ETC) gives a total exposure time of 1589 s to obtain this S/N in a single exposure. Although the non-destructive MULTIACCUM sequences on the IR channel can mitigate cosmic rays in a single read sequence, users are encouraged to dither their observations so that there are least 2 read sequences per field, to mitigate hot pixels and resample the point spread function. Re-running the calculation with 2 exposures gives an exposure time of 1745 s. If we assume (as in Example 1) that we can fit two 1200-second exposures in an orbit, this program fits within a single orbit. Two SPARS100 sequences, with 13 samples (1203 s) per sequence should work well for this program.

Using the pencil-and-paper method, Table 9.2 gives the integral $\int QTd\lambda/\lambda$ as 0.1147. We will assume that the elliptical galaxy resembles an old (10 Gyr) burst of star formation; looking in Table A.2, the AB_v correction term is –1.41. We will assume that the 9×9 pixel box encloses all of the light for this object. The count rate can then be calculated from the equation

$$C = 2.5 \times 10^{11} \varepsilon_f \left(\int QT d\lambda/\lambda\right) \times 10^{-0.4(V + AB_v)}$$

or $2.5\text{x}10^{11}*0.1147*1.0*10^{-0.4(26.7-1.41)} = 2.20$ counts s^{-1}, which is close to the ETC-returned value of 2.39. The exposure time can then be found by using the equation

$$t = \frac{\Sigma^2[C + N_{pix}(B_{sky} + B_{det})] + \sqrt{\Sigma^4[C + N_{pix}(B_{sky} + B_{det})]^2 + 4\Sigma^2 C^2\left[\frac{N_{pix}}{N_{bin}} N_{read} R^2\right]}}{2C^2}$$

to give $t = 1911$ s, which is close to the ETC-derived value of 1745 s. We have inserted the background rates of $B_{sky} = 0.8720$ (Table 9.2), $B_{det} = 0.02$ (Chapter 5), an effective read noise of 14.6 e$^-$ per read (Chapter 5, assuming we are fitting the MULTIACCUM sequence), and 2 reads.

CHAPTER 10:

Overheads and Orbit Time Determinations

In this chapter . . .

10.1 Overview

This chapter provides information for Phase I proposers who plan to use WFC3 for some or all of their planned HST observations. Because your Phase I proposal must state a specific integer number of HST orbits that are requested for your program, it is important that this number be as accurate as possible.

After you establish a set of scientific exposures, as well as any additional calibration exposures required for your program, you are ready to determine the total number of orbits to request in your Phase I proposal. The time requested should include not only the total exposure time, but also the additional time for the observatory and instrument operations needed to support those exposures. Those operations will usually include acquiring (and possibly re-acquiring) guide stars, configuring WFC3 in preparation for an exposure, transferring data, and possibly repositioning the target in the focal plane between exposures.

It will often be necessary or desirable to achieve the total exposure time through a sequence of shorter exposures. For example, an exposure totalling several hours will be interrupted by target occultations. Moreover, UVIS exposures will almost always be obtained as a sequence of shorter exposures, in order to remove cosmic-ray hits. For your Phase I proposal, you should plan the sequences of exposures and overhead

activities for each of the requested orbits. An overview of observation planning is given in Chapter 4.

Generally, you will need to compile the overheads for your individual exposures, having packed an integer number of exposures and their supporting activities into individual orbits. Some activities may be executed while the target is occulted by the Earth, allowing more efficient utilization of an orbit. Finally, you will tally the exposure times and resulting overhead times required during visibility of the target in order to determine the total number of orbits needed. This may be an iterative process as you refine your exposures to better use the targets' orbit visibility (for non-CVZ targets).

The Phase I Call for Proposals includes instructions on observatory policies and practices regarding orbit time requests; see

http://www.stsci.edu/hst/hst/proposing/documents/cp/cp_cover.html

The HST Primer provides additional specific advice on how to determine the number of required orbits for your scientific program; see

http://www.stsci.edu/hst/proposing/documents/cp/primer_cover_.html

In the following sections, we provide a summary of the WFC3-specific overheads and give several examples that illustrate how to calculate your orbit request for a Phase I proposal.

The overheads presented below are approximate. These overhead times are to be used, in conjunction with the exposure times you determine and the instructions in the HST Primer, in order to estimate the total number of orbits for your Phase I proposal. If your HST proposal is accepted, you will then develop and submit a Phase II proposal to support the actual scheduling of your approved observations. At that time you will use the APT scheduling software (which employs more precise values for the various overheads) to craft exposure sequences that match orbital target visibility intervals and your allocation of orbits. Therefore, requesting sufficient time in your Phase I proposal for overhead operations is important; additional time to cover unplanned overhead will not be granted later.

10.2 Observatory Overheads

This section discusses the overheads involved in preparing the telescope for observations of a target. The next section describes the additional instrument-specific overheads involved in obtaining and storing the actual individual WFC3 exposures.

At the beginning of a sequence of WFC3 exposures, the telescope must acquire guide stars. The time required for this initial guide-star acquisition is 6 minutes. If the observations extend into the following orbit(s) following Earth occultation, you must also include the overhead for guide-star re-acquisition (another 5 minutes at the beginning of each new orbit). The only exception to this re-acquisition overhead occurs when you are observing a target in the Continuous Viewing Zone (CVZ; see the

Phase I Proposal Instructions), in which case guide-star re-acquisitions are unnecessary.

Following guide-star acquisition (or re-acquisition) and the first exposure during the orbit, it is likely that you will want to make a series of small telescope motions for the purpose of obtaining dithered observations. Each commanded movement of the telescope requires an amount of time ranging from 0.3 to 1.3 minutes, depending on the size of the motion. Furthermore, each time the telescope is moved more than 2 arcmin (e.g., for the purpose of constructing a mosaicked image), an additional guide-star acquisition will be necessary, requiring another 6 minutes.

When using WFC3's UVIS quad filters, it will often be necessary to repoint the telescope to place the target in the desired quadrant. This repositioning will require 1 minute.

Table 10.1 summarizes the observatory-level overheads involved in WFC3 observing.

Table 10.1: Observatory Overhead Times.

Action	Overhead Time
Guide-star acquisition	6 minutes (first orbit)
Guide-star re-acquisitions	5 minutes at beginning of each new orbit for non-CVZ observing
	0 minutes for CVZ observing
New guide-star acquisition following dither of >2 arcmin	6 minutes
Spacecraft maneuvers	1 minute for offsets between 60 and 120 arcseconds
	0.8 minute for offsets between 28 and 60 arcseconds
	0.6 minute for offsets between 10 and 28 arcseconds
	0.5 minute for offsets between 1.25 and 10 arcseconds
	0.3 minute for offsets less than 1.25 arcsecond
	1 minute to offset to different UVIS quad filter

10.3 Instrument Overheads

10.3.1 Exposure Overheads

The instrument-specific overhead times for WFC3 exposures are dominated by the time to move the filter wheels, to read out the detector, and especially to transfer and store the data. Although in a Phase II proposal the overheads computed with APT may prove to be smaller than the values given in this section, it is nevertheless important to

plan your Phase I proposal using the conservative values given here in order to ensure the award of time adequate to attain your scientific goals.

Several kinds of overhead activities are associated with each exposure, and the specific activities depend on whether the exposure is a new one, or part of a series of identical ones. Identical exposures are defined as second and subsequent exposures on the same target, with the same filter.

For UVIS ACCUM exposures (i.e., CCD exposures), identical exposures are generated if the observer does any of the following: (1) specifies a CR-SPLIT number greater than 1; (2) does not specify the CR-SPLIT Optional Parameter, in which case it defaults to CR-SPLIT=2 for all exposures regardless of exposure time; (3) specifies the Special Requirement PATTERN (in order to dither, or to mosaic, a set of images); or (4) specifies a Number of Iterations greater than 1.

For IR MULTIACCUM exposures, CR-splitting is not used, and only items (3) and (4) in the preceding list apply. Furthermore, unless otherwise specified, a full 16-read (i.e., 15-sample, specified with NSAMP=15) sequence will be obtained for each IR MULTIACCUM exposure. The full set of samples (i.e., images) is considered to be one exposure.

At the end of each UVIS or IR exposure, images are read into WFC3's internal buffer memory, where they are stored until they are transferred to HST's solid-state data recorder. The time needed to read a UVIS CCD image is 98 seconds. The time needed for a single read of an IR image is 3 seconds, leading to a total of 48 seconds for a full 16-read exposure. These times are included in the overhead times for the first and subsequent exposures presented in Table 10.2 below.

The WFC3 internal buffer memory holds 64 MB of data, which is the equivalent of two full UVIS CCD exposures, or two 16-read IR exposures. Thus, after obtaining two full UVIS exposures, or two IR exposures, the internal buffer memory must be dumped to the telescope's solid-state recorder (SSR) before the next exposure can be taken. It is also possible to dump the buffer after each exposure, which can be advantageous. A buffer dump of one CCD or IR exposure takes 349 seconds (5.8 minutes), and cannot occur while WFC3 is being commanded. Of this time, 339 seconds (for one UVIS image) or 346 seconds (for one 16-read IR exposure) are spent dumping the image.

In regard to planning observations, there are three cases of interest. (1) The buffer dump can be done during the next exposure if its exposure time is longer than the dump time of 339 seconds (UVIS) or 346 seconds (IR). This is called a "parallel" buffer dump. (2) If the next exposure is not longer, then the buffer dump must occur first, and thus will create an extra 5.8 minutes of overhead. This is called a "serial" buffer dump. (3) If an exposure ends just before target occultation, the buffer can be dumped to the SSR during occultation, and no overhead time is required.

This means that a repeating sequence of one short UVIS exposure and one long UVIS exposure will incur no overhead if the short exposure is taken first and the long exposure is more than 339 seconds. Similarly, a repeating sequence of two 15-sample MULTIACCUM IR exposures will incur no overhead if the second exposure is longer than 346 seconds.

If the next exposure time is longer than 339 seconds (for UVIS) or 346 seconds (for IR), the buffer dump will occur during that exposure, and no overhead is imposed. However, if the next exposure time is shorter than 339 seconds (UVIS) or 346 seconds (IR), then the dump must occur before the next exposure can start.

A sequence of many short exposures will fill the WFC3 buffer before the target is occulted, requiring serial buffer dumps while the target is visible. Similarly, this will be required in all cases for CVZ targets. In these cases, the time needed to dump each exposure from WFC3's buffer (5.8 minutes) is an overhead that must be included in the orbit time budget. This overhead can severely constrain the number of short exposures that can be obtained in an orbit. However, subarrays can be used to lower the data volume for some applications and reduce the overhead time for buffer dumps (see Section 10.3.2)

Both the UVIS and IR channels may be used during a single orbit, although not simultaneously. The time required to reconfigure between the two channels is 1 minute. If the buffer is not empty when switching channels, then time must also be taken to dump it before the exposure can begin with the other channel. Because the centers of the fields of view of the UVIS and IR channels are the same, acquisition of new guide stars is not required when changing channels to observe the same target.

The overhead for each exposure includes an allowance for the time required to position the filter or grism; however, selecting a UVIS quad filter requires an additional 1 minute of overhead to re-position the telescope, as indicated in Table 10.1.

Table 10.2 summarizes all of the instrument overheads described in this subsection.

Table 10.2: WFC3 Instrument Overhead Times.

Action	Overhead Time (minutes)
Reconfiguration between UVIS & IR channels during a single orbit	1.0
UVIS ACCUM Mode	
Single exposure or first exposure in a set of identical exposures (e.g., the first sub-exposure of a CR-SPLIT set)	2.6
Subsequent exposures in set of identical exposures (e.g., subsequent exposures in a CR-SPLIT set, or a dithered exposure set), per exposure	2.1
Buffer dump if exposure is not last one in an orbit, or if next exposure is less than 339 seconds	5.8
IR MULTIACCUM Mode	
Each exposure	1.0
Buffer dump if 16-read exposure is not last one in an orbit, or if next exposure is less than 346 seconds	5.8

10.3.2 Reducing Overheads with Subarrays and Binning

If your science program is such that a field of view smaller than the full detector size is adequate and you require many short exposures, then one way to reduce the frequency of buffer dumps, and hence their associated overheads, is to use a WFC3 subarray. Subarrays are described for the UVIS channel in Section 6.4.4, and for the IR channel in Section 7.4.4. When subarrays are used, only a small region of the detector is read out and stored in WFC3's buffer. The reduced data volume permits a larger number of exposures to be stored in the buffer before it becomes necessary to transfer them to the telescope's solid-state recorder. Use of subarrays reduces the amount of time spent dumping the buffer, and also reduces detector readout time.

The subarrays supported by STScI (and recommended for your use) are specified for the UVIS and IR channels by apertures with "SUB" in their names. See Sections 6.4.4 and Section 7.4.4 further details**.**

The areas (A_{SA}) of the supported UVIS subarrays are 1/2, 1/4, or 1/64 of the area (A_{FF}) of a full-frame image. The areas of the IR subarrays are 1/4, 1/16, 1/64, or 1/256 of the area of a full-frame image. The number of subarray exposures that may be stored in the buffer is $n = 2\ (A_{FF}/A_{SA})$. For example, eight 1/4-area exposures may be stored in the buffer, which would allow eight 4-minute exposures to be taken and stored before having to dump the buffer. If the exposures were full-frame, the buffer would have to be dumped after each pair of observations, thus leading very low observing efficiency.

You may also define a UVIS subarray of arbitrary size and location, on an "available-but-unsupported" basis. However, in that case, matching bias frames will not be provided automatically by STScI and you therefore must specify them yourself. Those bias frames will typically be scheduled during the following occultation of a non-CVZ target (i.e., they do not add to the overheads during the visibility time), but the overhead must be added for CVZ targets. Dark frames and flat fields will be extracted from STScI's full-frame calibration images.

Data volume and overhead time can also be reduced for UVIS images by using on-chip binning of adjacent pixels, as described in Section 6.4.4. By using 2×2 pixel binning, the data volume is reduced by a factor of 4, although the readout time is only reduced by about a factor of 2 to 50 sec. For 3×3 pixel binning it is reduced by a factor of 9, and the readout time by a factor of 4 to 23 s. IR readouts cannot be binned, but data volume may be reduced by taking less than the default 15 samples during an exposure.

10.4 Orbit Use Examples

The easiest way to learn to estimate total orbit time requests is to work through a few examples. Below we provide five different examples:

1. A simple UVIS CR-SPLIT image using one filter.
2. A set of short UVIS exposures that require large overheads associated with buffer dumps.
3. A one-orbit IR observation using two different filters.
4. A two-orbit UVIS observation using dithering.
5. A one orbit IR grism spectroscopic observation.

These examples represent fairly typical usage scenarios of WFC3. However, it should be noted that in several of the examples we have used un-dithered images. In most actual cases, observers are advised to use dithering. Furthermore, although observers can use the shadow or low-sky target visibility restrictions, the examples below are all for the standard (i.e., unrestricted) target visibility (see the HST Primer, Section 6.3, for further discussion).

10.4.1 Example 1: UVIS, 1 orbit, 1 filter

Consider a target to be imaged with UVIS in a given filter in one orbit. Let us suppose that, by using the Exposure Time Calculator (ETC) (see Chapter 9), we find that we need a total exposure time of 2400 s (40 minutes) to reach the desired S/N. Given that we desire the observation to be split into two exposures for cosmic-ray removal (using the default CR-SPLIT=2), we map the overheads and the science exposure times onto the orbit as follows:

Table 10.3: Orbit Calculation for Example 1

Action	Time (minutes)	Explanation
Guide-star acquisition	6.0	Needed at start of observation of new target
UVIS overhead for first sub-exposure	2.6	Includes filter change, camera set-up, and readout
First science sub-exposure	20.0	
UVIS overhead for second sub-exposure	2.1	Includes readout
Second science sub-exposure	20.0	Total exposure time is 40 min
Total time used	50.7	

Thus, with a total time of nearly 51 minutes, this set of observations would fit into all unrestricted HST orbits. The exposure time could, if needed, be adjusted so as to fill the actual target visibility interval (which depends on several factors, including the date and target location in the sky, as described in Chapter 6 of the HST Primer). The time needed to dump the buffer following the second sub-exposure incurs no overhead in this example, because it can be performed during target occultation.

It should be noted that this simple sequence of two fairly long, non-dithered exposures would produce an image with a gap between the two CCD chips, and that cosmic-ray removal might not be optimal.

10.4.2 Example 2: UVIS, 1 orbit, short exposures

This example illustrates the impact of short exposures on the useful time in the orbit. Suppose we intend to use one orbit to observe a target with UVIS in two filters, F606W and F814W. The observation consists of two sequences, each one with two identical CR-SPLIT exposures, for a total of four individual sub-exposures. Suppose that the ETC shows that the exposure time must be 540 seconds for each of the filters, so each of the CR-SPLIT sub-exposures must be at least 270 seconds long. For the target declination, which in this example is –35°, we find that the unrestricted visibility time is 55 minutes. The time budget for the orbit is as follows:

Table 10.4: Orbit Calculation for Example 2

Action	Time (minutes)	Explanation
Guide-star acquisition	6.0	Needed at start of observation of new target
UVIS overheads for first sub-exposures in both series	2 × 2.6 = 5.2	Includes filter change, camera set-up, and readouts
UVIS overheads for subsequent sub-exposures in both series	2 × 2.1 = 4.2	Includes readouts
Buffer dump after 2nd sub-exposure	2 × 5.8 = 11.6	Full buffer must be dumped in target visibility in order to obtain last two exposures, which are too short to accommodate dump (270 sec < 339 sec).
Science exposures	4 × 4.5 = 18.0	
Total time used	45.0	

Compared with Example 1, we see that the efficiency is very low due to the large overheads associated with buffer dumps. We have achieved only 18 minutes of exposure time during 45 minutes of target visibility, whereas in Example 1 we obtained 40 minutes of exposure time during 51 minutes of visibility. Of course, this is caused by the short exposures of this example, versus the long exposures of Example 2, where "short" and "long" are relative to the time to dump the buffer, 339 seconds.

This time that is "lost" to dumping the buffer can be recovered by sufficiently increasing the exposure time. For example, if the 540-second exposure time is required to obtain a minimum S/N (and not to avoid saturation), then increasing the exposure times to 720 s will improve the S/N and require the same amount of target visibility time, 45 min.

Alternatively, if compatible with the scientific goals, a subarray could have been used to read out only a fraction of the detector area, allowing more frames to be stored in the buffer before requiring a dump. In this example, using UVIS 2k×4k subarrays for 4 short (<339 seconds) exposures would save about 4 minutes of readout time and could save 12 minutes of dump time.

10.4.3 Example 3: IR, 1 orbit, 2 filters

The third example demonstrates the orbit calculation for a simple IR observation. We want to obtain full-frame images of a target in two filters, F110W and F160W. Suppose that the ETC has shown that the exposure times adequate for our scientific goals are 10 minutes in F110W and 20 minutes in F160W. These times can be achieved with the up-the-ramp MULTIACCUM sequences SPARS50 (11.7 min) and SPARS100 (23.4 min), respectively. From the orbit visibility table (see Chapter 6 of the HST Primer), suppose that we find that at the target declination (here assumed to be 0°) the unrestricted target visibility time is 54 minutes. The orbit calculation goes like this:

Table 10.5: Orbit Calculation for Example 3

Action	Time (minutes)	Explanation
Guide-star acquisition	6.0	Needed at start of observation of new target
IR overheads for 2 exposures	2 × 1.0 = 2.0	Includes filter changes, camera set-ups, and readouts
Science exposure in F110W	11.7	
Science exposure in F160W	23.4	
Total time used	43.1	

The total time used in the orbit shows that our target can indeed be imaged in the selected filters within one orbit. Furthermore, the first exposure can be dumped from the buffer during the second exposure. The ~9 minutes of unused time could be used for an additional exposure, during which the second exposure would be dumped.

10.4.4 Example 4: UVIS, dithering, 2 orbits, 1 filter

This example illustrates the orbit calculation for a UVIS observation with a WFC3 UVIS box dithering pattern, which implements imaging at four pointings. The goal of

the observation is to obtain a dithered image of a field in such a way that would allow us to bridge the ~2 arcsec inter-chip gap between the UVIS CCDs in the combined image. As indicated in Table 10.1, for a 2-arcsec offset maneuver, the three dithers will take 0.5 minutes each. Suppose we have determined that the exposure time necessary to reach the desired S/N ratio is 80 minutes, and that the visibility time at our target declination, assumed to be +53°, is 58 minutes. Furthermore, we will use the cosmic-ray removal provided by the dither data-reduction package, and therefore set CR-SPLIT=1. As a result, the orbit calculation will involve a sequence of four exposures of 20-minutes duration (i.e., one exposure at each of the four dither pointings). These observations will be distributed across two HST orbits, as shown in the following Table 10.6.

Table 10.6: Orbit Calculation for Example 4.

Action	Time (minutes)	Explanation
	Orbit 1	
Guide-star acquisition	6.0	Needed at start of observation of new target
UVIS overhead for first exposure	2.6	Includes filter change, camera set-up, and readout
UVIS overhead for second exposure	2.1	Includes readout
Spacecraft maneuver	0.5	To offset from first to second dither pointing
Two science exposures	2 × 20 = 40.0	Exposures at the first two pointings in the dither pattern
Total time used in orbit 1	51.2	
	Orbit 2	
Guide-star re-acquisition	5.0	Needed at start of new orbit to observe same target
UVIS overheads for 3rd and 4th exposures	2 × 2.1 = 4.2	Includes readouts
Spacecraft manaeuvers	2 × 0.5 = 1.0	To offset to the 3rd and 4th dither pointings
Two science exposures	2 × 20 = 40.0	Exposures at the final two pointings in the dither pattern
Total time used in orbit 2	50.2	

No overhead is incurred to dump the exposures, because they are all longer than 339 seconds. Thus the desired exposures can be accomplished within the two orbits, and in fact there are ~7-8 minutes of unused visibility time per orbit that could be used to increase the exposure times.

10.4.5 Example 5: IR, 1 orbit, grism

This example illustrates the orbit calculation for an IR G102 grism spectroscopic observation. We will use the full-frame, up-the-ramp MULTIACCUM sequence SPARS200 with NSAMP=13, requiring 40 minutes to expose. We will also obtain undispersed images to calibrate target positions and wavelengths, using a SPARS10 (2.4-minute) exposure before and after the grism exposure. The overhead calculations are presented in Table 10.7.

Table 10.7: Orbit Calculation for Example 5.

Action	Time (minutes)	Explanation
Guide-star acquisition	6.0	Needed at start of observation of new target
IR overheads for 3 exposures	3 × 1.0 = 3.0	Includes filter changes, camera set-ups, and readouts
Science exposure (undispersed)	2 × 2.4 = 4.8	SPARS10, NSAMP=15
Science exposure (grism)	40.0	SPARS200, NSAMP=13
Total time used	53.8	

The buffer dumps incur no overhead because the first undispersed exposure can be dumped during the long grism exposures, and the last two can be dumped during the subsequent target occultation. Thus, since at least 54 minutes of target visibility are available at any target's declination, this set of observations can be obtained in one orbit.

APPENDIX A:

WFC3 Filter Throughputs

In this appendix . . .

A.1 Introduction

This appendix contains plots of throughputs and sensitivities for each WFC3 filter. It is organized by *filter* and *detector*. For each imaging mode the following are provided:

- Plots of integrated system throughput as a function of wavelength.
- Plots of the time needed to achieve a desired signal-to-noise ratio vs. magnitude for all filters for a point-source and for a 1"×1" extended source.
- Tables of color corrections AB_V to go from Johnson *V* magnitude to *AB* magnitude for stellar spectra (as a function of effective temperature) and composite populations (as a function of age). The stellar spectra come from the Lejeune et al. (1997, *A&AS*, **125**, 229) grid, and assume a surface gravity of log $g = 5$ and solar metallicity. The composite populations come from the "instantaneous burst" and "continuous star formation" models of Bruzual & Charlot (1993, *ApJ*, **405**, 539), updated in 1995, assuming a Salpeter IMF spanning 0.1 to 125 solar masses.

A.2 Using the Information in this Chapter

A.2.1 Sensitivity Units and Conversions

This appendix contains plots of throughputs for each WFC3 filter. Section 9.3 explains how to use these throughputs to calculate expected count rates from your source.

The first figure for each filter gives the integrated system throughput. This is the combination of the efficiencies of the detector and of the optical elements in the light path. The throughputs in this Handbook are based on ground test data. The throughput is defined as the number of detected counts/second/cm^2 of telescope area relative to the incident flux in photons/cm^2/s. For the both channels (UVIS and IR), "counts" is the number of electrons detected. In both channels the detected counts obey Poisson statistics, except that at short wavelengths in the UVIS channel, a single incoming photon has a finite chance of producing two electrons in the CCD; the plots shown in this appendix have been corrected for this "quantum yield" effect (see Section 5.4.2). The throughput includes all obscuration effects in the optical train (e.g., due to the HST secondary).

All wavelength measurements for the UVIS and IR channel filters were done in air. The UVIS laboratory measurements were done at a temperature of 20°C, whereas the filters will be operated on orbit at 0°C; this may lead to wavelength shifts which are expected to be small. The IR laboratory measurements were done at a temperature of

-30°C, whereas the filters will be operated on orbit at -35°C; this may lead to wavelength shifts which are expected to be very small.

Note that the tables in the ***synphot*** package and the WFC3 Exposure Time Calculator will all assume air wavelengths for both the UVIS and IR filter transmission data.

Because we have corrected the throughputs for quantum yield in order to derive appropriate counting statistics for the source, the sensitivity calculations shown here are conservative in background- or read-noise-dominated regimes; the additional signal electrons from the >1 quantum yield will increase the detection of faint sources in the 200-300 nm range somewhat vs. these sample calculations.

To recalculate the throughput with the most recent detector QE tables in ***synphot***, you can create total-system-throughput tables (instrument plus OTA) using the ***synphot calcband*** task. ***calcband*** takes any valid obsmode command string as input and produces an STSDAS table with two columns of data called "wavelength" and "throughput" as its output. For example, to evaluate the throughput for the F475W filter and the UVIS detector, Chip 1, you would use the command ***calcband wfc3,uvis1,f475w sdssg_thpt.*** The resulting throughput table is stored in ***sdssg_thpt***.

A.2.2 Signal-to-Noise Ratio

For each imaging mode, plots are provided to estimate the signal-to-noise ratio (S/N) for a representative source. The first figure shows S/N for point sources. The second figure shows S/N for uniform extended sources of area 1 arcsec^2.

The different line styles in the S/N figures delineate regions where different sources of noise dominate. If the total noise from backgrounds (read noise, sky, thermal, dark) is larger than the noise from the source, the observation is considered to be background-dominated, and the line style reflects which of these background is largest. Note that for the WFC3 detectors, the dark current can never be the largest source of noise when a source is background-dominated, because the read noise is always larger than the dark count noise when exposures are 1000 s or less. The point- and extended-source S/N figures assume average sky levels. These plots also indicate where an observation will saturate the full well of the detector.

For point sources, an aperture size of 5×5 pixels has been used for the UVIS channel, while an aperture size of 3×3 pixels has been used for the IR channel. For extended sources, a 1 arcsec^2 aperture was used. The read noise has been computed assuming a number of readouts `NREAD`= integer (t / 1000 s), where t is the exposure time, with a minimum `NREAD=2`.

In situations requiring more detailed calculations (non-stellar spectra, extended sources, other sky background levels, unknown target V magnitude, etc.), the WFC3 Exposure Time Calculator should be used.

Follow these steps to use the signal-to-noise plots:

1. Determine the *AB* magnitude of your source at the wavelength of interest. There are several ways to do this.

- Examine Tables A.1, A.2, or A.3 and find AB_ν for the desired spectral type and filter. Sum the *V* magnitude of the target and AB_ν derived from the table.
- Alternatively, compute ABMAG (=V+AB_ν) from the source flux, using the relation $ABMAG = -2.5\log f_\nu - 48.60$, or $ABMAG = -2.5\log f_\lambda - 5\log\lambda - 2.406$.

2. Find the appropriate plot for the filter in question, and locate V+AB_ν on the horizontal axis. Then read off the signal-to-noise ratio for the desired exposure time, or vice-versa.

Note that the plots show the S/N as a function of source magnitude for exposure times as short as 0.1 s, although the minimum exposure time for the UVIS channel is actually 0.5 s.

UVIS/F200LP

Description

Clear; grism reference filter.

Figure A.1: Integrated system throughput for F200LP.

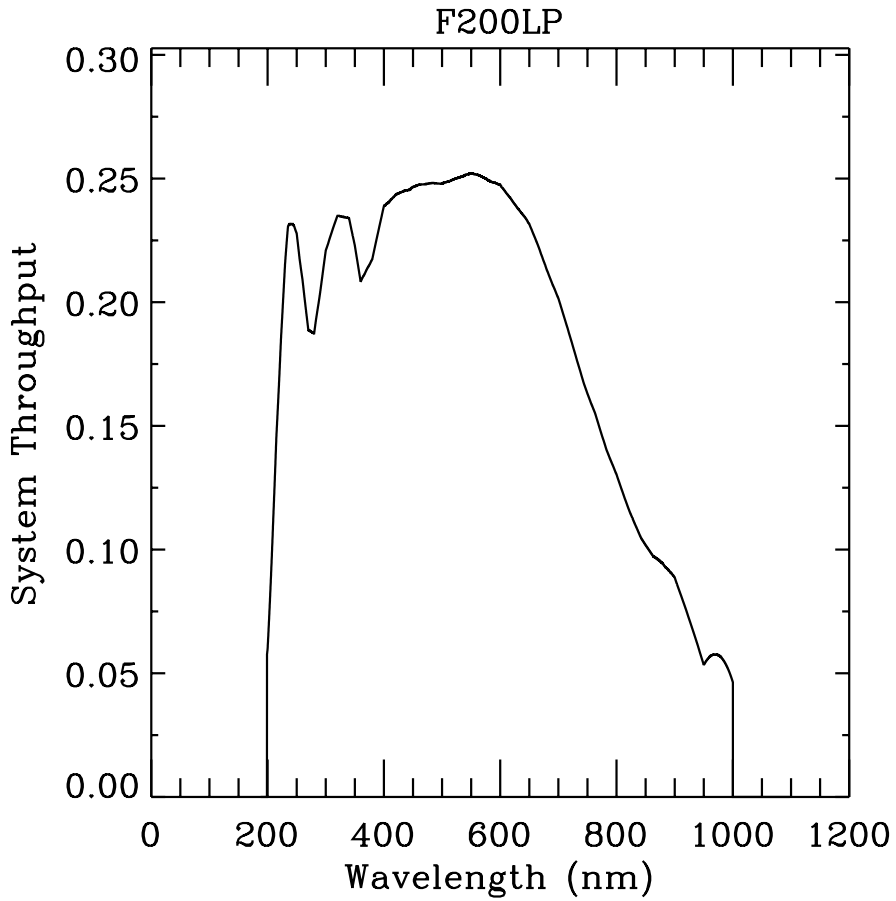

Figure A.2: Point source S/N vs. V+AB$_\nu$ for the F200LP filter, assuming high sky backgrounds and a 5×5 pixel aperture.

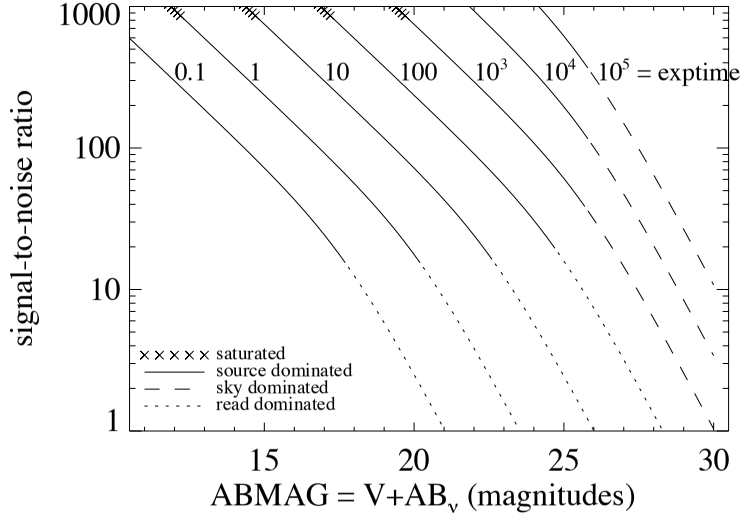

Figure A.3: Extended source S/N vs. V+ABν for the F200LP filter, assuming high sky backgrounds and a source uniformly filling a 1 arcsec^2 aperture.

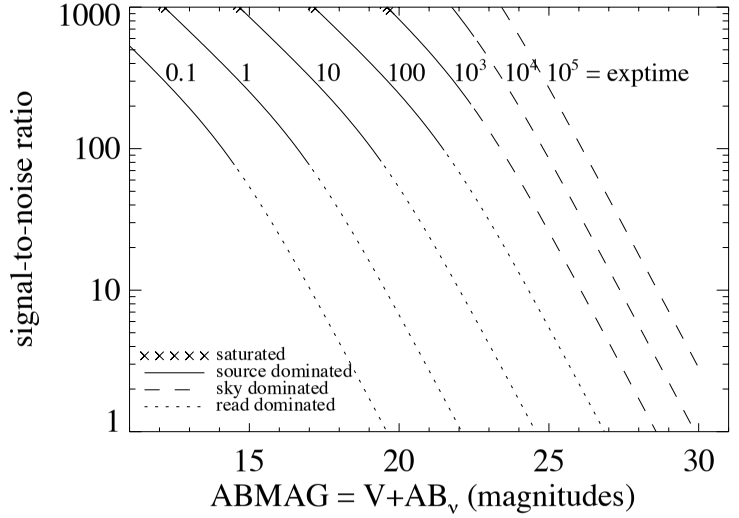

UVIS/F218W

Description

ISM feature filter.

Figure A.4: Integrated system throughput for F218W.

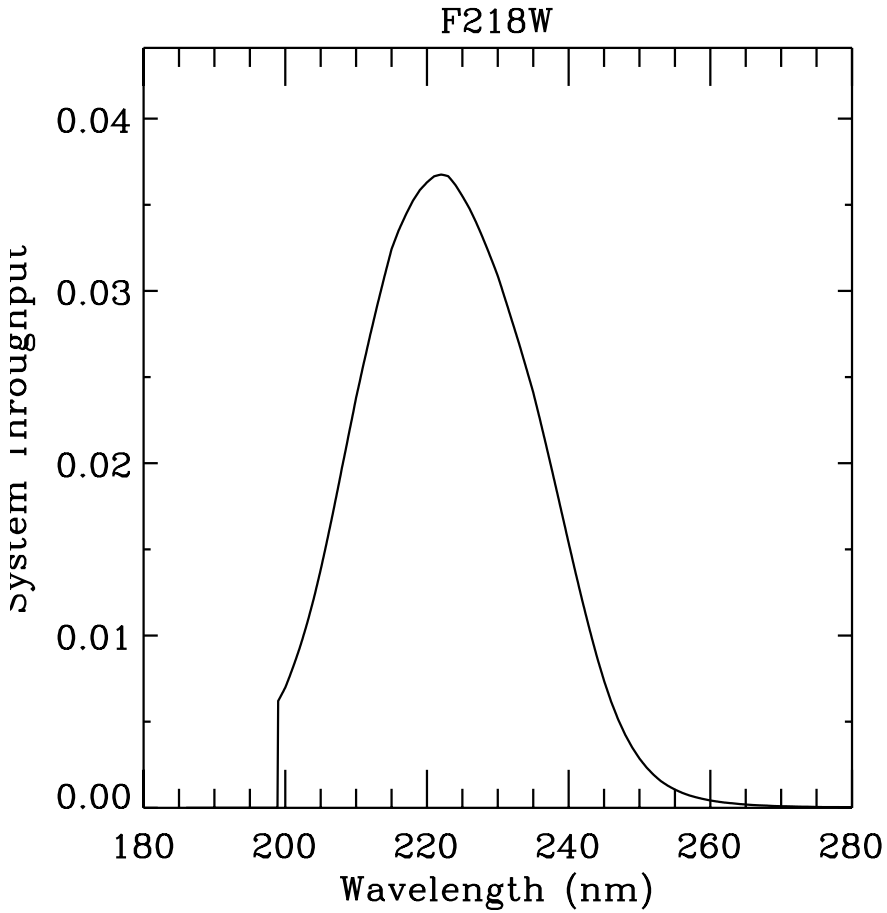

Figure A.5: Point source S/N vs. V+ABν for the F218W filter, assuming high sky backgrounds and a 5×5 pixel aperture.

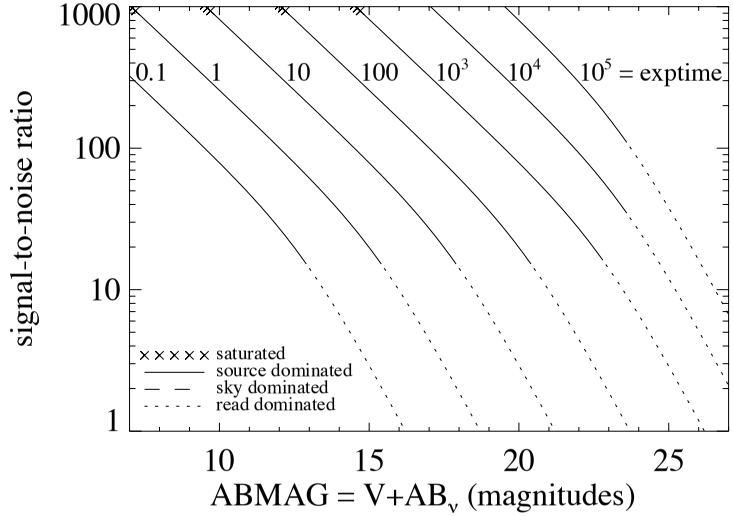

Figure A.6: Extended source S/N vs. V+ABν for the F218W filter, assuming high sky backgrounds and a source uniformly filling a 1 arcsec^2 aperture.

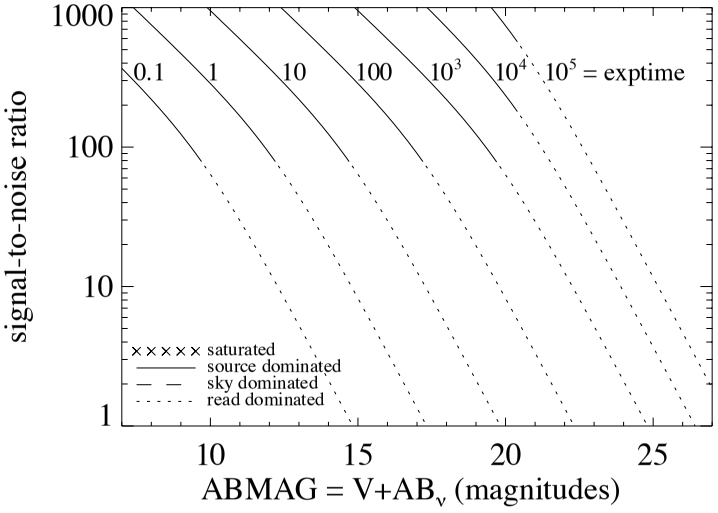

UVIS/F225W

Description

UV wide filter.

Figure A.7: Integrated system throughput for F225W.

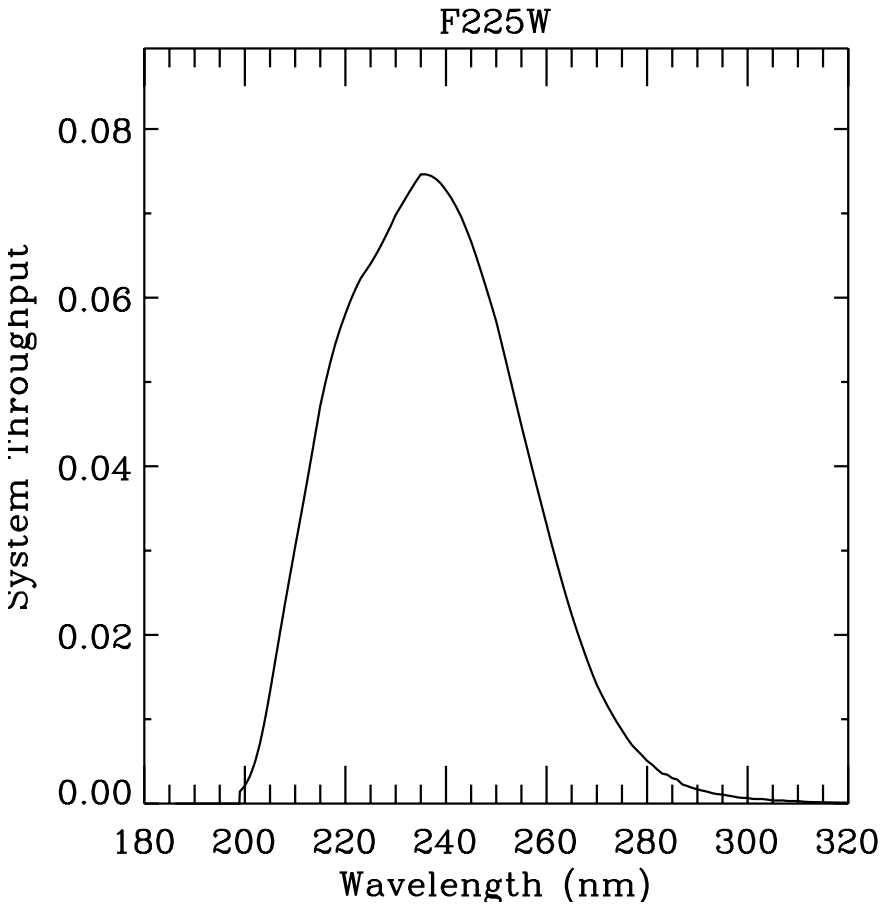

Figure A.8: Point source S/N vs. V+ABν for the F225W filter, assuming high sky backgrounds and a 5×5 pixel aperture.

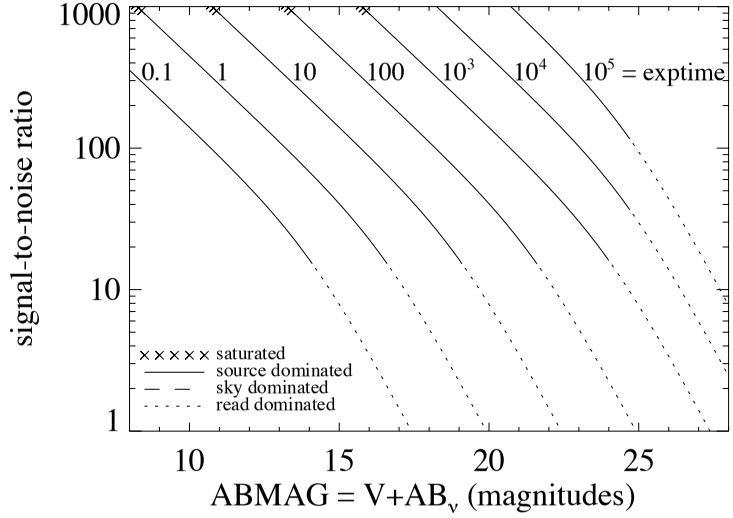

Figure A.9: Extended source S/N vs. V+ABν for the F225W filter assuming high sky backgrounds and a source uniformly filling a 1 arcsec^2 aperture.

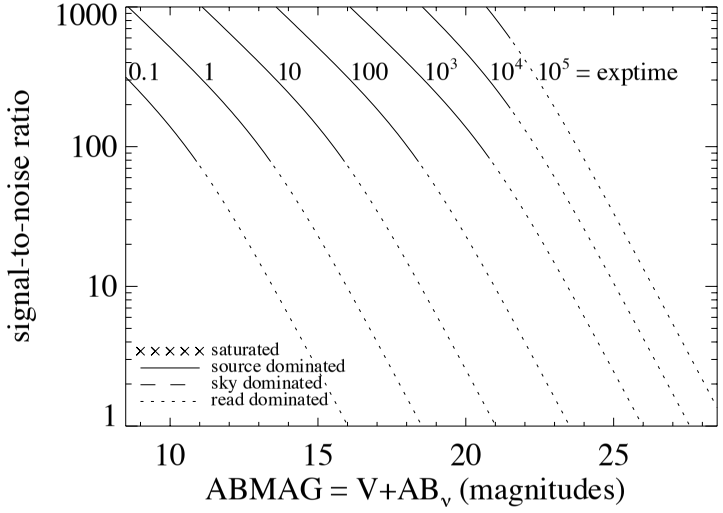

UVIS/F275W

Description

UV wide filter.

Figure A.10: Integrated system throughput for F275W.

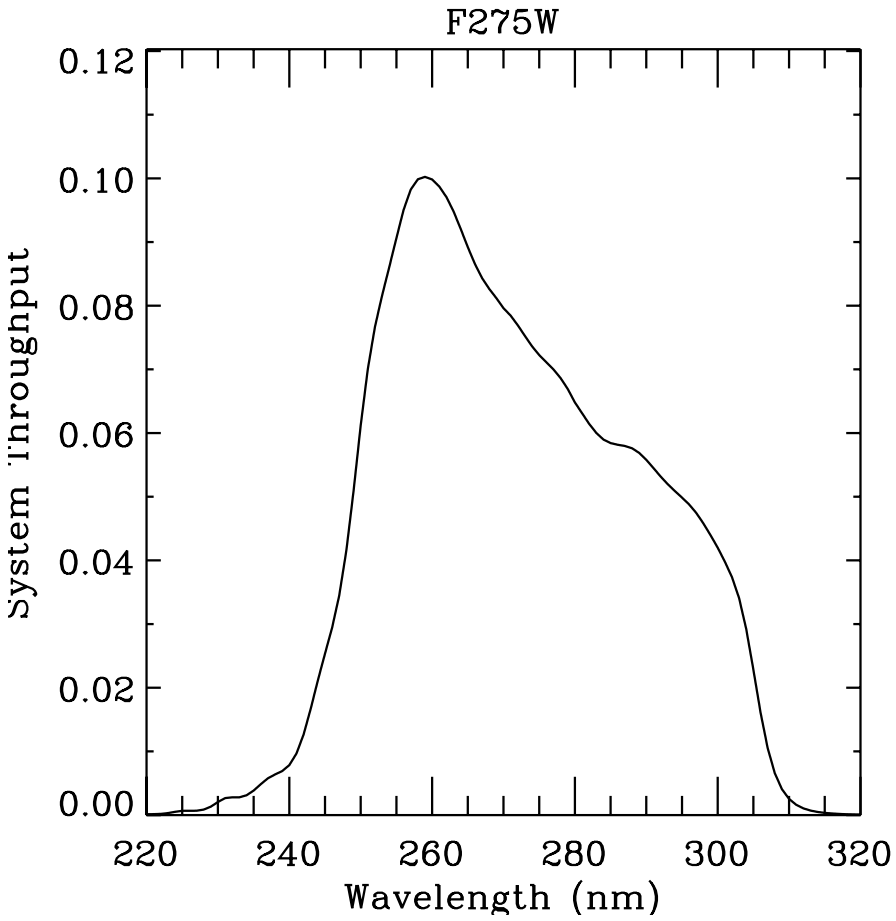

Figure A.11: Point source S/N vs. V+ABν for the F275W filter, assuming high sky backgrounds and a 5×5 pixel aperture.

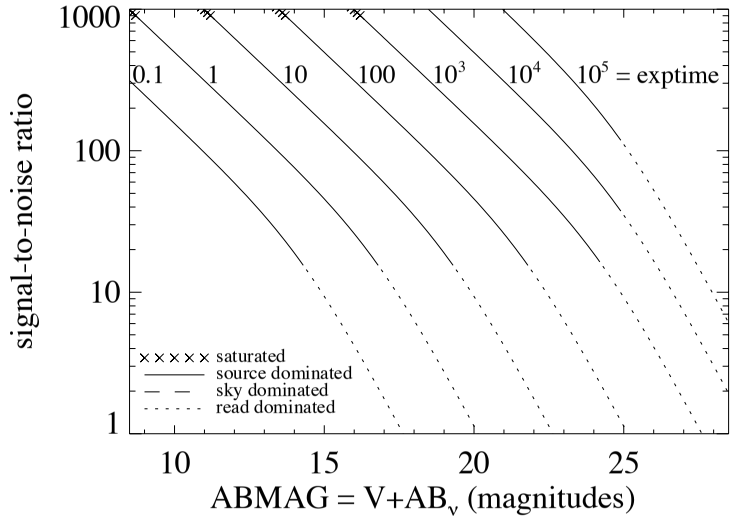

Figure A.12: Extended source S/N vs. V+ABν for the F275W filter, assuming high sky backgrounds and a source uniformly filling a 1 arcsec^2 aperture.

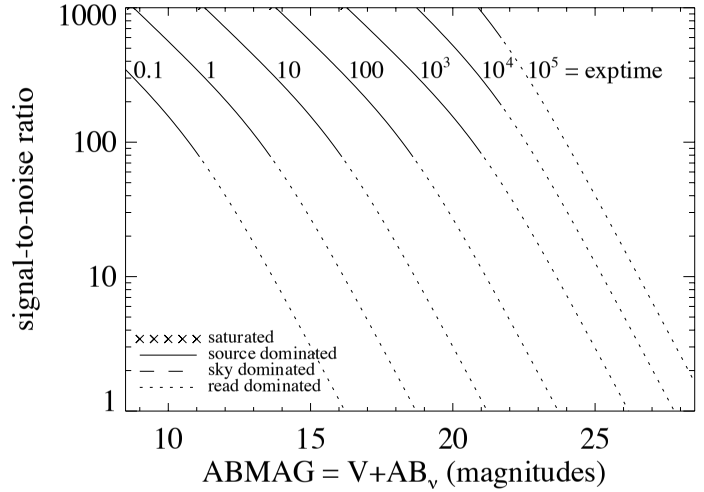

UVIS/F280N

Description

Mg II 2795/2802 filter.

Figure A.13: Integrated system throughput for F280N.

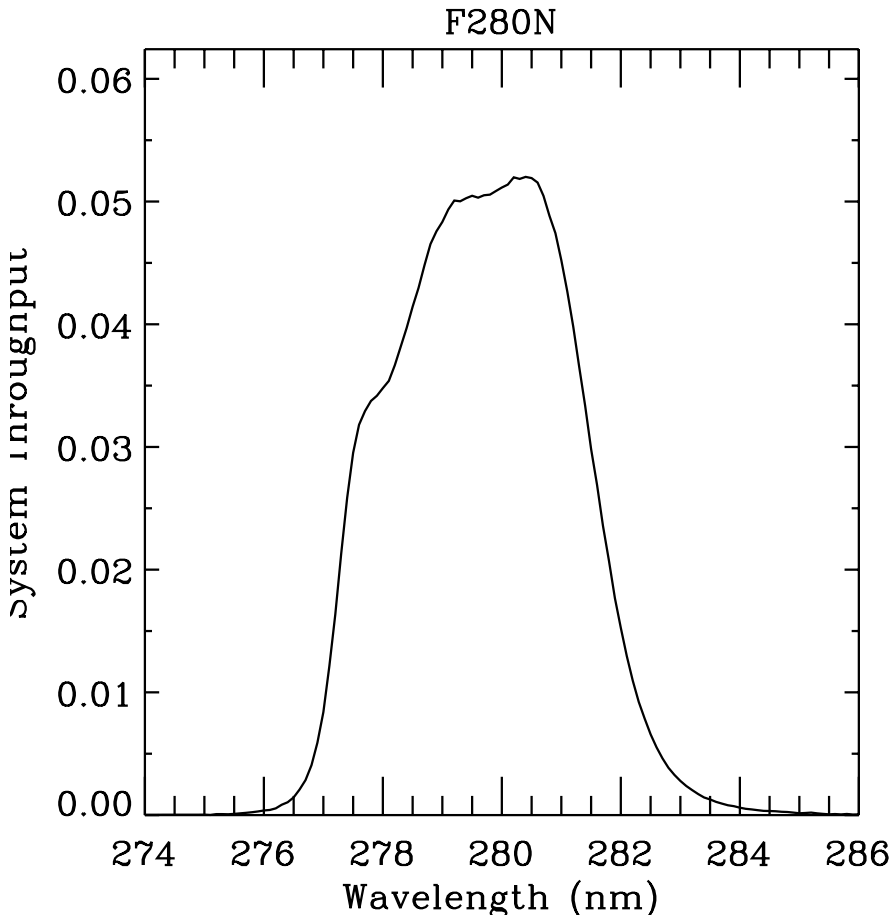

Figure A.14: Point source S/N vs. V+ABν for the F280N filter, assuming high sky backgrounds and a 5×5 pixel aperture.

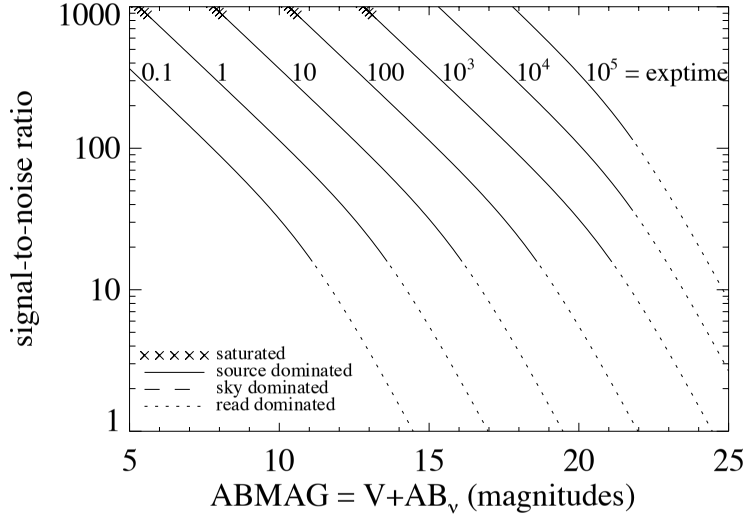

Figure A.15: Extended source S/N vs. V+ABν for the F280N filter, assuming high sky backgrounds and a source uniformly filling a 1 arcsec^2 aperture.

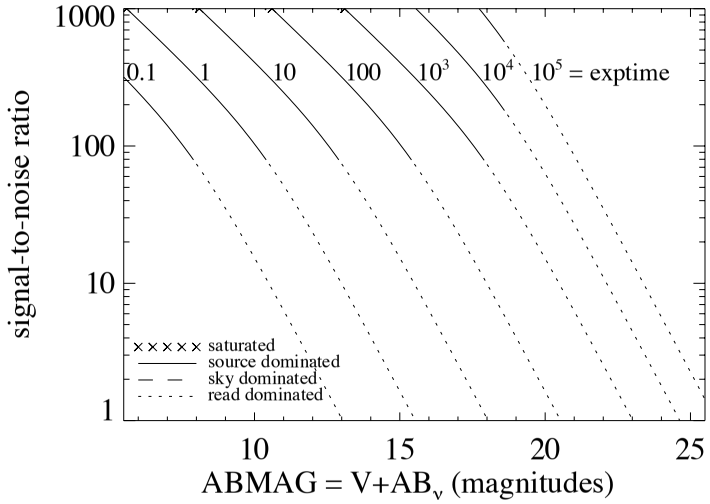

UVIS/F300X

Description

Extremely wide UV filter.

Figure A.16: Integrated system throughput for F300X.

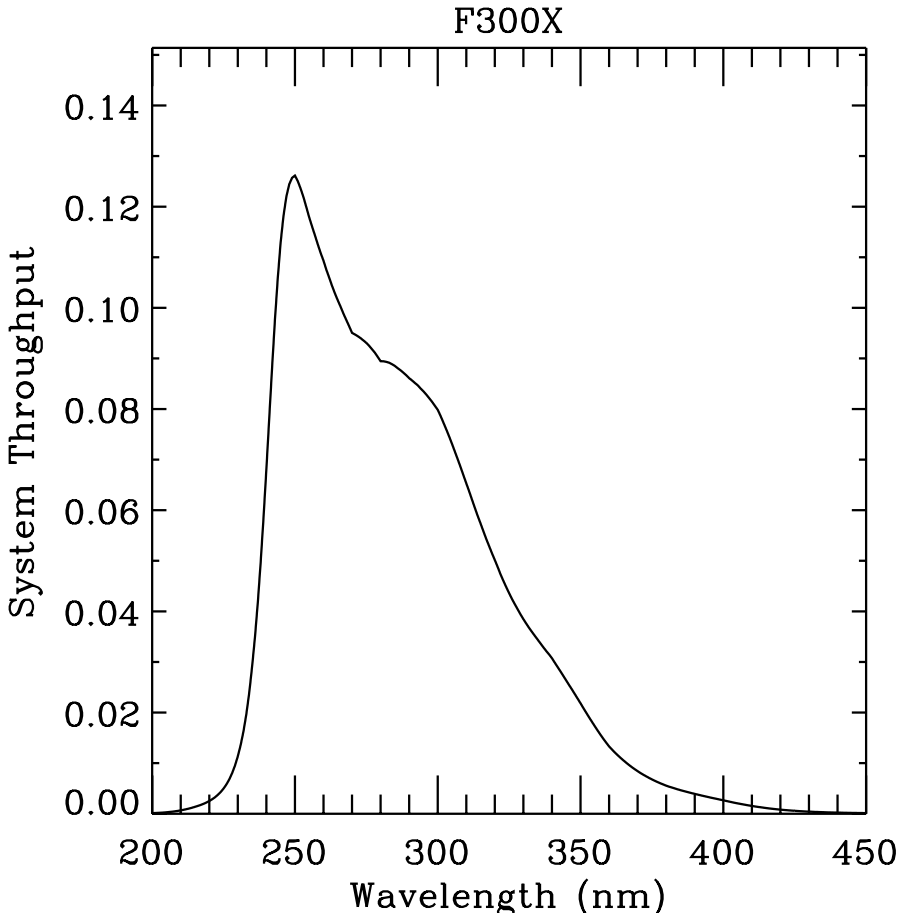

Figure A.17: Point source S/N vs. V+ABν for the F300X filter, assuming high sky backgrounds and a 5×5 pixel aperture.

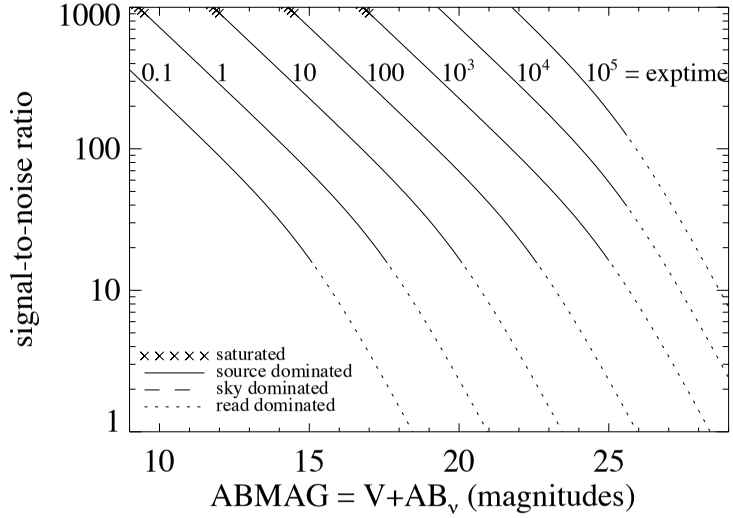

Figure A.18: Extended source S/N vs. V+ABν for the F300X, assuming high sky backgrounds and a source uniformly filling a 1 arcsec^2 aperture.

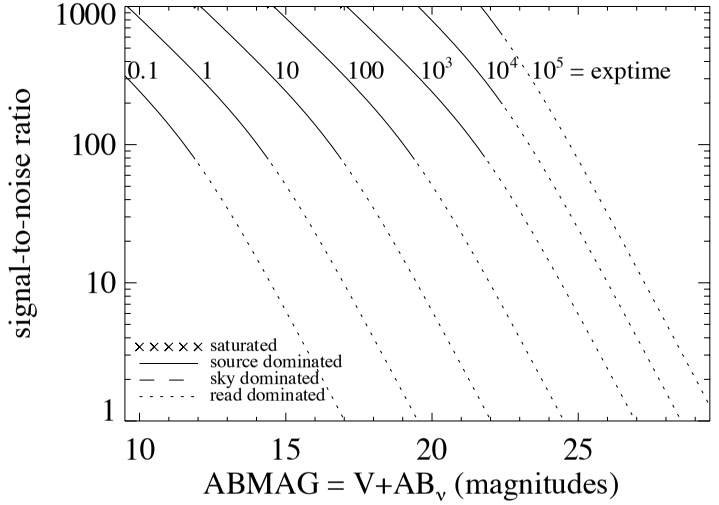

UVIS/F336W

Description

U, Strömgren *u* filter.

Figure A.19: Integrated system throughput for F336W.

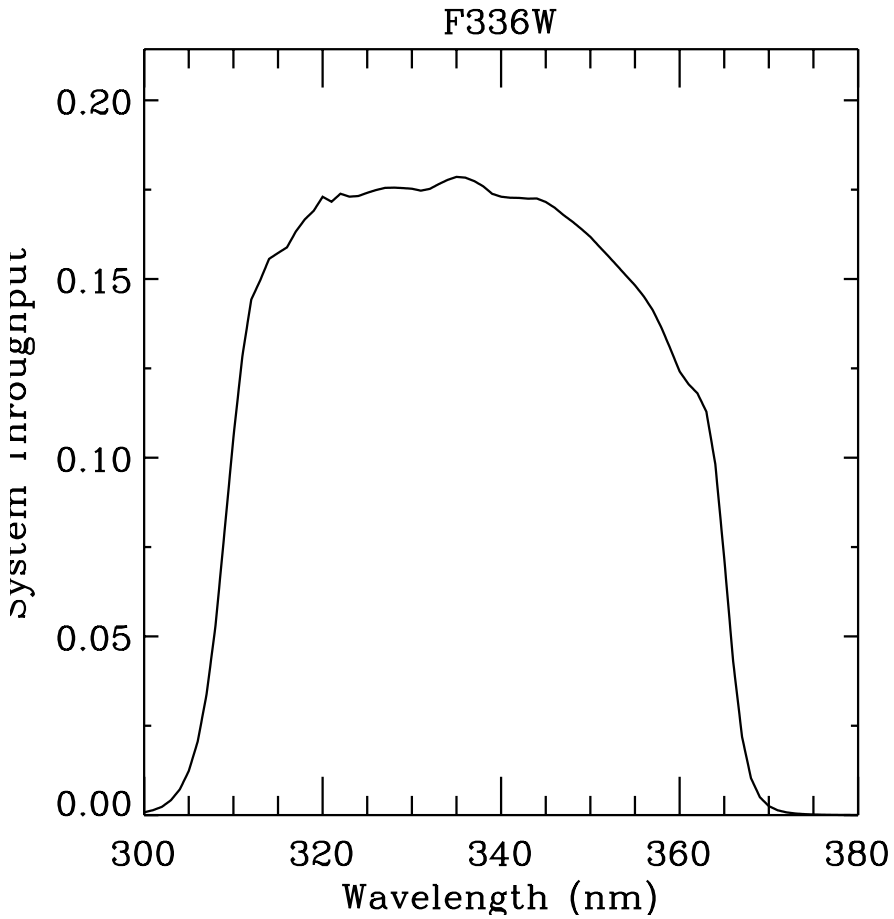

Figure A.20: Point source S/N vs. V+ABν for the F336W filter, assuming high sky backgrounds and a 5×5 pixel aperture.

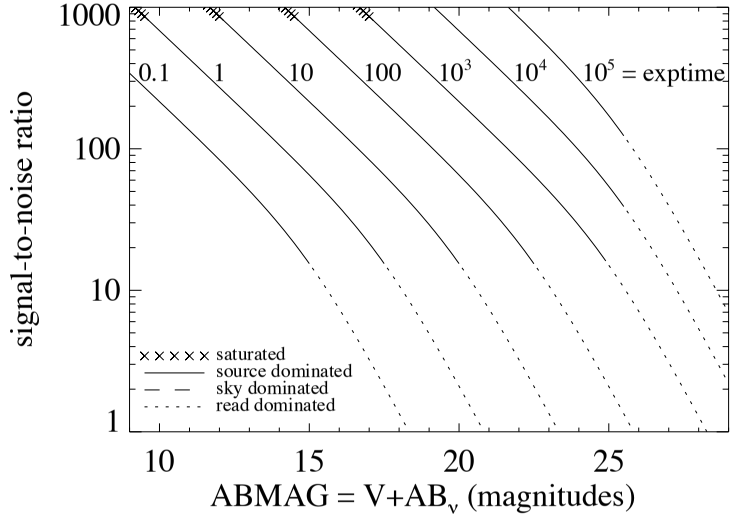

Figure A.21: Extended source S/N vs. V+ABν for the F336W filter, assuming high sky backgrounds and a source uniformly filling a 1 arcsec^2 aperture.

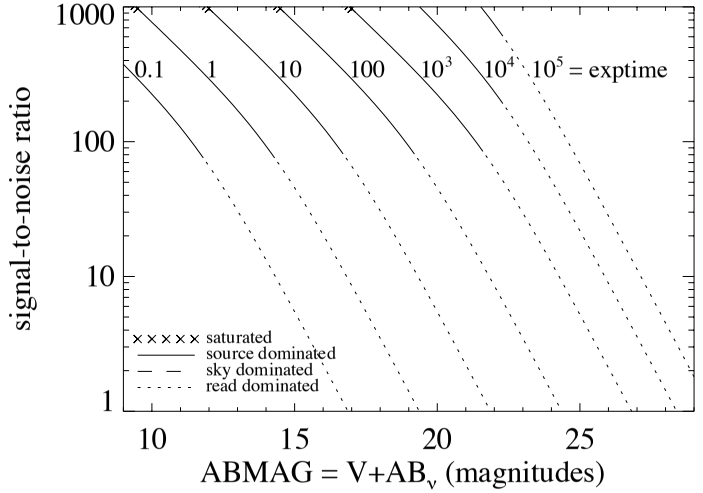

UVIS/F343N

Description

[Ne V] 3426 filter.

Figure A.22: Integrated system throughput for F343N.

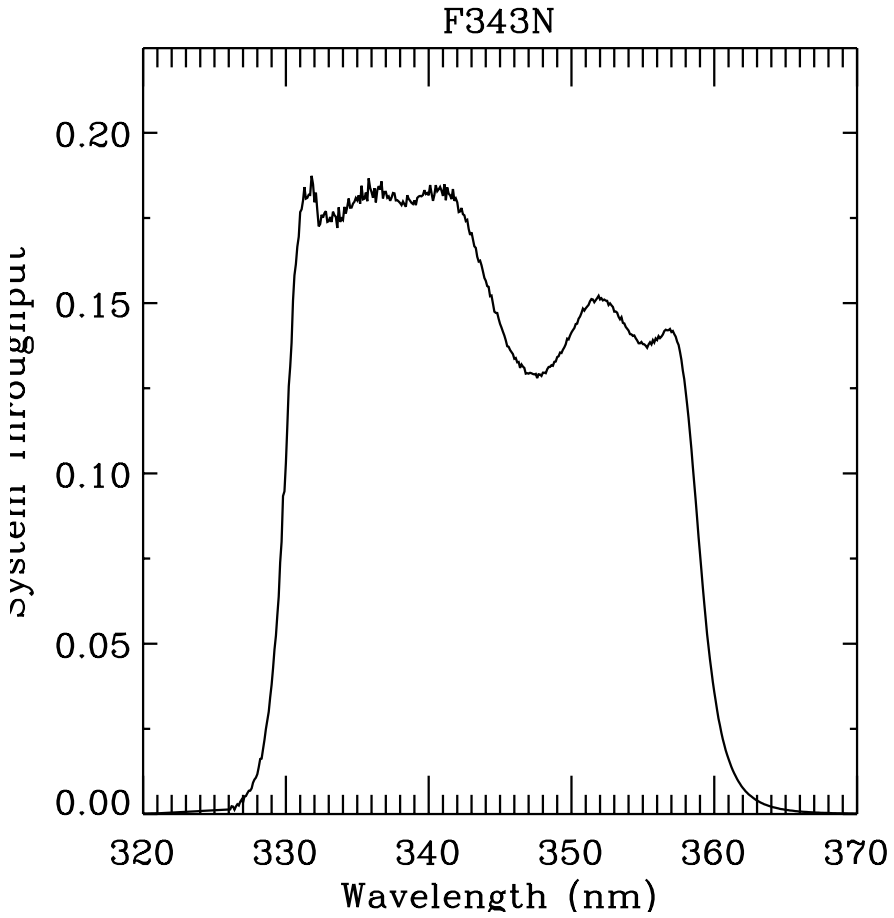

Figure A.23: Point source S/N vs. V+ABν for the F343N filter, assuming high sky backgrounds and a 5×5 pixel aperture.

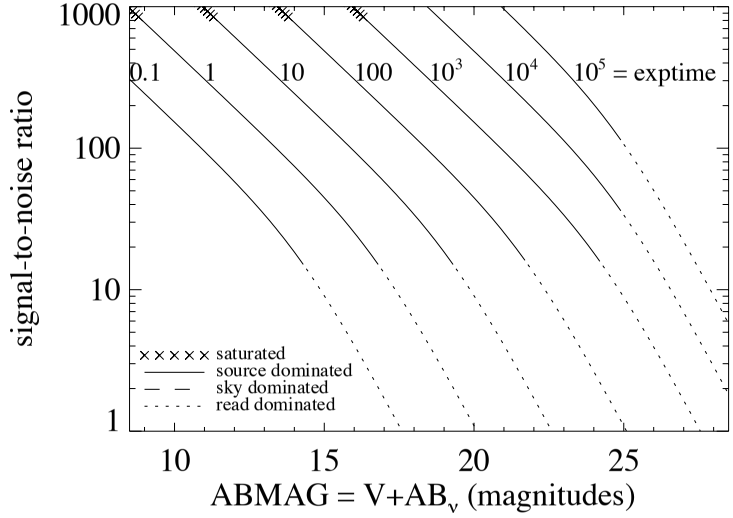

Figure A.24: Extended source S/N vs. V+ABν for the F343N filter, assuming high sky backgrounds and a source uniformly filling a 1 arcsec^2 aperture.

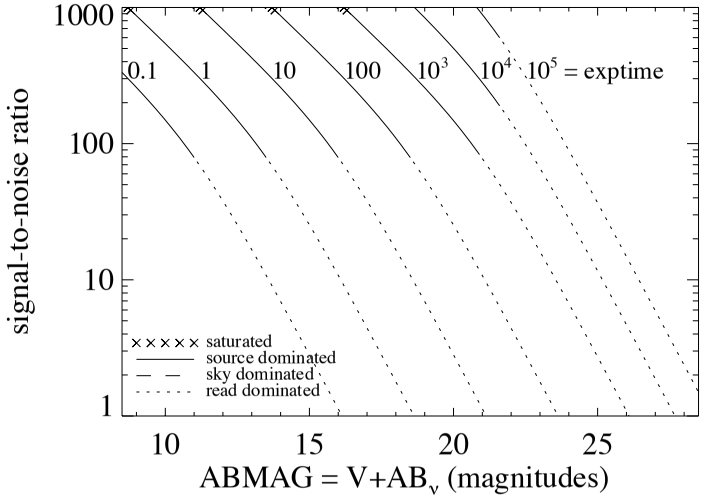

UVIS/F350LP

Description

Long pass filter.

Figure A.25: Integrated system throughput for F350LP.

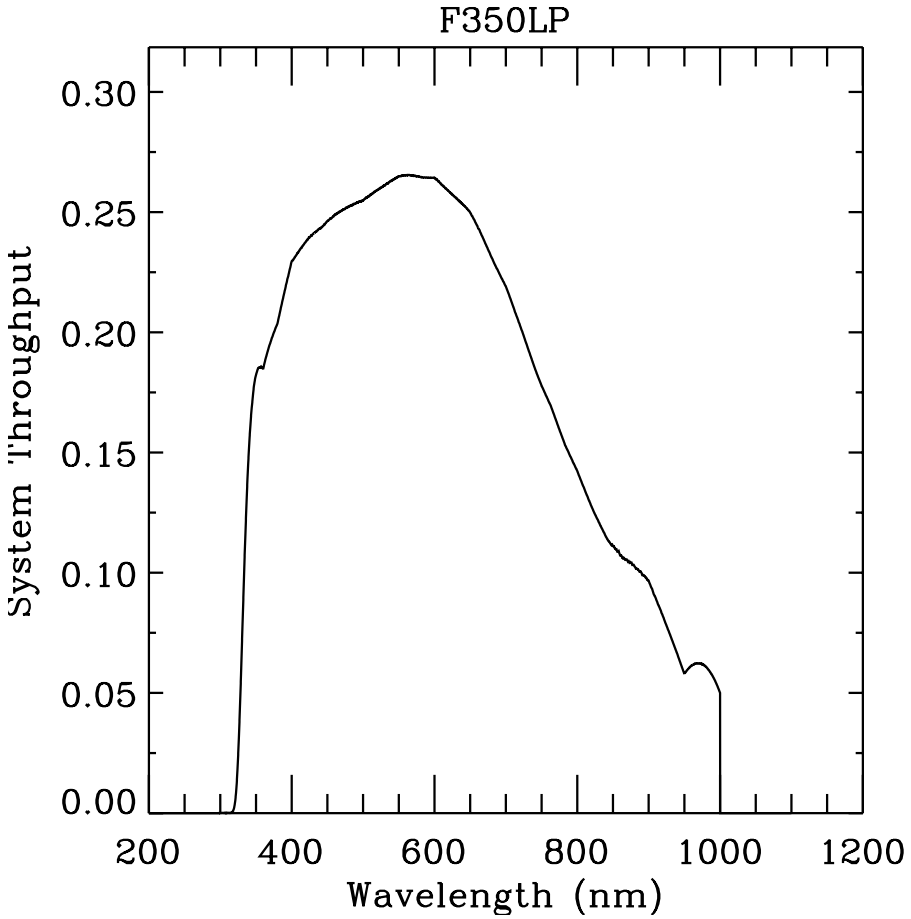

Figure A.26: Point source S/N vs. V+ABν for the F350LP filter, assuming high sky backgrounds and a 5×5 pixel aperture.

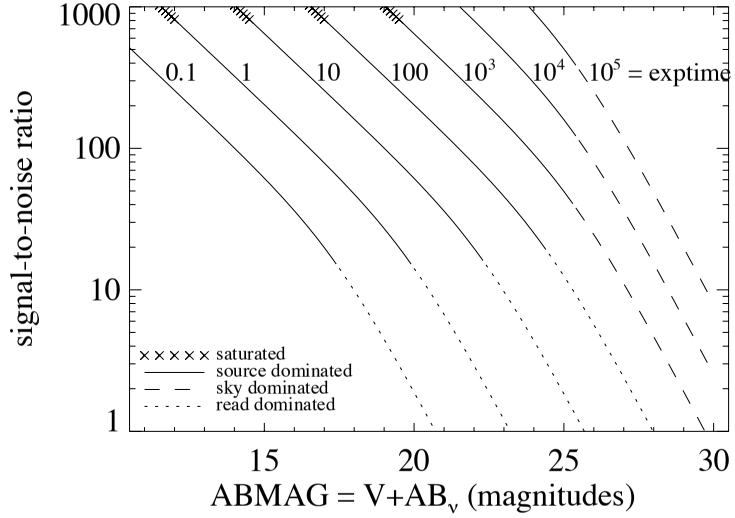

Figure A.27: Extended source S/N vs. V+ABν for the F350LP filter, assuming high sky backgrounds and a source uniformly filling a 1 arcsec^2 aperture.

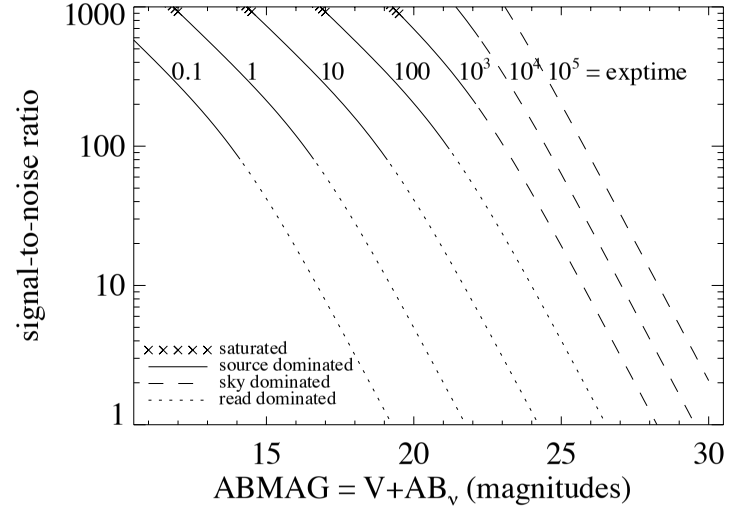

UVIS/F373N

Description

[O II] 3726/3728 filter.

Figure A.28: Integrated system throughput for F373N.

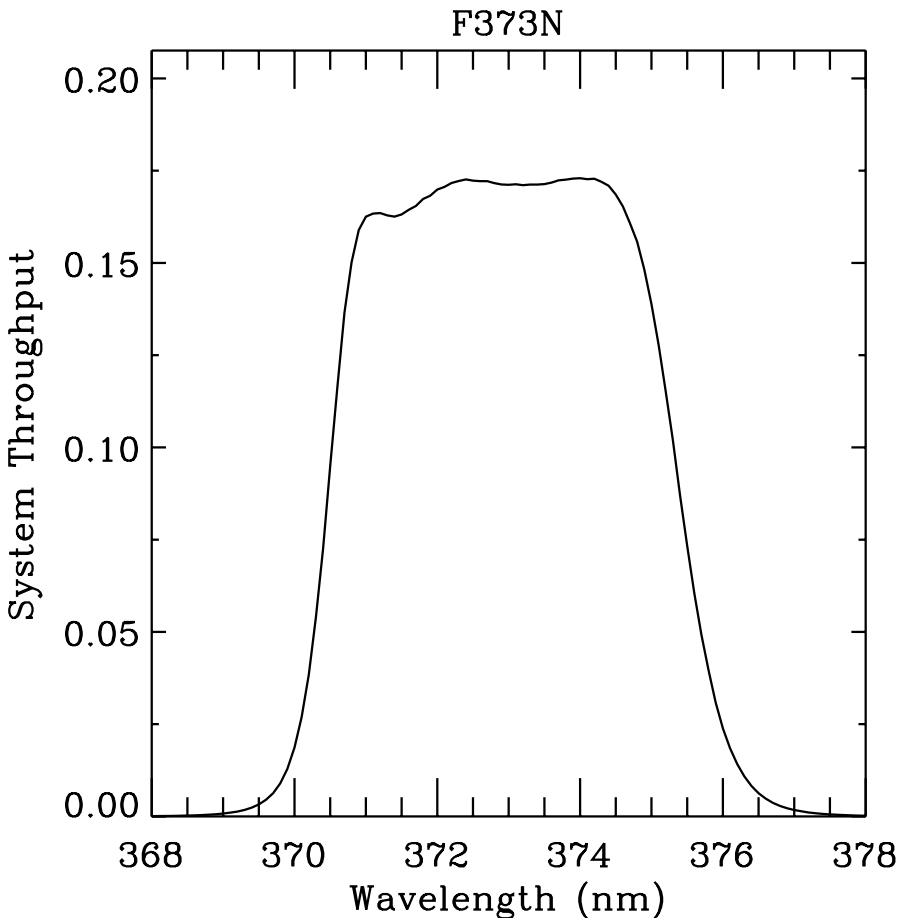

Figure A.29: Point source S/N vs. V+ABν for the F373N. filter, assuming high sky backgrounds and a 5×5 pixel aperture.

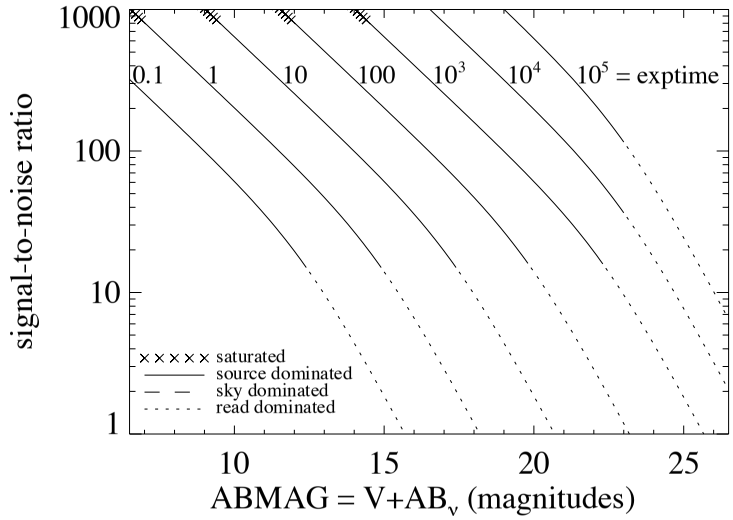

Figure A.30: Extended source S/N vs. V+ABν for the F373N. filter, assuming high sky backgrounds and a source uniformly filling a 1 arcsec^2 aperture.

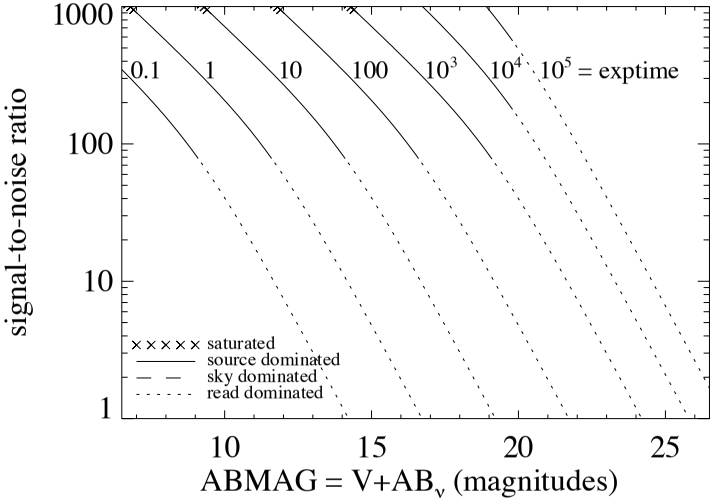

UVIS/F390M

Description

Ca II continuum filter.

Figure A.31: Integrated system throughput for F390M.

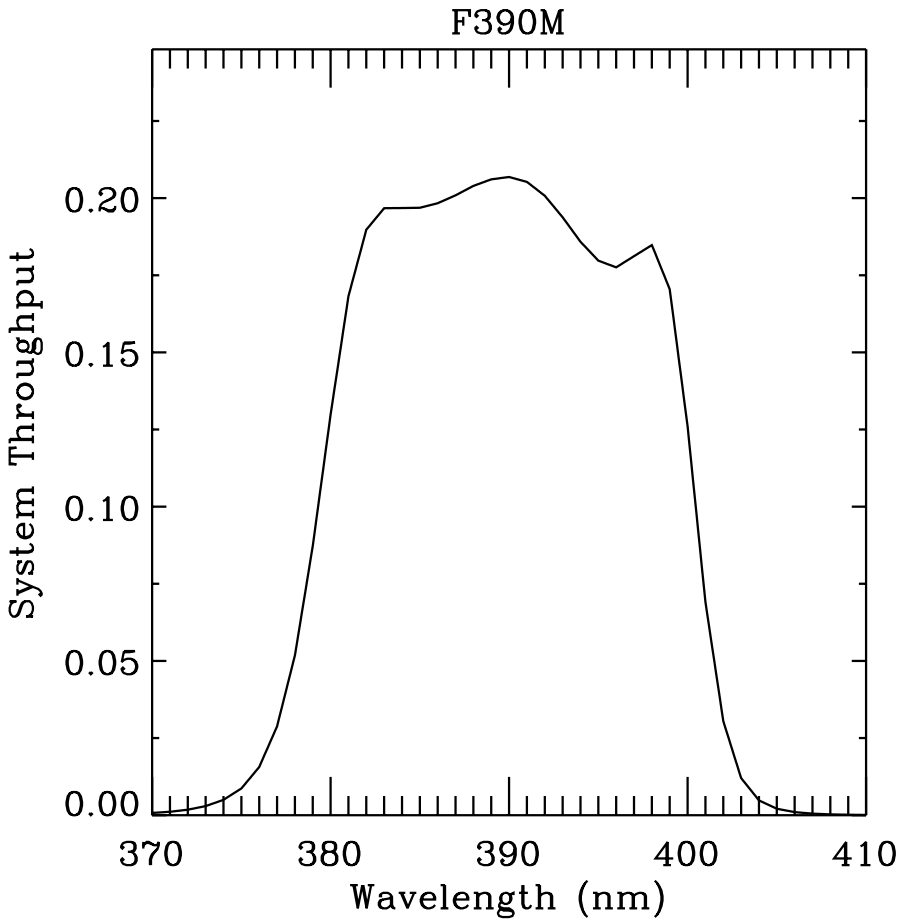

Figure A.32: Point source S/N vs. V+ABν for the F390M filter, assuming high sky backgrounds and a 5×5 pixel aperture.

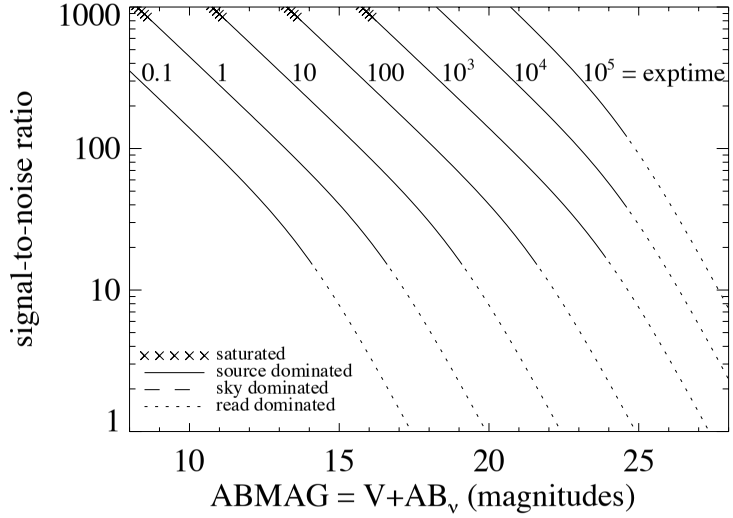

Figure A.33: Extended source S/N vs. V+ABν for the F390M filter, assuming high sky backgrounds and a source uniformly filling a 1 arcsec^2 aperture.

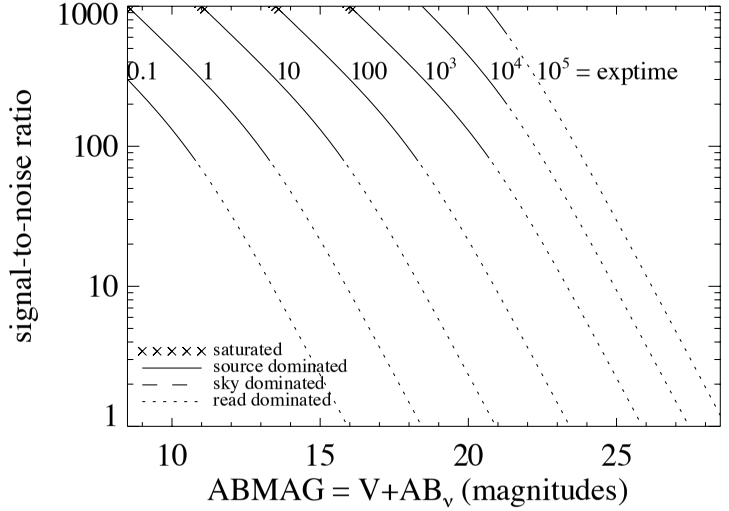

UVIS/F390W

Description

Washington *C* filter.

Figure A.34: Integrated system throughput for F390W.

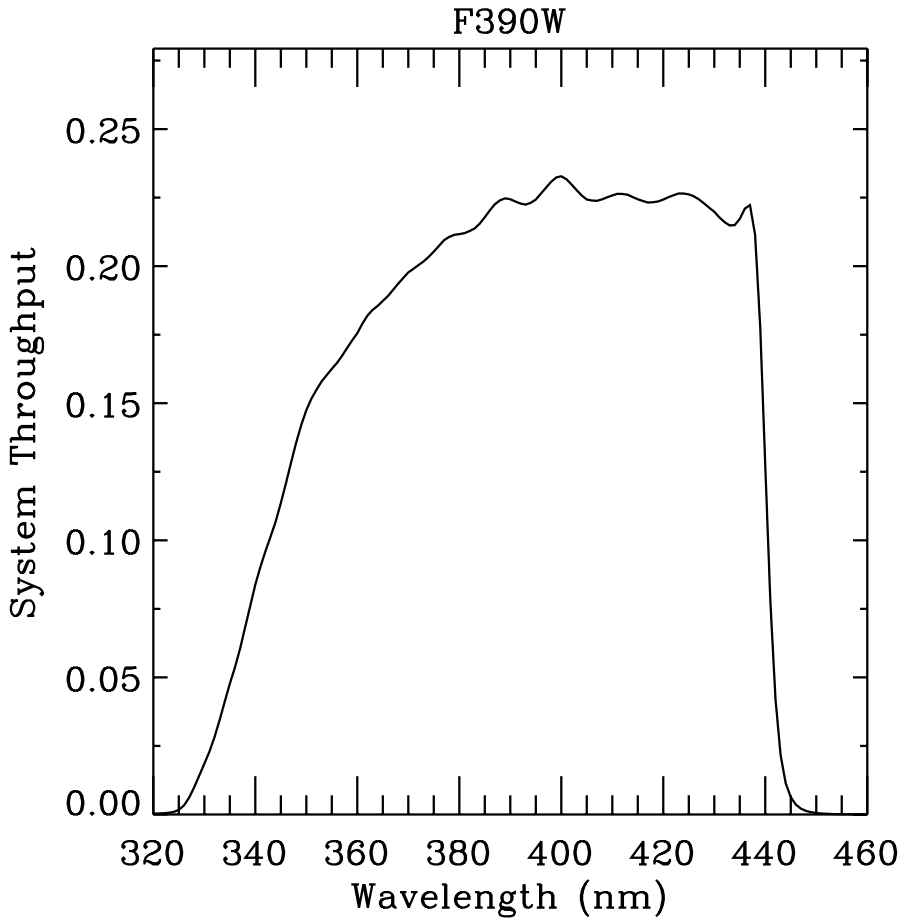

Figure A.35: Point source S/N vs. V+ABν for the F390W filter, assuming high sky backgrounds and a 5×5 pixel aperture.

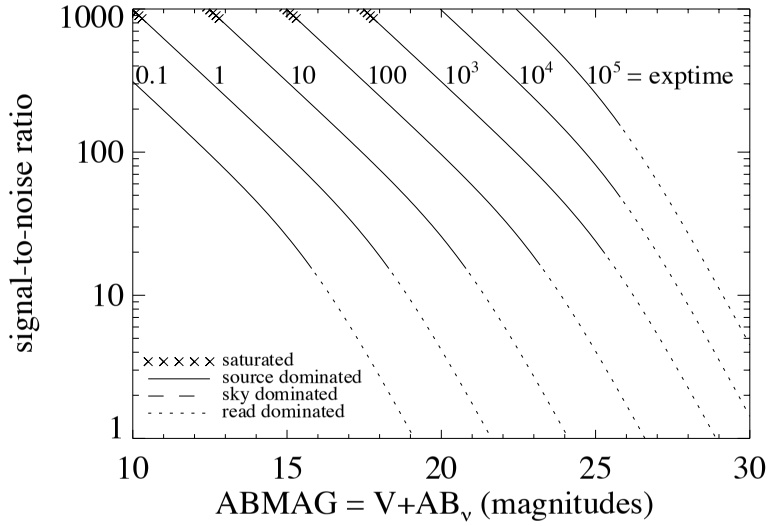

Figure A.36: Extended source S/N vs. V+ABν for the F390W filter, assuming high sky backgrounds and a source uniformly filling a 1 arcsec^2 aperture.

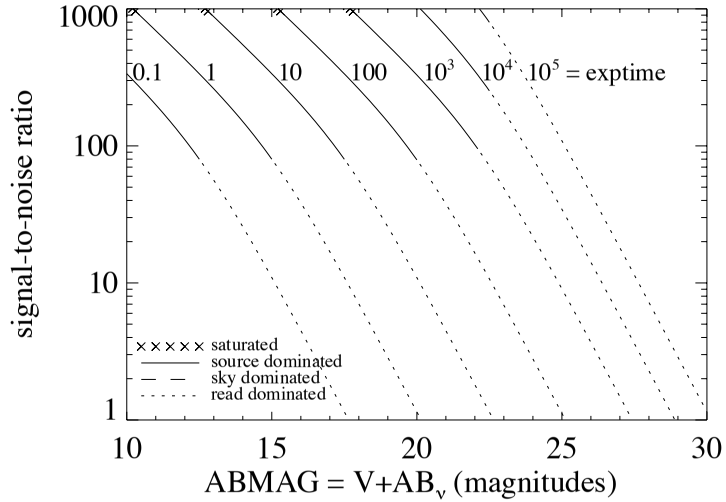

UVIS/F395N

Description

Ca II 3933/3968 filter.

Figure A.37: Integrated system throughput for F395N.

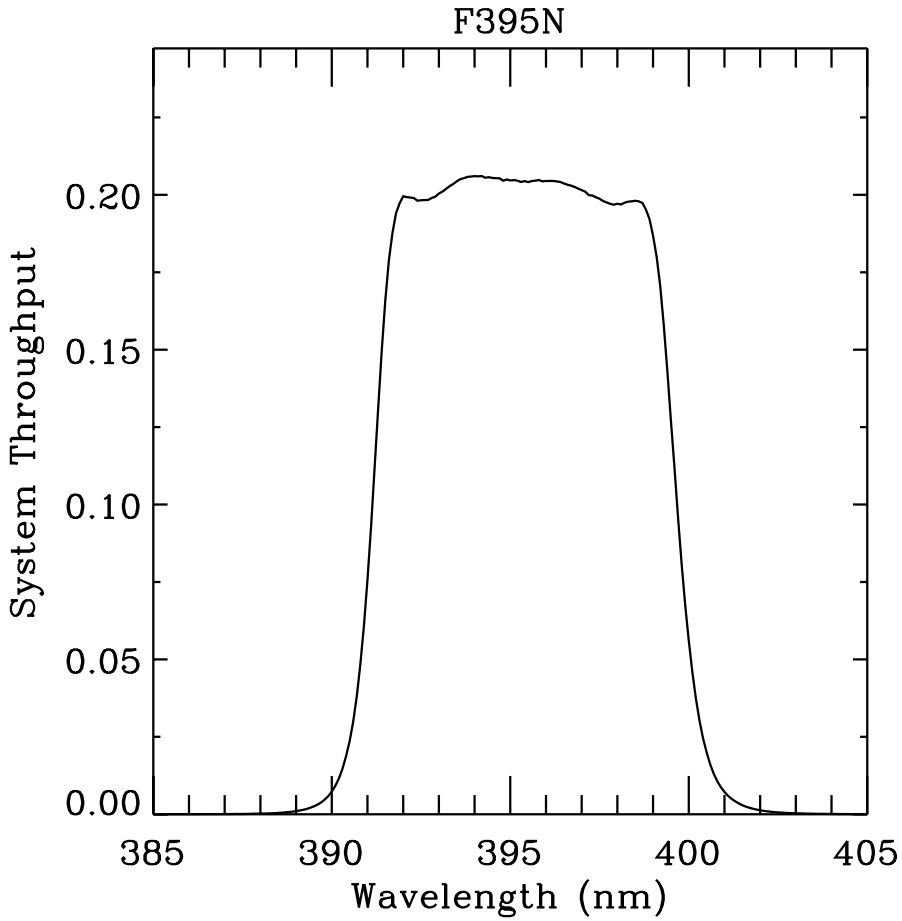

Figure A.38: Point source S/N vs. V+ABν for the F395N filter, assuming high sky backgrounds and a 5×5 pixel aperture.

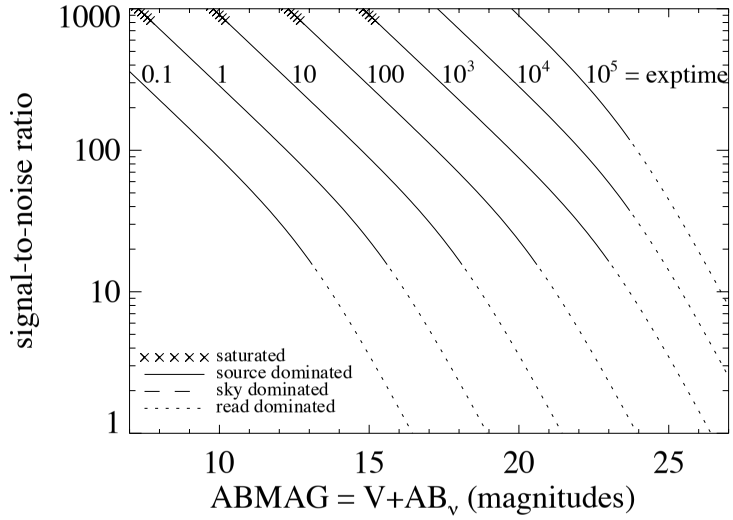

Figure A.39: Extended source S/N vs. V+ABν for the F395N filter, assuming high sky backgrounds and a source uniformly filling a 1 arcsec^2 aperture.

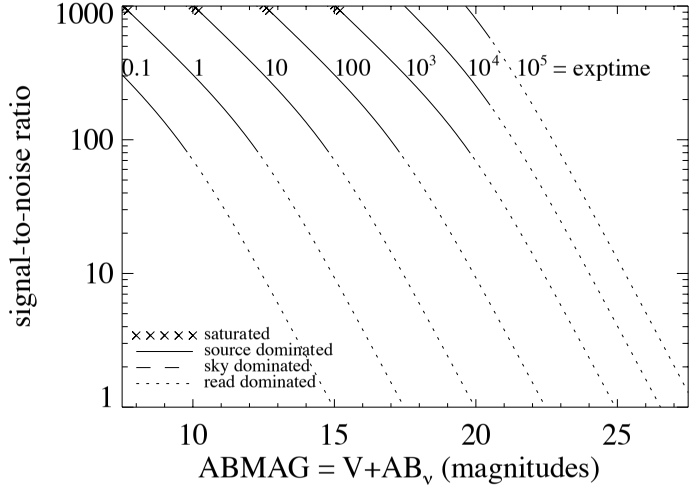

UVIS/F410M

Description

Strömgren *v* filter.

Figure A.40: Integrated system throughput for F410M.

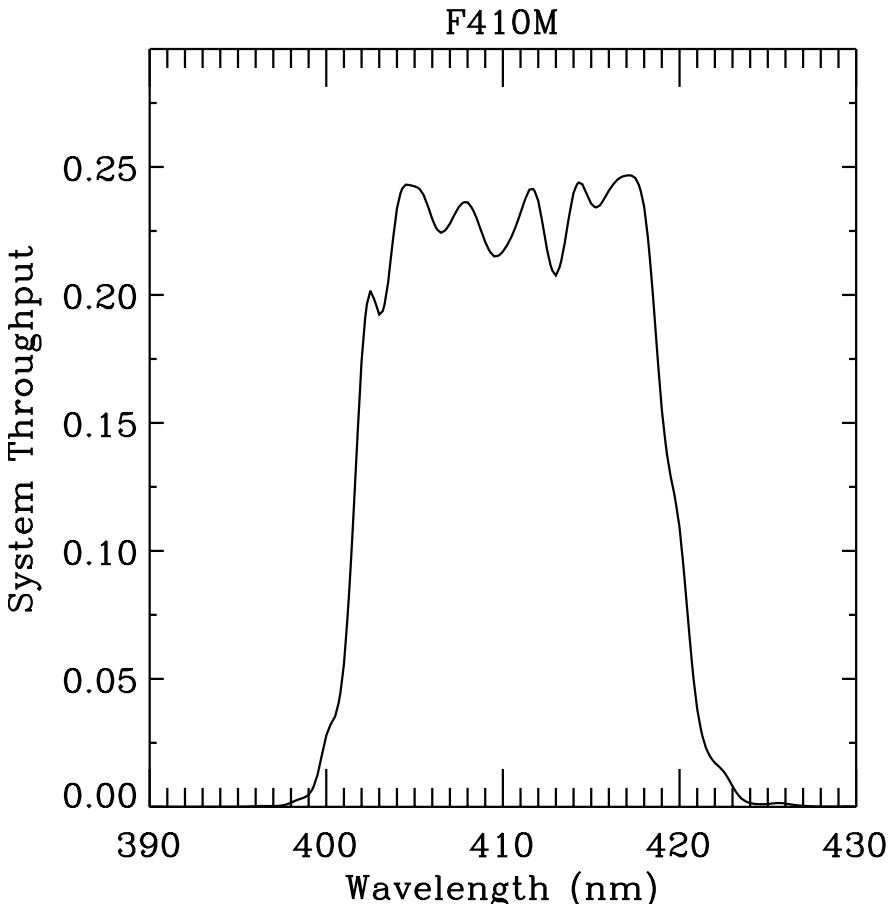

Figure A.41: Point source S/N vs. V+ABν for the F410M filter, assuming high sky backgrounds and a 5×5 pixel aperture.

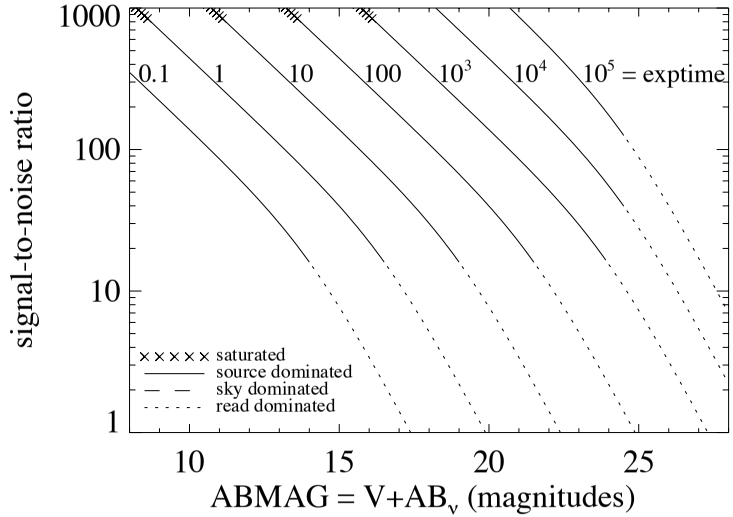

Figure A.42: Extended source S/N vs. V+ABν for the F410M filter, assuming high sky backgrounds and a source uniformly filling a 1 arcsec^2 aperture.

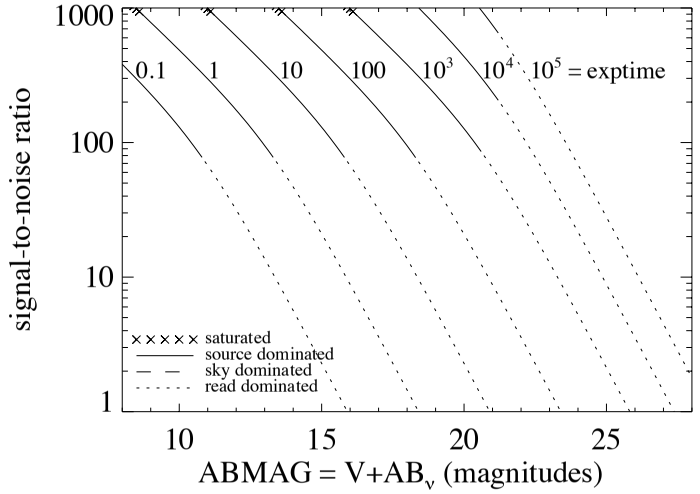

UVIS/F438W

Description

WFPC2 *B* filter.

Figure A.43: Integrated system throughput for F438W.

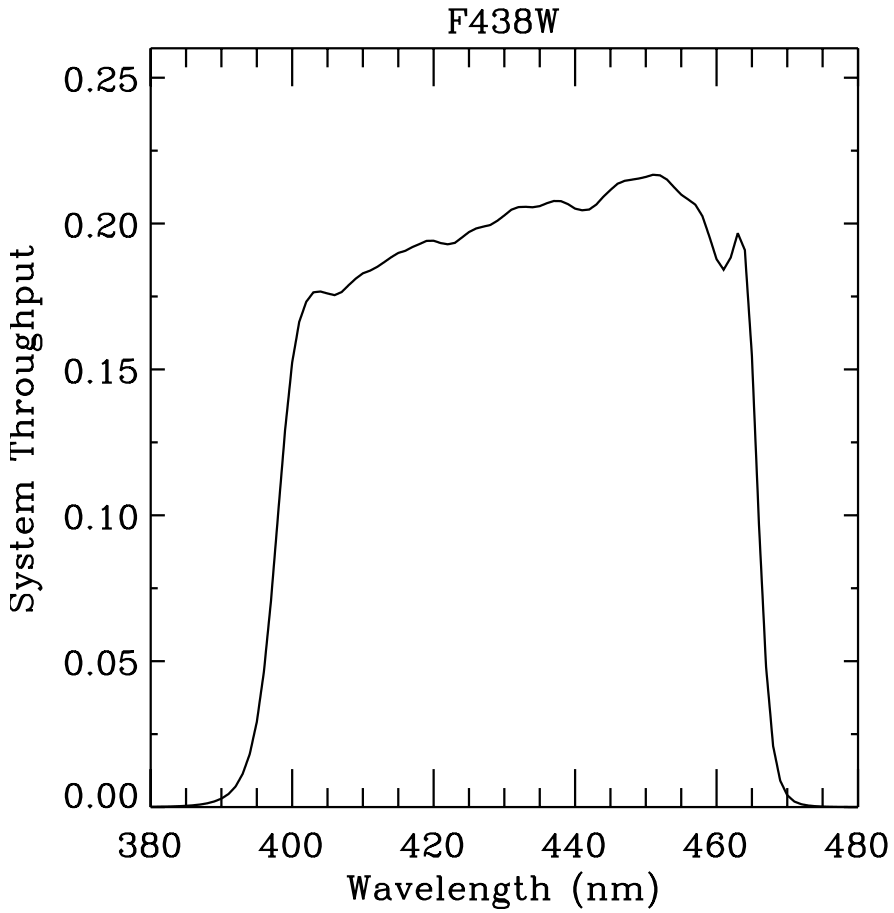

Figure A.44: Point source S/N vs. V+ABν for the F438W filter, assuming high sky backgrounds and a 5×5 pixel aperture.

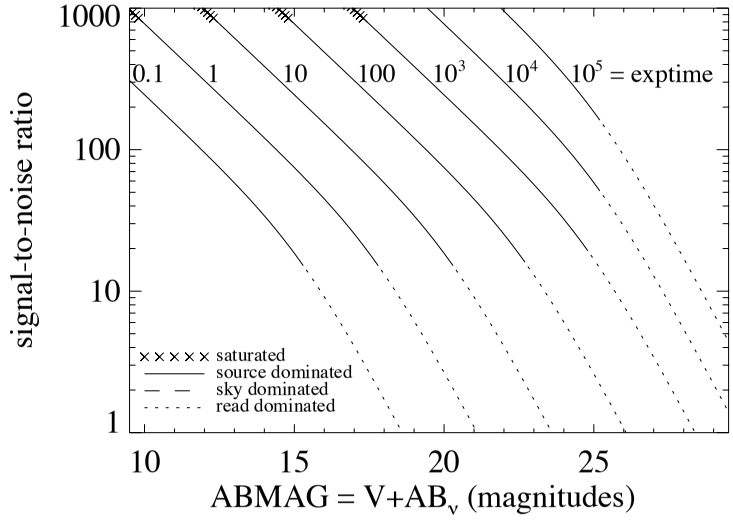

Figure A.45: Extended source S/N vs. V+ABν for the F438W filter, assuming high sky backgrounds and a source uniformly filling a 1 arcsec^2 aperture.

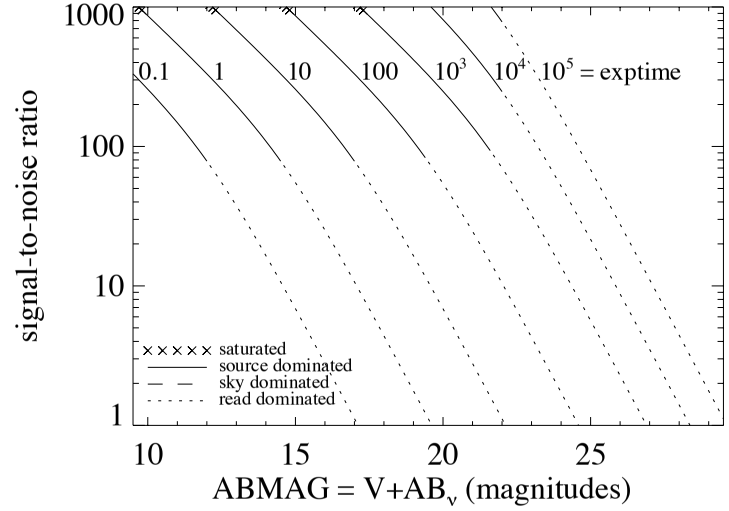

UVIS/F467M

Description

Strömgren *b* filter.

Figure A.46: Integrated system throughput for F467M.

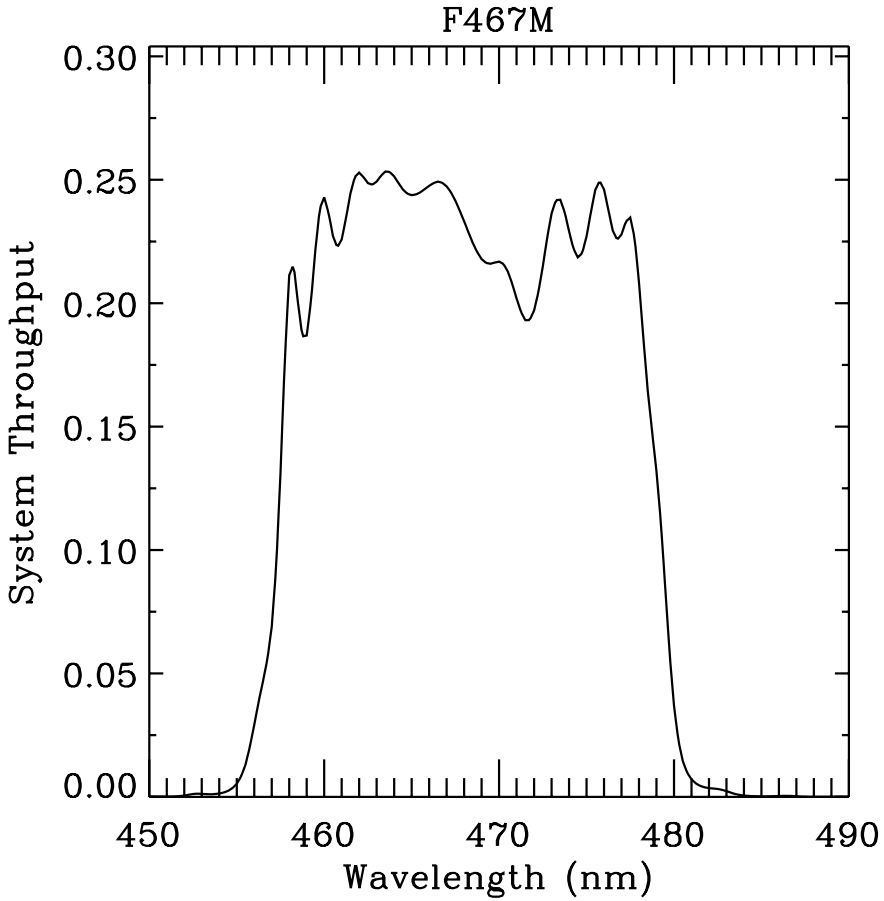

Figure A.47: Point Source S/N vs. V+ABν for the F467M filter, assuming high sky backgrounds and a 5×5 pixel aperture.

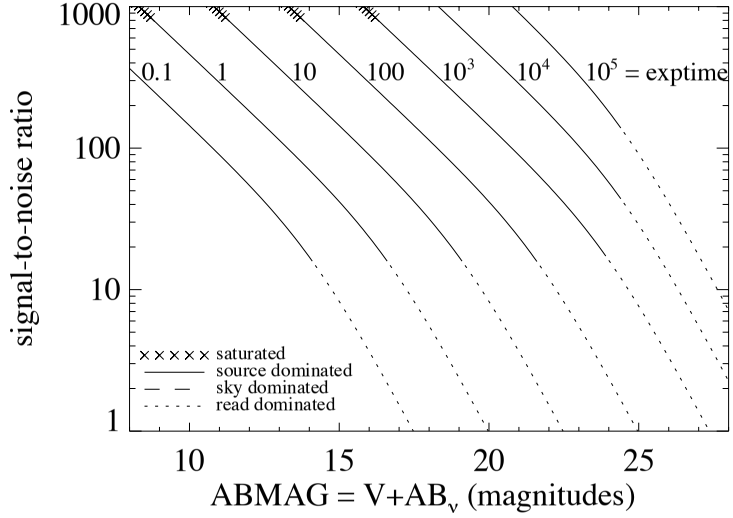

Figure A.48: Extended Source S/N vs. V+ABν for the F467M filter, assuming high sky backgrounds and a source uniformly filling a 1 arcsec^2 aperture.

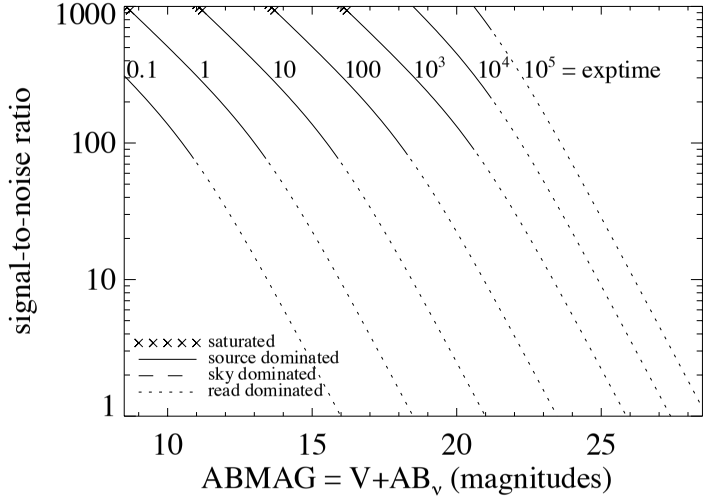

UVIS/F469N

Description

He II 4686 filter.

Figure A.49: Integrated system throughput for F469N.

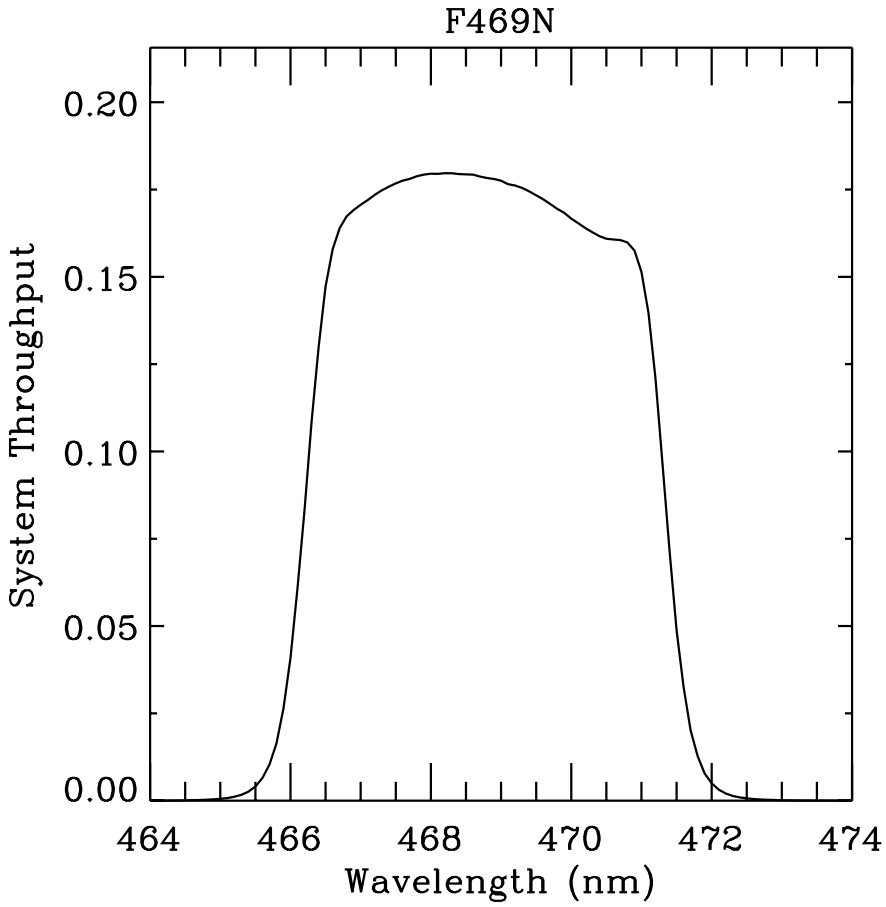

Figure A.50: Point source S/N vs. V+ABν for the F469N filter, assuming high sky backgrounds and a 5×5 pixel aperture.

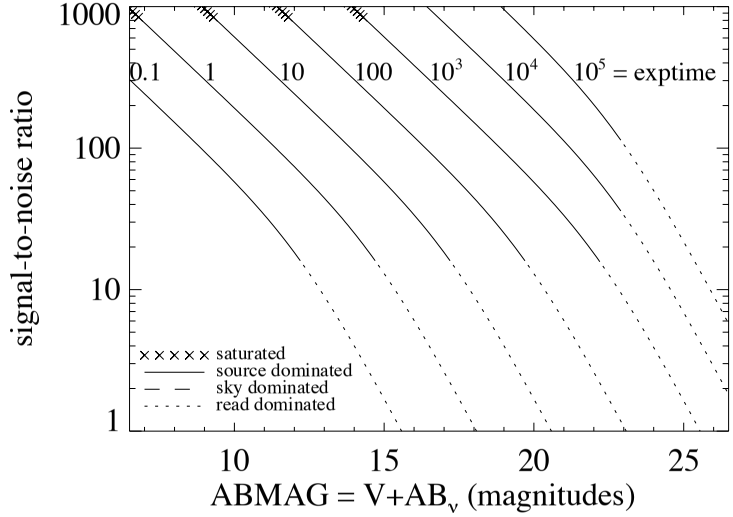

Figure A.51: Extended source S/N vs. V+ABν for the F469N filter, assuming high sky backgrounds and a source uniformly filling a 1 arcsec^2 aperture.

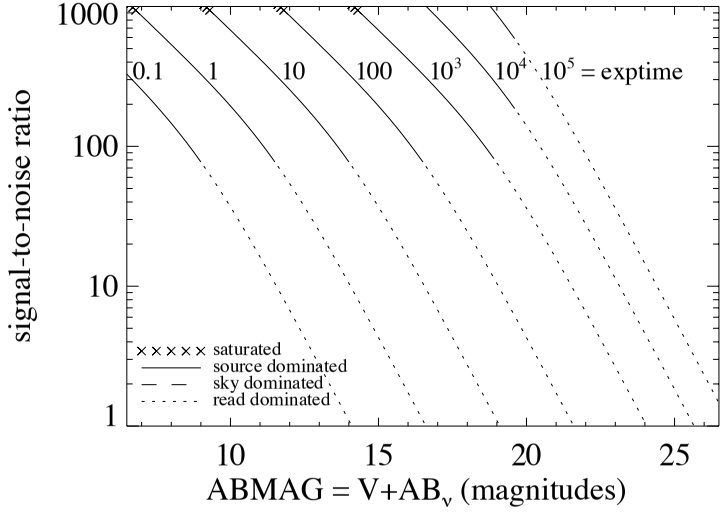

UVIS/F475W

Description

Sloan Digital Sky Survey g' filter.

Figure A.52: Integrated system throughput for F475W.

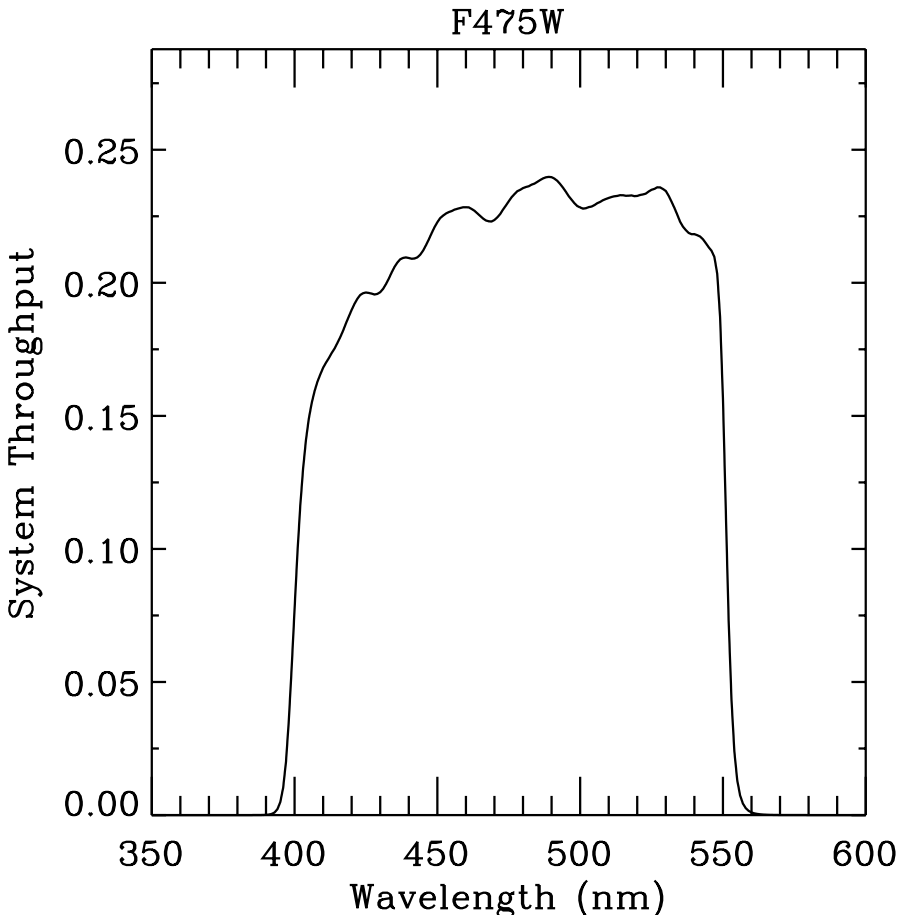

Figure A.53: Point source S/N vs. V+ABν for the F475W filter, assuming high sky backgrounds and a 5×5 pixel aperture.

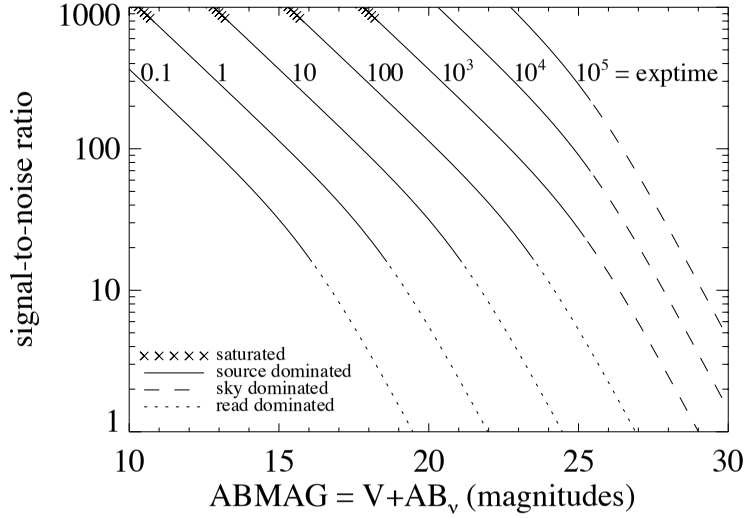

Figure A.54: Extended source S/N vs. V+ABν for the F475W filter, assuming high sky backgrounds and a source uniformly filling a 1 arcsec^2 aperture.

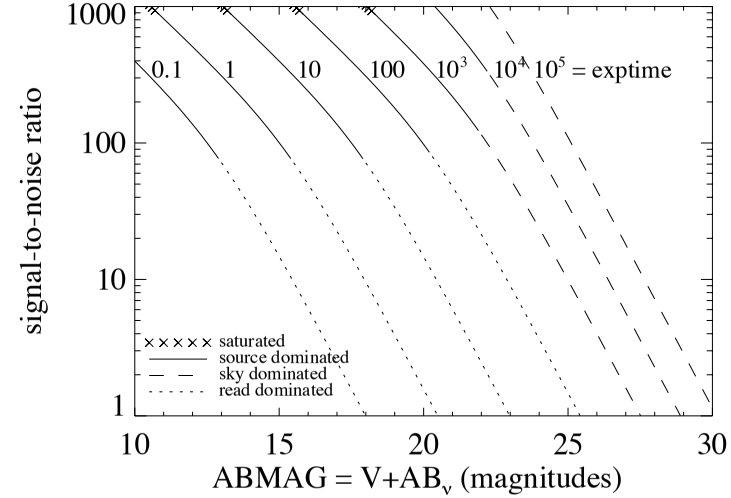

UVIS/F475X

Description

Extremely wide blue filter.

Figure A.55: Integrated system throughput for F475X.

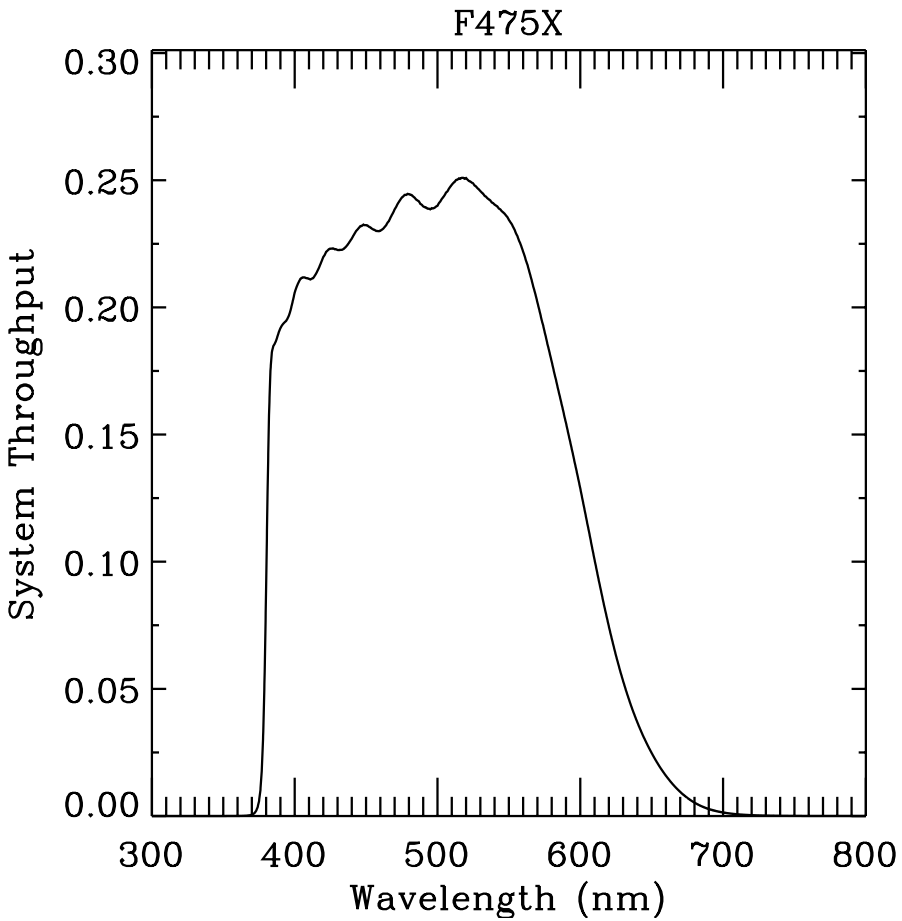

Figure A.56: Point source S/N vs. V+ABν for the F475X filter, assuming high sky backgrounds and a 5×5 pixel aperture.

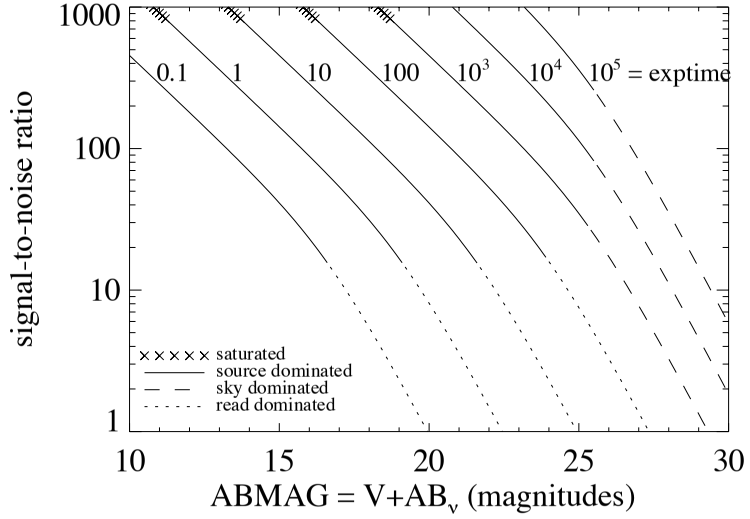

Figure A.57: Extended source S/N vs. V+ABν for the F475X filter, assuming high sky backgrounds and a source uniformly filling a 1 arcsec^2 aperture.

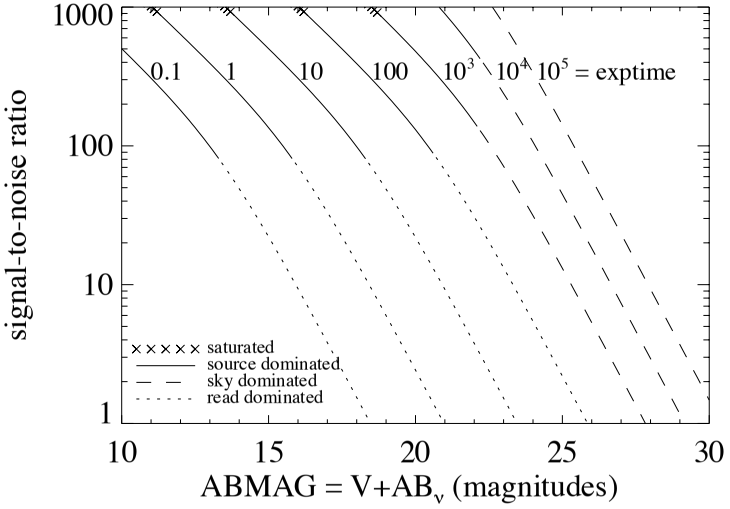

UVIS/F487N

Description

Hβ 4861 filter.

Figure A.58: Integrated system throughput for F487N.

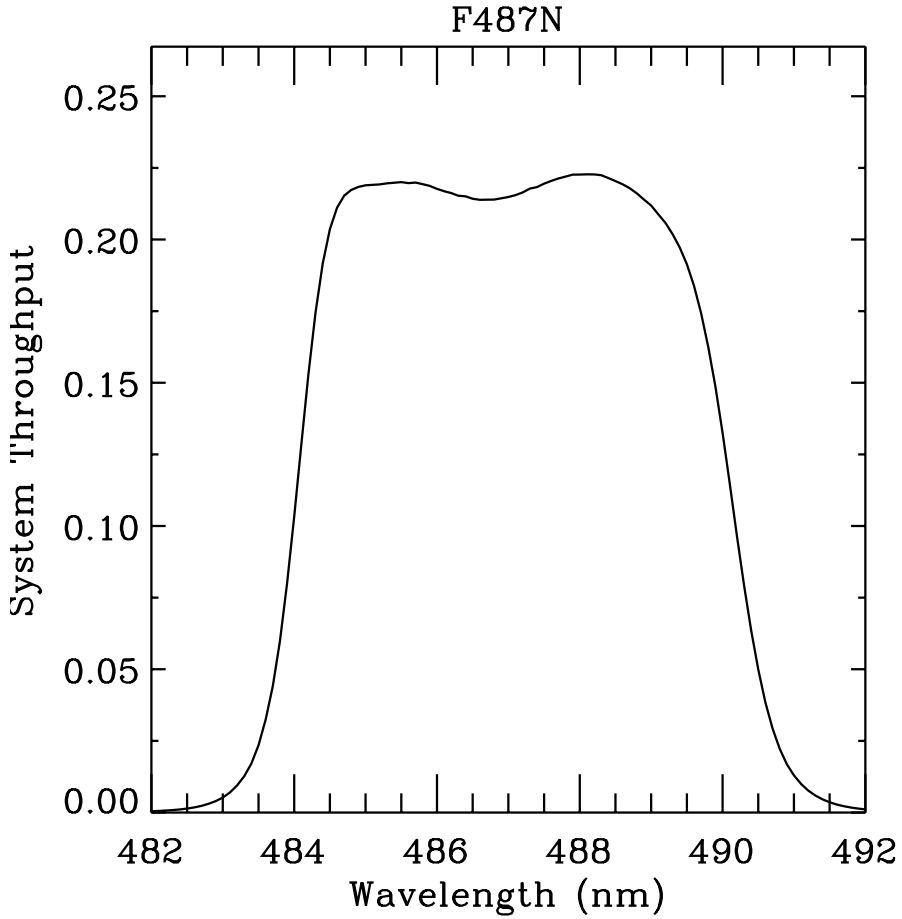

Figure A.59: Point source S/N vs. V+ABν for the F487N filter, assuming high sky backgrounds and a 5×5 pixel aperture.

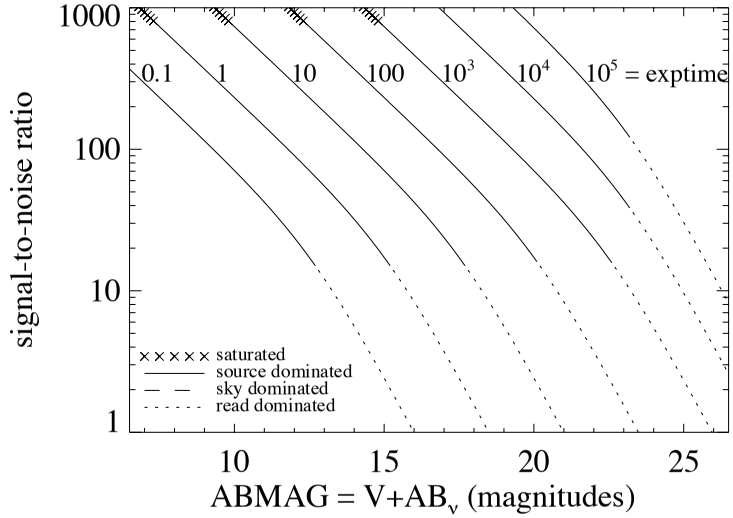

Figure A.60: Extended source S/N vs. V+ABν for the F487N filter, assuming high sky backgrounds and a source uniformly filling a 1 arcsec^2 aperture.

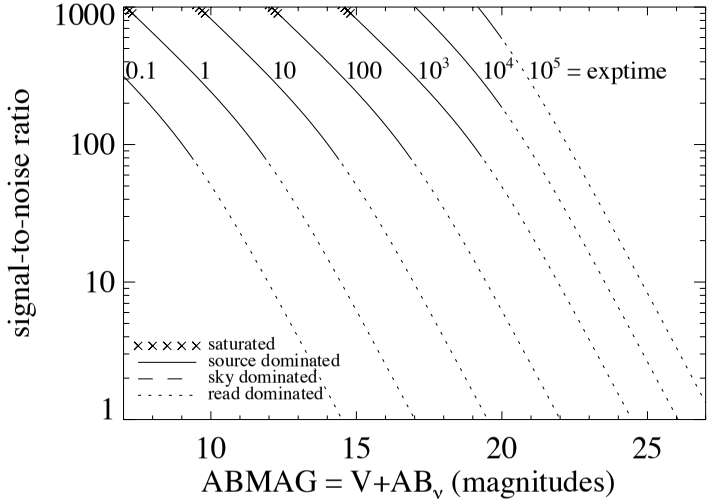

UVIS/F502N

Description

[O III] 5007 filter.

Figure A.61: Integrated system throughput for F502N.

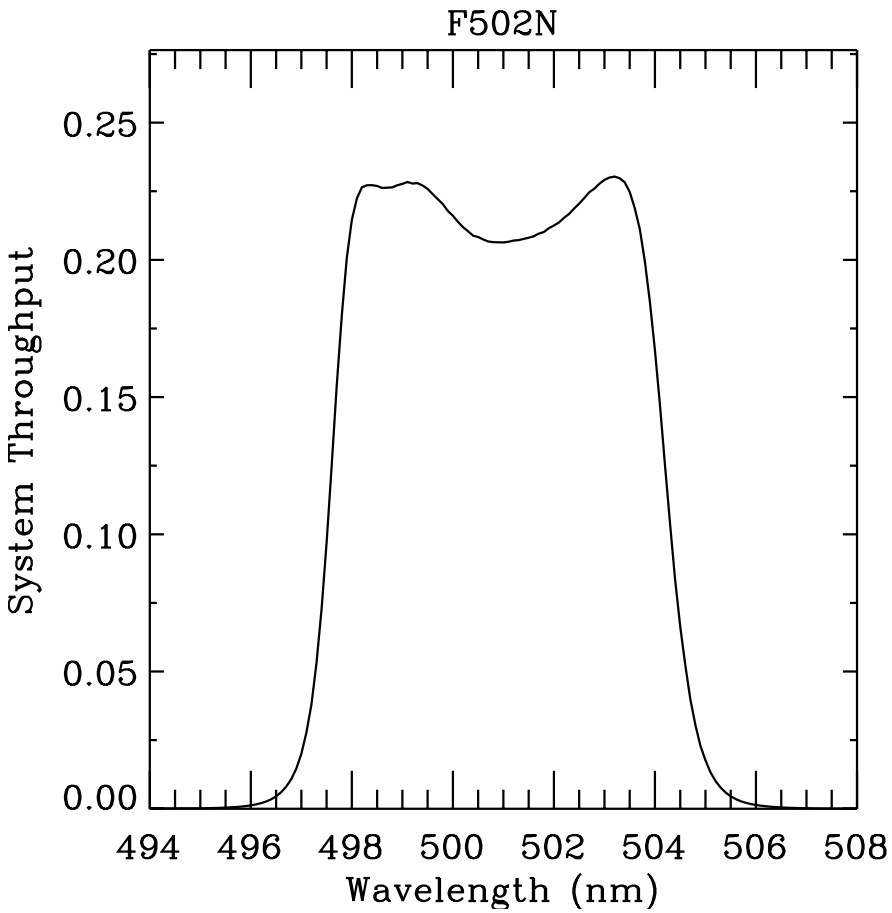

Figure A.62: Point source S/N vs. V+ABν for the F502N filter, assuming high sky backgrounds and a 5×5 pixel aperture.

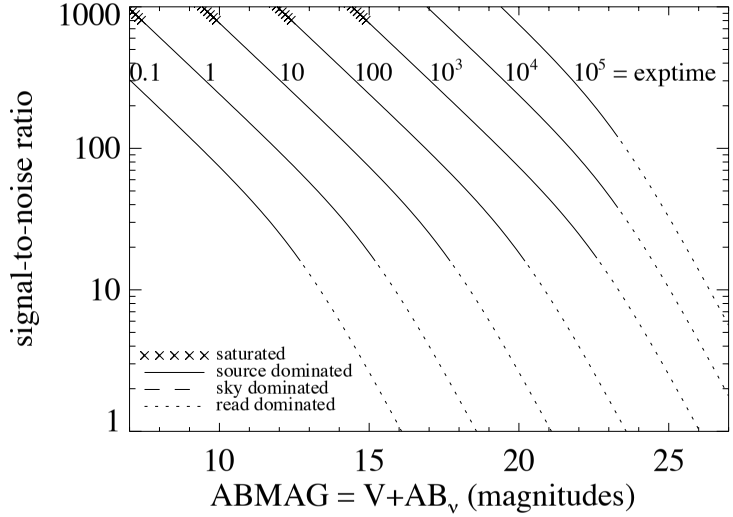

Figure A.63: Extended source S/N vs. V+ABν for the F502N filter, assuming high sky backgrounds and a source uniformly filling a 1 arcsec^2 aperture.

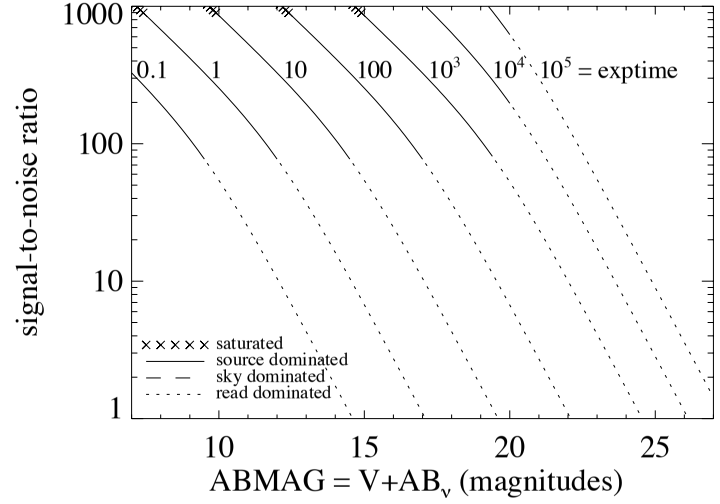

UVIS/F547M

Description

Strömgren *y* filter.

Figure A.64: Integrated system throughput for F547M.

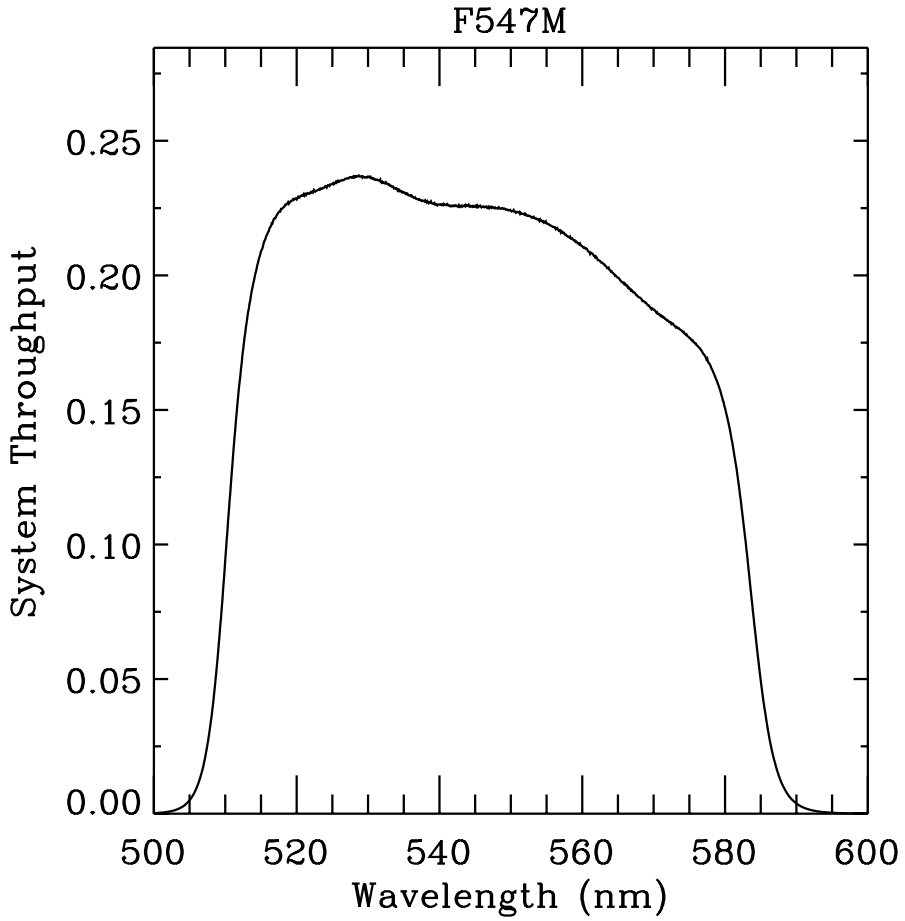

Figure A.65: Point source S/N vs. V+ABν for the F547M filter, assuming high sky backgrounds and a 5×5 pixel aperture.

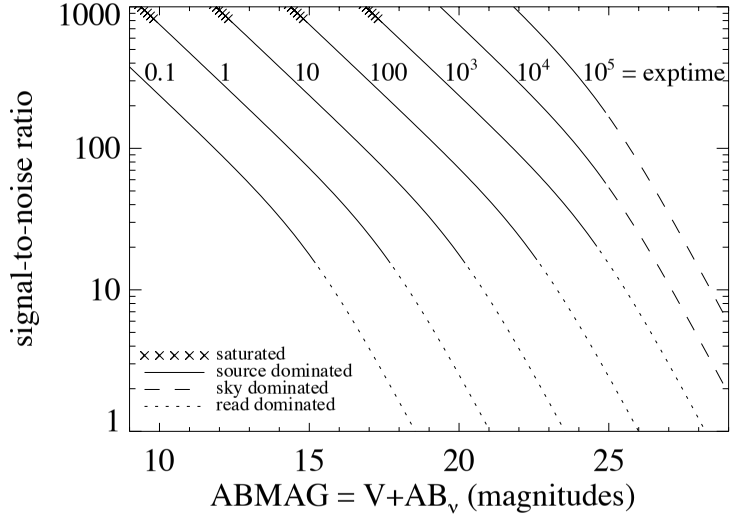

Figure A.66: Extended source S/N vs. V+ABν for the F547M filter, assuming high sky backgrounds and a source uniformly filling a 1 arcsec^2 aperture.

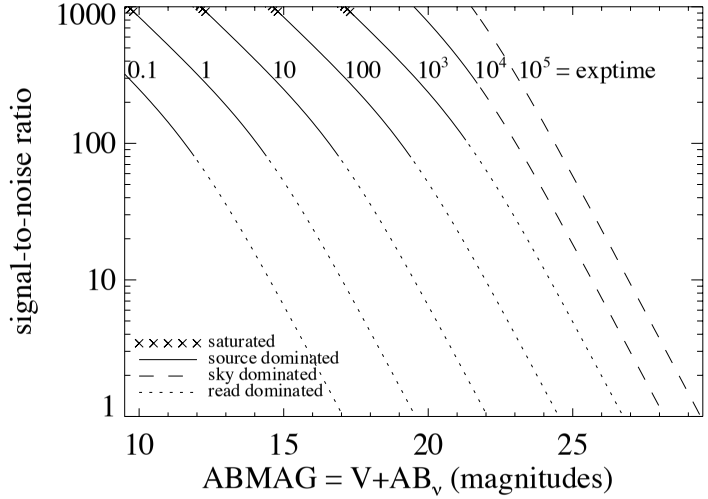

UVIS/F555W

Description

WFPC2 *V* filter.

Figure A.67: Integrated system throughput for F555W.

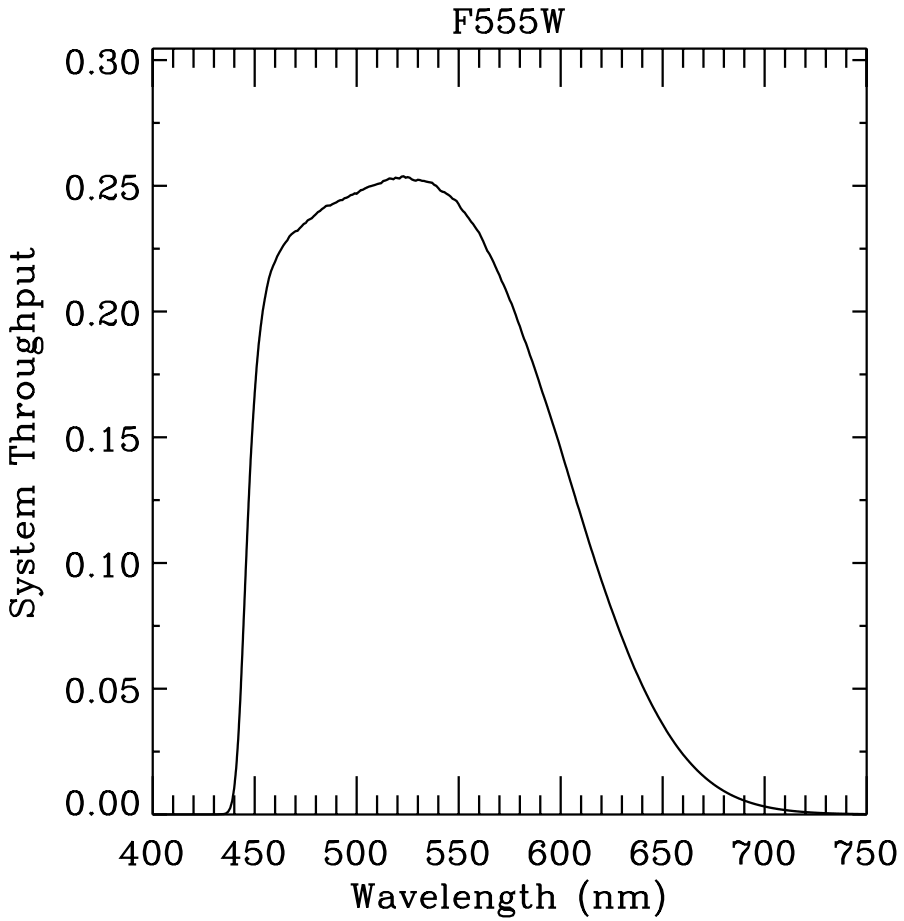

Figure A.68: Point source S/N vs. V+ABν for the F555W filter, assuming high sky backgrounds and a 5×5 pixel aperture.

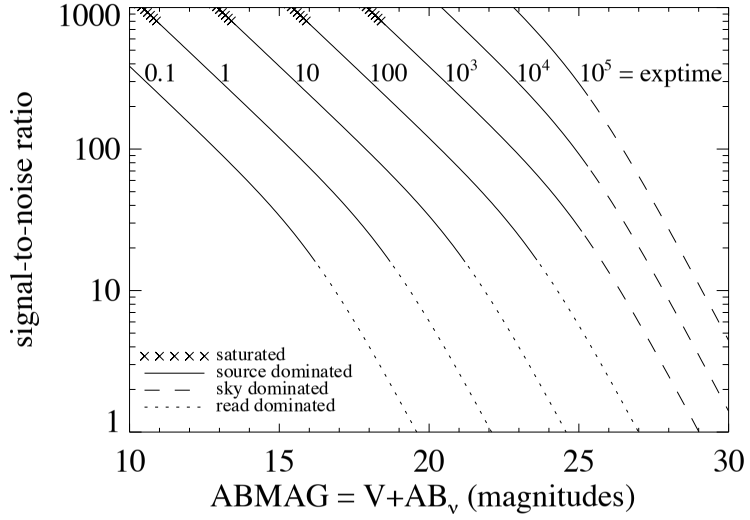

Figure A.69: Extended source S/N vs. V+ABν for the F555W filter, assuming high sky backgrounds and a source uniformly filling a 1 arcsec^2 aperture.

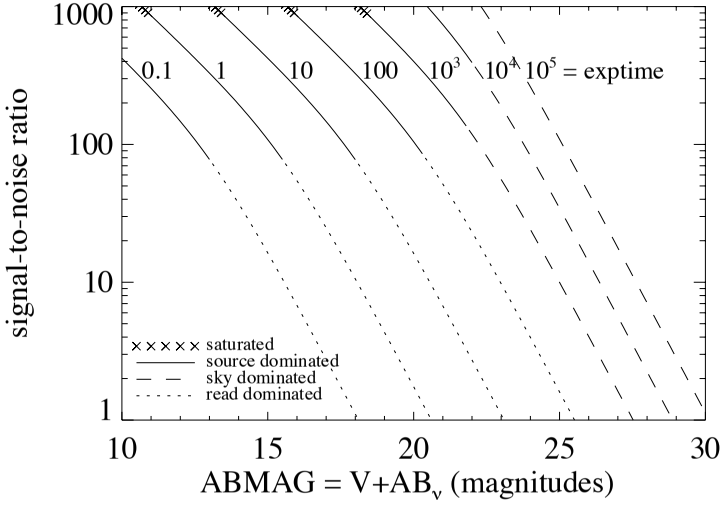

UVIS/F600LP

Description

Long-pass filter.

Figure A.70: Integrated system throughput for F600LP.

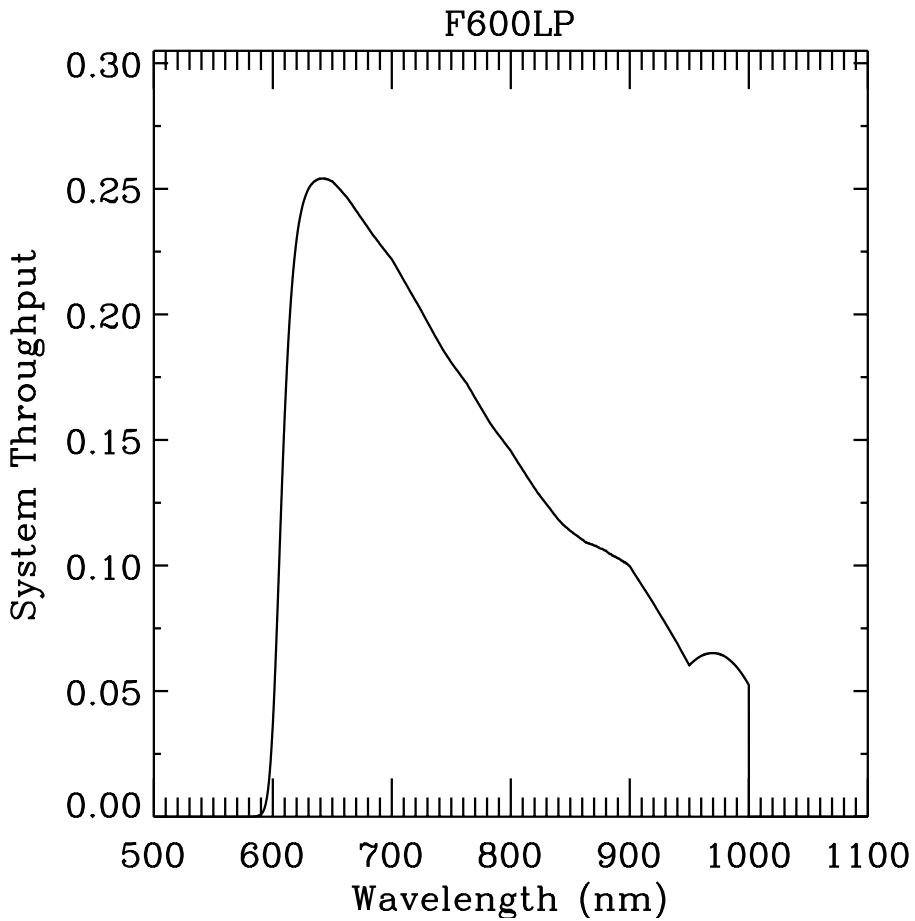

Figure A.71: Point source S/N vs. V+ABν for the F600LP filter, assuming high sky backgrounds and a 5×5 pixel aperture.

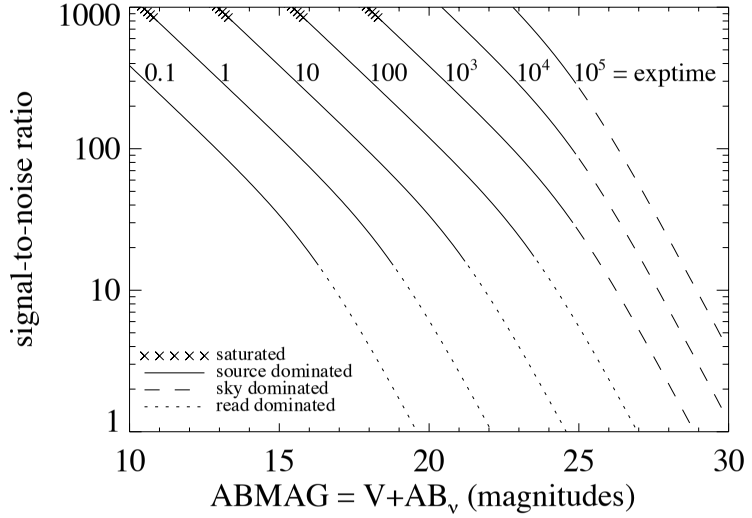

Figure A.72: Extended source S/N vs. V+ABν for the F600LP filter, assuming high sky backgrounds and a source uniformly filling a 1 arcsec^2 aperture.

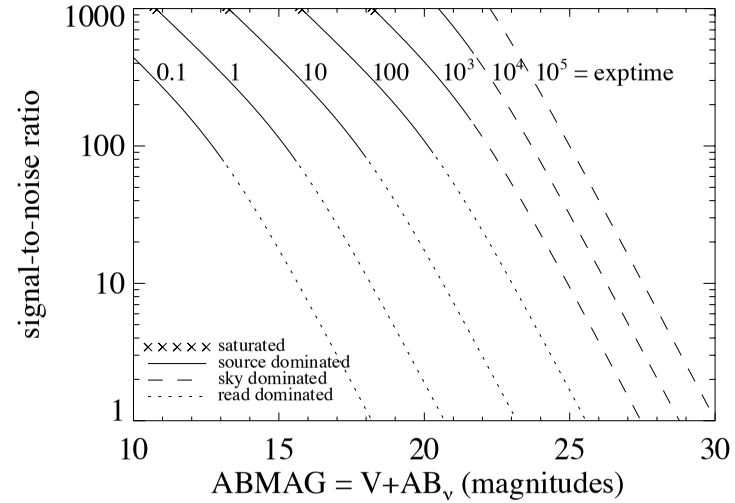

UVIS/F606W

Description

WFPC2 Wide *V* filter.

Figure A.73: Integrated system throughput for F606W.

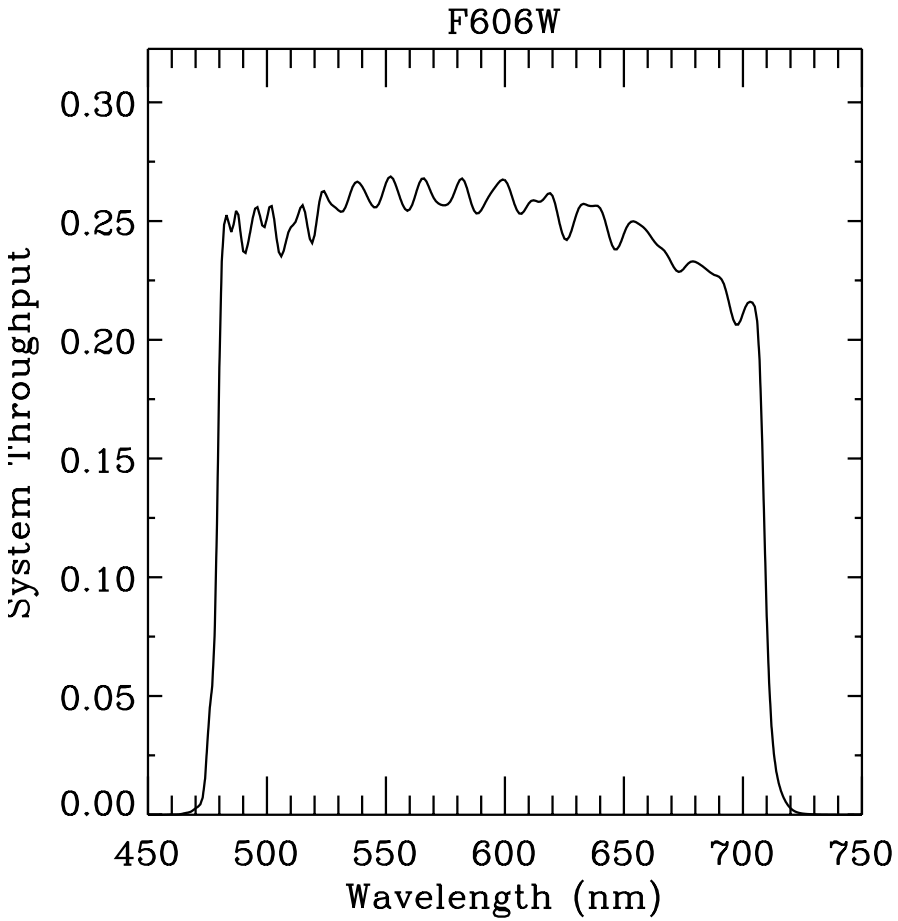

Figure A.74: Point source S/N vs. V+ABν for the F606W filter, assuming high sky backgrounds and a 5×5 pixel aperture.

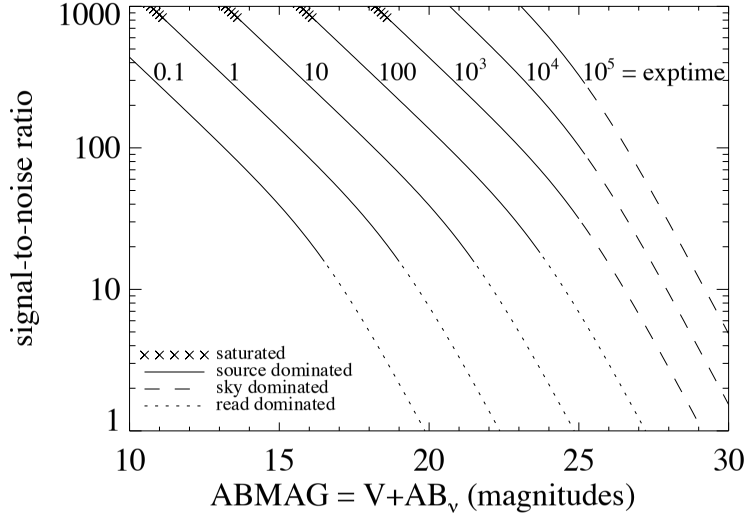

Figure A.75: Extended source S/N vs. V+ABν for the F606W filter, assuming high sky backgrounds and a source uniformly filling a 1 arcsec^2 aperture.

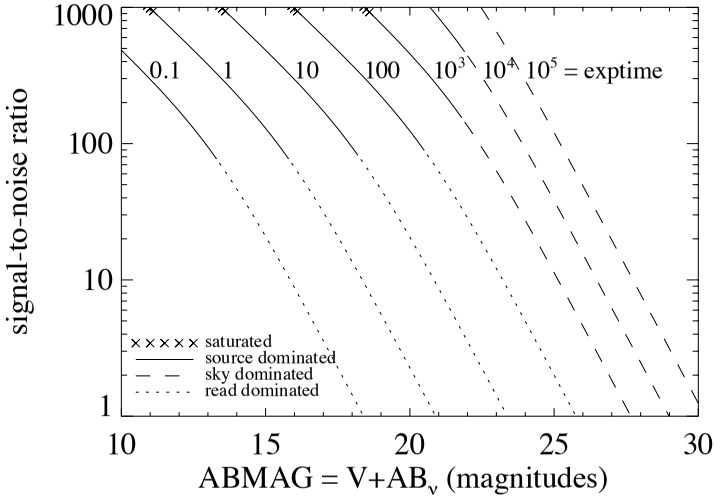

UVIS/F621M

Description

11% passband filter.

Figure A.76: Integrated system throughput for F621M.

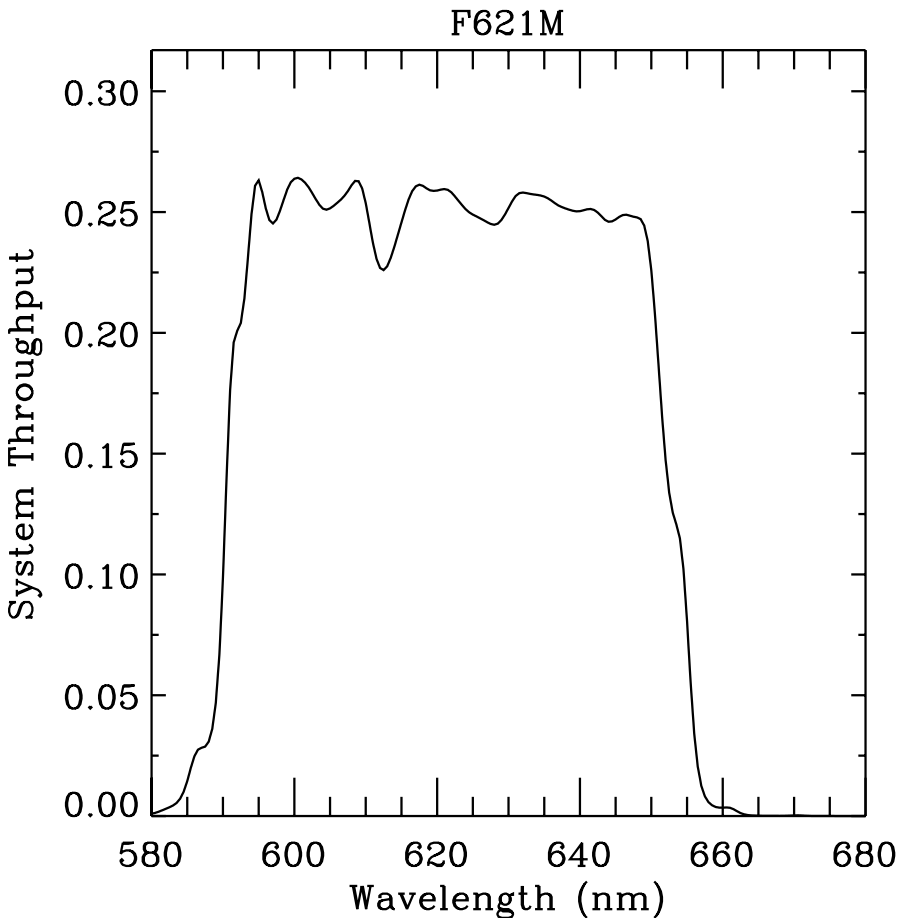

Figure A.77: Point source S/N vs. V+ABν for the F621M filter, assuming high sky backgrounds and a 5×5 pixel aperture.

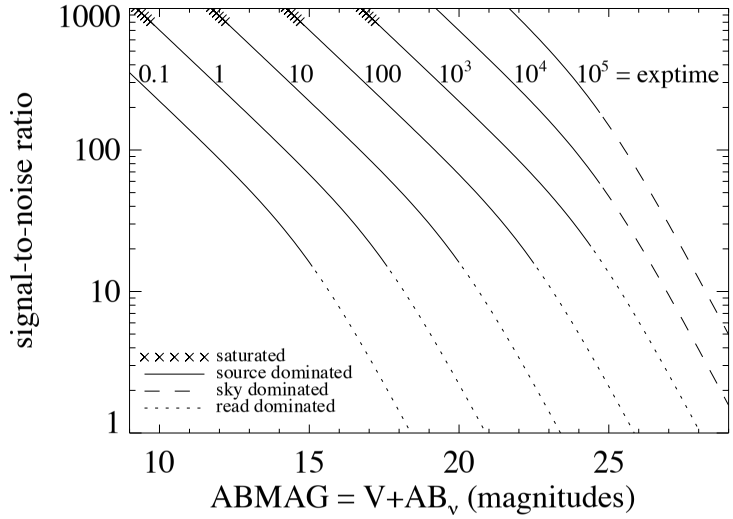

Figure A.78: Extended source S/N vs. V+ABν for the F621M filter, assuming high sky backgrounds and a source uniformly filling a 1 arcsec^2 aperture.

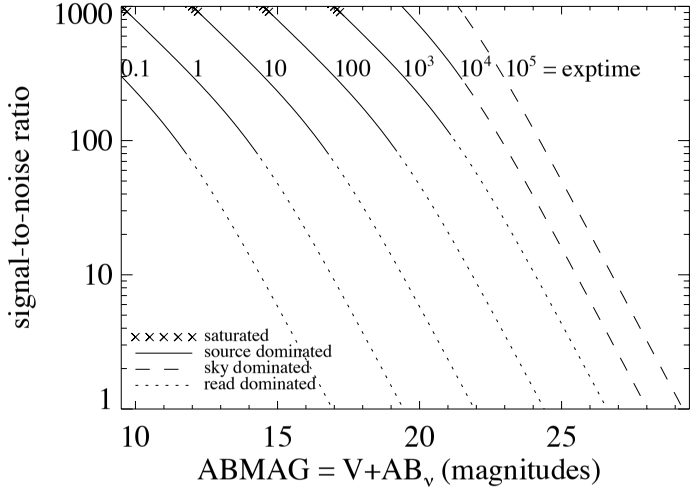

UVIS/F625W

Description

Sloan Digital Sky Survey r' filter.

Figure A.79: Integrated system throughput for F625W.

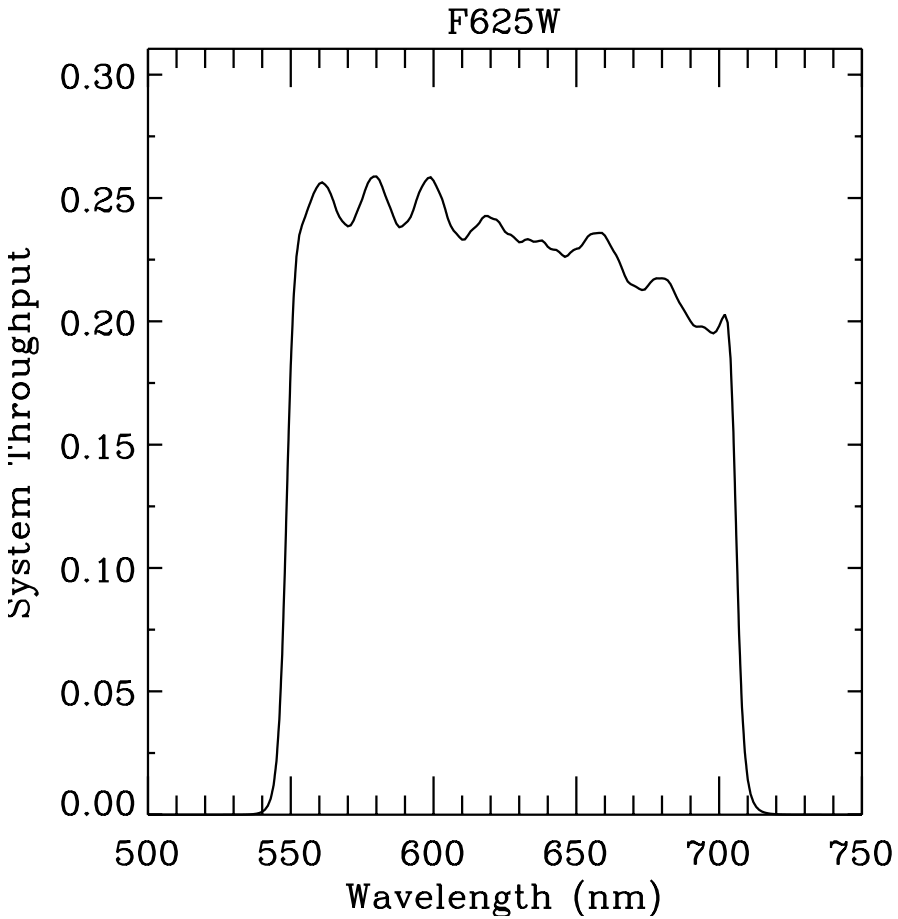

Figure A.80: Point source S/N vs. V+ABν for the F625W filter, assuming high sky backgrounds and a 5×5 pixel aperture.

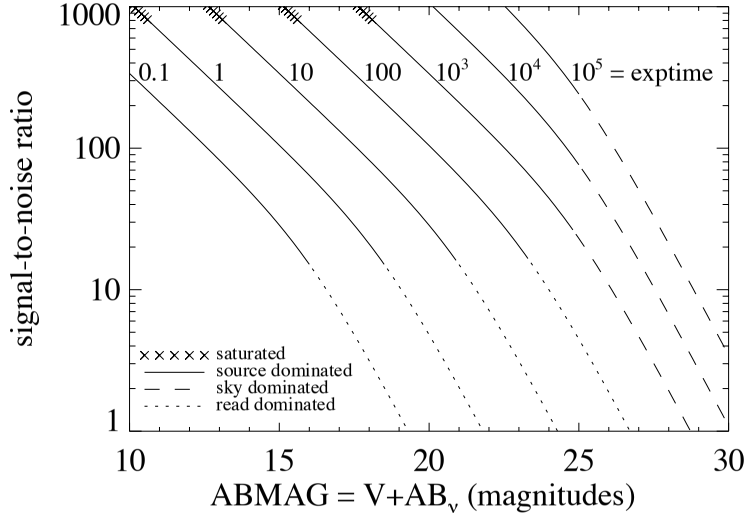

Figure A.81: Extended source S/N vs. V+ABν for the F625W filter, assuming high sky backgrounds and a source uniformly filling a 1 arcsec^2 aperture.

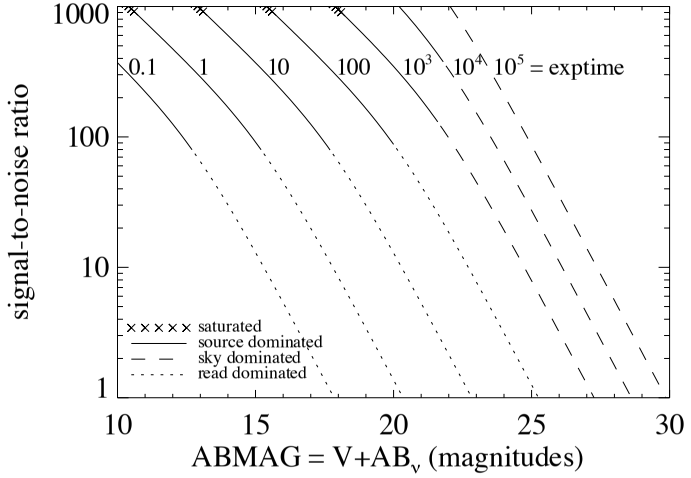

UVIS/F631N

Description

[O I] 6300 filter.

Figure A.82: Integrated system throughput for F631N.

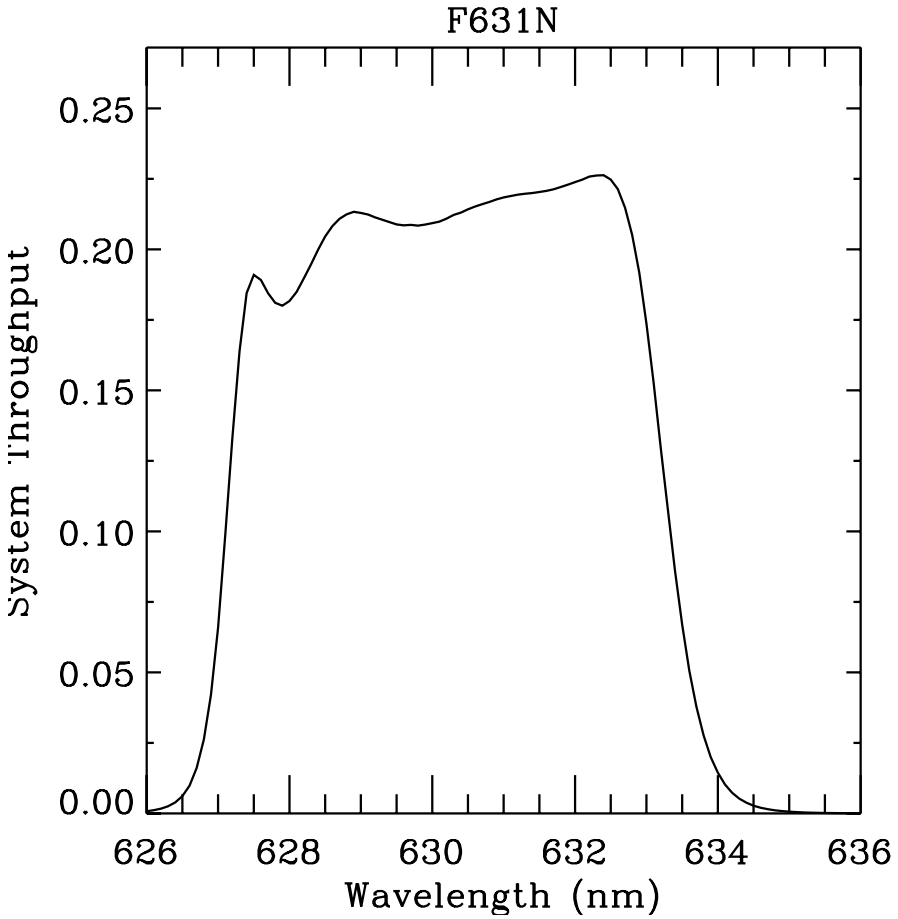

Figure A.83: Point source S/N vs. V+ABν for the F631N filter, assuming high sky backgrounds and a 5×5 pixel aperture.

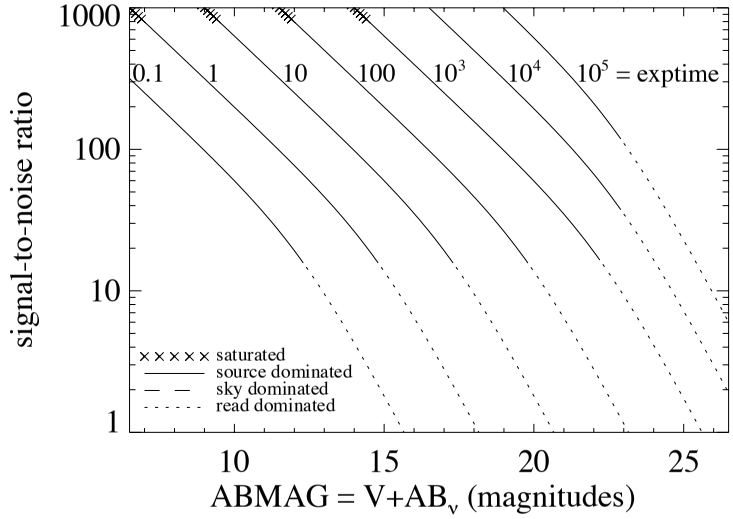

Figure A.84: Extended source S/N vs. V+ABν for the F631N filter, assuming high sky backgrounds and a source uniformly filling a 1 arcsec^2 aperture.

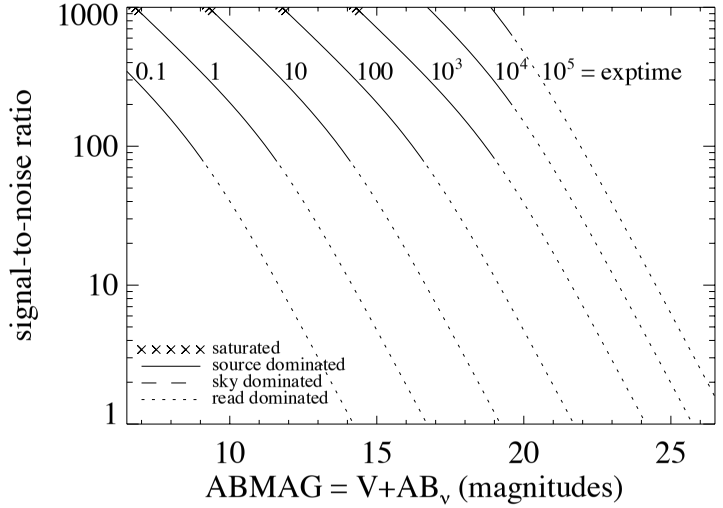

UVIS/F645N

Description

Continuum filter.

Figure A.85: Integrated system throughput for F645N.

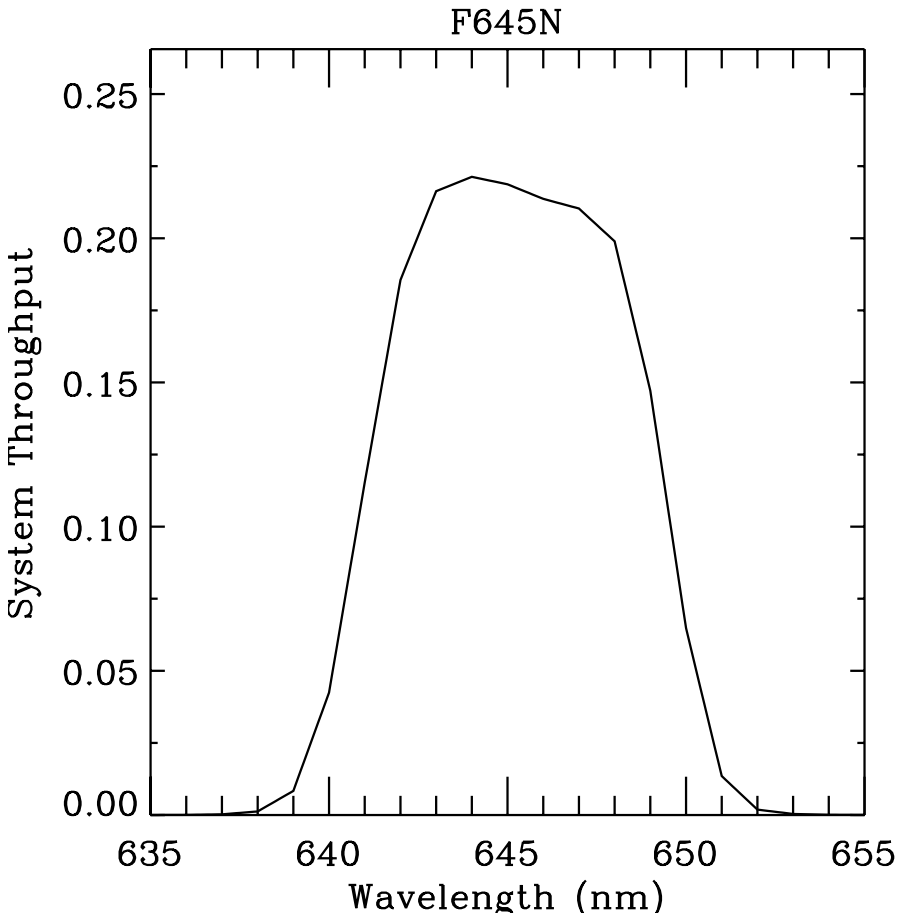

Figure A.86: Point source S/N vs. V+ABν for the F645N filter, assuming high sky backgrounds and a 5×5 pixel aperture.

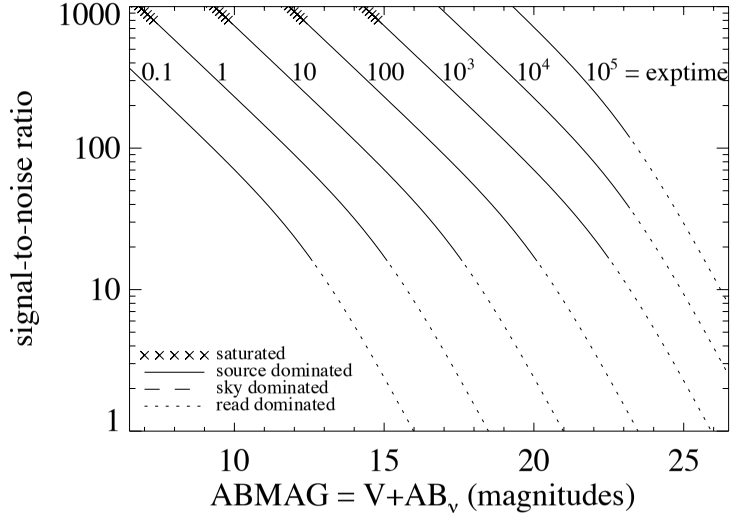

Figure A.87: Extended source S/N vs. V+ABν for the F645N filter, assuming high sky backgrounds and a source uniformly filling a 1 arcsec^2 aperture.

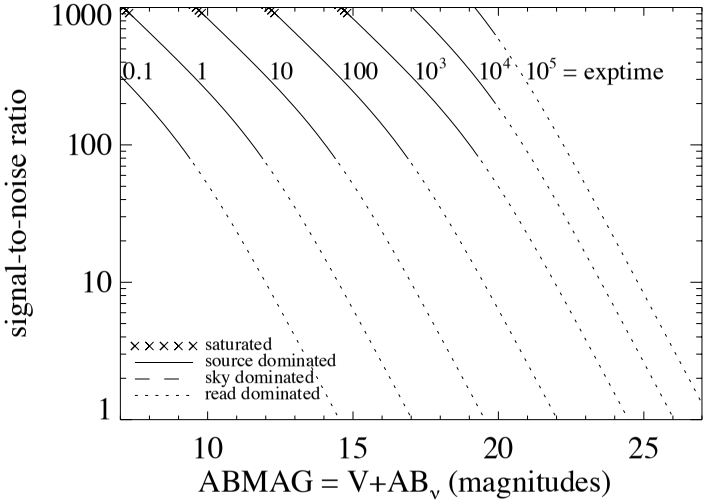

UVIS/F656N

Description

Hα 6562 filter.

Figure A.88: Integrated system throughput for F656N.

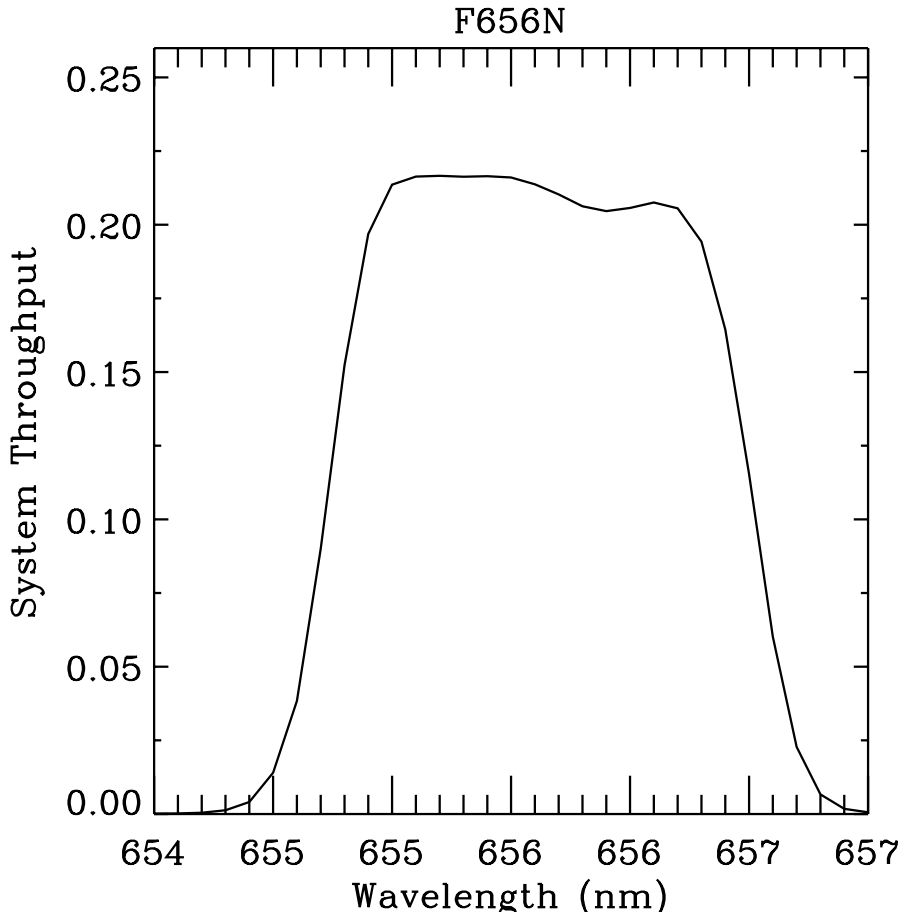

Figure A.89: Point source S/N vs. V+ABν for the F656N filter, assuming high sky backgrounds and a 5×5 pixel aperture.

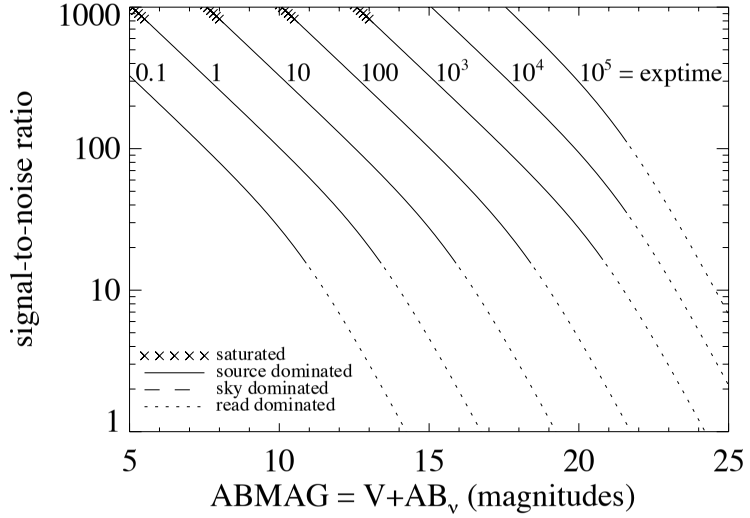

Figure A.90: Extended source S/N vs. V+ABν for the F656N filter, assuming high sky backgrounds and a source uniformly filling a 1 arcsec^2 aperture.

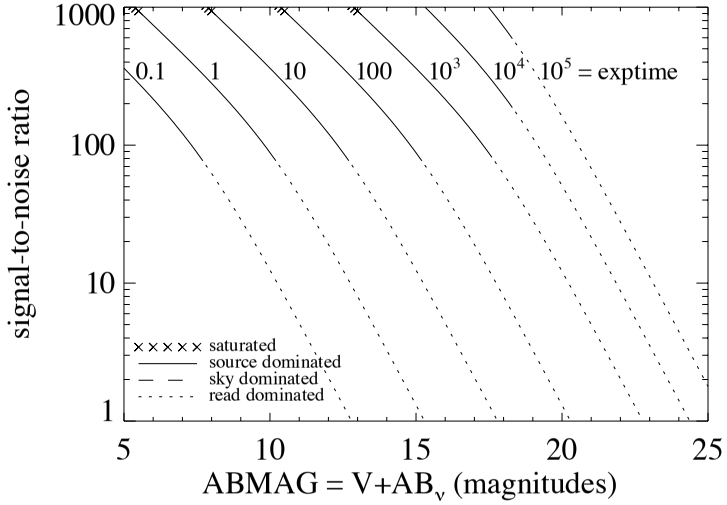

UVIS/F657N

Description

Wide Hα + [N II] filter.

Figure A.91: Integrated system throughput for F657N.

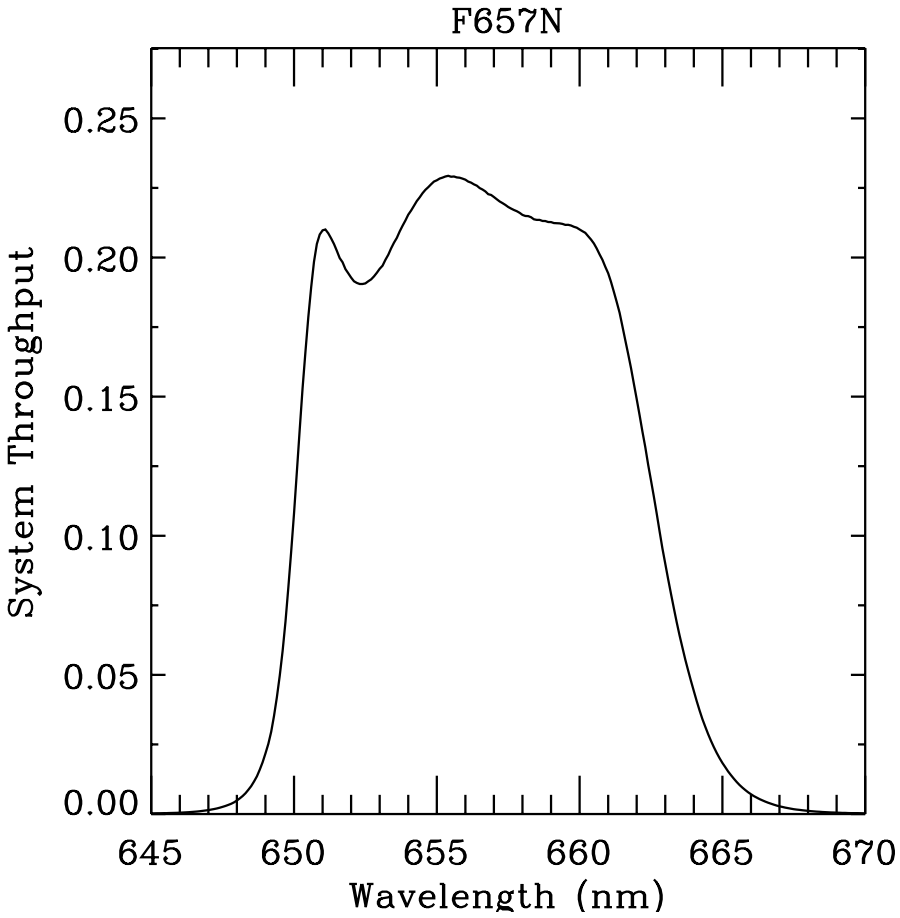

Figure A.92: Point source S/N vs. V+ABν for the F657N filter, assuming high sky backgrounds and a 5×5 pixel aperture.

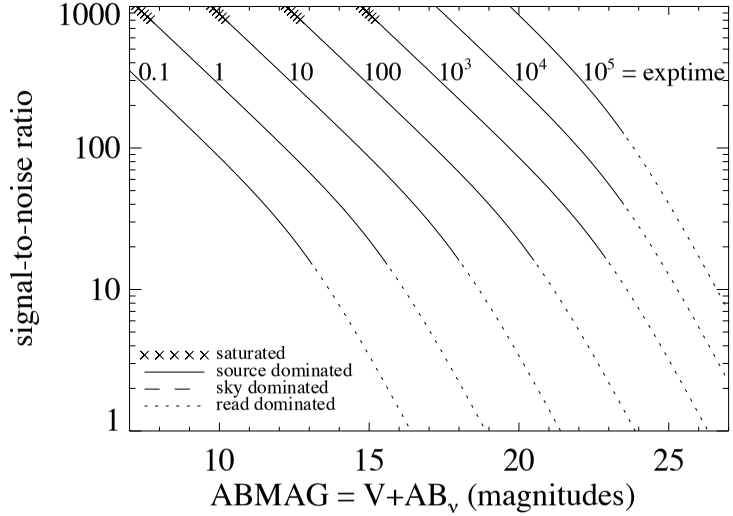

Figure A.93: Extended source S/N vs. V+ABν for the F657N filter, assuming high sky backgrounds and a source uniformly filling a 1 arcsec^2 aperture.

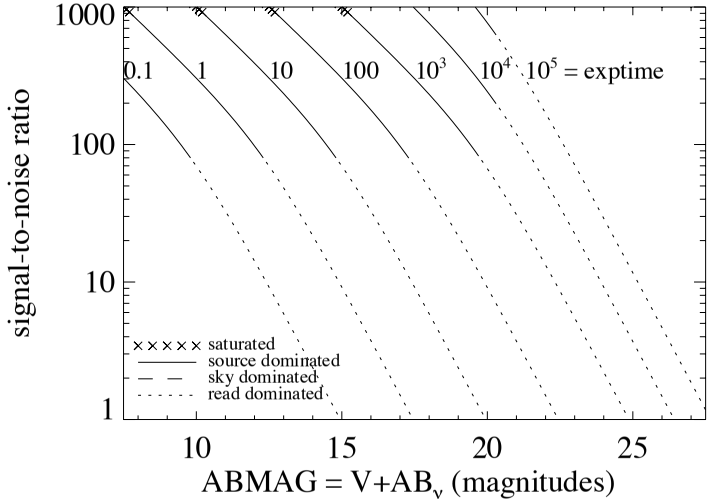

UVIS/F658N

Description

[N II] 6583 filter.

Figure A.94: Integrated system throughput for F658N.

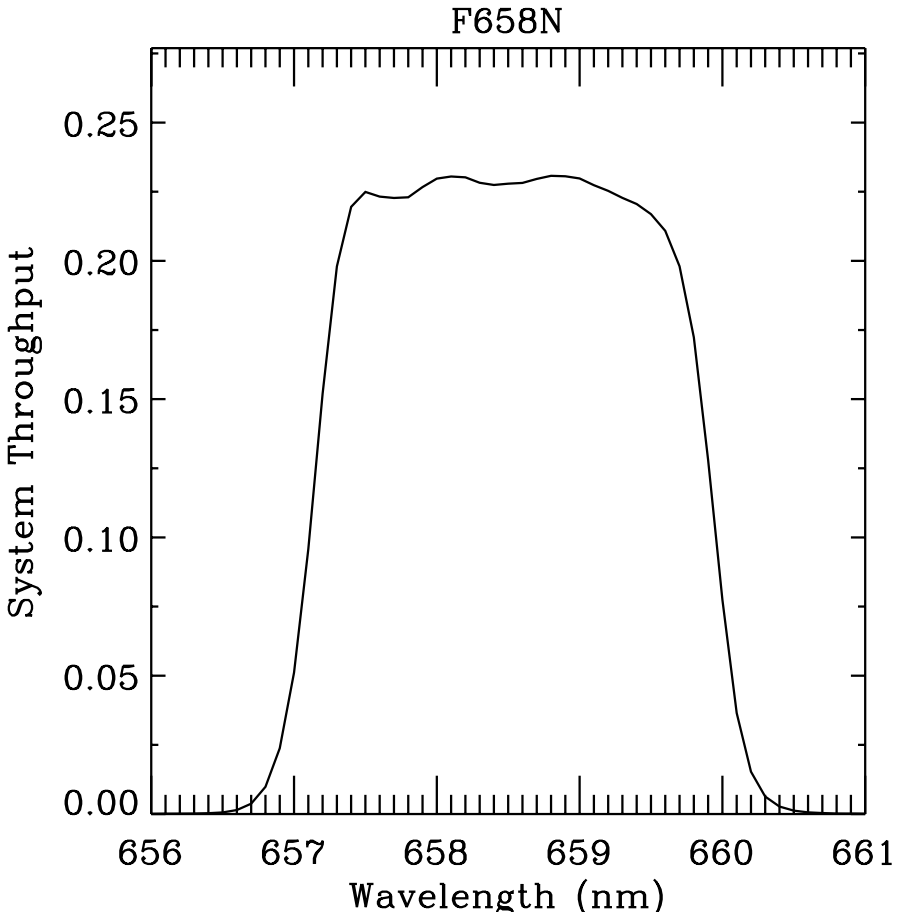

Figure A.95: Point source S/N vs. V+ABν for the F658N filter, assuming high sky backgrounds and a 5×5 pixel aperture.

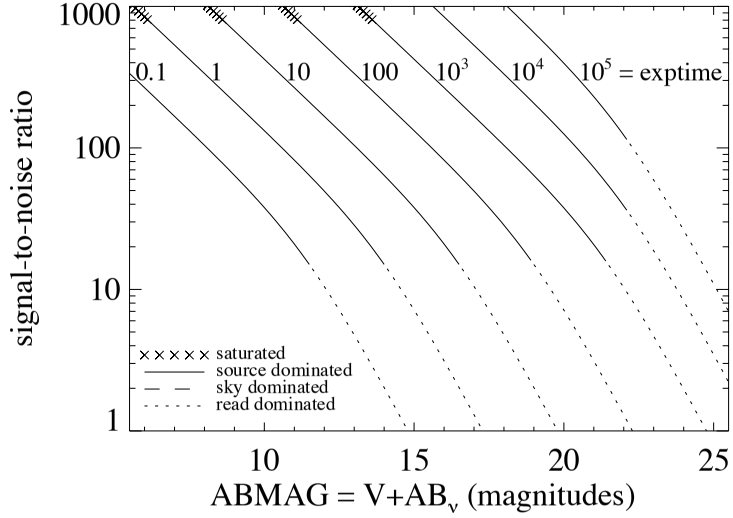

Figure A.96: Extended source S/N vs. V+ABν for the F658N filter, assuming high sky backgrounds and a source uniformly filling a 1 arcsec^2 aperture.

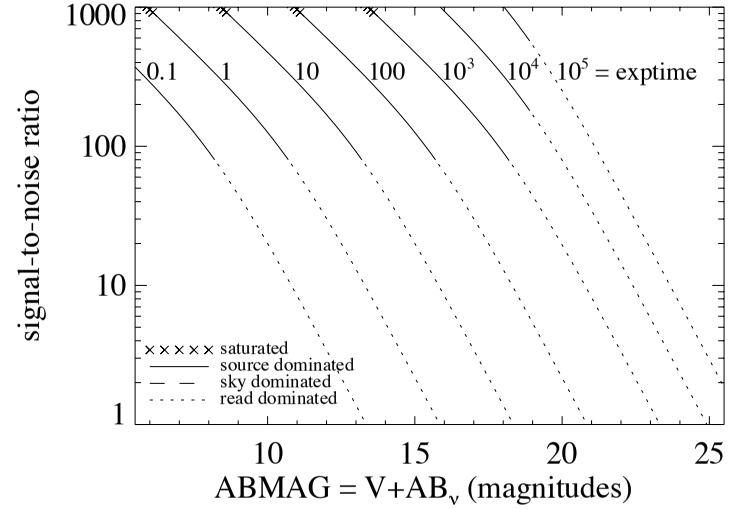

UVIS/F665N

Description

z (Hα + [N II]) filter.

Figure A.97: Integrated system throughput for F665N.

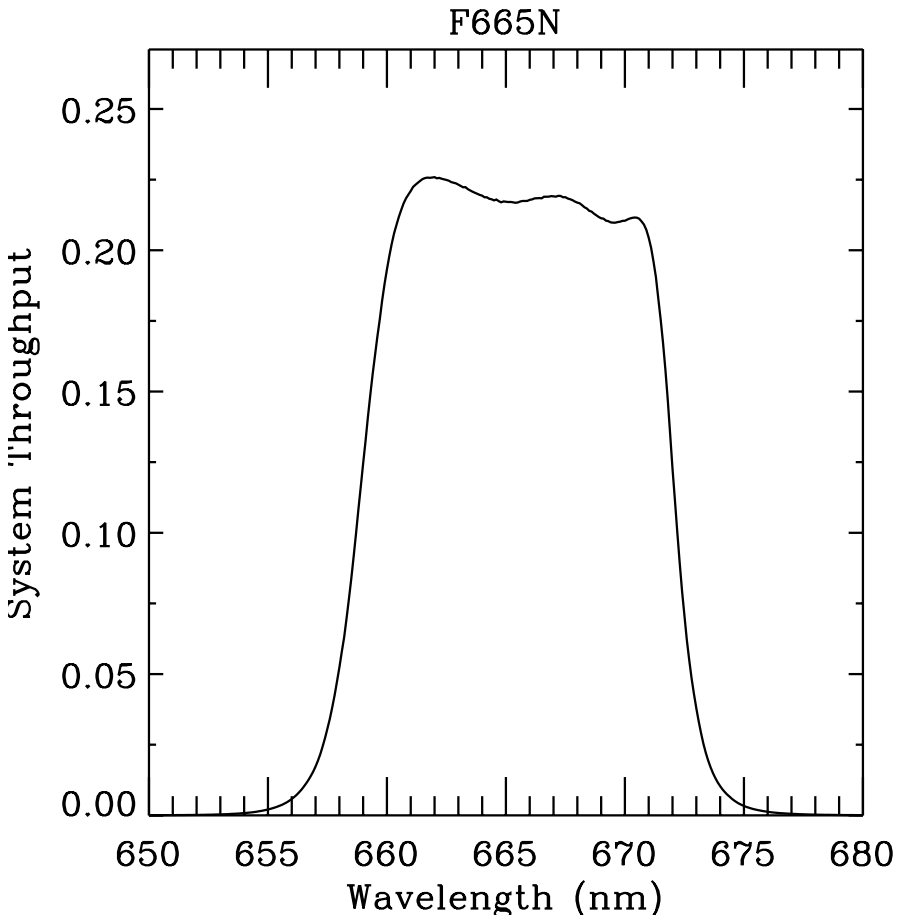

Figure A.98: Point source S/N vs. V+ABν for the F665N filter, assuming high sky backgrounds and a 5×5 pixel aperture.

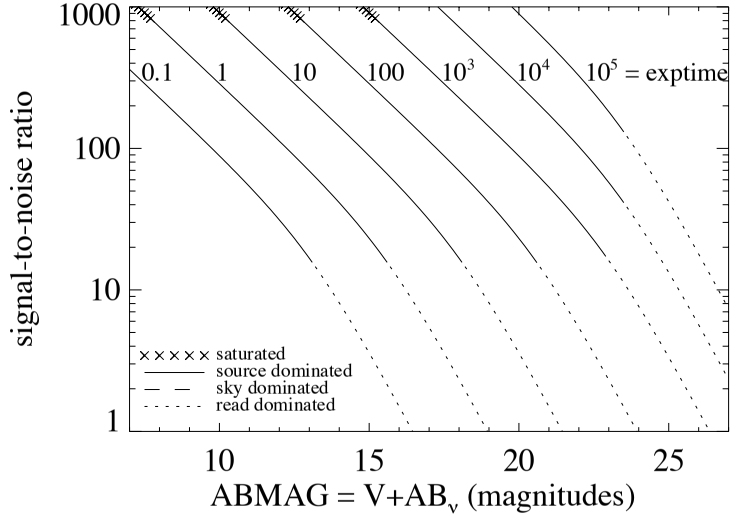

Figure A.99: Extended source S/N vs. V+ABν for the F665N filter, assuming high sky backgrounds and a source uniformly filling a 1 arcsec^2 aperture.

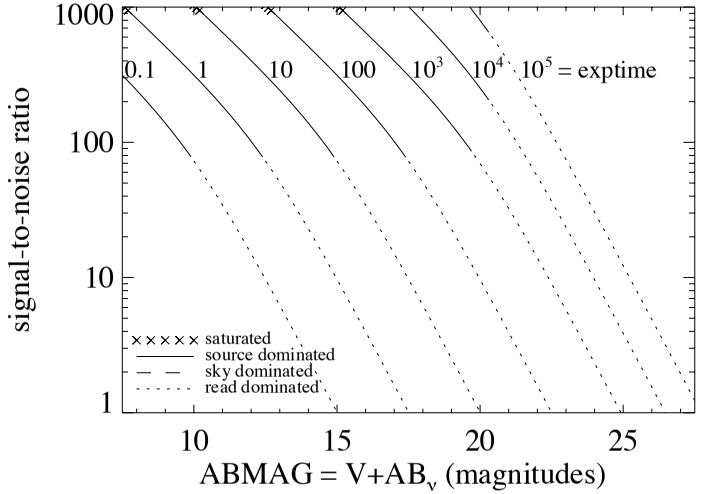

UVIS/F673N

Description

[S II] 6717/6731 filter.

Figure A.100: Integrated system throughput for F673N.

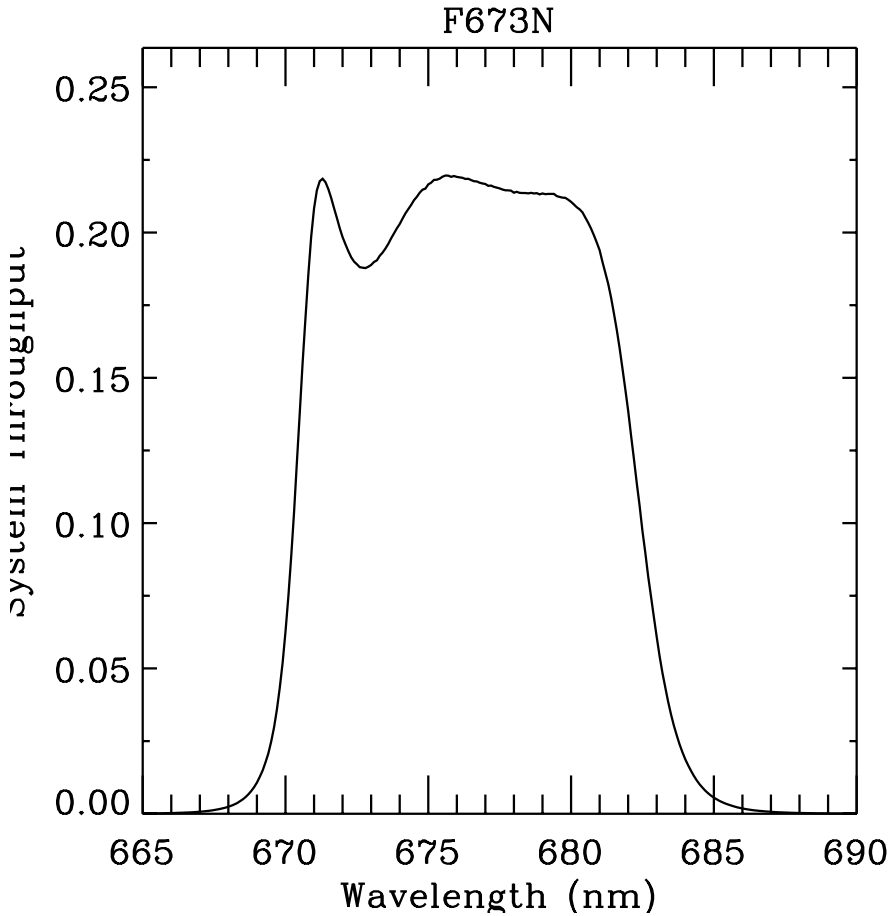

Figure A.101: Point source S/N vs. V+ABν for the F673N filter, assuming high sky backgrounds and a 5×5 pixel aperture.

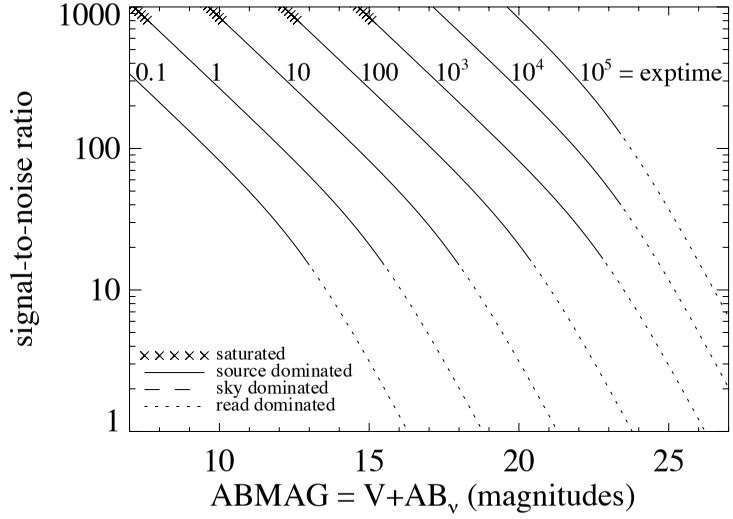

Figure A.102: Extended source S/N vs. V+ABν for the F673N filter, assuming high sky backgrounds and a source uniformly filling a 1 arcsec^2 aperture.

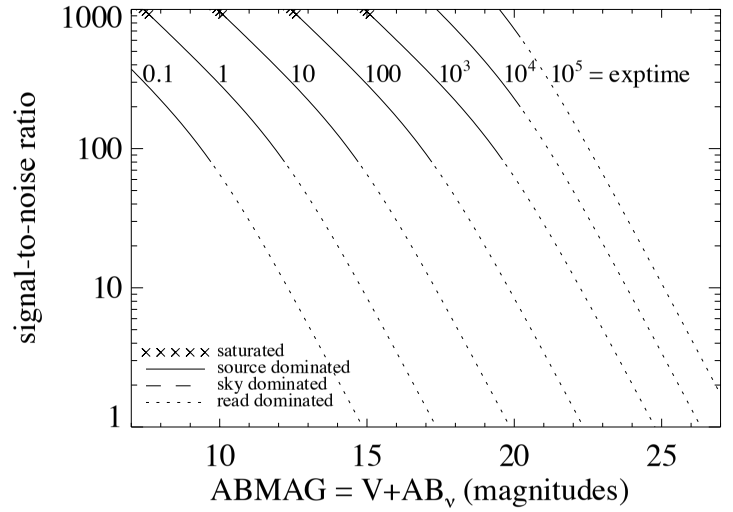

UVIS/F680N

Description

z (Hα + [N II]) filter.

Figure A.103: Integrated system throughput for F680N.

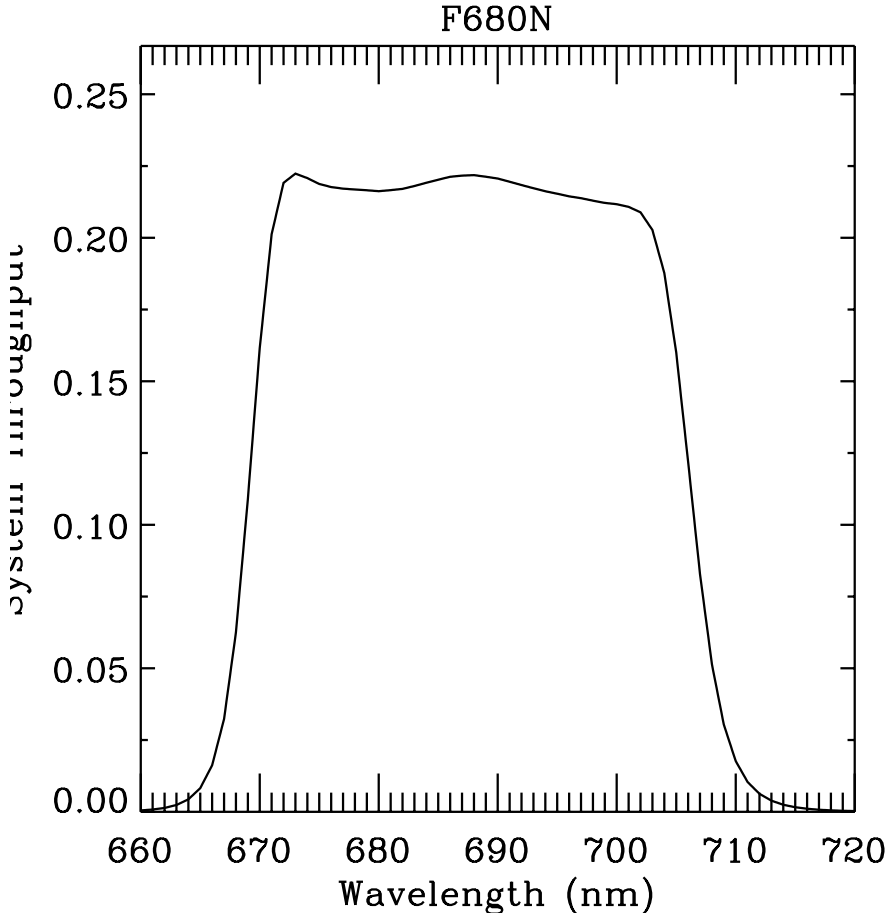

Figure A.104: Point source S/N vs. V+ABν for the F680N filter, assuming high sky backgrounds and a 5×5 pixel aperture.

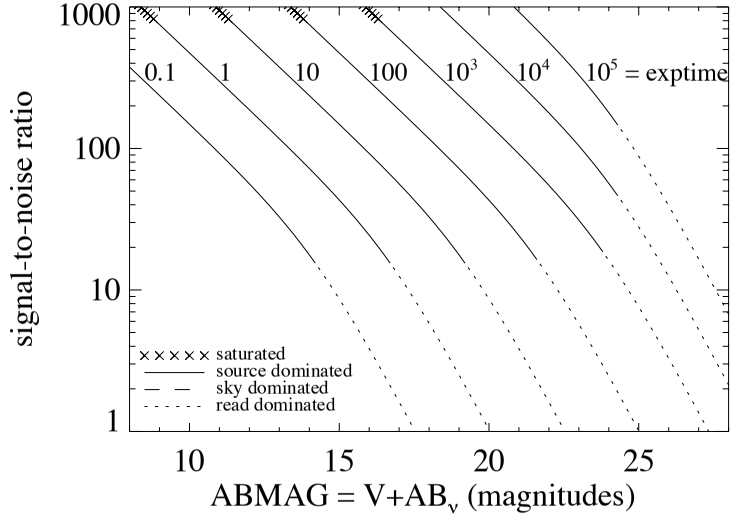

Figure A.105: Extended source S/N vs. V+ABν for the F680N filter, assuming high sky backgrounds and a source uniformly filling a 1 arcsec^2 aperture.

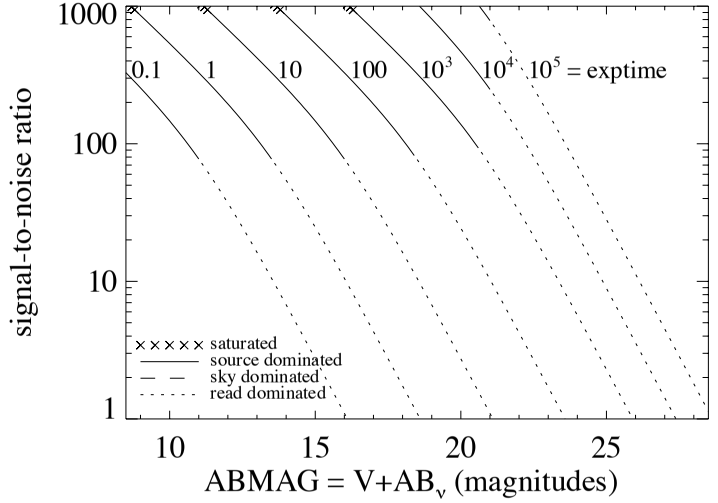

UVIS/F689M

Description

11% passband filter.

Figure A.106: Integrated system throughput for F689M.

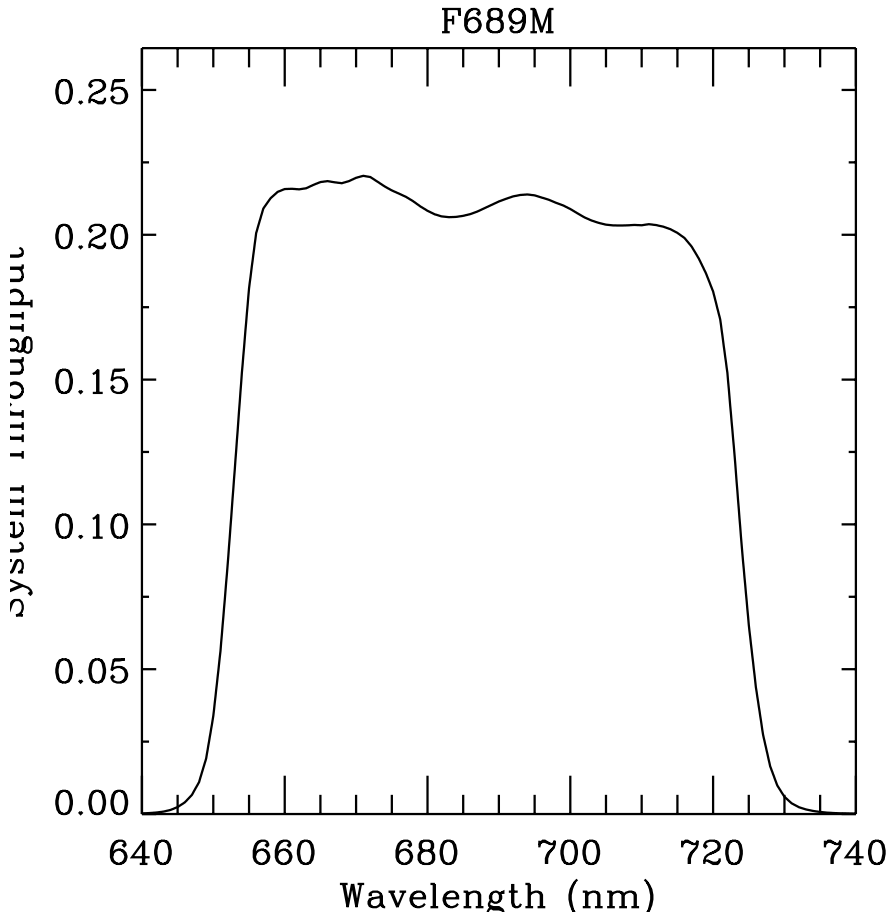

Figure A.107: Point source S/N vs. V+ABν for the F689M filter. Top curves are for low sky; bottom curves are for average sky.

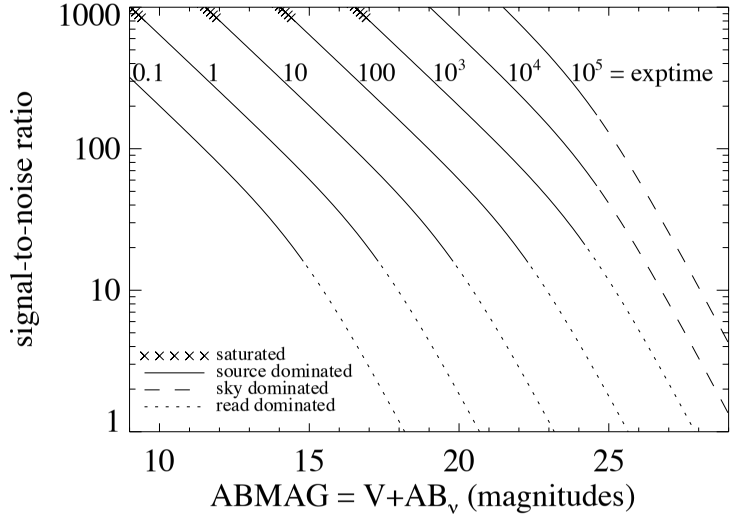

Figure A.108: Extended source S/N vs. V+ABν for the F689M filter, assuming high sky backgrounds and a source uniformly filling a 1 arcsec^2 aperture.

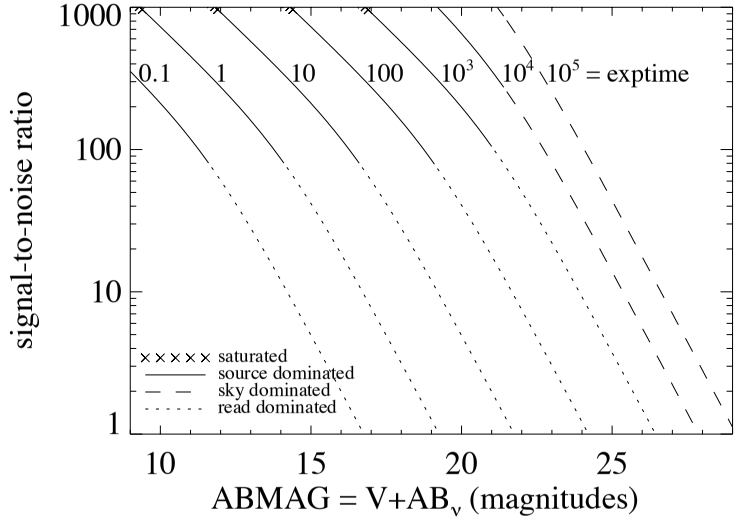

UVIS/F763M

Description

11% passband filter.

Figure A.109: Integrated system throughput for F763M.

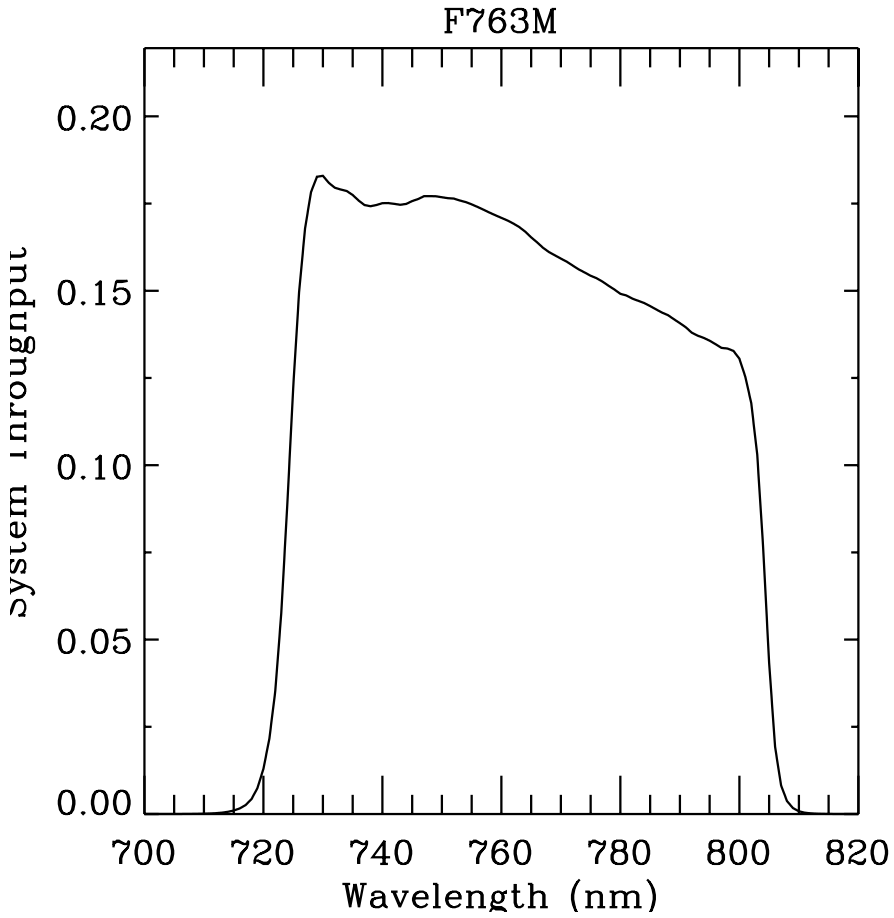

Figure A.110: Point source S/N vs. V+ABν for the F763M filter. Top curves are for low sky; bottom curves are for average sky.

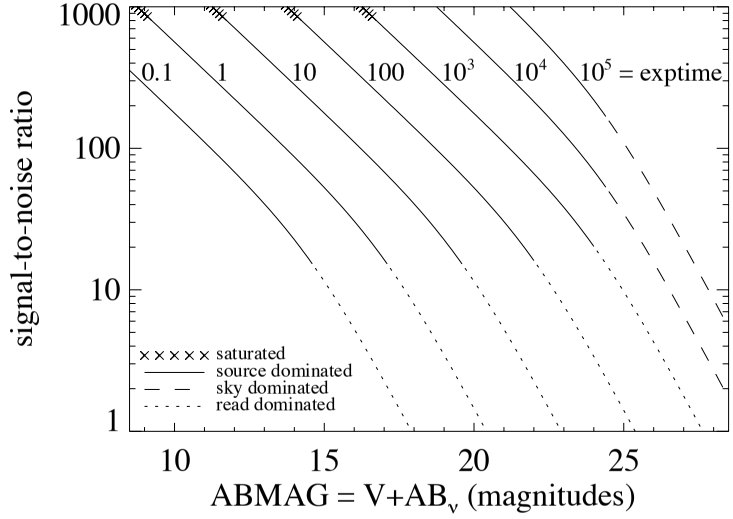

Figure A.111: Extended source S/N vs. V+ABν for the F763M filter, assuming high sky backgrounds and a source uniformly filling a 1 arcsec^2 aperture.

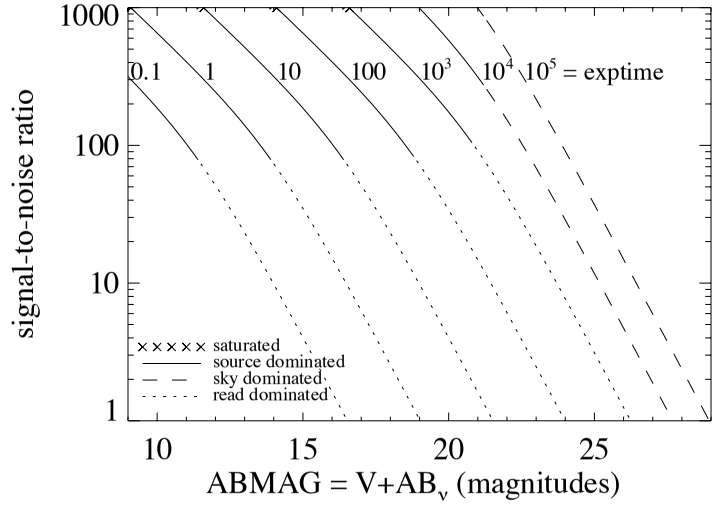

UVIS/F775W

Description

Sloan Digital Sky Survey *i′* filter.

Figure A.112: Integrated system throughput for F775W.

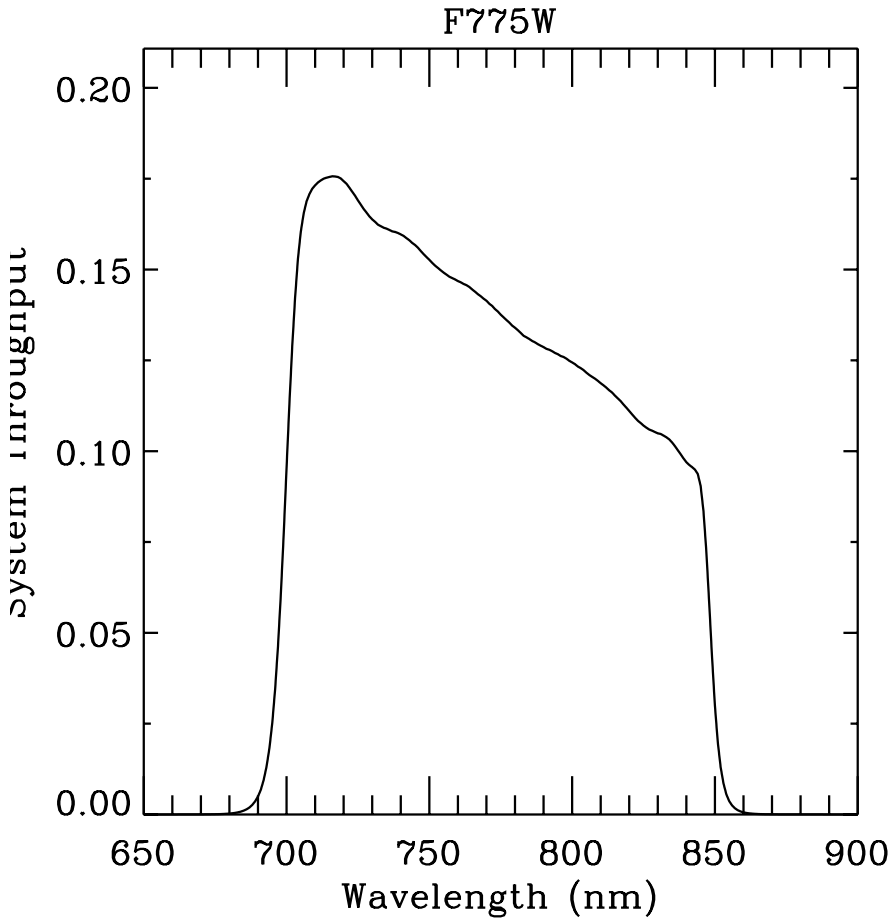

Figure A.113: Point source S/N vs. V+ABν for the F775W filter, assuming high sky backgrounds and a 5×5 pixel aperture.

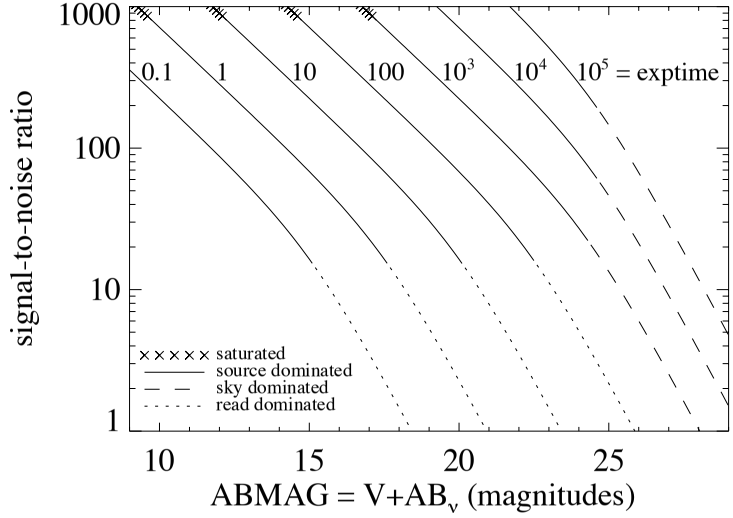

Figure A.114: Extended source S/N vs. V+ABν for the F775W filter, assuming high sky backgrounds and a source uniformly filling a 1 arcsec^2 aperture.

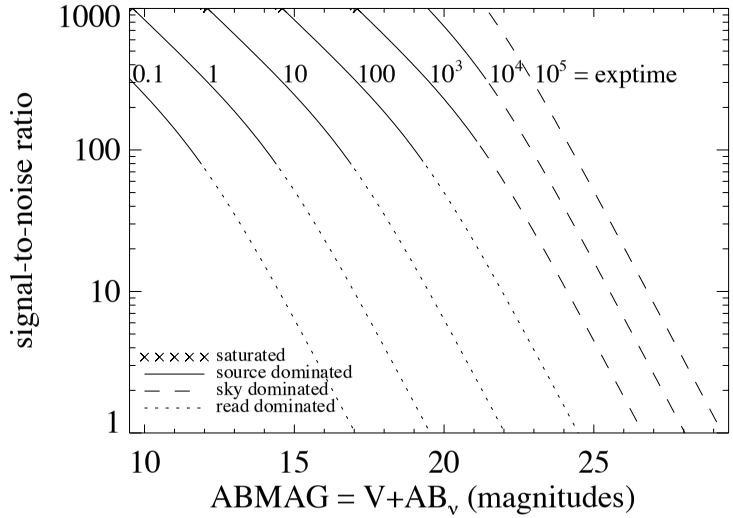

UVIS/F814W

Description

WFPC2 Wide *I* filter.

Figure A.115: Integrated system throughput for F814W.

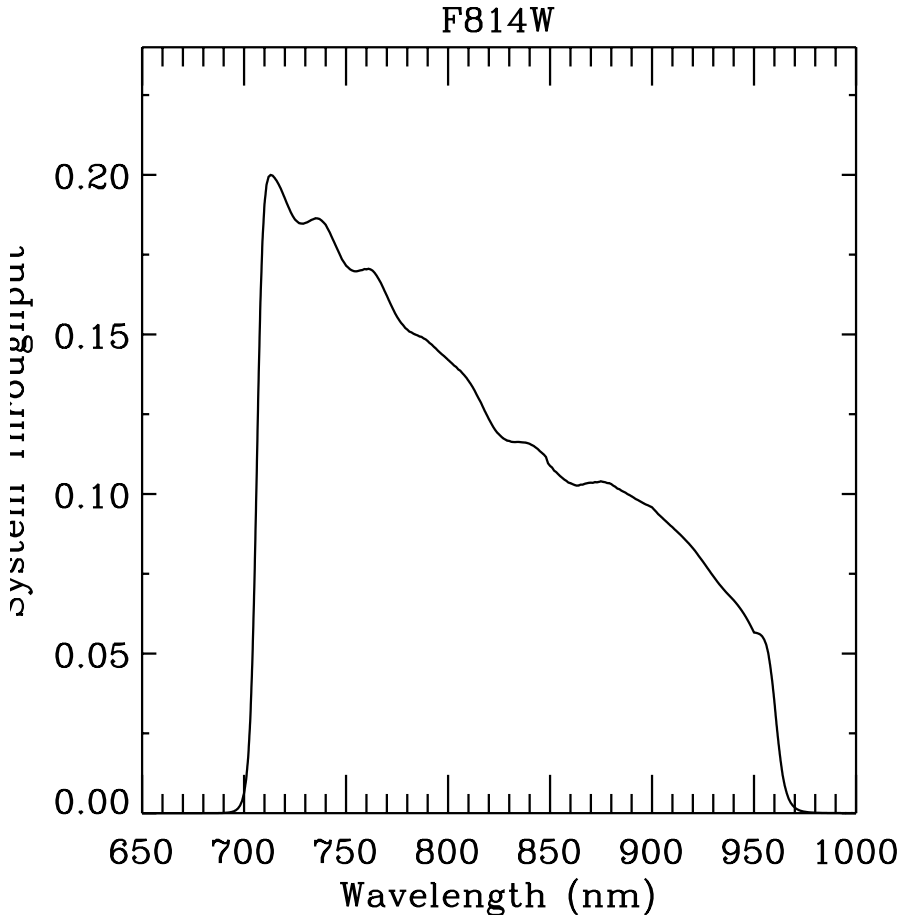

Figure A.116: Point source S/N vs. V+ABν for the F814W filter, assuming high sky backgrounds and a 5×5 pixel aperture.

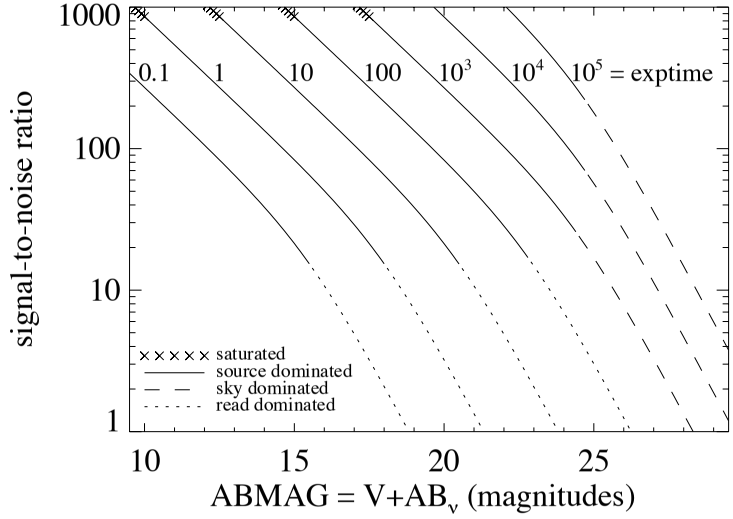

Figure A.117: Extended source S/N vs. V+ABν for the F814W filter, assuming high sky backgrounds and a source uniformly filling a 1 arcsec^2 aperture.

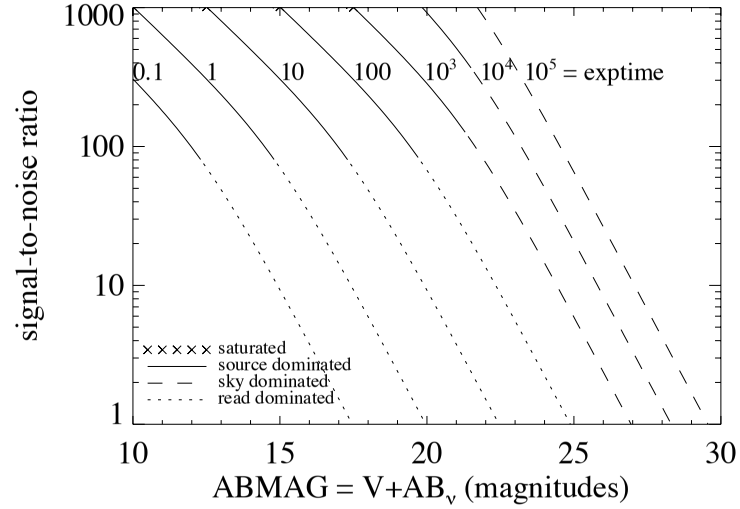

UVIS/F845M

Description

11% passband filter.

Figure A.118: Integrated system throughput for F845M.

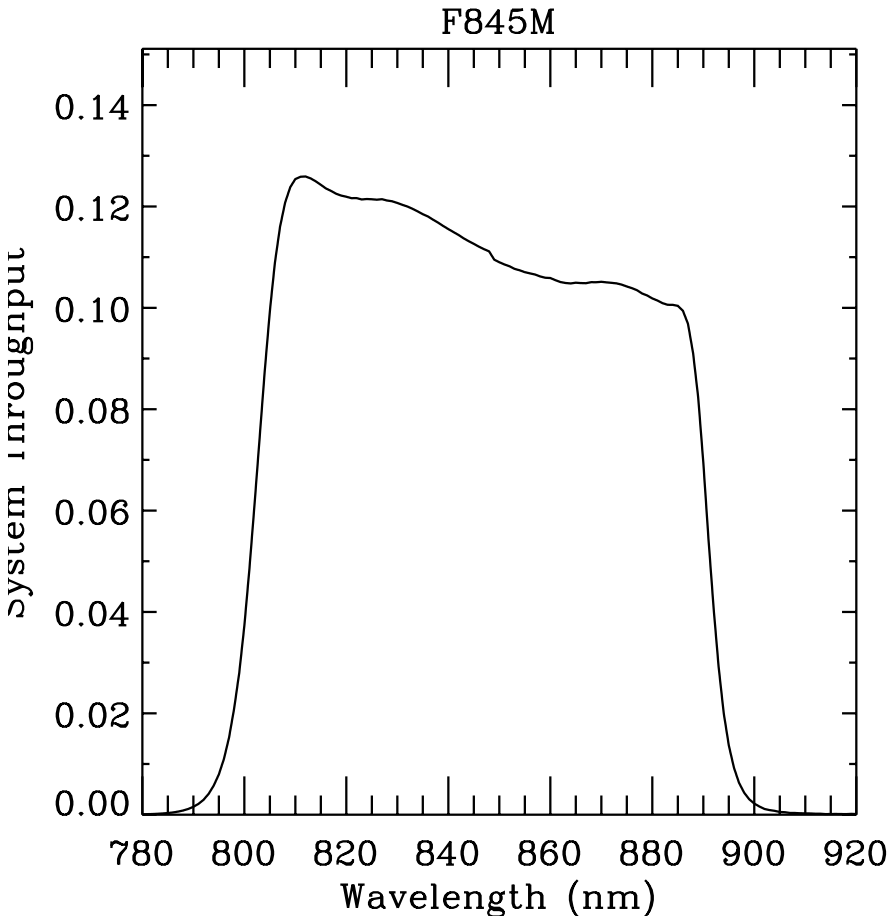

Figure A.119: Point source S/N vs. V+ABν for the F845M filter, assuming high sky backgrounds and a 5×5 pixel aperture.

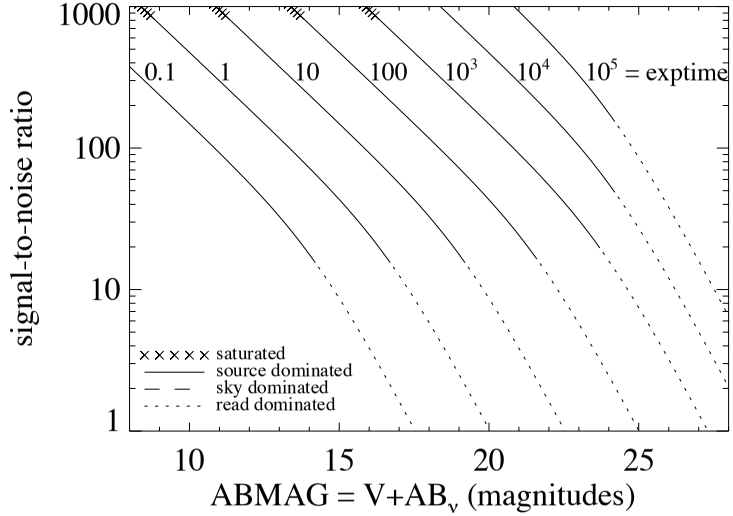

Figure A.120: Extended source S/N vs. V+ABν for the F845M filter, assuming high sky backgrounds and a source uniformly filling a 1 arcsec^2 aperture.

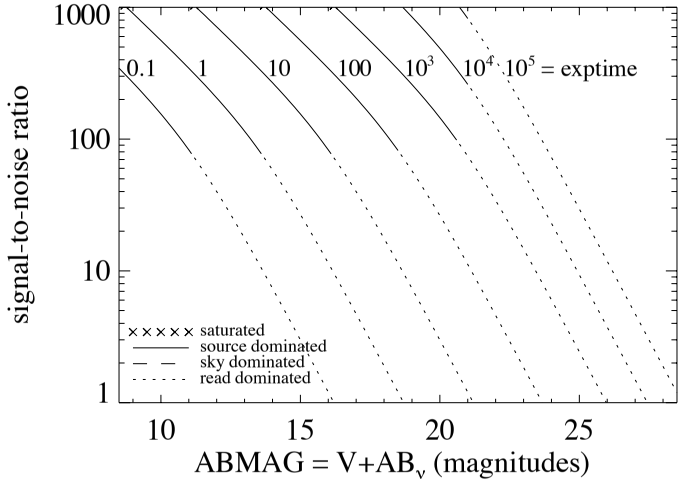

UVIS/F850LP

Description

Sloan Digital Sky Survey z' filter.

Figure A.121: Integrated system throughput for F850LP.

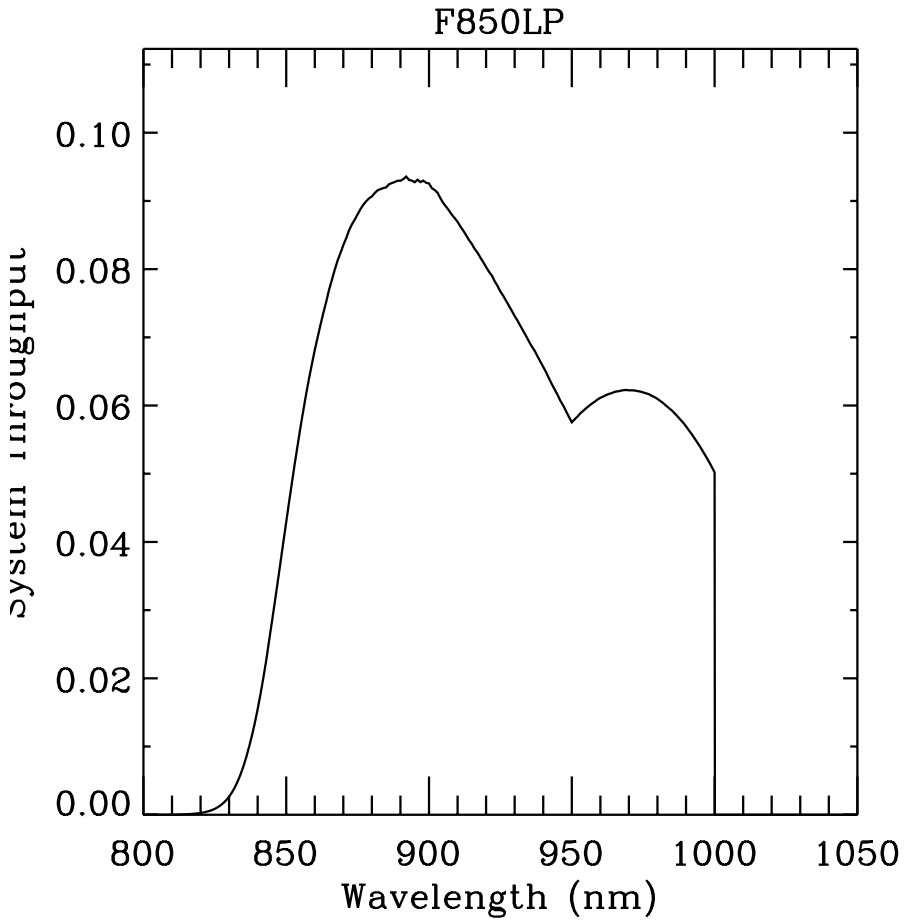

Figure A.122: Point source S/N vs. V+ABν for the F850LP filter.Top curves are for low sky; bottom curves are for average sky.

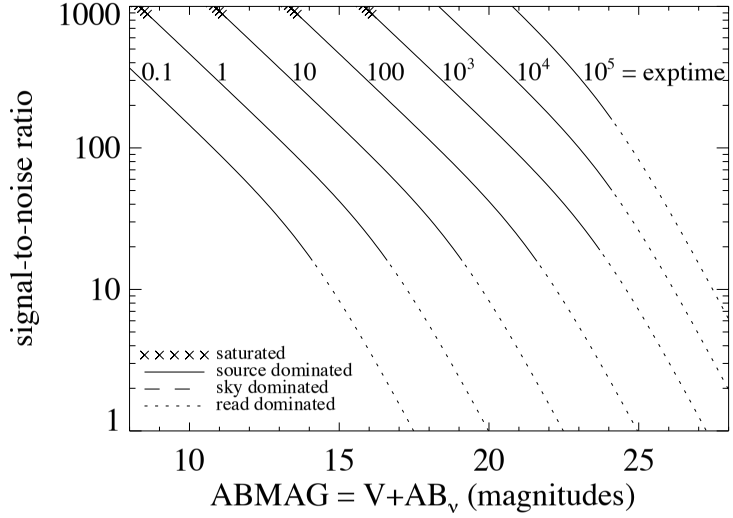

Figure A.123: Extended source S/N vs. V+ABν for the F850LP filter, assuming high sky backgrounds and a source uniformly filling a 1 arcsec^2 aperture.

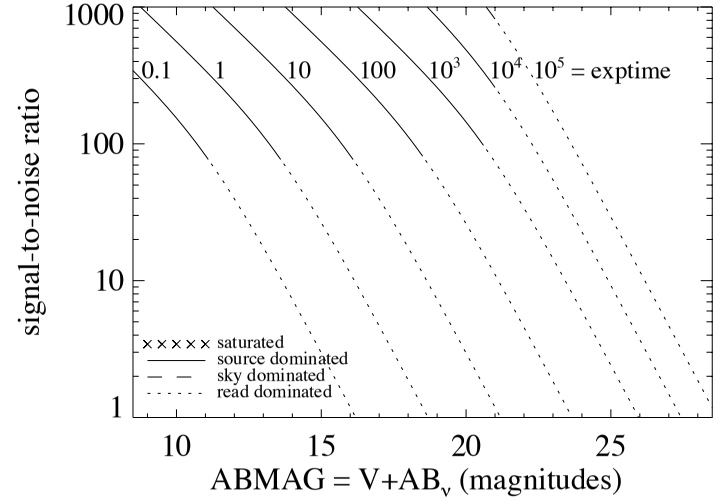

UVIS/F953N

Description

[S III] 9532 filter.

Figure A.124: Integrated system throughput for F953N.

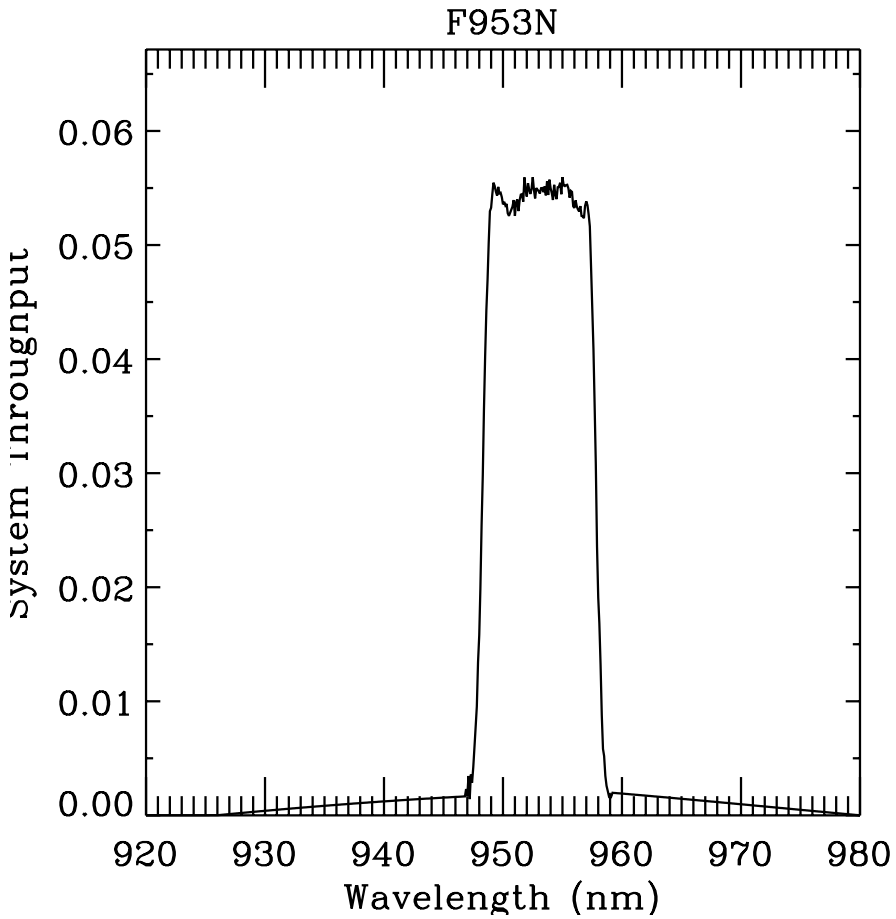

Figure A.125: Point source S/N vs. V+ABν for the F953N filter, assuming high sky backgrounds and a 5×5 pixel aperture.

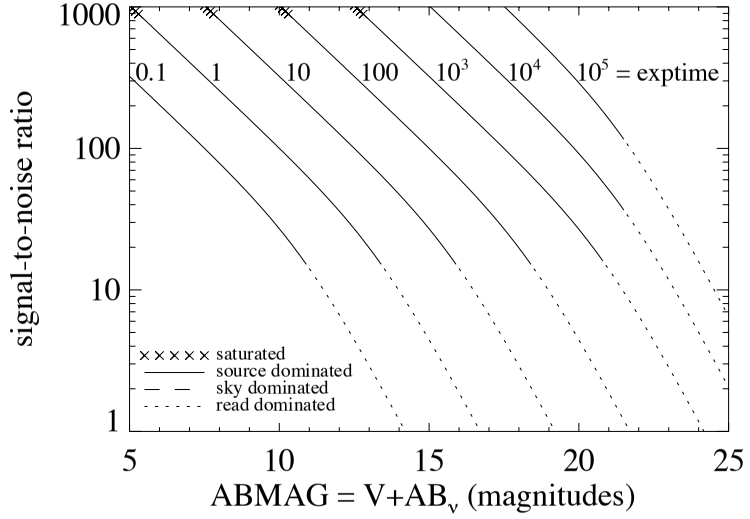

Figure A.126: Extended source S/N vs. V+ABν for the F953N filter, assuming high sky backgrounds and a source uniformly filling a 1 arcsec^2 aperture.

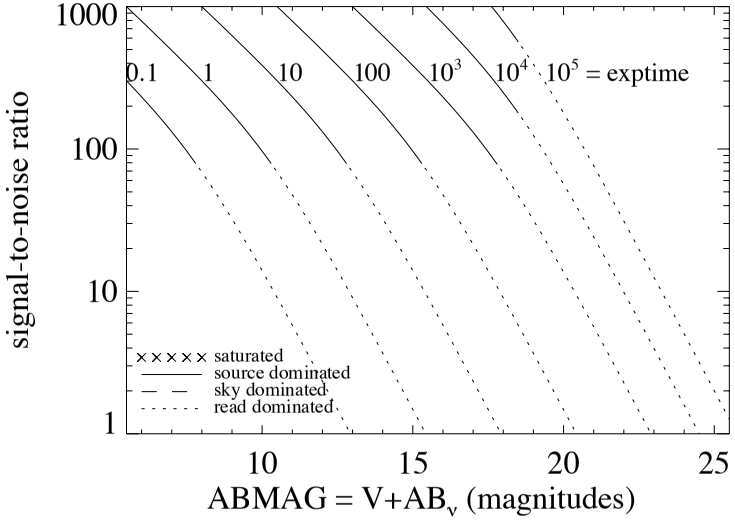

UVIS/FQ232N

Description

C II] 2326 filter.

Figure A.127: Integrated system throughput for FQ232N.

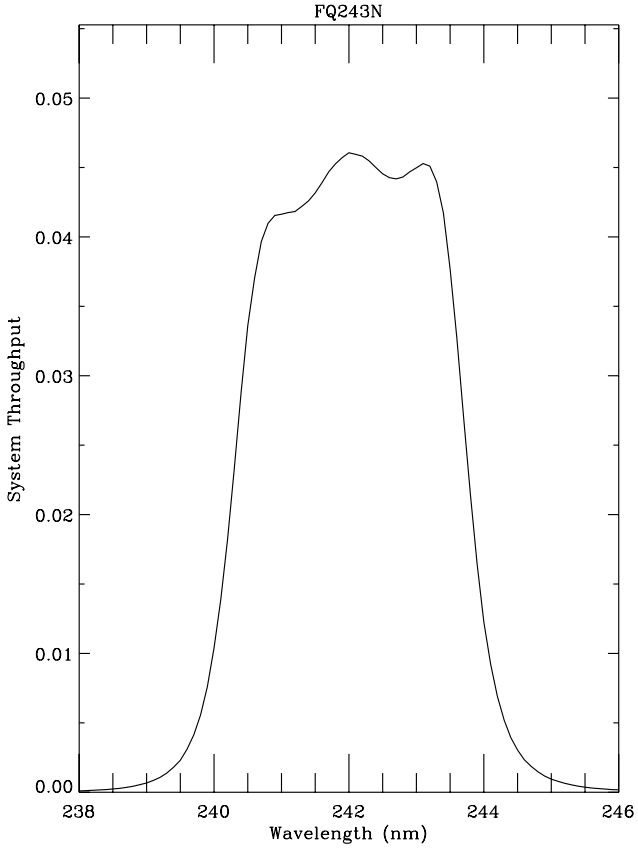

Figure A.128: Point source S/N vs. V+ABν for the FQ232N filter, assuming high sky backgrounds and a 5×5 pixel aperture.

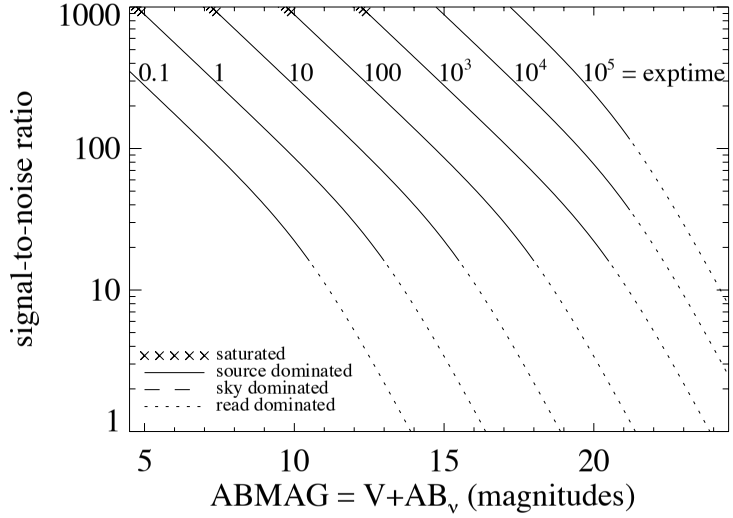

Figure A.129: Extended source S/N vs. V+ABν for the FQ232N filter, assuming high sky backgrounds and a source uniformly filling a 1 arcsec^2 aperture.

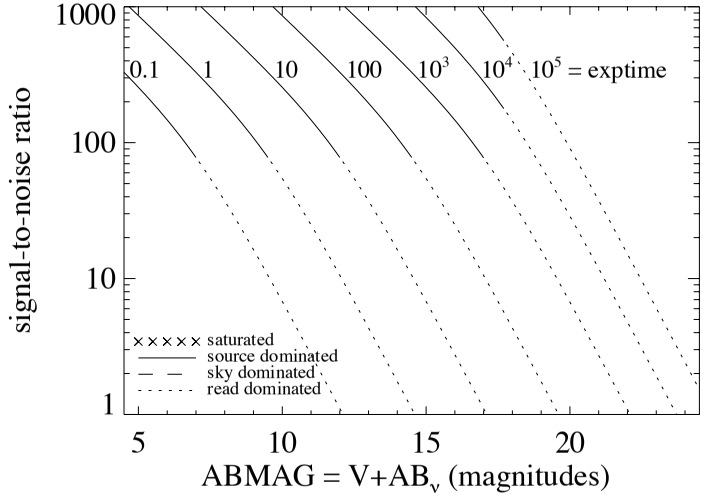

UVIS/FQ243N

Description

[Ne IV] 2425 filter.

Figure A.130: Integrated system throughput for FQ243N.

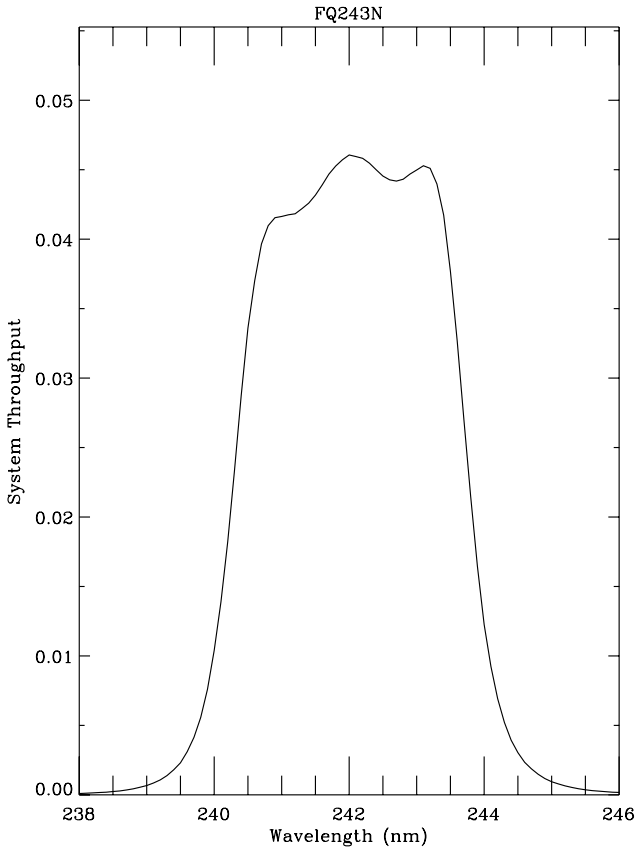

Figure A.131: Point source S/N vs. V+ABν for the FQ243N filter, assuming high sky backgrounds and a 5×5 pixel aperture.

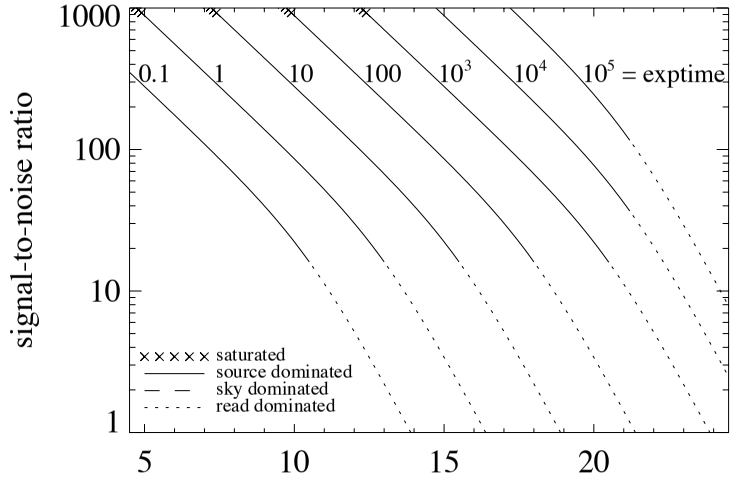

Figure A.132: Extended source S/N vs. V+ABν for the FQ243N filter, assuming high sky backgrounds and a source uniformly filling a 1 arcsec^2 aperture.

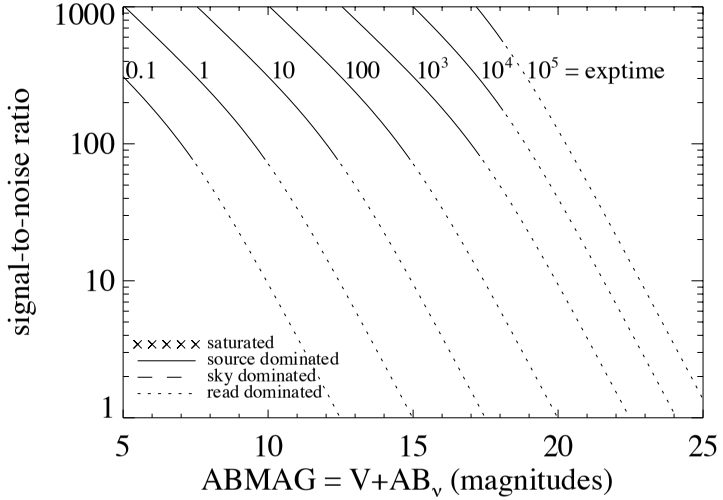

UVIS/FQ378N

Description

z ([O II] 3726) filter.

Figure A.133: Integrated system throughput for FQ378N.

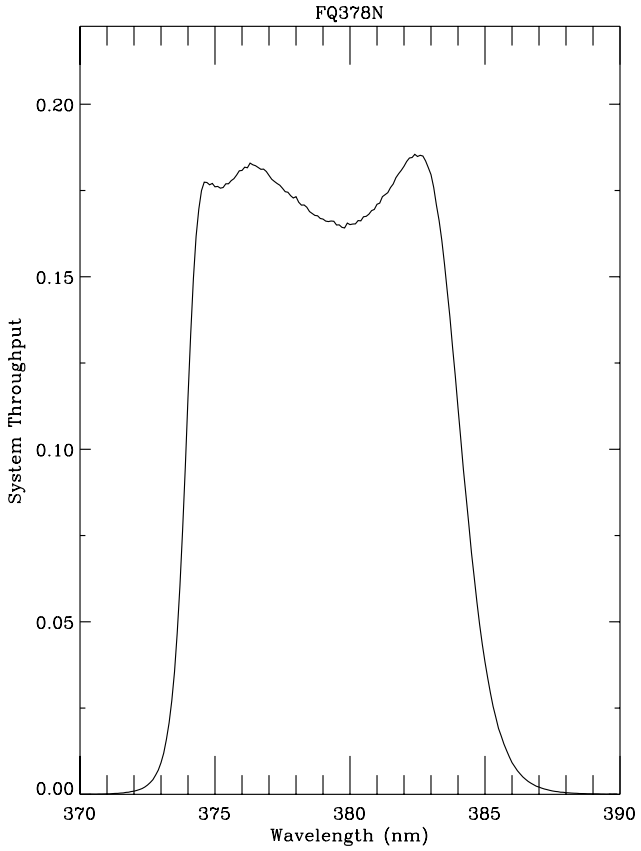

Figure A.134: Point source S/N vs. V+ABν for the FQ378N filter, assuming high sky backgrounds and a 5×5 pixel aperture.

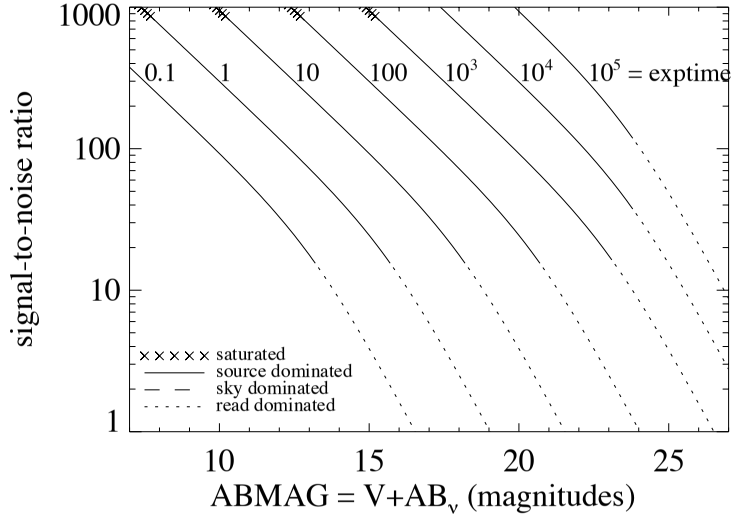

Figure A.135: Extended source S/N vs. V+ABν for the FQ378N filter, assuming high sky backgrounds and a source uniformly filling a 1 arcsec^2 aperture.

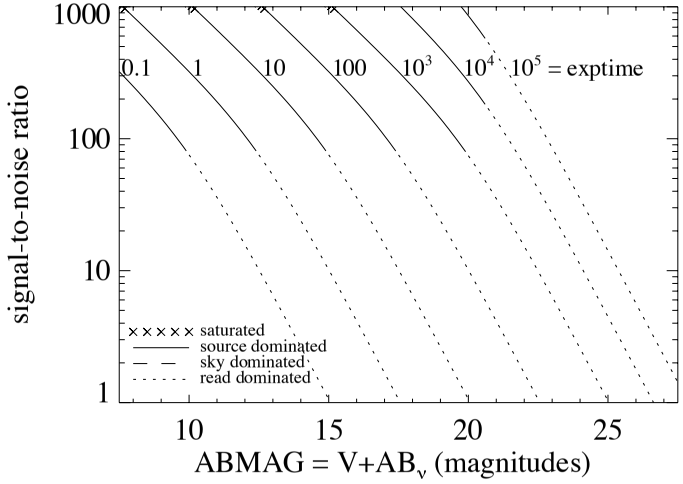

UVIS/FQ387N

Description

[Ne III] 3868 filter.

Figure A.136: Integrated system throughput for FQ387N.

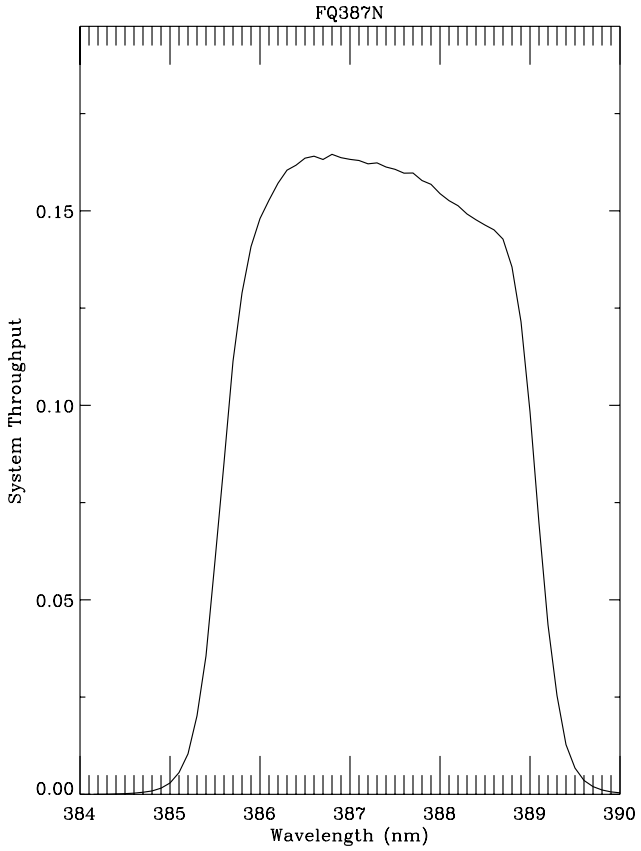

Figure A.137: Point source S/N vs. V+ABν for the FQ387N filter, assuming high sky backgrounds and a 5×5 pixel aperture.

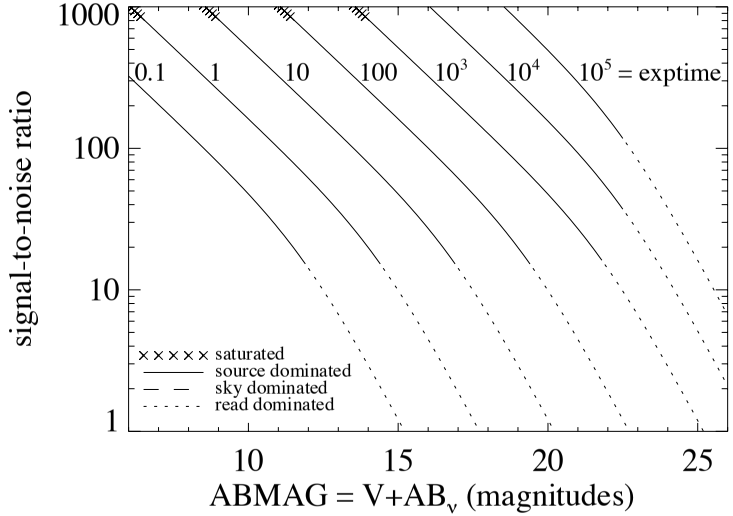

Figure A.138: Extended source S/N vs. V+ABν for the FQ387N filter, assuming high sky backgrounds and a source uniformly filling a 1 arcsec^2 aperture.

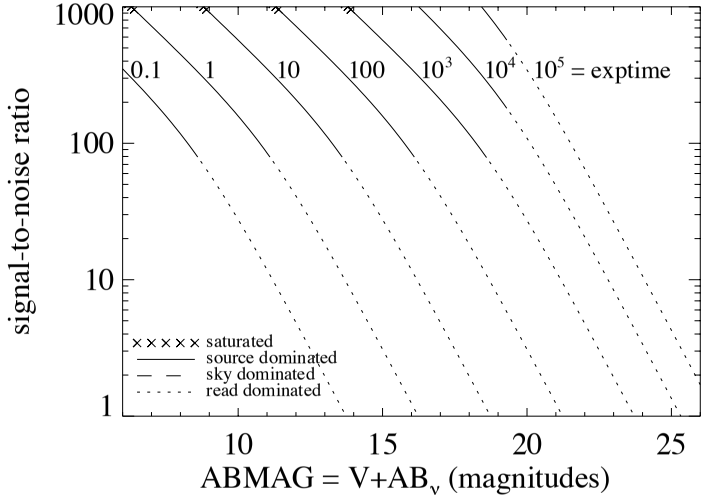

UVIS/FQ422M

Description

Blue continuum filter.

Figure A.139: Integrated system throughput for FQ422M.

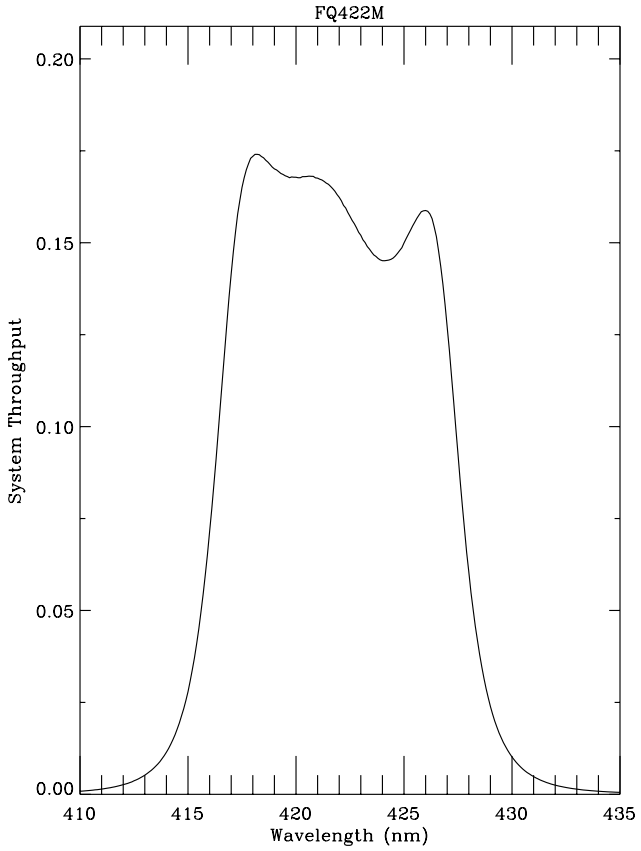

Figure A.140: Point source S/N vs. V+ABν for the FQ422M filter, assuming high sky backgrounds and a 5×5 pixel aperture.

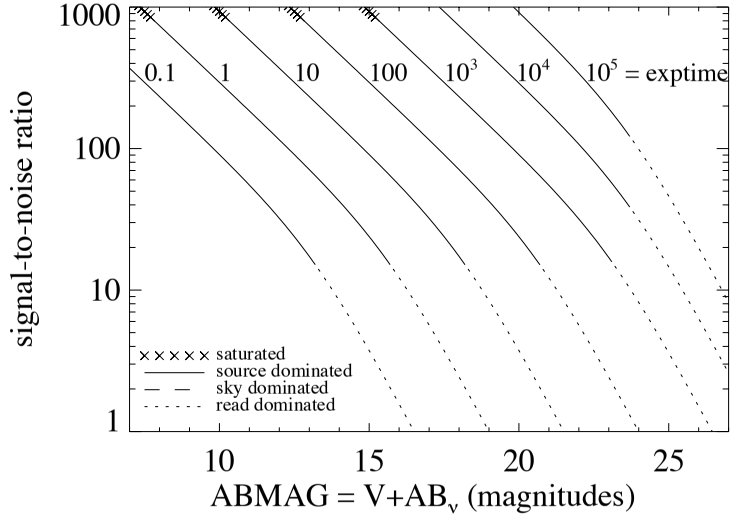

Figure A.141: Extended source S/N vs. V+ABν for the FQ422M filter, assuming high sky backgrounds and a source uniformly filling a 1 arcsec^2 aperture.

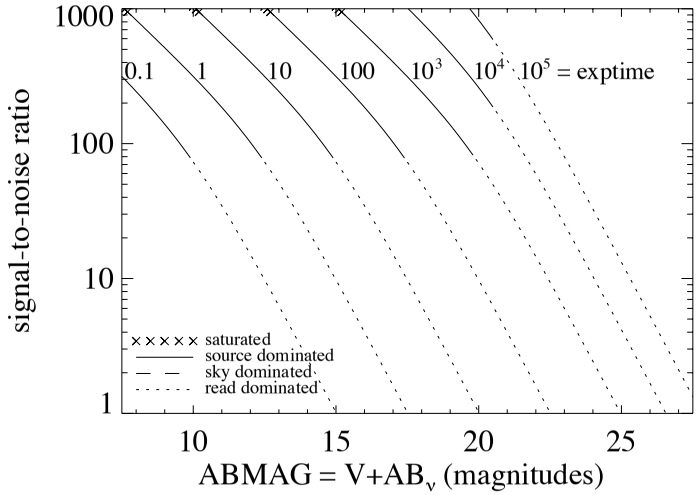

UVIS/FQ436N

Description

Hγ 4340 + [O III] 4363 filter.

Figure A.142: Integrated system throughput for FQ436N.

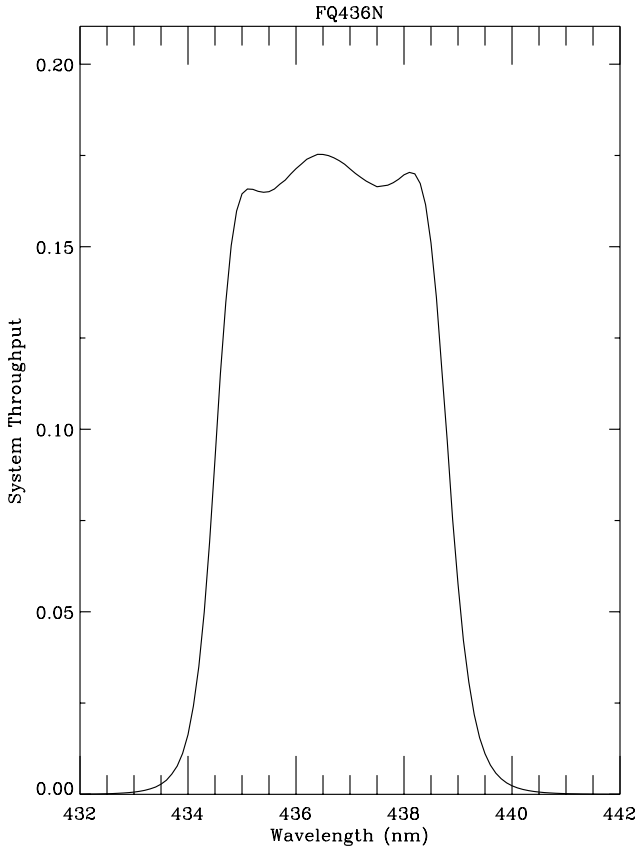

Figure A.143: Point source S/N vs. V+ABν for the FQ436N filter, assuming high sky backgrounds and a 5×5 pixel aperture.

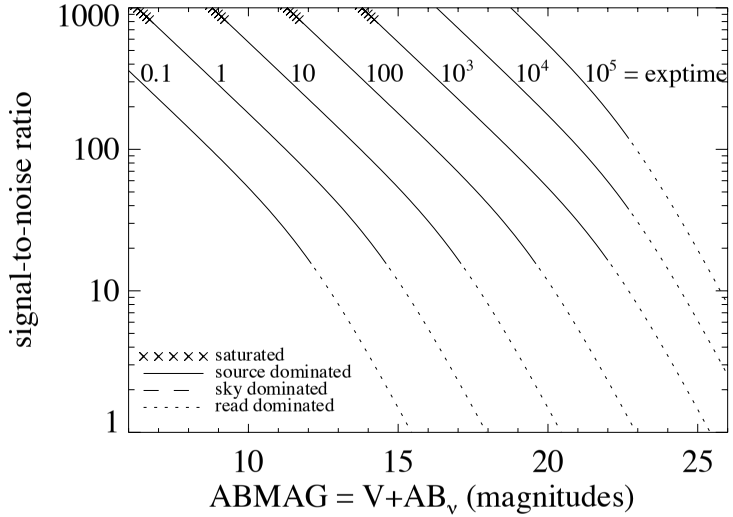

Figure A.144: Extended source S/N vs. V+ABν for the FQ436N filter, assuming high sky backgrounds and a source uniformly filling a 1 arcsec^2 aperture.

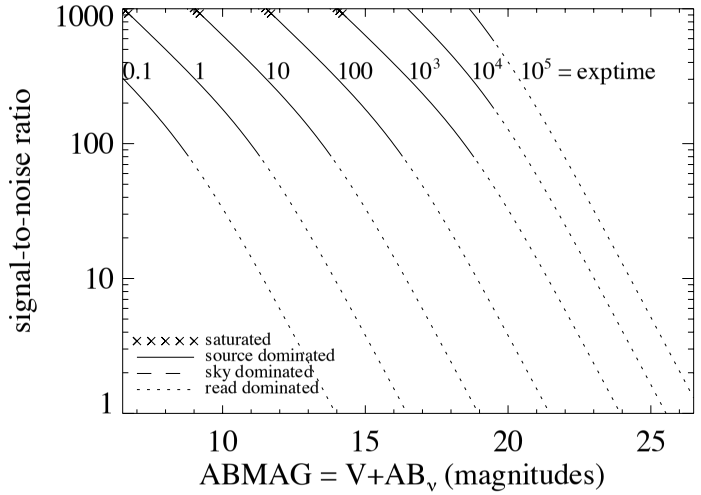

UVIS/FQ437N

Description

[O III] 4363 filter.

Figure A.145: Integrated system throughput for FQ437N.

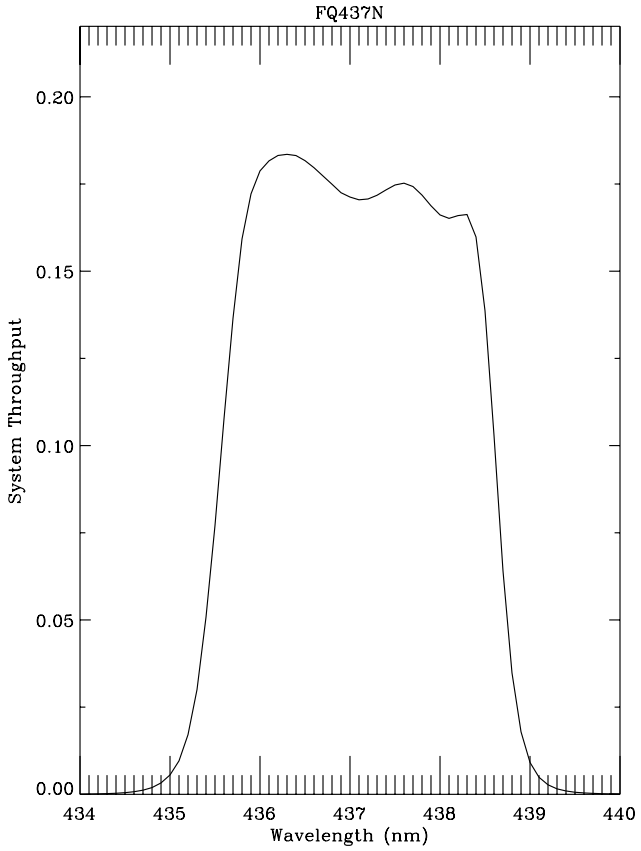

Figure A.146: Point source S/N vs. V+ABν for the FQ437N filter, assuming high sky backgrounds and a 5×5 pixel aperture.

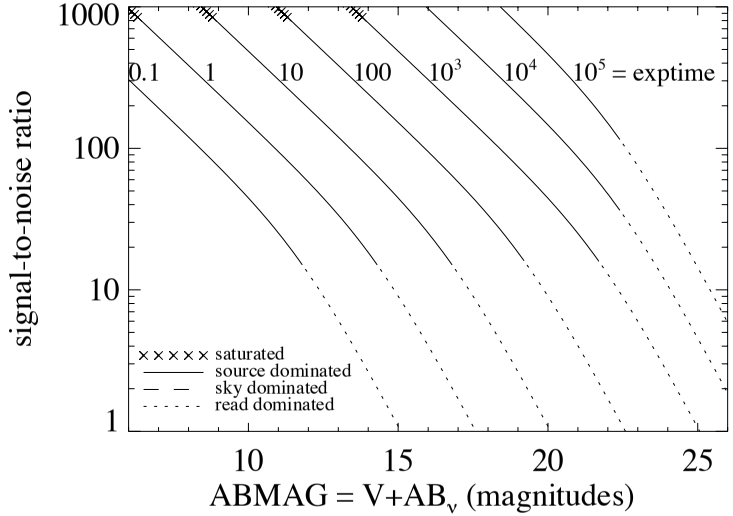

Figure A.147: Extended source S/N vs. V+ABν for the FQ437N filter, assuming high sky backgrounds and a source uniformly filling a 1 arcsec^2 aperture.

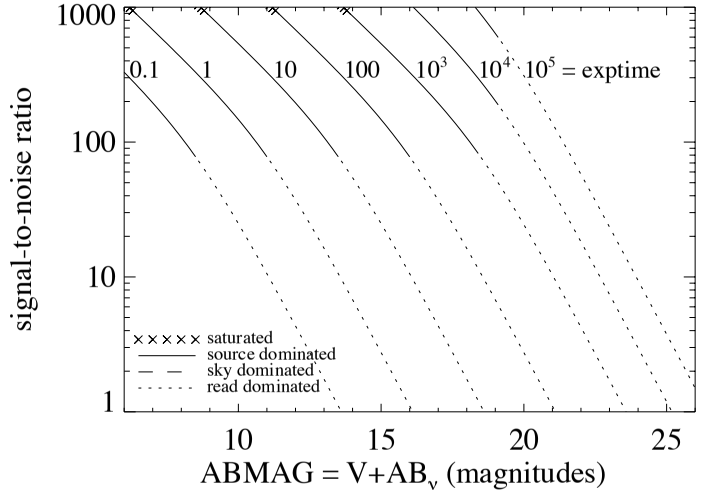

UVIS/FQ492N

Description

z (Hβ) filter.

Figure A.148: Integrated system throughput for FQ492N.

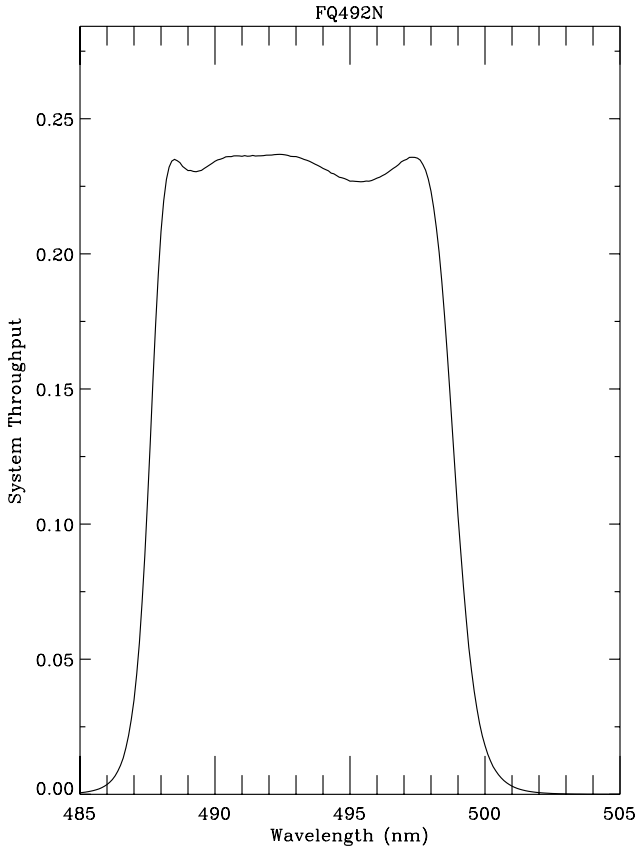

Figure A.149: Point source S/N vs. V+ABν for the FQ492N filter, assuming high sky backgrounds and a 5×5 pixel aperture.

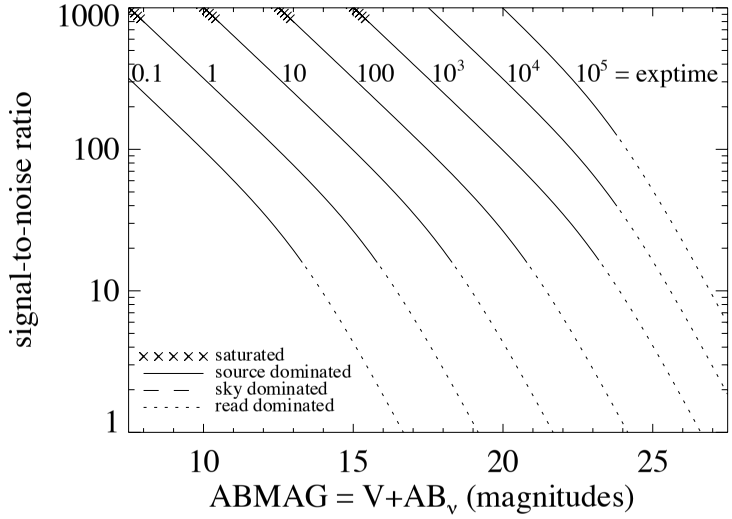

Figure A.150: Extended source S/N vs. V+ABν for the FQ492N filter, assuming high sky backgrounds and a source uniformly filling a 1 arcsec^2 aperture.

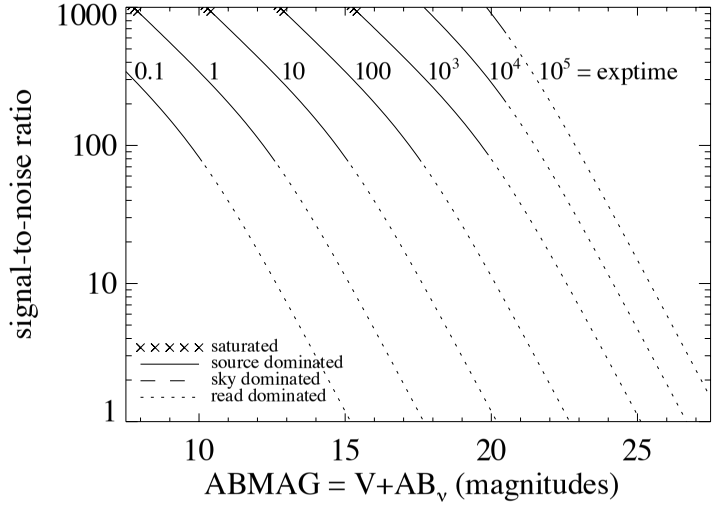

UVIS/FQ508N

Description

z ([O III] 5007) filter.

Figure A.151: Integrated system throughput for FQ508N.

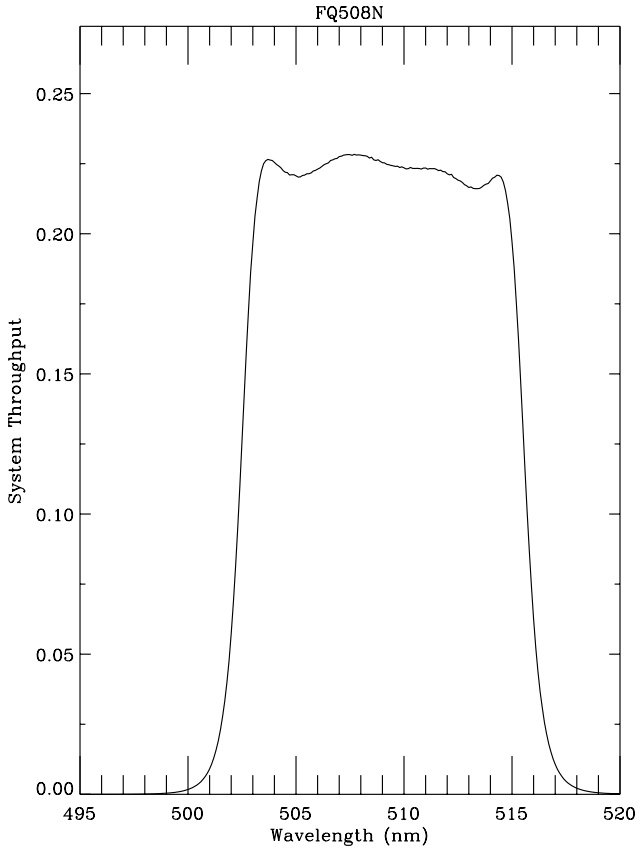

Figure A.152: Point source S/N vs. V+ABν for the FQ508N filter, assuming high sky backgrounds and a 5×5 pixel aperture.

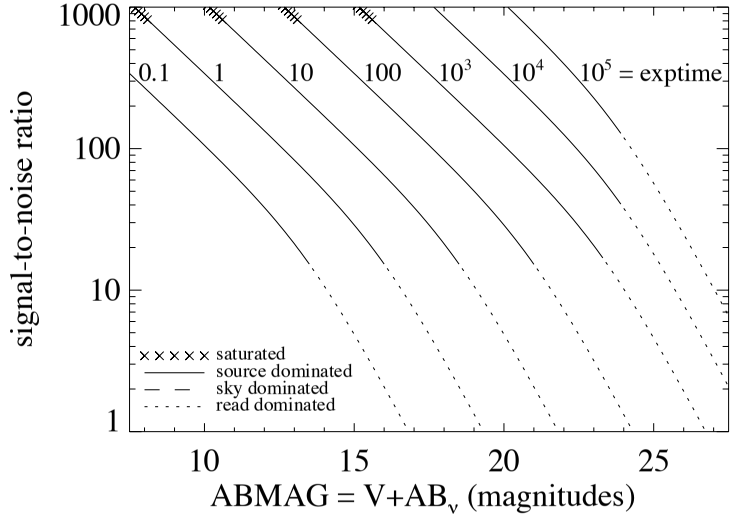

Figure A.153: Extended source S/N vs. V+ABν for the FQ508N filter, assuming high sky backgrounds and a source uniformly filling a 1 arcsec^2 aperture.

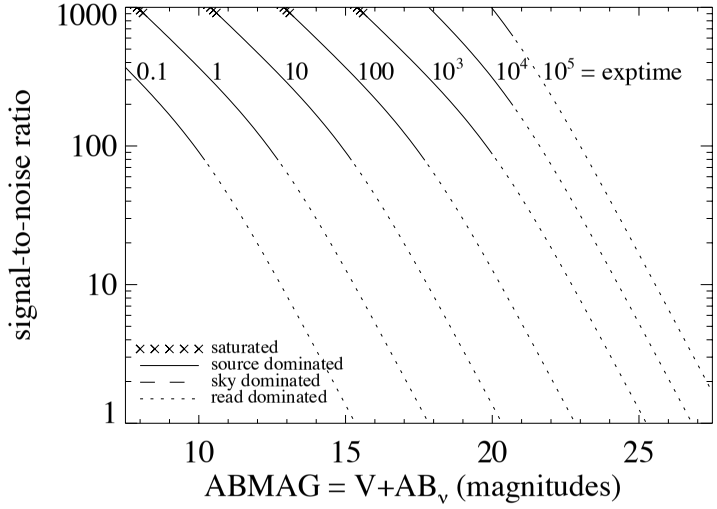

UVIS/FQ575N

Description

[N II] 5754 filter.

Figure A.154: Integrated system throughput for FQ575N.

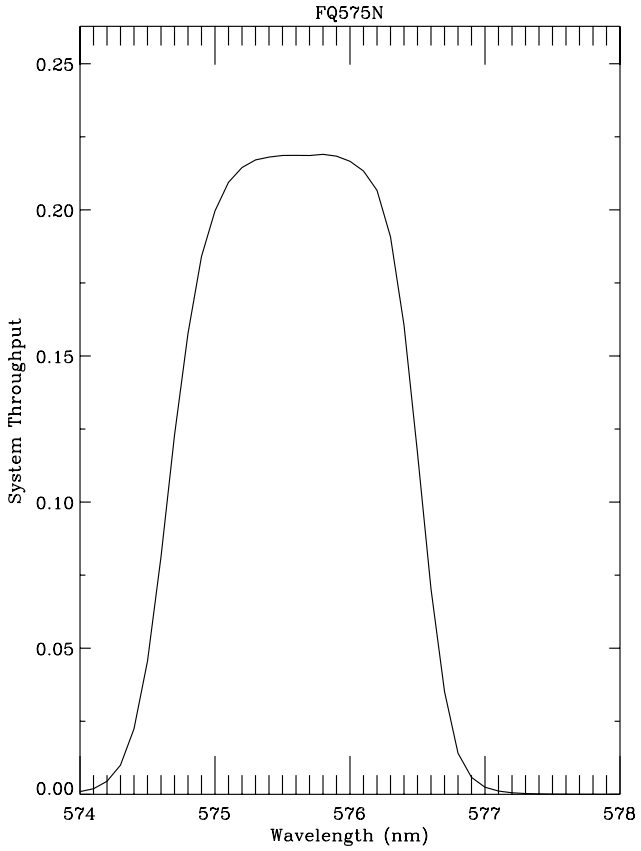

Figure A.155: Point source S/N vs. V+ABν for the FQ575N filter, assuming high sky backgrounds and a 5×5 pixel aperture.

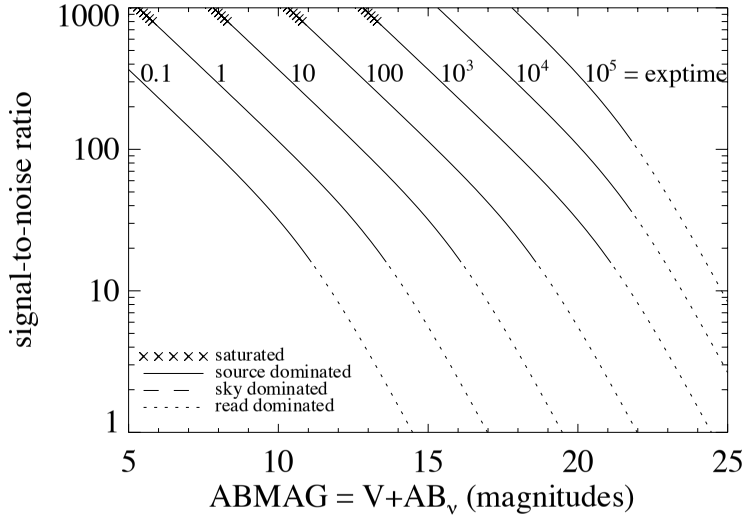

Figure A.156: Extended source S/N vs. V+ABν for the FQ575N filter, assuming high sky backgrounds and a source uniformly filling a 1 arcsec^2 aperture.

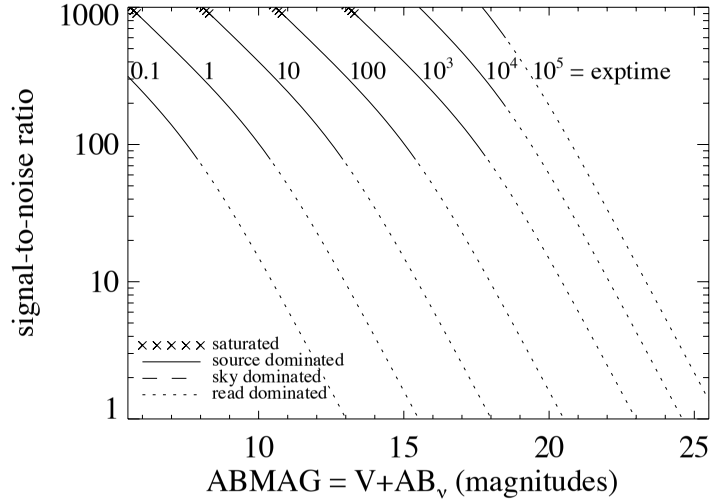

UVIS/FQ619N

Description

CH_4 6194 filter.

Figure A.157: Integrated system throughput for FQ619N.

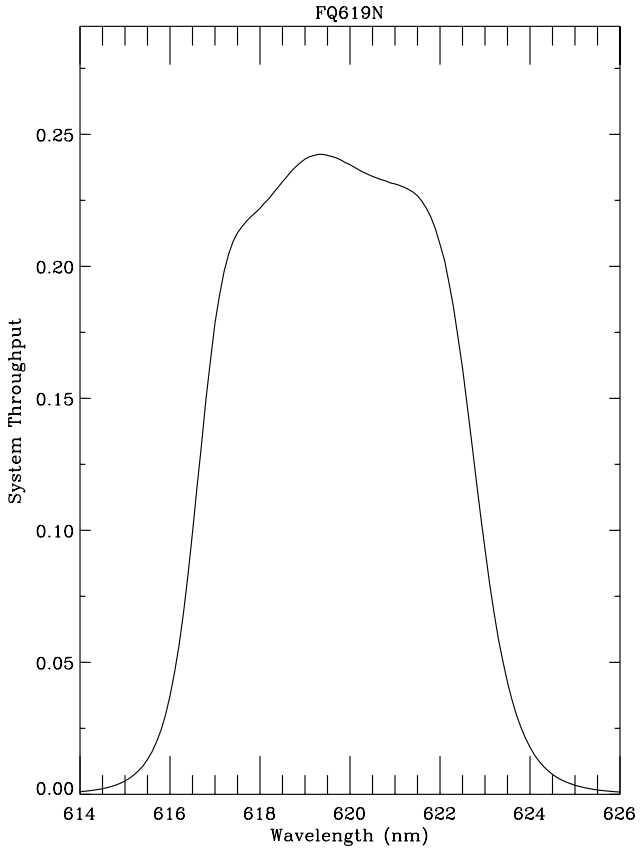

Figure A.158: Point source S/N vs. V+ABν for the FQ619N filter, assuming high sky backgrounds and a 5×5 pixel aperture.

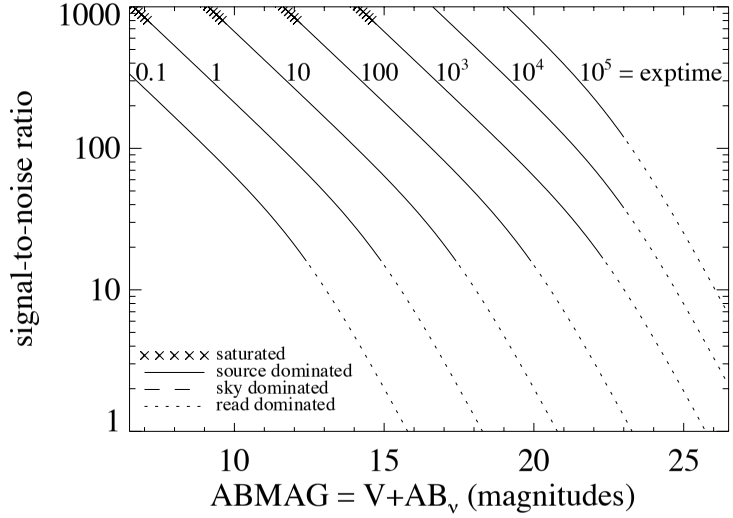

Figure A.159: Extended source S/N vs. V+ABν for the FQ619N filter, assuming high sky backgrounds and a source uniformly filling a 1 arcsec^2 aperture.

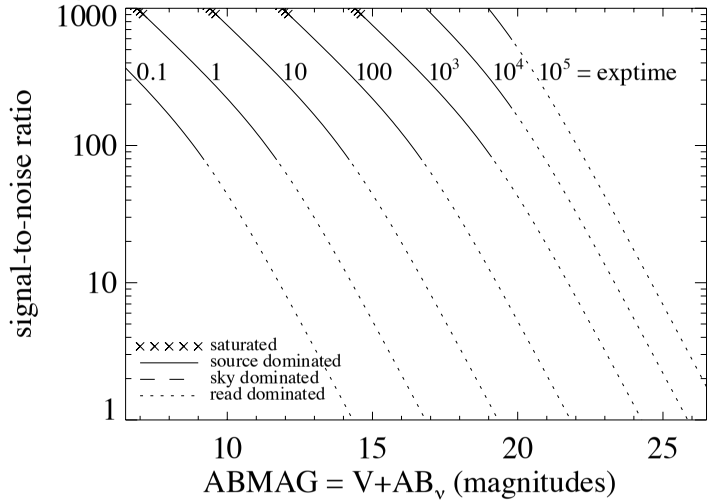

UVIS/FQ634N

Description

6194 continuum filter.

Figure A.160: Integrated system throughput for FQ634N.

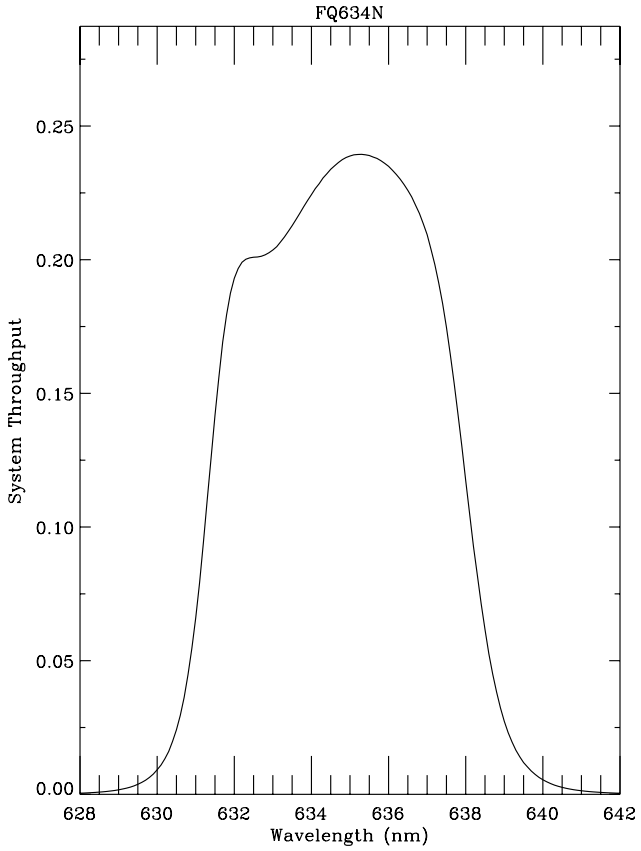

Figure A.161: Point source S/N vs. V+ABν for the FQ634N filter, assuming high sky backgrounds and a 5×5 pixel aperture.

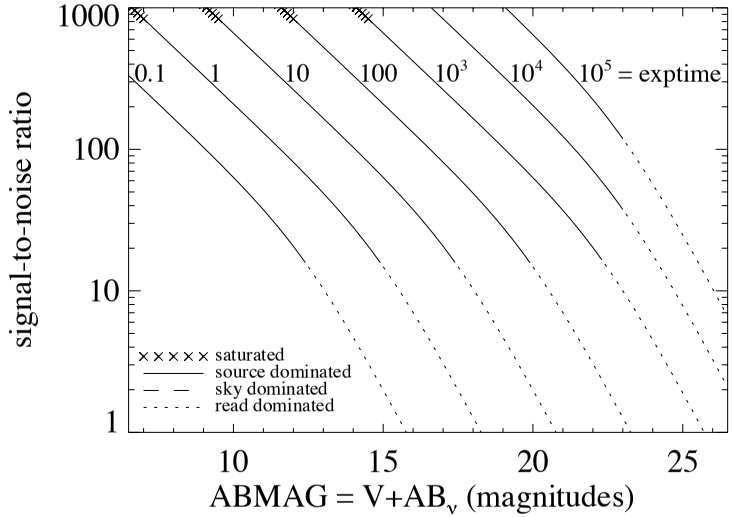

Figure A.162: Extended source S/N vs. V+ABν for the FQ634N filter, assuming high sky backgrounds and a source uniformly filling a 1 arcsec^2 aperture.

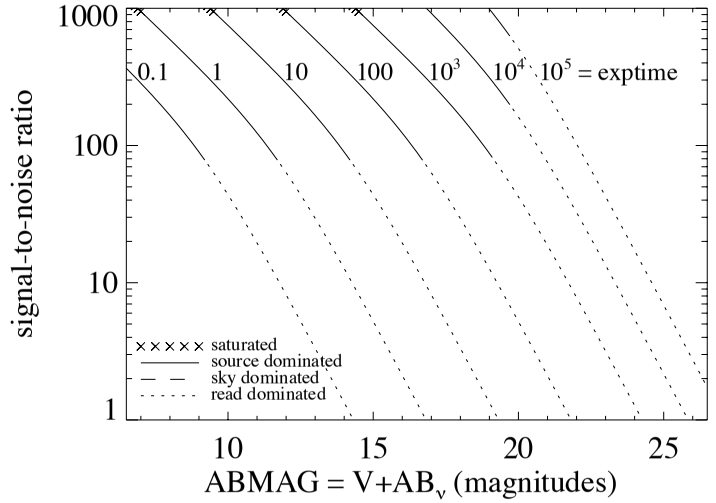

UVIS/FQ672N

Description

[S II] 6717 filter.

Figure A.163: Integrated system throughput for FQ672N.

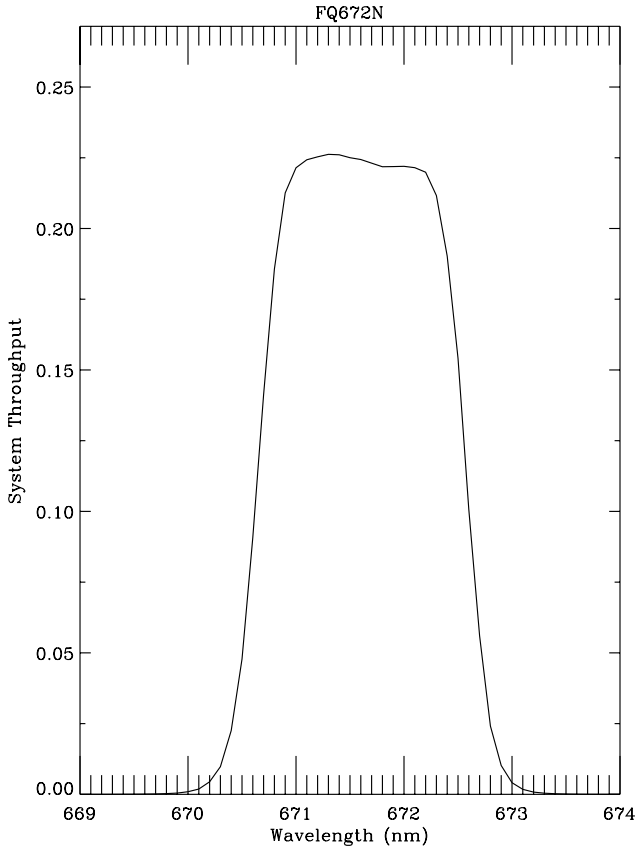

Figure A.164: Point source S/N vs. V+ABν for the FQ672N filter, assuming high sky backgrounds and a 5×5 pixel aperture.

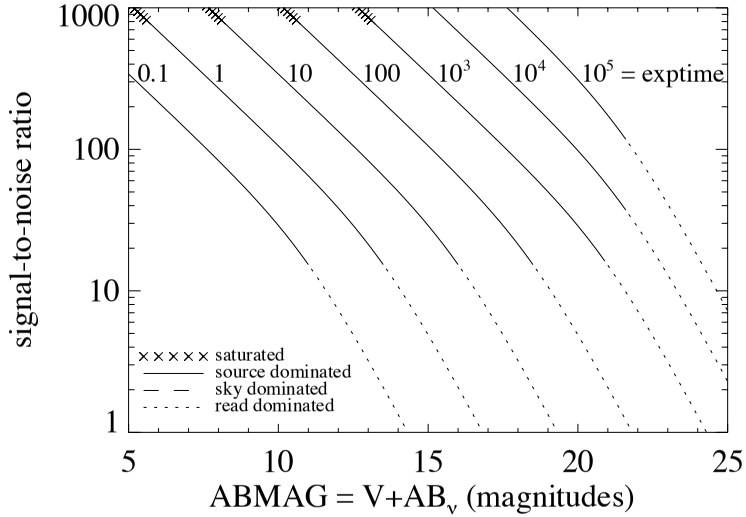

Figure A.165: Extended source S/N vs. V+ABν for the FQ672N filter, assuming high sky backgrounds and a source uniformly filling a 1 arcsec^2 aperture.

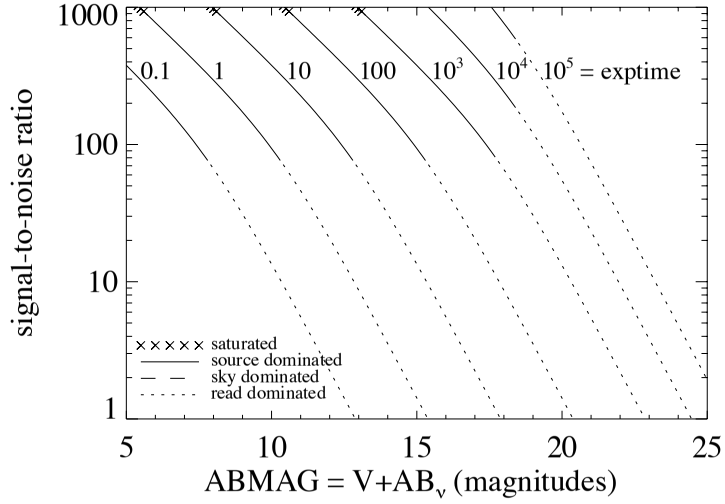

UVIS/FQ674N

Description

[S II] 6731 filter.

Figure A.166: Integrated system throughput for FQ674N.

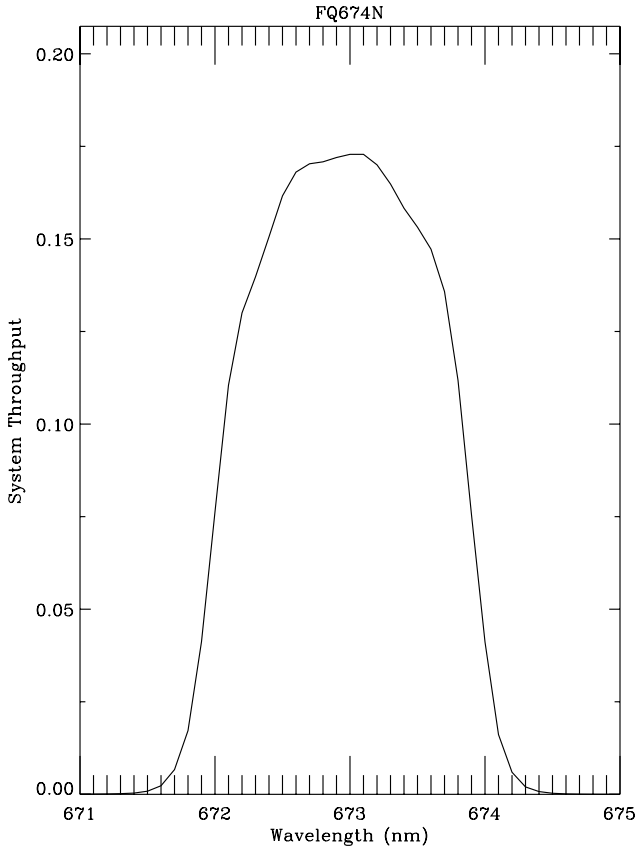

Figure A.167: Point source S/N vs. V+ABν for the FQ674N filter, assuming high sky backgrounds and a 5×5 pixel aperture.

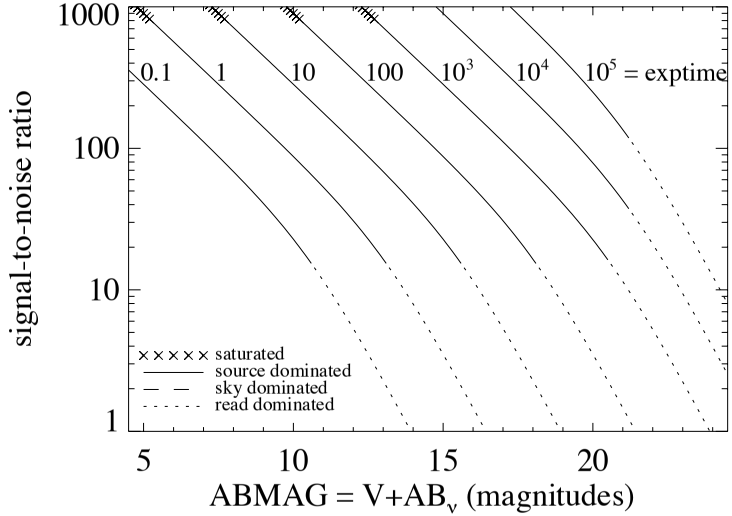

Figure A.168: Extended source S/N vs. V+ABν for the FQ674N filter, assuming high sky backgrounds and a source uniformly filling a 1 arcsec^2 aperture.

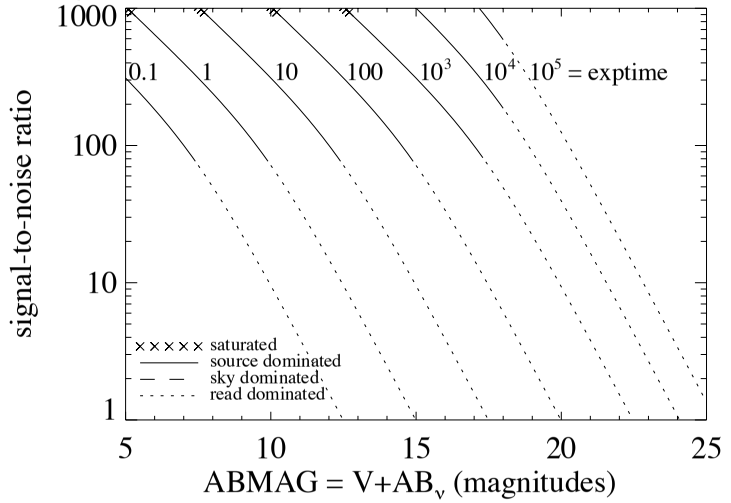

UVIS/FQ727N

Description

CH_4 7270 filter.

Figure A.169: Integrated system throughput for FQ727N.

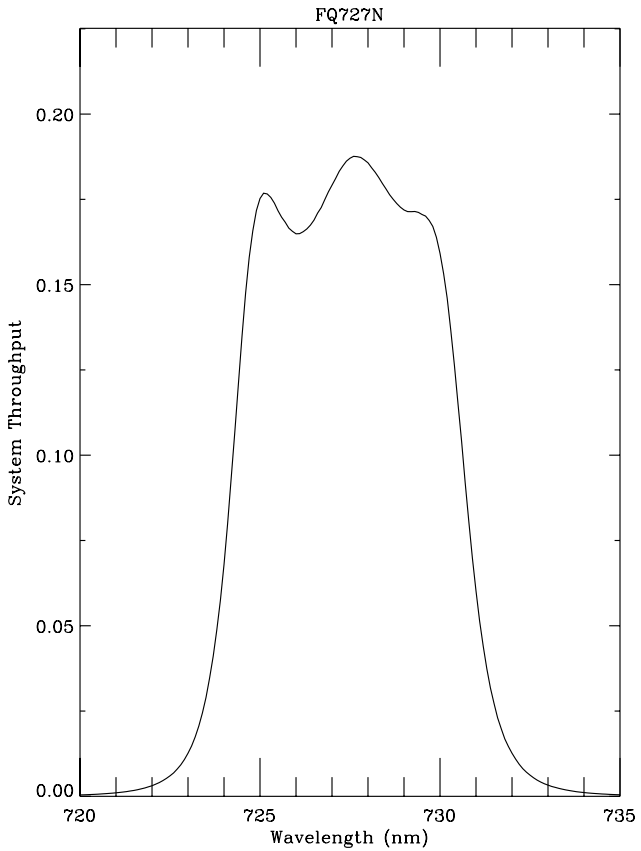

Figure A.170: Point source S/N vs. V+ABν for the FQ727N filter, assuming high sky backgrounds and a 5×5 pixel aperture.

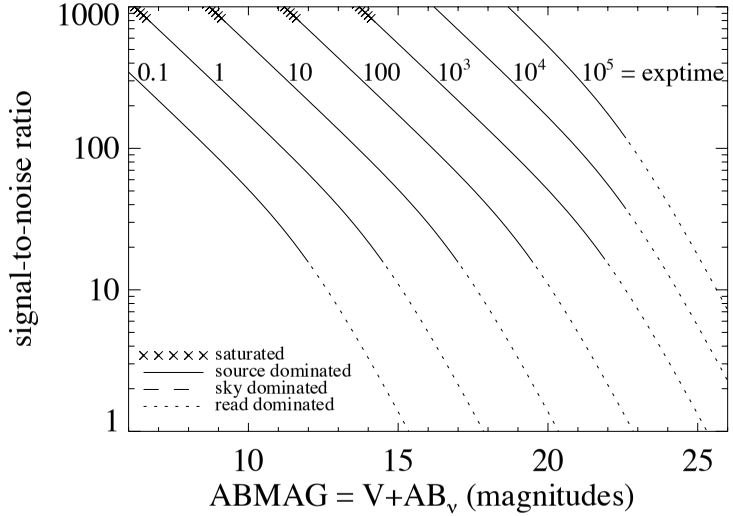

Figure A.171: Extended source S/N vs. V+ABν for the FQ727N filter, assuming high sky backgrounds and a source uniformly filling a 1 arcsec^2 aperture.

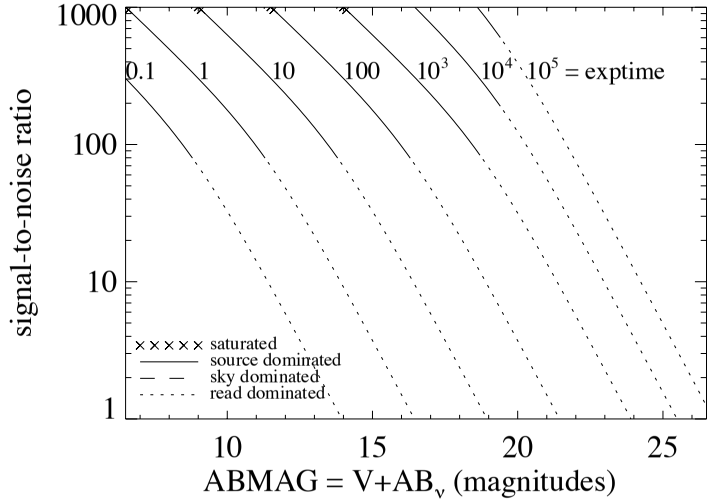

UVIS/FQ750N

Description

7270 continuum filter.

Figure A.172: Integrated system throughput for FQ750N.

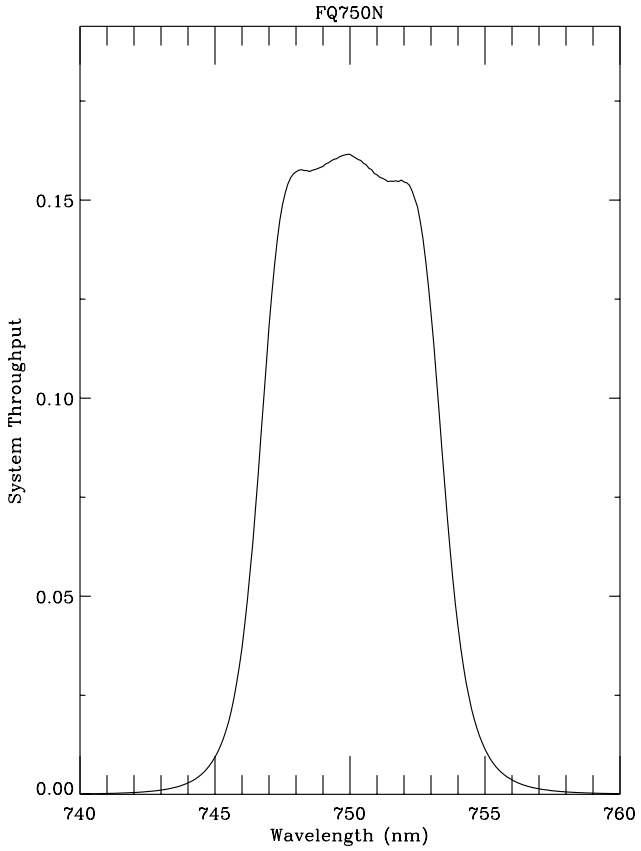

Figure A.173: Point source S/N vs. V+ABν for the FQ750N filter, assuming high sky backgrounds and a 5×5 pixel aperture.

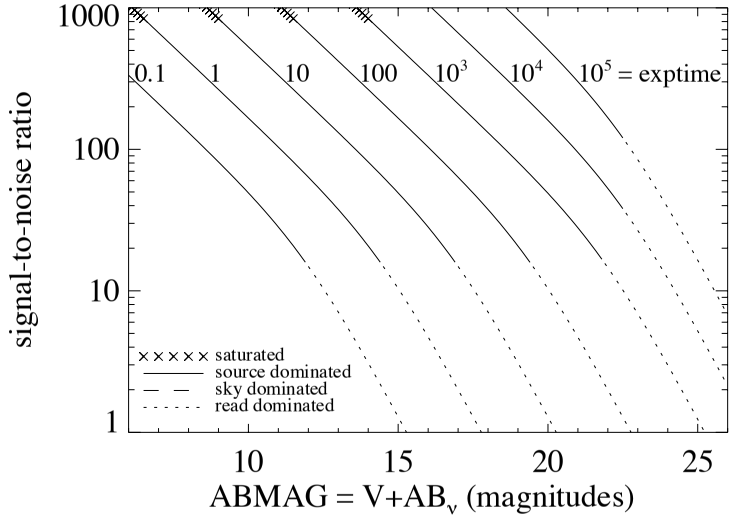

Figure A.174: Extended source S/N vs. V+ABν for the FQ750N filter, assuming high sky backgrounds and a source uniformly filling a 1 arcsec^2 aperture.

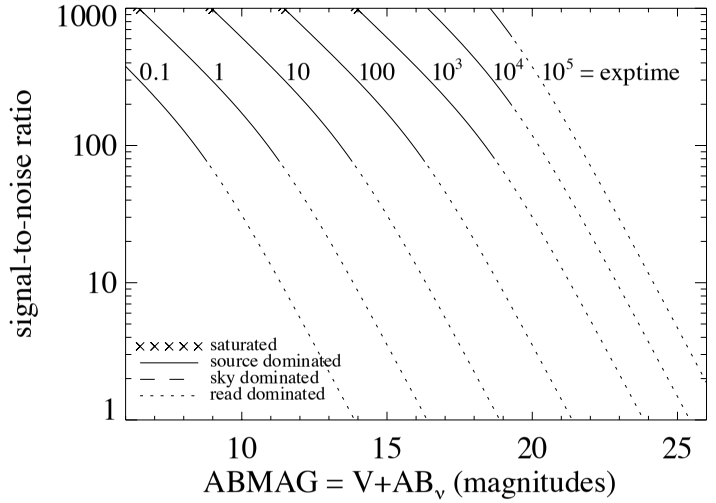

UVIS/FQ889N

Description

CH_4 25 km-agt filter.

Figure A.175: Integrated system throughput for FQ889N.

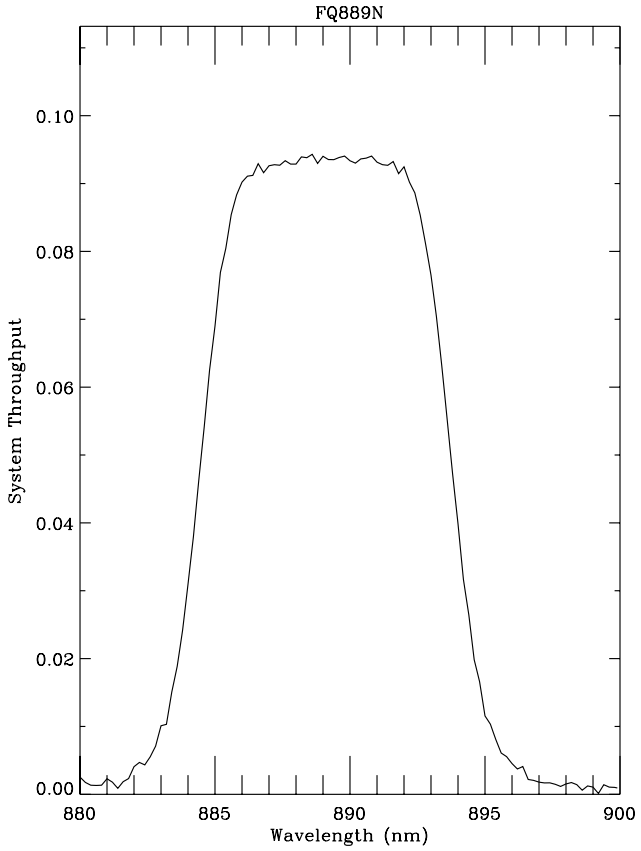

Figure A.176: Point source S/N vs. V+ABν for the FQ889N filter, assuming high sky backgrounds and a 5×5 pixel aperture.

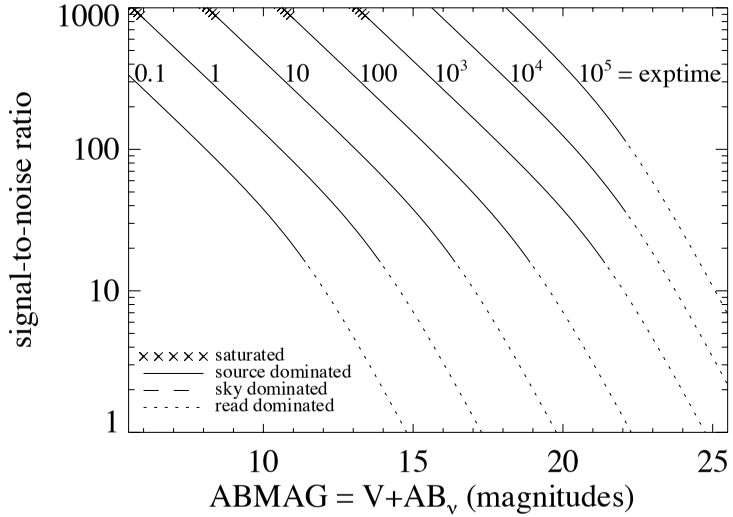

Figure A.177: Extended source S/N vs. V+ABν for the FQ889N filter, assuming high sky backgrounds and a source uniformly filling a 1 arcsec^2 aperture.

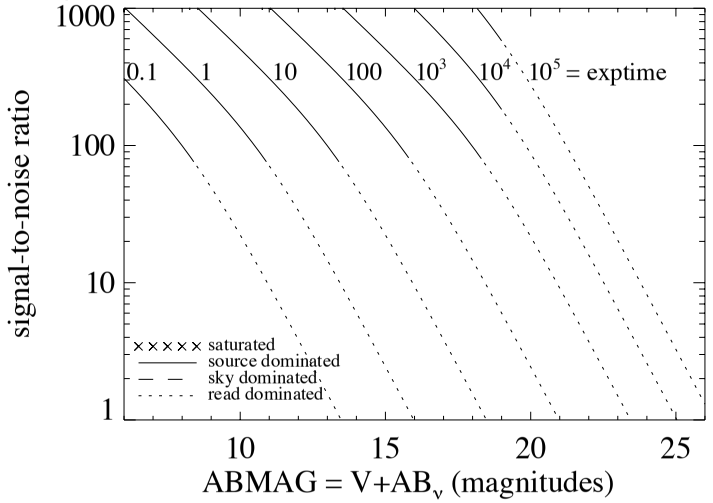

UVIS/FQ906N

Description

CH_4 2.5 km-agt filter.

Figure A.178: Integrated system throughput for FQ906N.

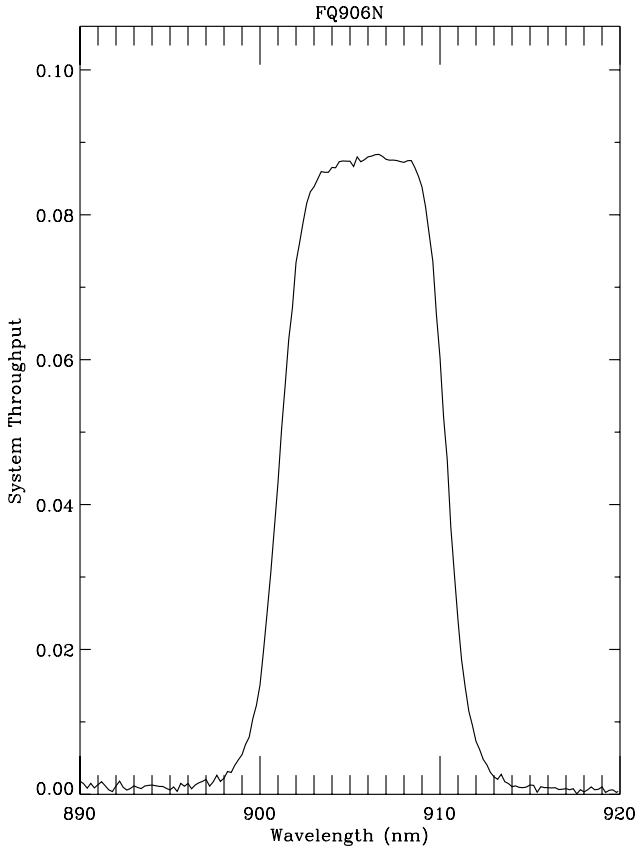

Figure A.179: Point source S/N vs. V+ABν for the FQ906N filter, assuming high sky backgrounds and a 5×5 pixel aperture.

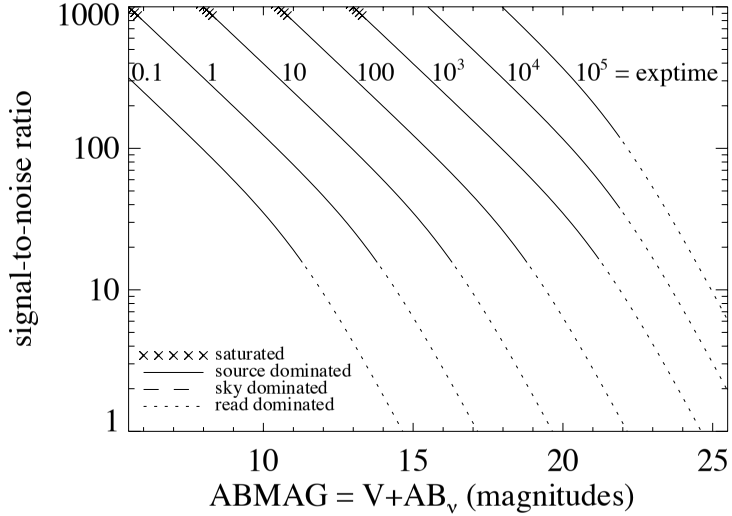

Figure A.180: Extended source S/N vs. V+ABν for the FQ906N filter, assuming high sky backgrounds and a source uniformly filling a 1 arcsec^2 aperture.

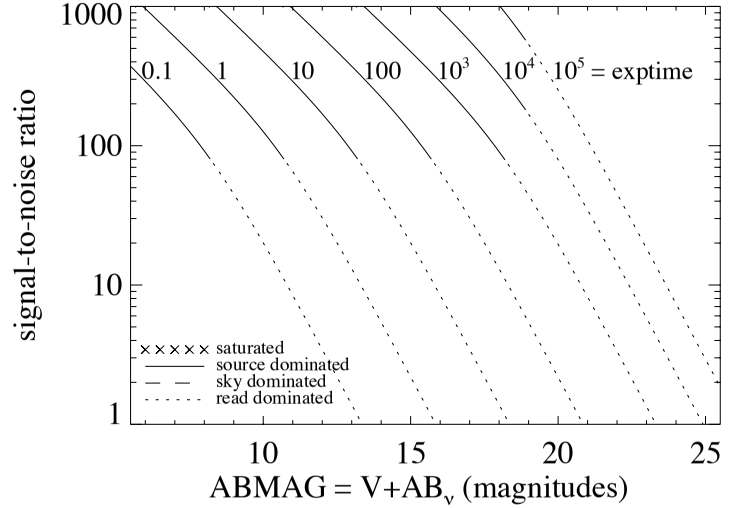

UVIS/FQ924N

Description

CH_4 0.25 km-agt filter.

Figure A.181: Integrated system throughput for FQ924N.

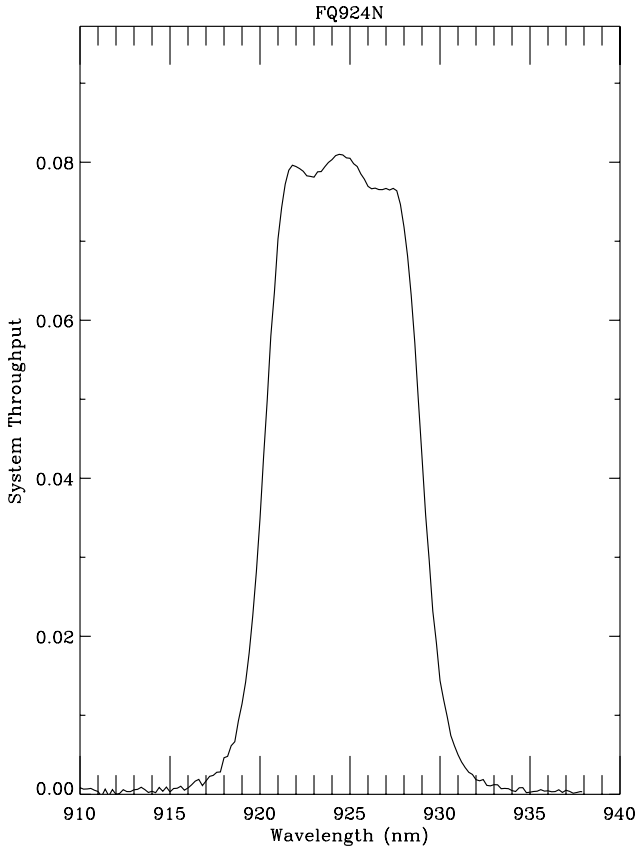

Figure A.182: Point source S/N vs. V+ABν for the FQ924N filter, assuming high sky backgrounds and a 5×5 pixel aperture.

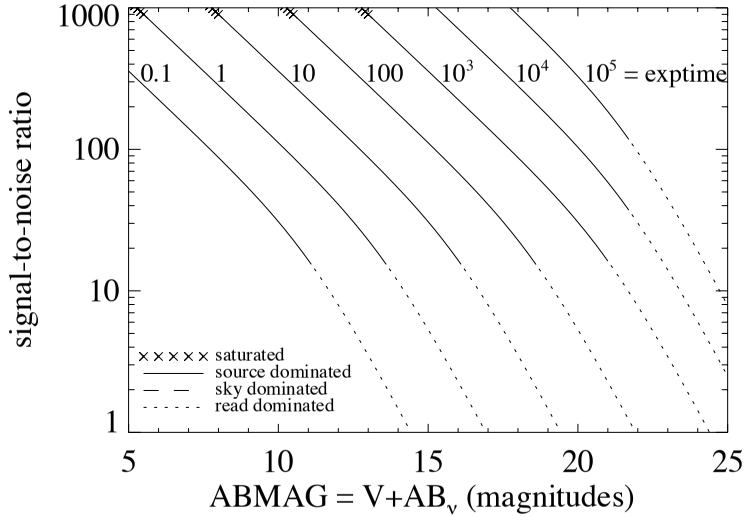

Figure A.183: Extended source S/N vs. V+ABν for the FQ924N filter, assuming high sky backgrounds and a source uniformly filling a 1 arcsec^2 aperture.

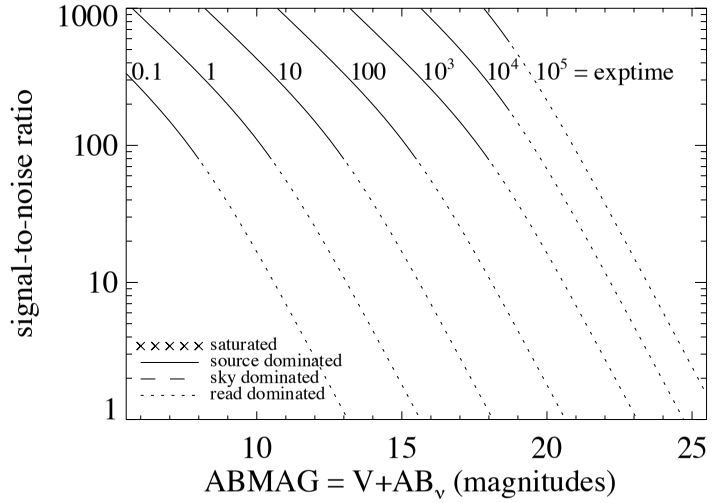

UVIS/FQ937N

Description

CH_4 0.025 km-agt filter.

Figure A.184: Integrated system throughput for FQ937N.

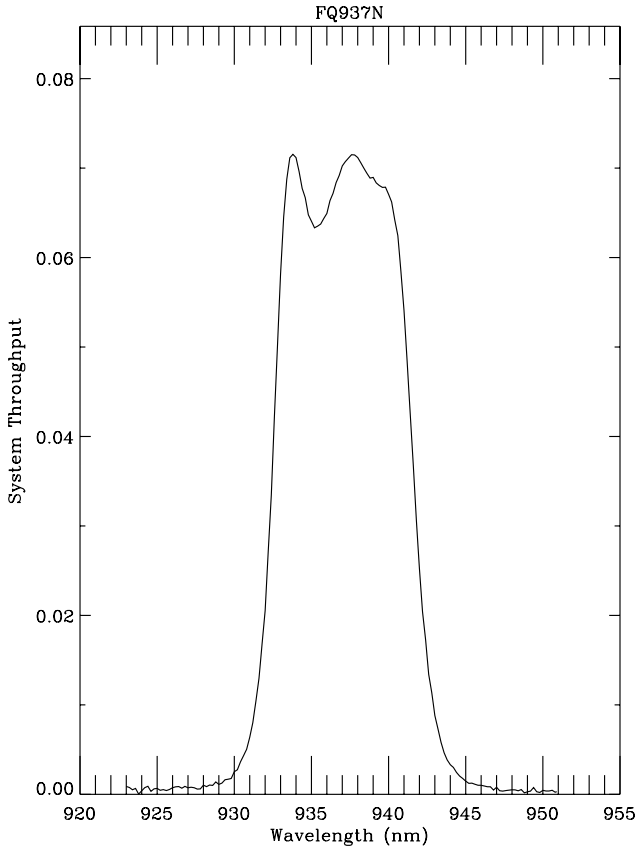

Figure A.185: Point source S/N vs. V+ABν for the FQ937N filter, assuming high sky backgrounds and a 5×5 pixel aperture.

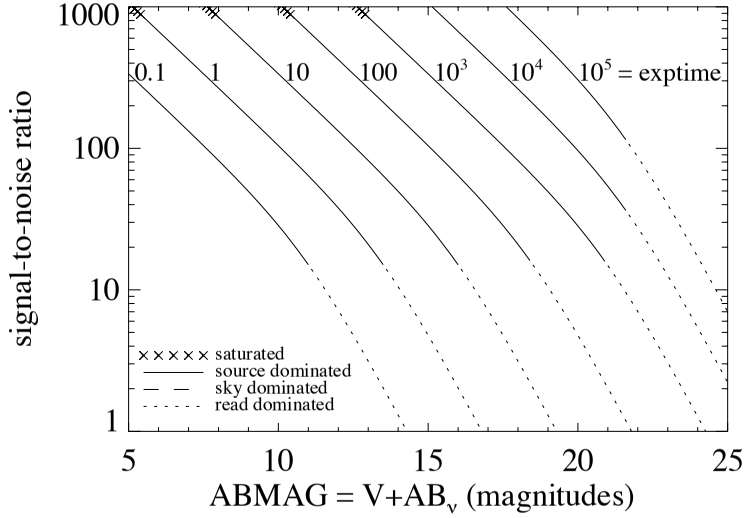

Figure A.186: Extended source S/N vs. V+ABν for the FQ937N filter, assuming high sky backgrounds and a source uniformly filling a 1 arcsec^2 aperture.

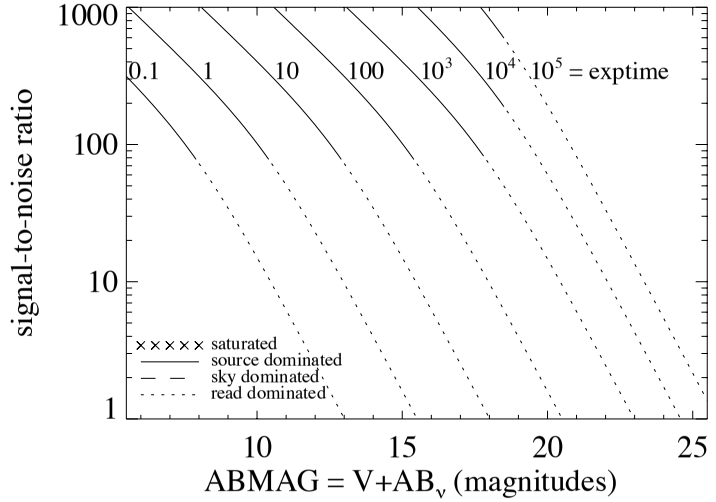

IR/F098M

Description

Blue grism reference filter.

Figure A.187: Integrated system throughput for F098M.

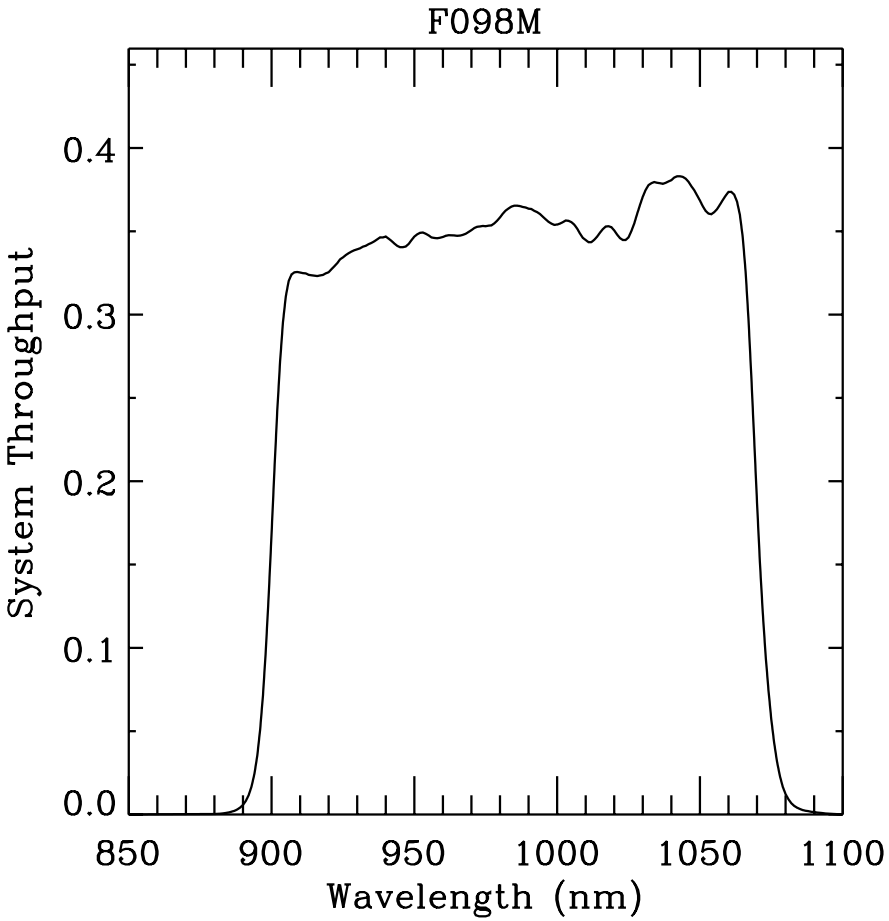

Figure A.188: Point source S/N vs. V+ABν for the F098M filter, assuming high sky backgrounds and a 3×3 pixel aperture.

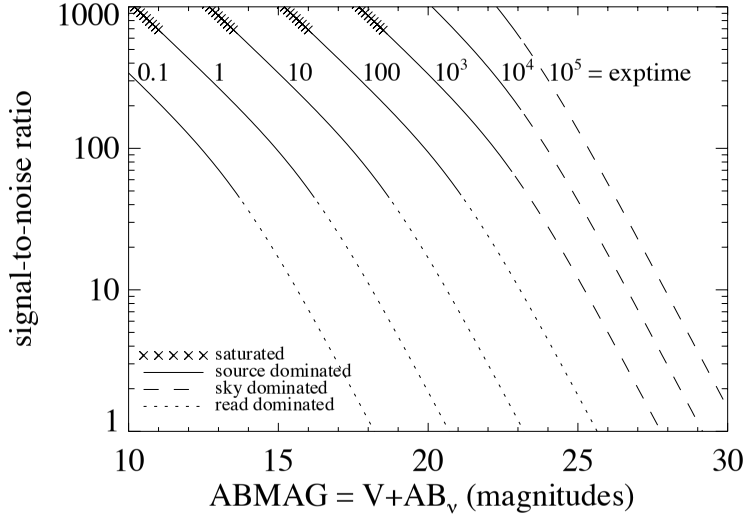

Figure A.189: Extended source S/N vs. V+ABν for the F098M filter, assuming high sky backgrounds and a source uniformly filling a 1 arcsec^2 aperture.

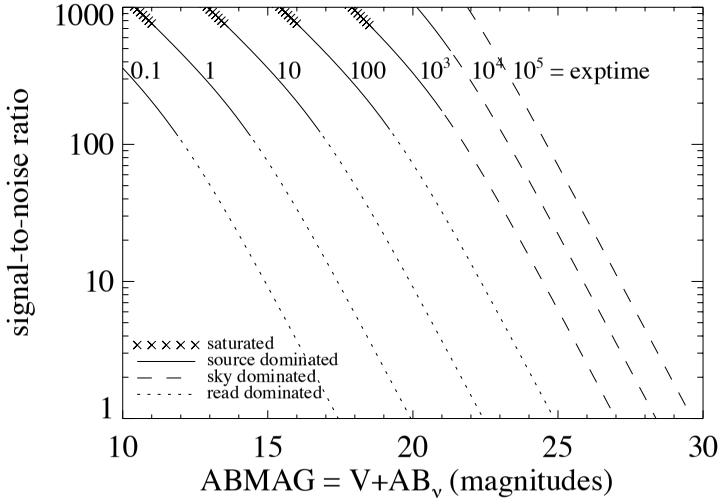

IR/F105W

Description

Wide *Y* filter.

Figure A.190: Integrated system throughput for F105W.

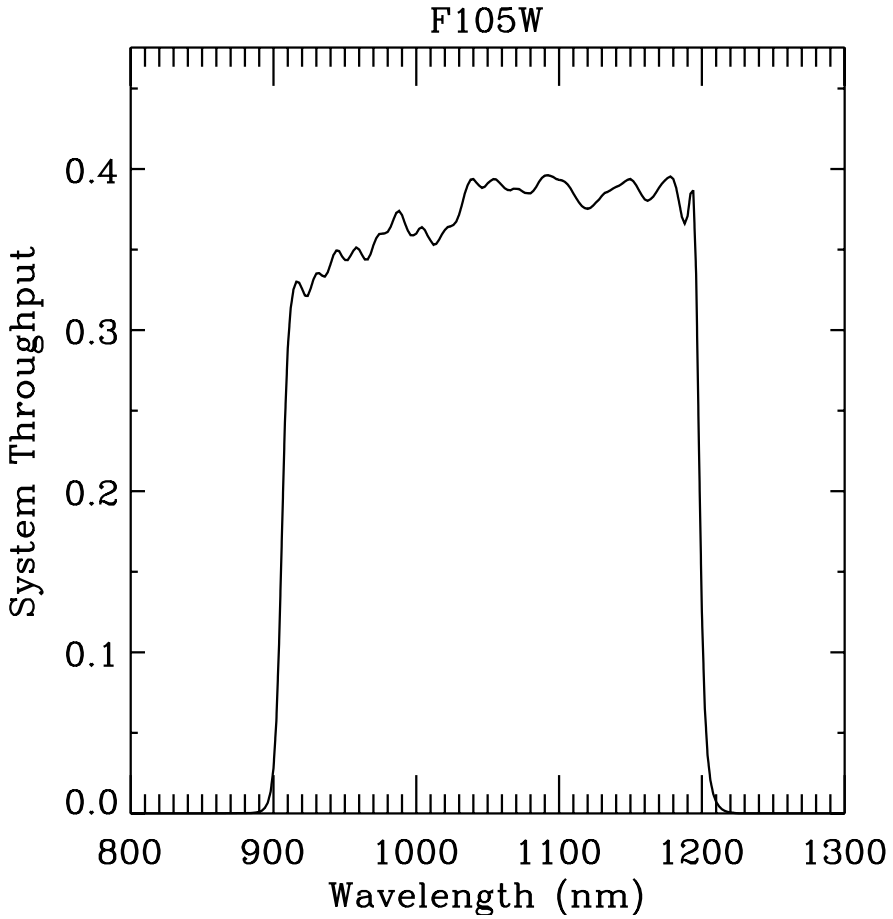

Figure A.191: Point source S/N vs. V+ABν for the F105W filter, assuming high sky backgrounds and a 3×3 pixel aperture.

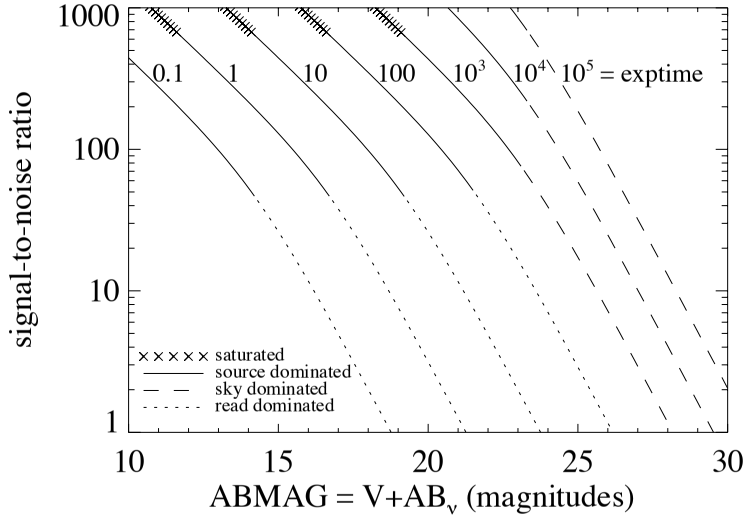

Figure A.192: Extended source S/N vs. V+ABν for the F105W filter, assuming high sky backgrounds and a source uniformly filling a 1 arcsec^2 aperture.

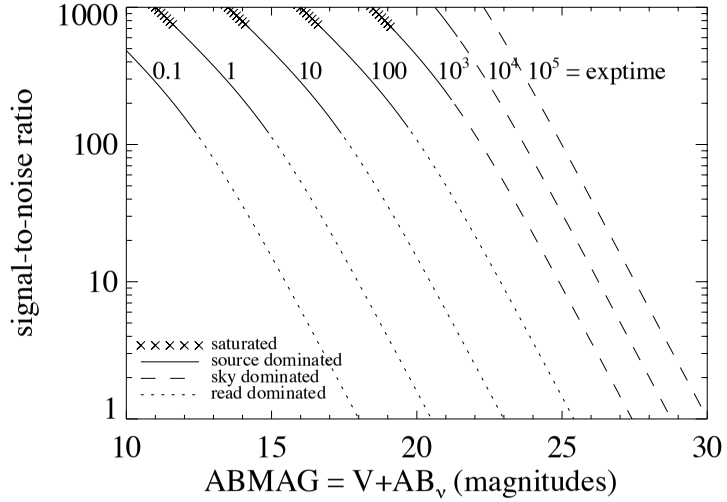

IR/F110W

Description

Wide *YJ* filter.

Figure A.193: Integrated system throughput for F110W.

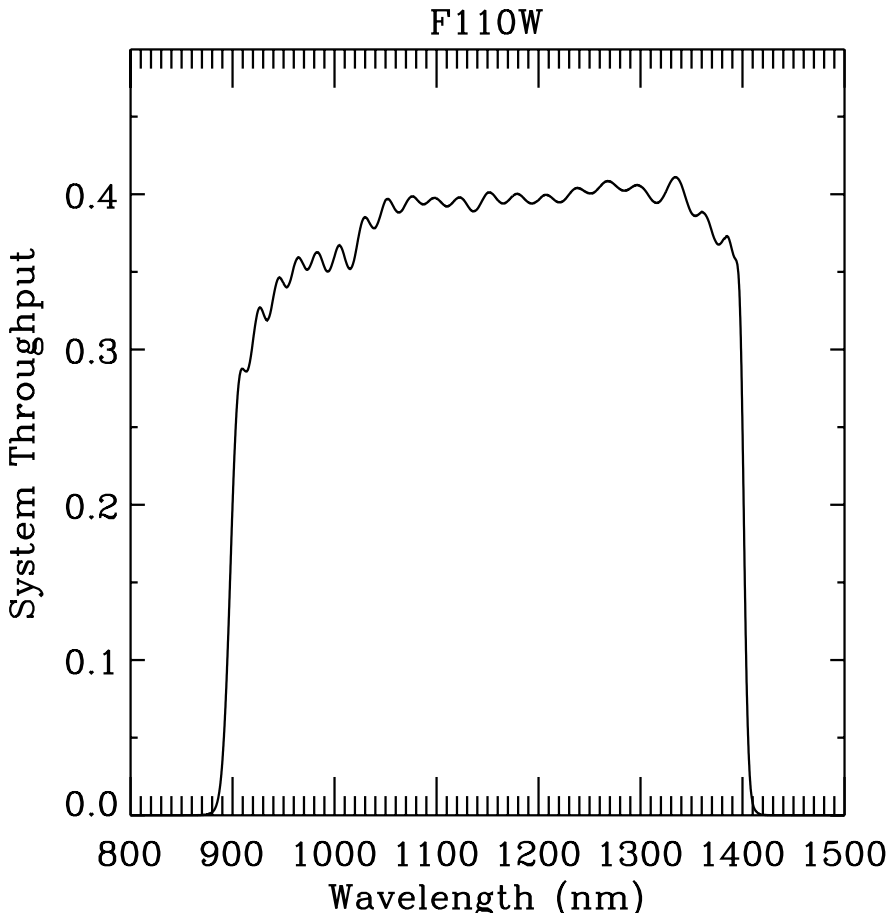

Figure A.194: Point source S/N vs. V+ABν for the F110W filter, assuming high sky backgrounds and a 3×3 pixel aperture.

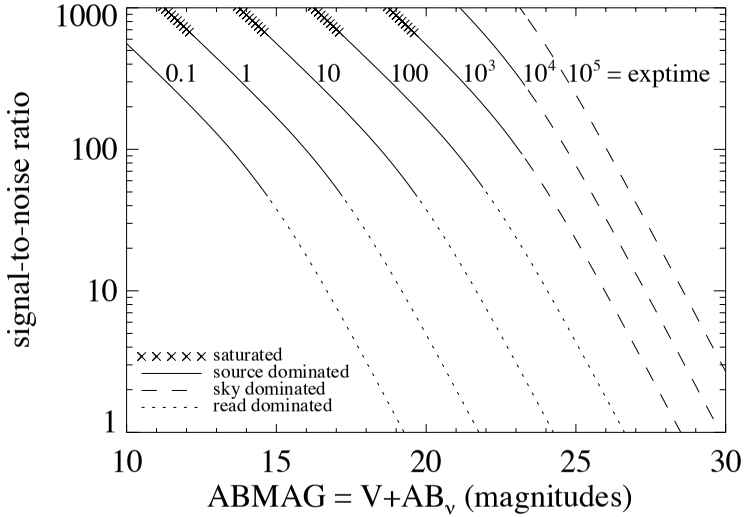

Figure A.195: Extended source S/N vs. V+ABν for the F110W filter, assuming high sky backgrounds and a source uniformly filling a 1 arcsec^2 aperture.

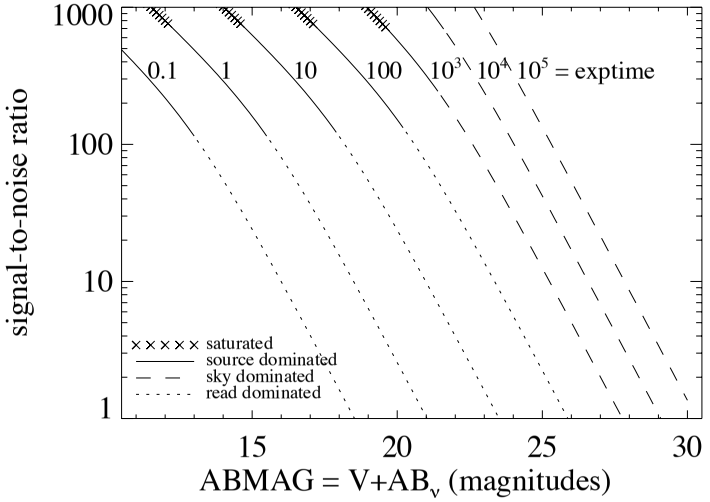

IR/F125W

Description

Wide *J* filter.

Figure A.196: Integrated system throughput for F125W.

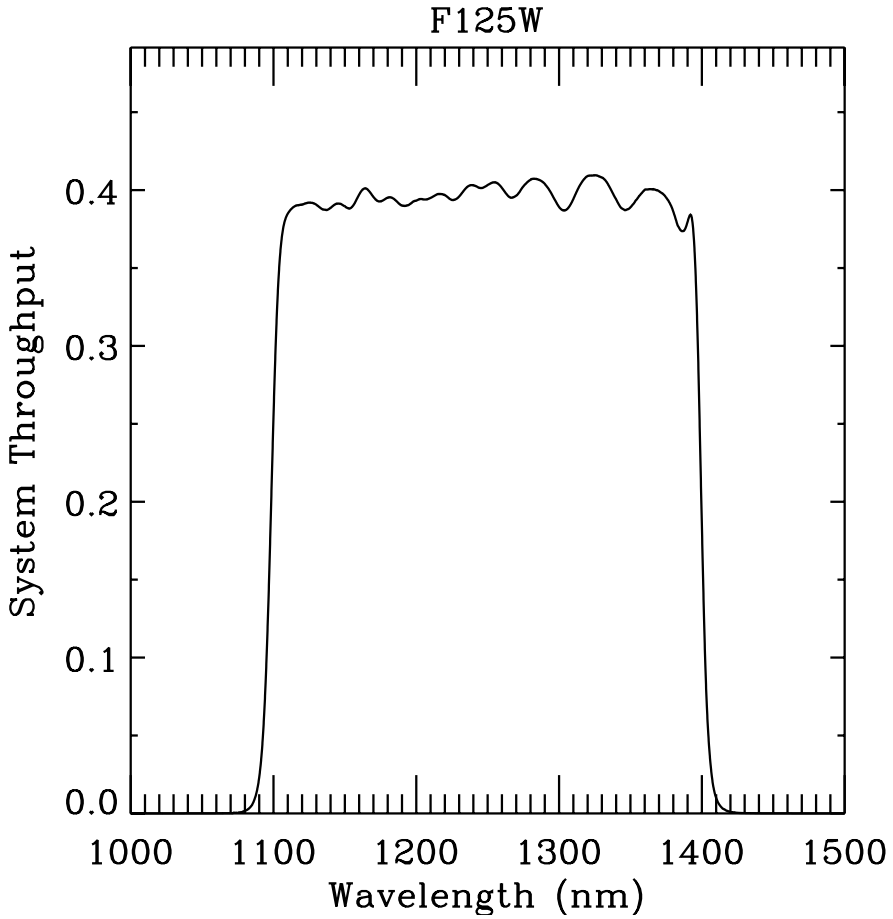

Figure A.197: Point source S/N vs. V+ABν for the F125W filter, assuming high sky backgrounds and a 3×3 pixel aperture.

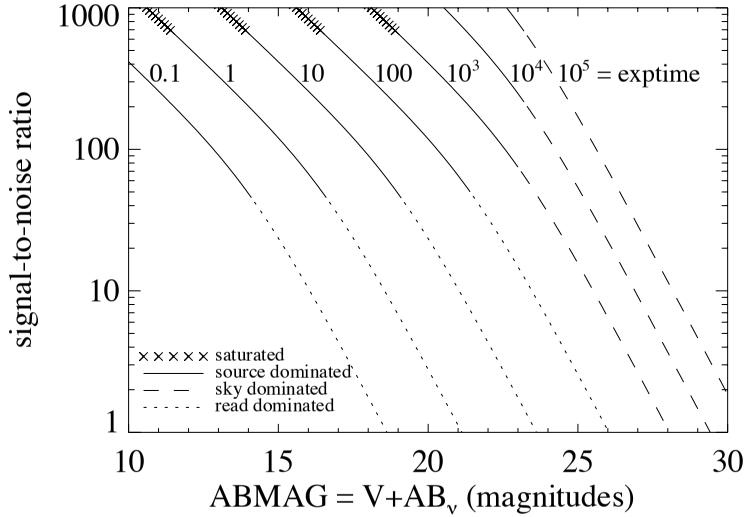

Figure A.198: Extended source S/N vs. V+ABν for the F125W filter, assuming high sky backgrounds and a source uniformly filling a 1 arcsec^2 aperture.

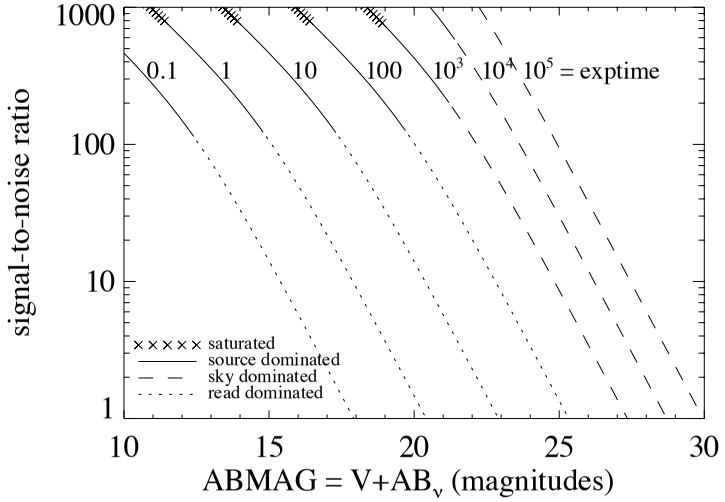

IR/F126N

Description

[Fe II] filter.

Figure A.199: Integrated system throughput for F126N.

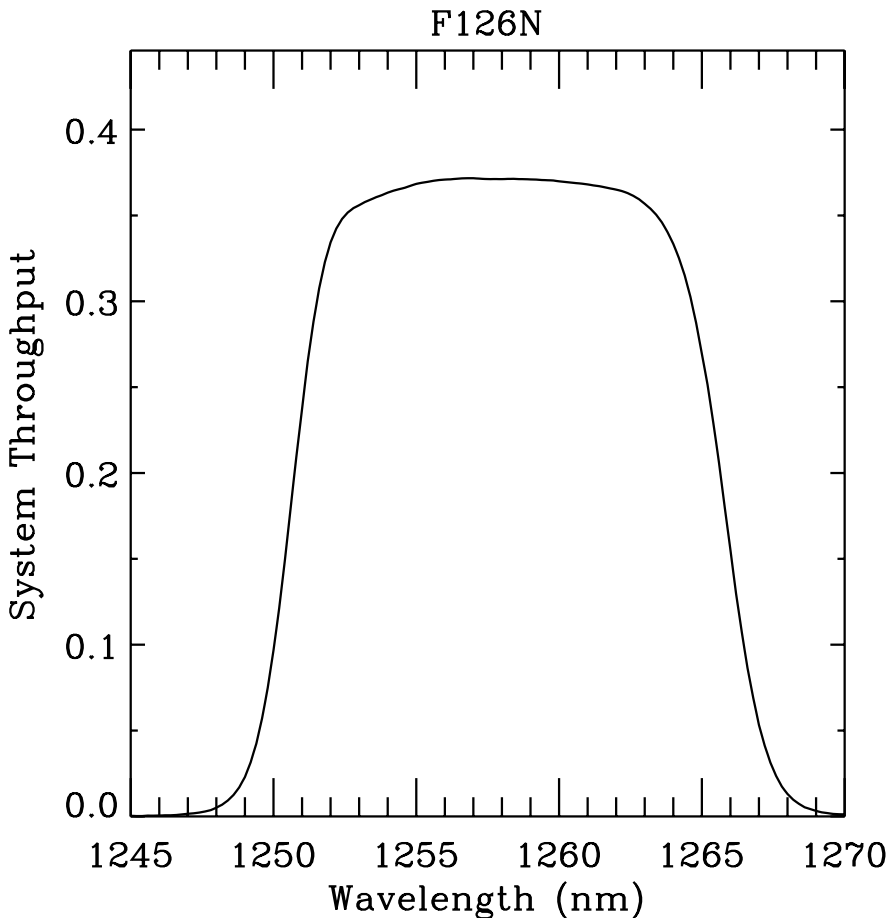

Figure A.200: Point source S/N vs. V+ABν for the F126N filter, assuming high sky backgrounds and a 3×3 pixel aperture.

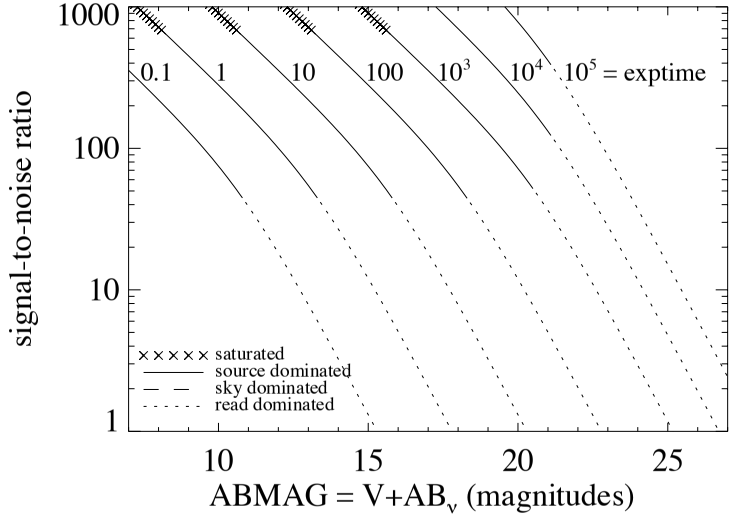

Figure A.201: Extended source S/N vs. V+ABν for the F126N filter, assuming high sky backgrounds and a source uniformly filling a 1 arcsec^2 aperture.

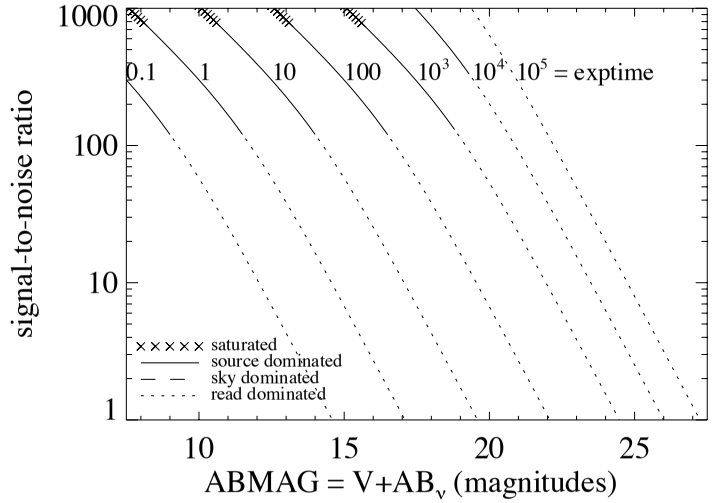

IR/F127M

Description

H_2O/CH_4 continuum filter.

Figure A.202: Integrated system throughput for F127M.

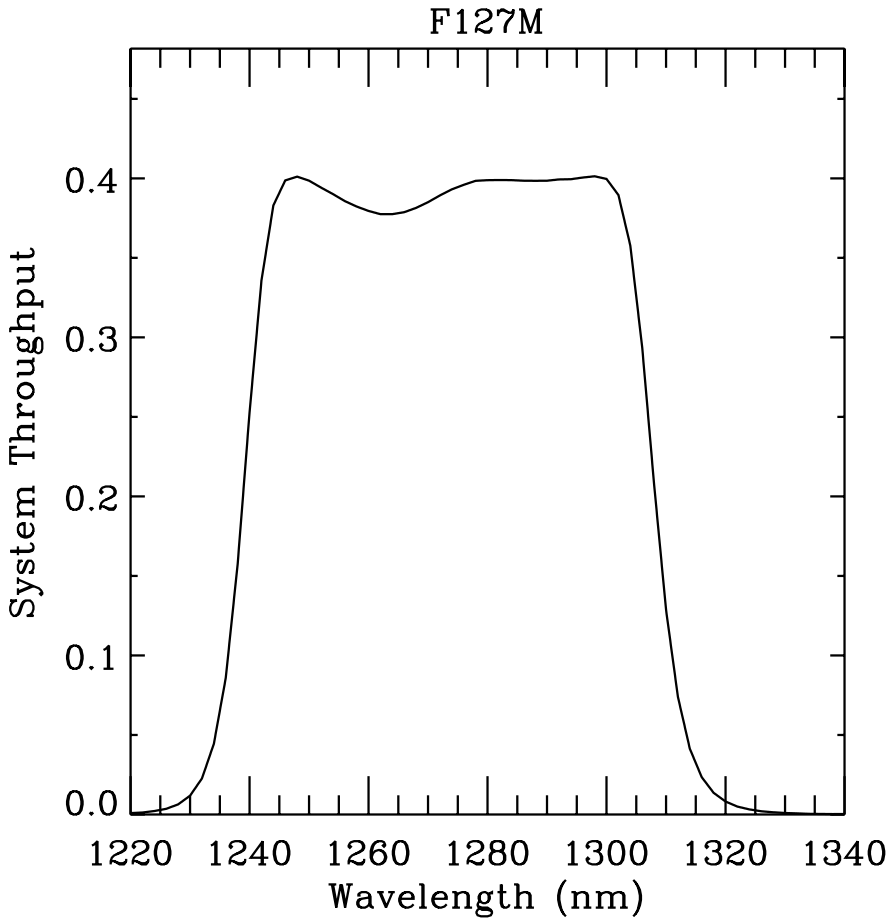

Figure A.203: Point source S/N vs. V+ABν for the F127M filter, assuming high sky backgrounds and a 3×3 pixel aperture.

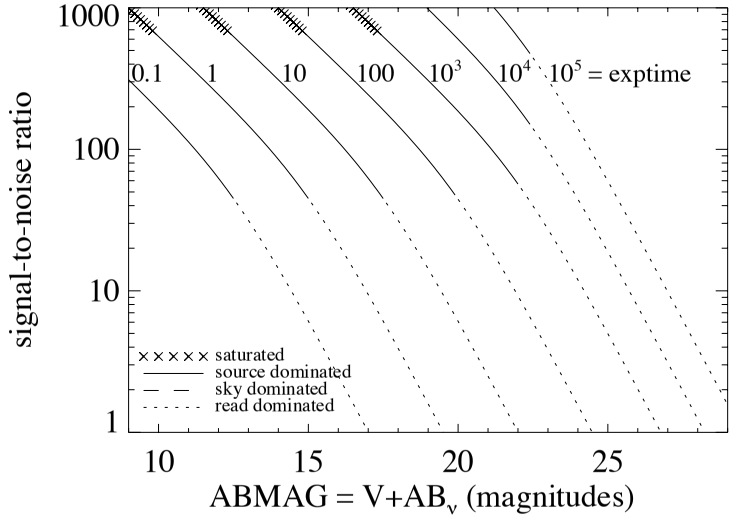

Figure A.204: Extended source S/N vs. V+ABν for the F127M filter, assuming high sky backgrounds and a source uniformly filling a 1 arcsec^2 aperture.

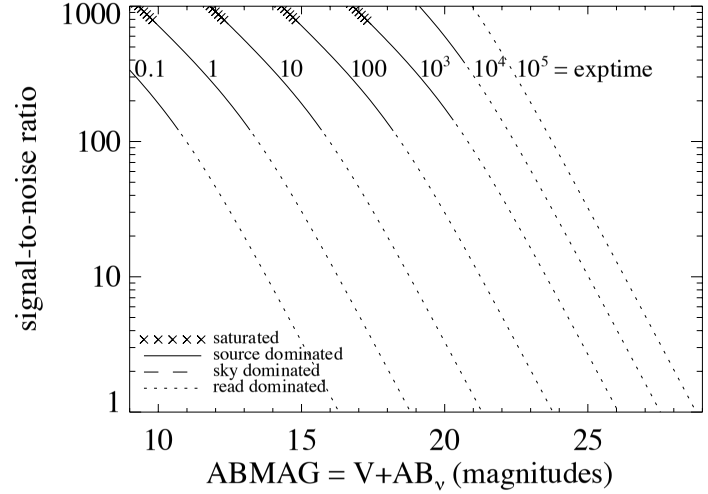

IR/F128N

Description

Paschen β filter.

Figure A.205: Integrated system throughput for F128N.

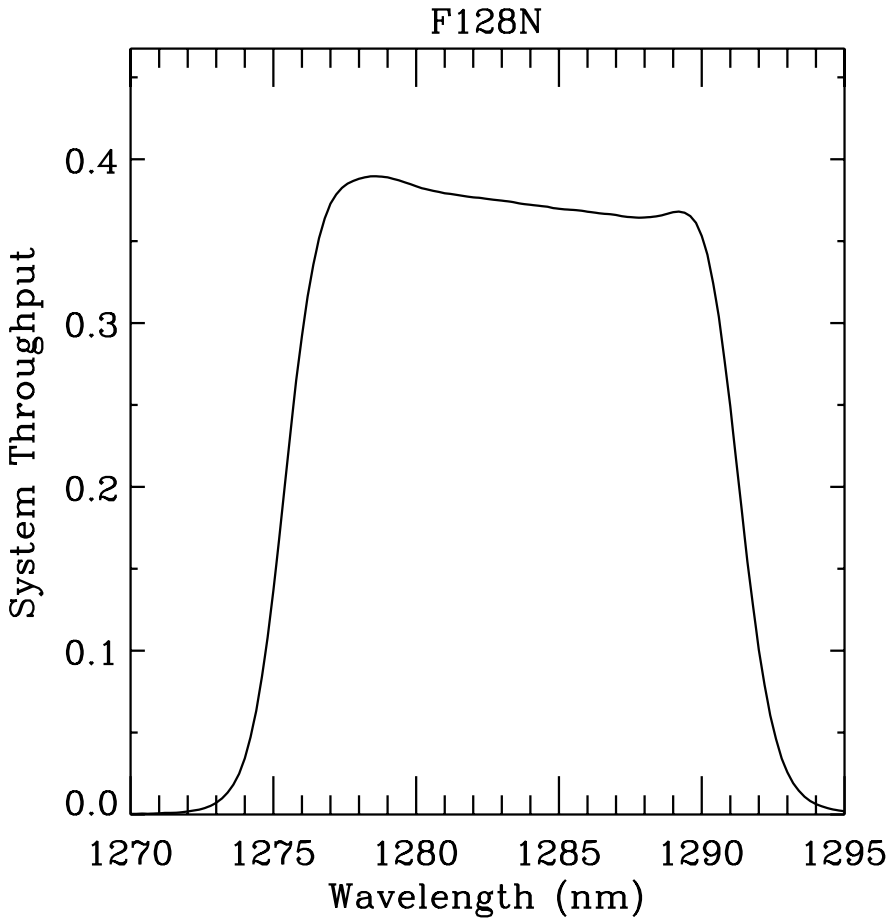

Figure A.206: Point source S/N vs. V+ABν for the F128N filter, assuming high sky backgrounds and a 3×3 pixel aperture.

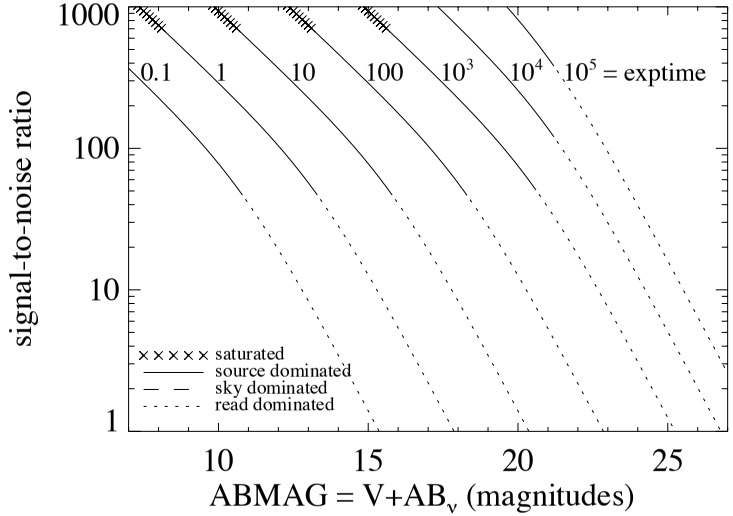

Figure A.207: Extended source S/N vs. V+ABν for the F128N filter, assuming high sky backgrounds and a source uniformly filling a 1 arcsec^2 aperture.

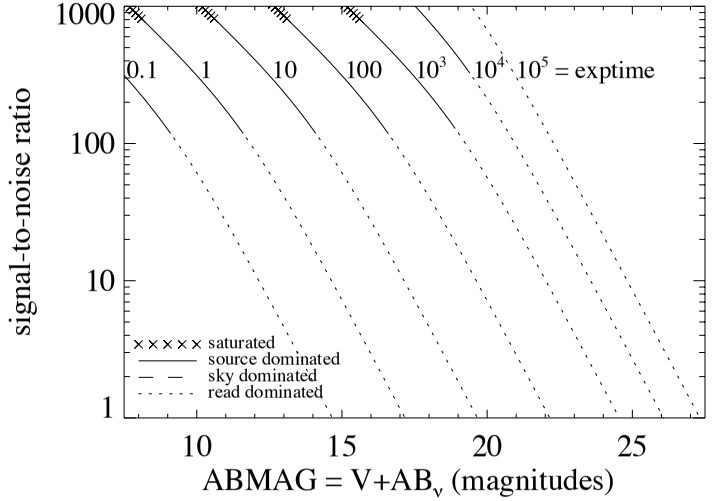

IR/F130N

Description

Paschen β continuum filter.

Figure A.208: Integrated system throughput for F130N.

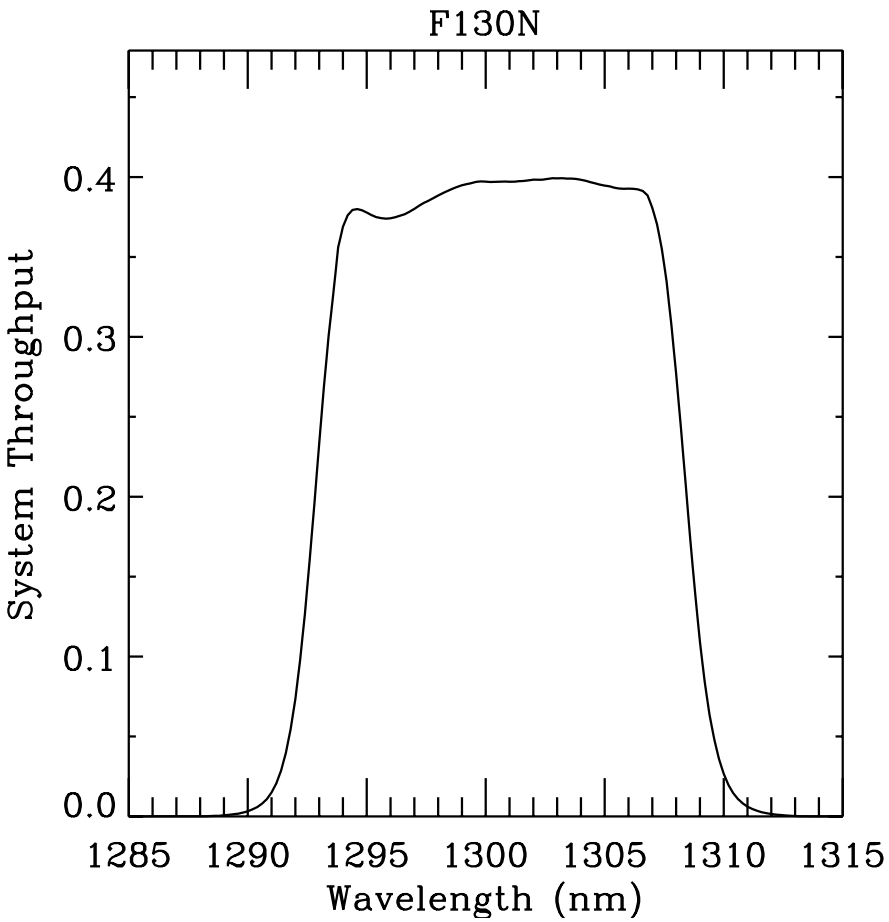

Figure A.209: Point source S/N vs. V+ABν for the F130N filter, assuming high sky backgrounds and a 3×3 pixel aperture.

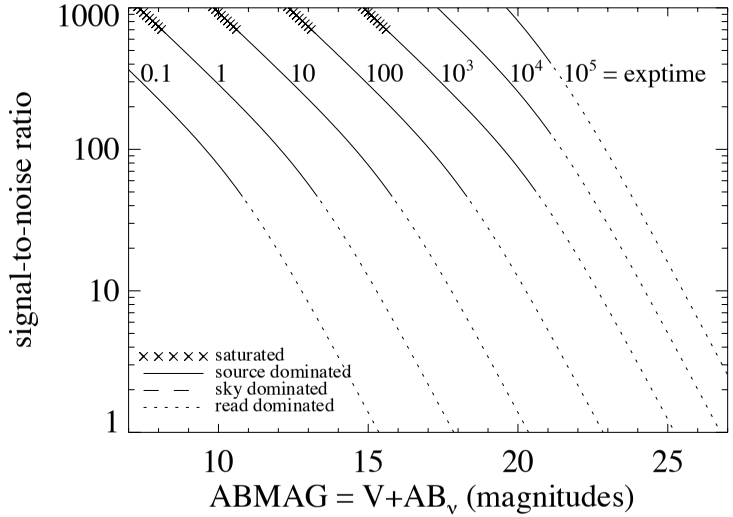

Figure A.210: Extended source S/N vs. V+ABν for the F130N filter, assuming high sky backgrounds and a source uniformly filling a 1 arcsec^2 aperture.

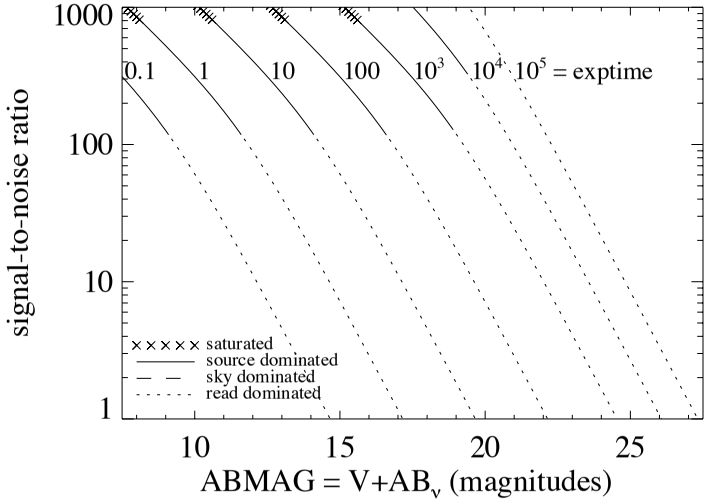

IR/F132N

Description

Paschen β (redshifted) filter.

Figure A.211: Integrated system throughput for F132N.

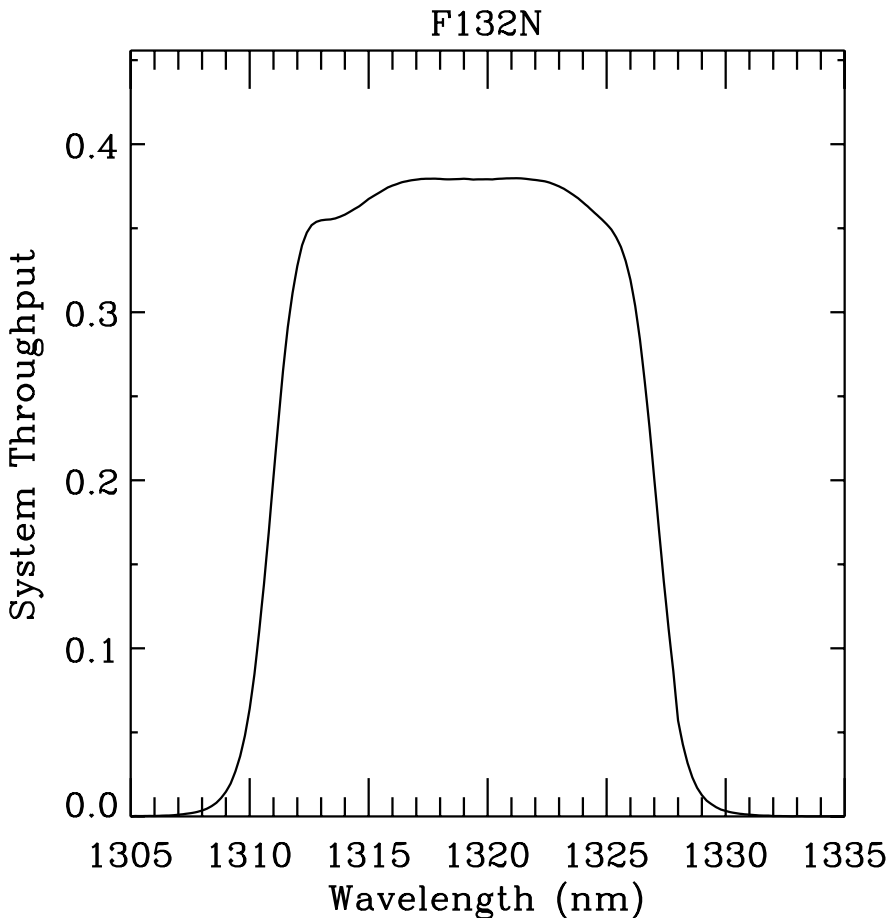

Figure A.212: Point source S/N vs. V+ABν for the F132N filter, assuming high sky backgrounds and a 3×3 pixel aperture.

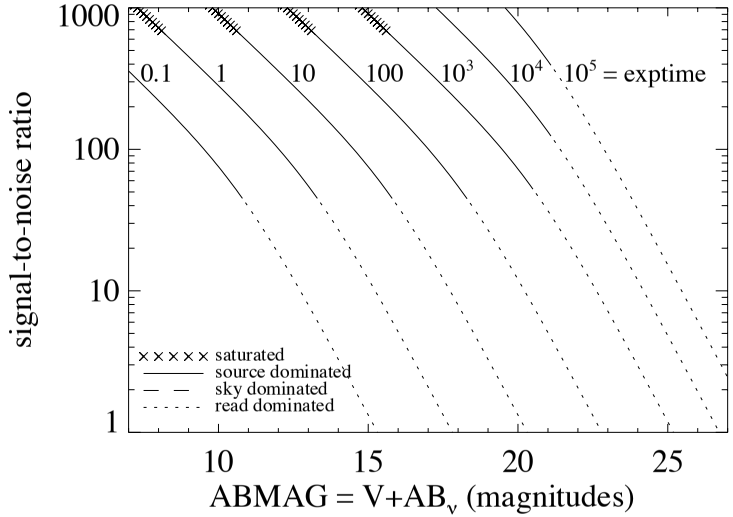

Figure A.213: Extended source S/N vs. V+ABν for the F132N filter, assuming high sky backgrounds and a source uniformly filling a 1 arcsec^2 aperture.

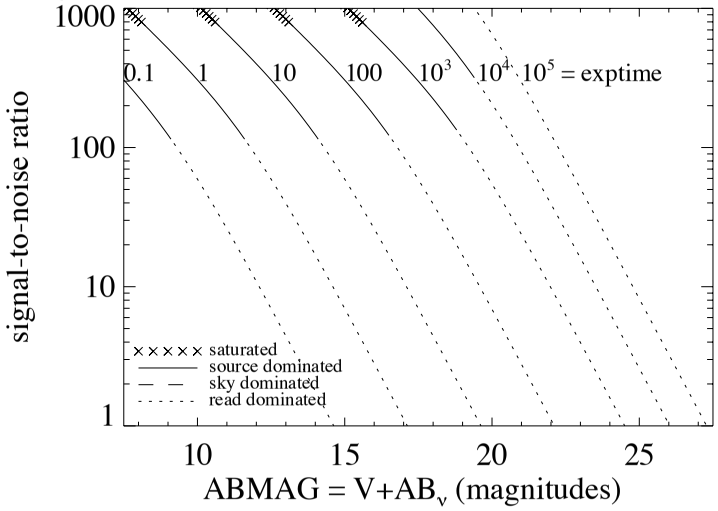

IR/F139M

Description

H_2O/CH_4 line filter.

Figure A.214: Integrated system throughput for F139M.

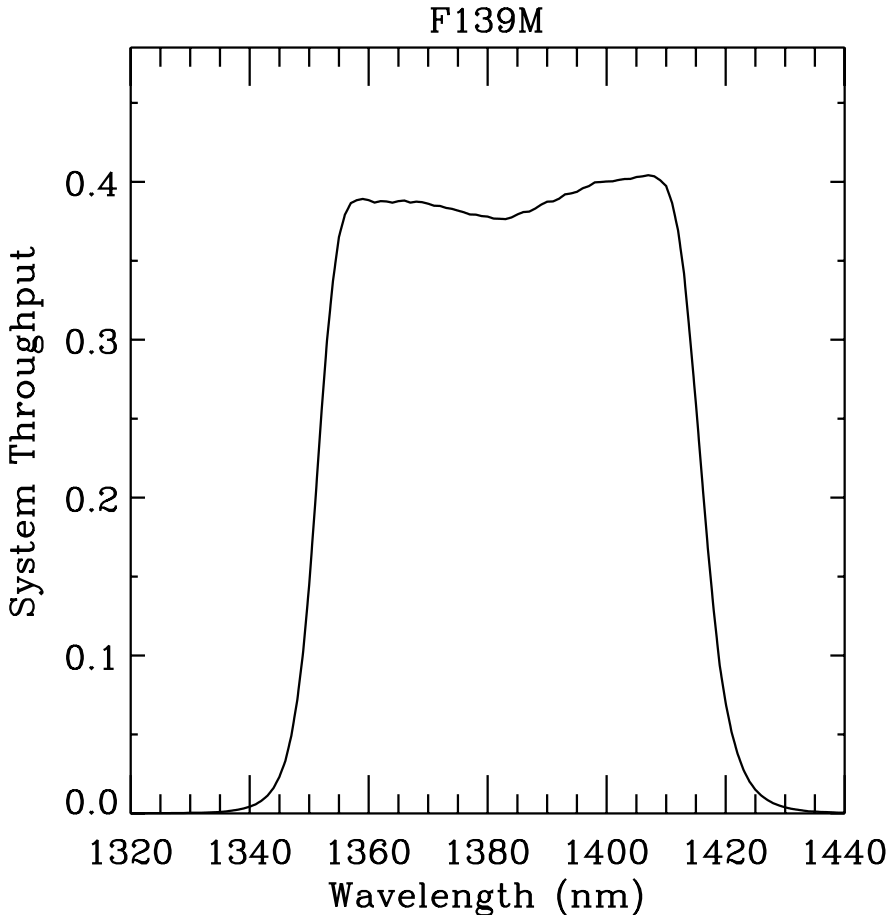

Figure A.215: Point source S/N vs. V+ABν for the F139M filter, assuming high sky backgrounds and a 3×3 pixel aperture.

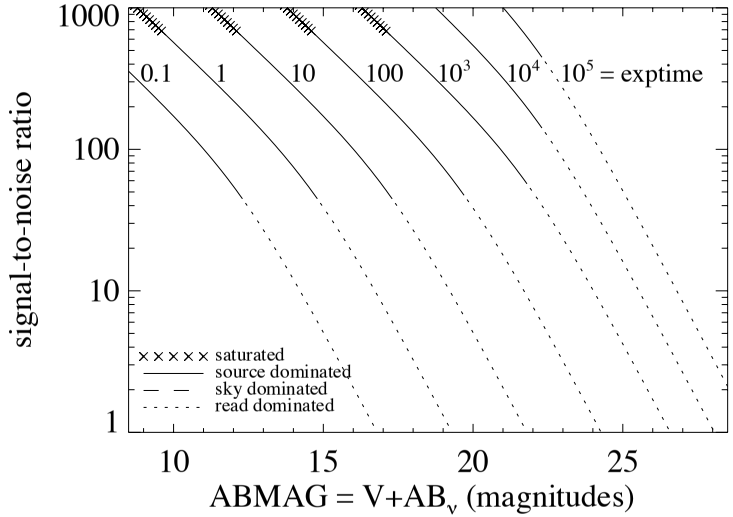

Figure A.216: Extended source S/N vs. V+ABν for the F139M filter, assuming high sky backgrounds and a source uniformly filling a 1 arcsec^2 aperture.

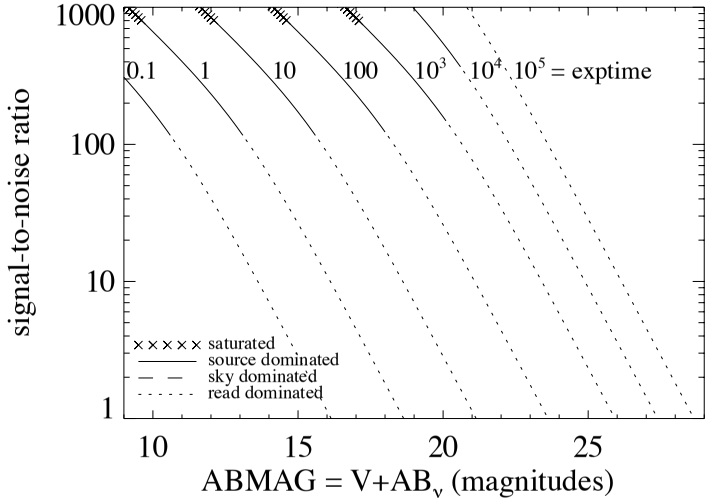

IR/F140W

Description

Wide *JH* gap; red grism reference filter.

Figure A.217: Integrated system throughput for F140W.

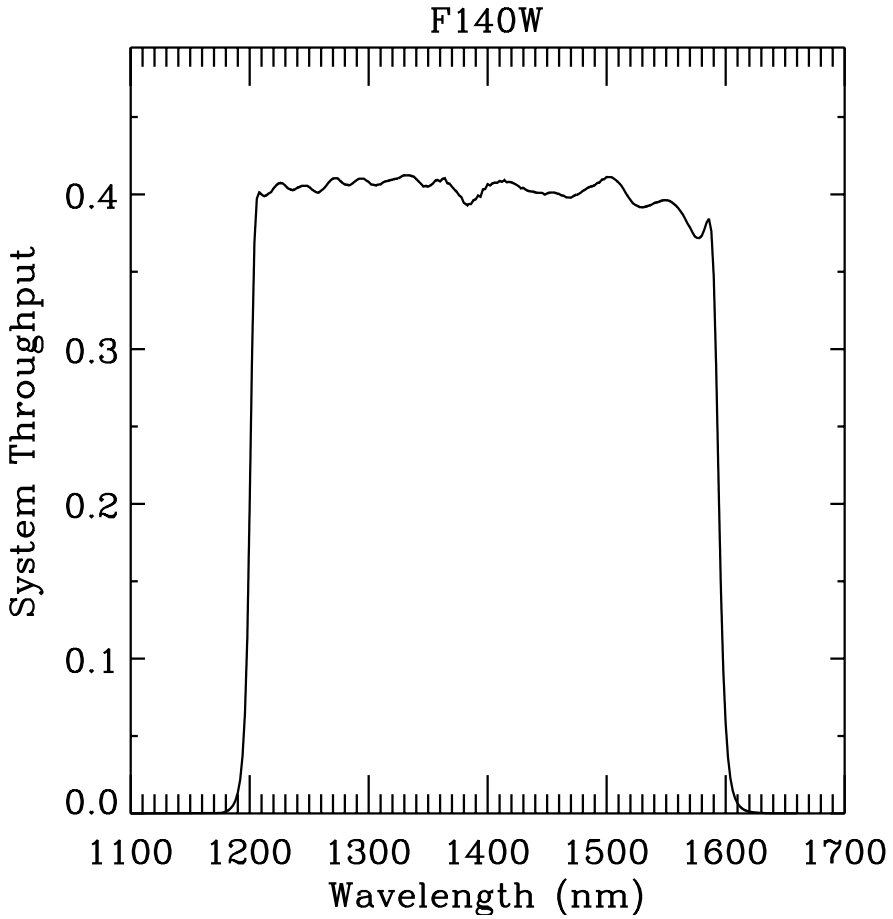

Figure A.218: Point source S/N vs. V+ABν for the F140W filter, assuming high sky backgrounds and a 3×3 pixel aperture.

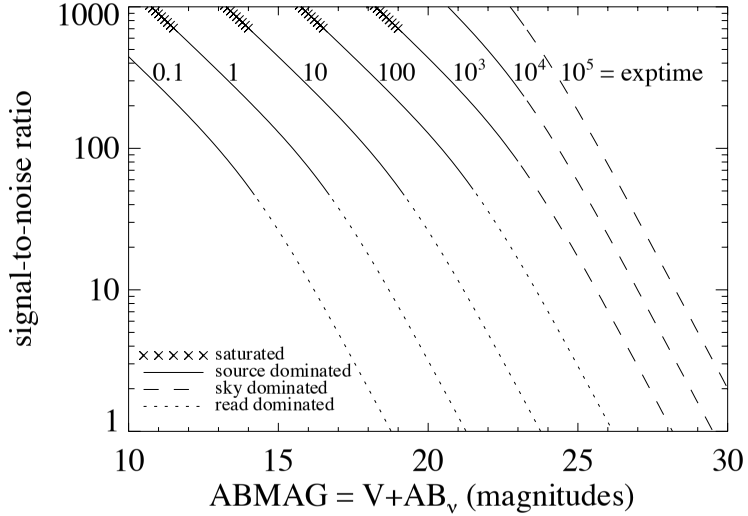

Figure A.219: Extended source S/N vs. V+ABν for the F140W filter, assuming high sky backgrounds and a source uniformly filling a 1 arcsec^2 aperture.

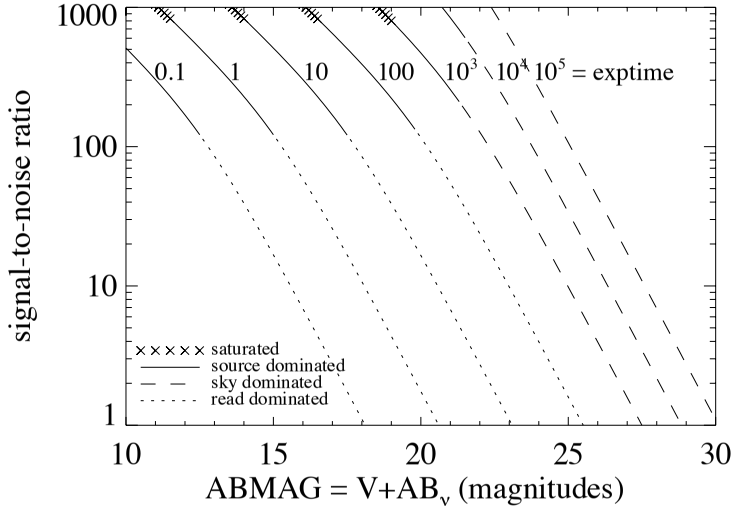

IR/F153M

Description

H_2O and NH_3 filter.

Figure A.220: Integrated system throughput for F153M.

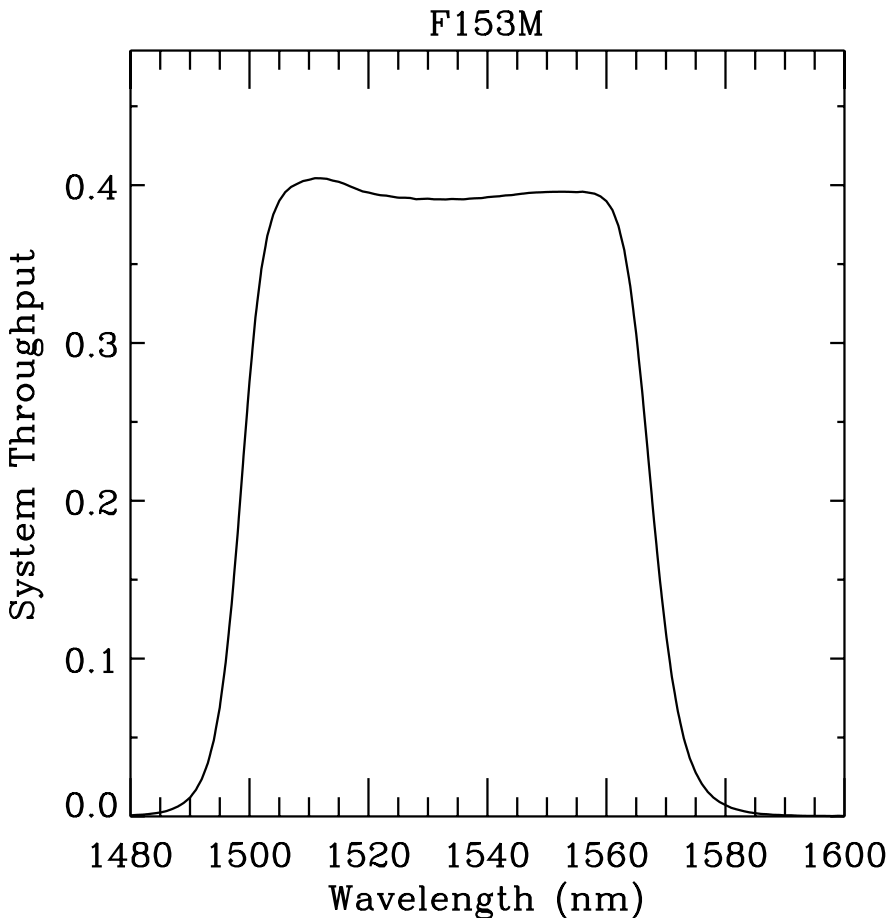

Figure A.221: Point source S/N vs. V+ABν for the F153M filter, assuming high sky backgrounds and a 3×3 pixel aperture.

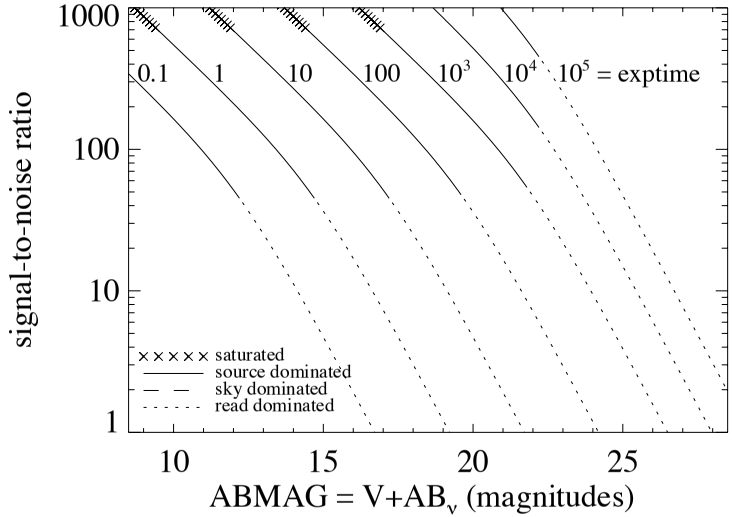

Figure A.222: Extended source S/N vs. V+ABν for the F153M filter, assuming high sky backgrounds and a source uniformly filling a 1 arcsec^2 aperture.

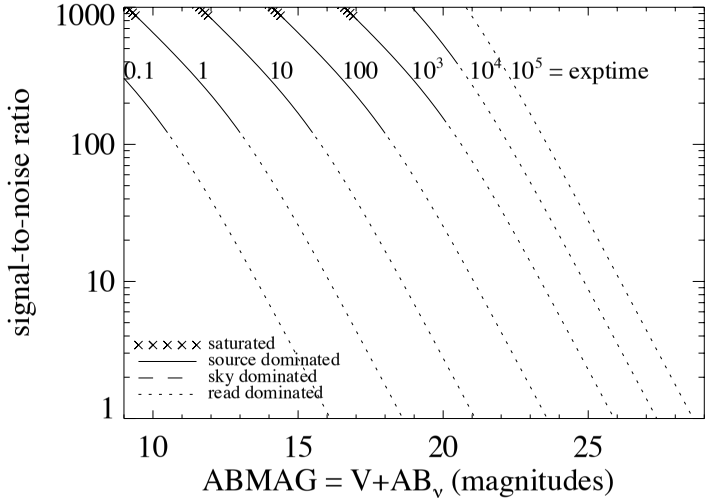

IR/F160W

Description

WFC3 *H* filter.

Figure A.223: Integrated system throughput for F160W.

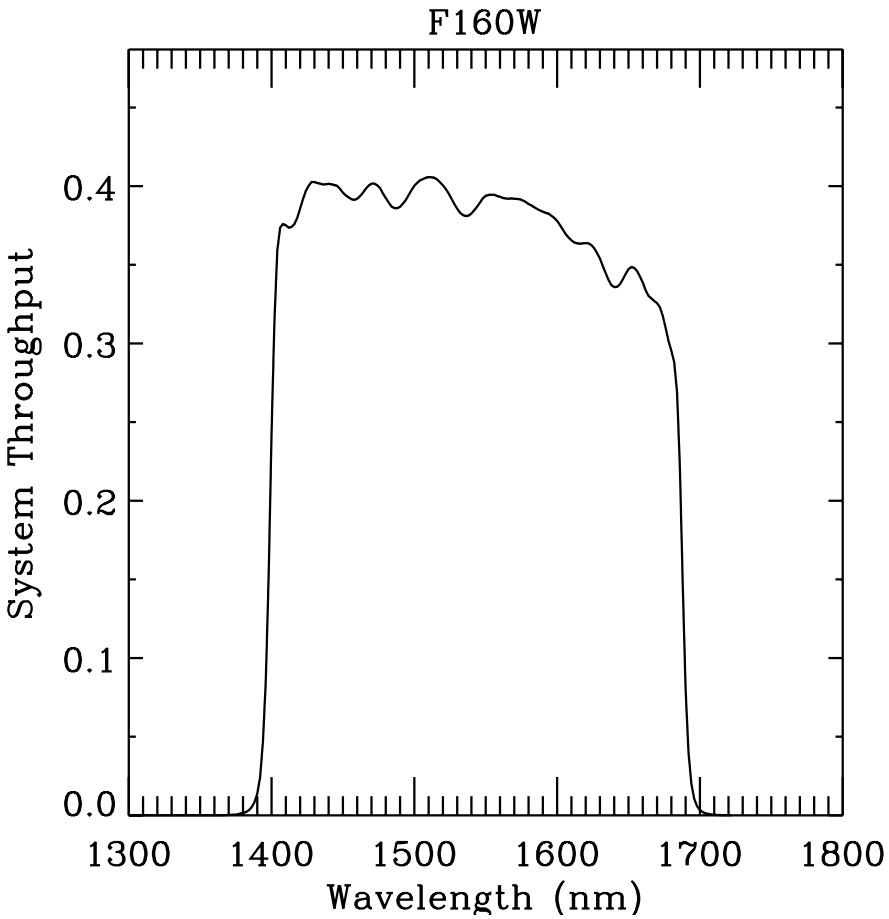

Figure A.224: Point source S/N vs. V+ABν for the F160W filter, assuming high sky backgrounds and a 3×3 pixel aperture.

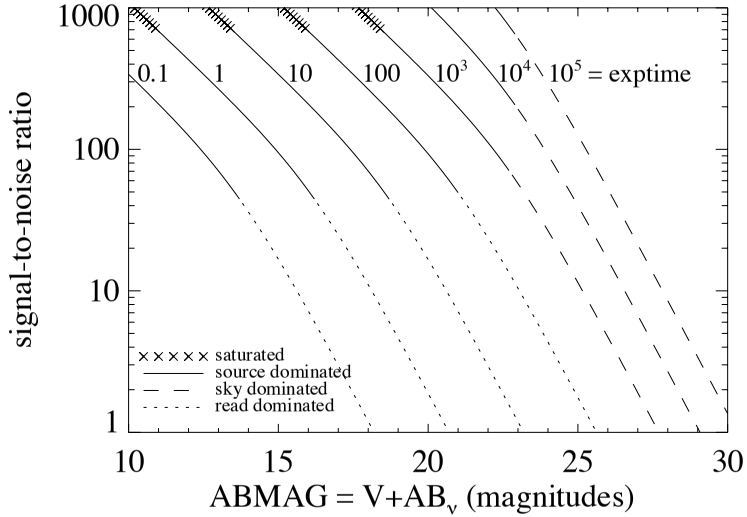

Figure A.225: Extended source S/N vs. V+ABν for the F160W filter, assuming high sky backgrounds and a source uniformly filling a 1 arcsec^2 aperture.

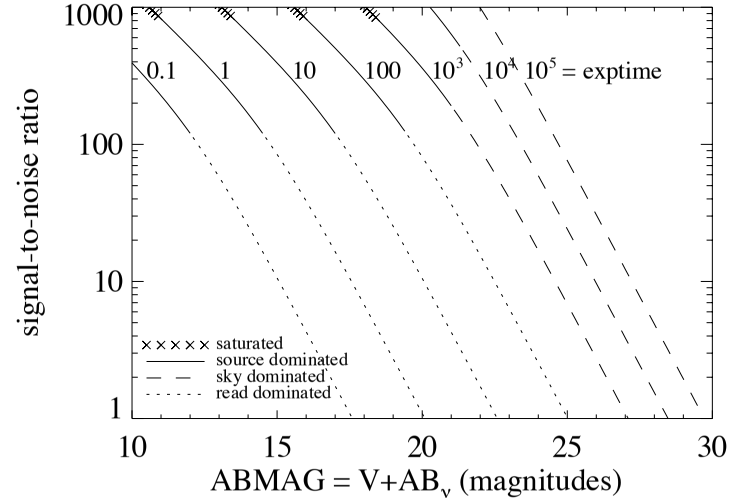

IR/F164N

Description

[Fe II] filter.

Figure A.226: Integrated system throughput for F164N.

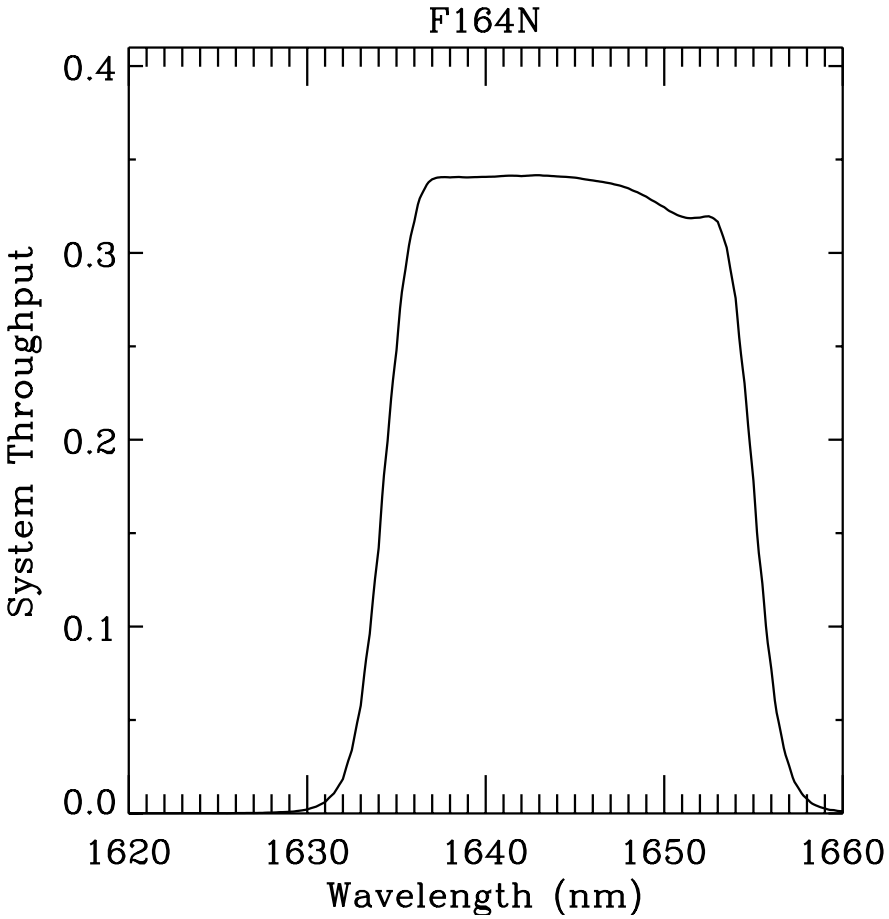

Figure A.227: Point source S/N vs. V+ABν for the F164N filter, assuming high sky backgrounds and a 3×3 pixel aperture.

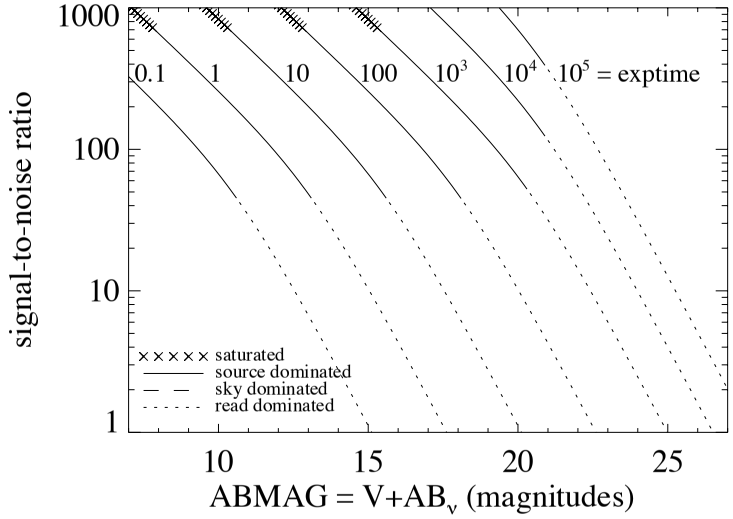

Figure A.228: Extended source S/N vs. V+ABν for the F164N filter, assuming high sky backgrounds and a source uniformly filling a 1 arcsec^2 aperture.

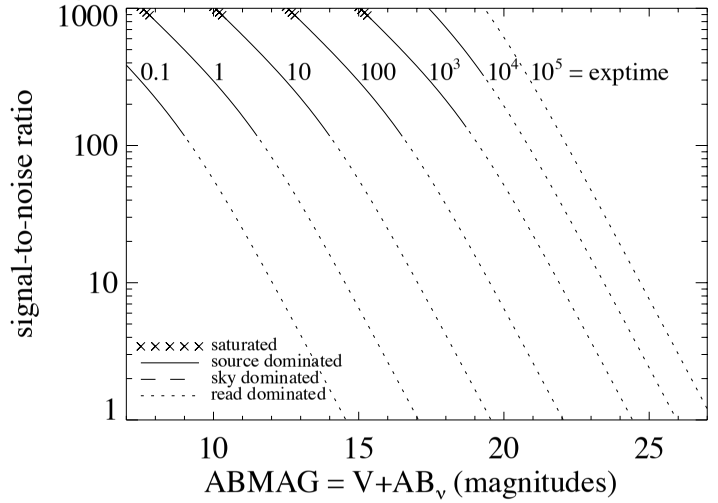

IR /F167N

Description

[Fe II] continuum filter.

Figure A.229: Integrated system throughput for F167N.

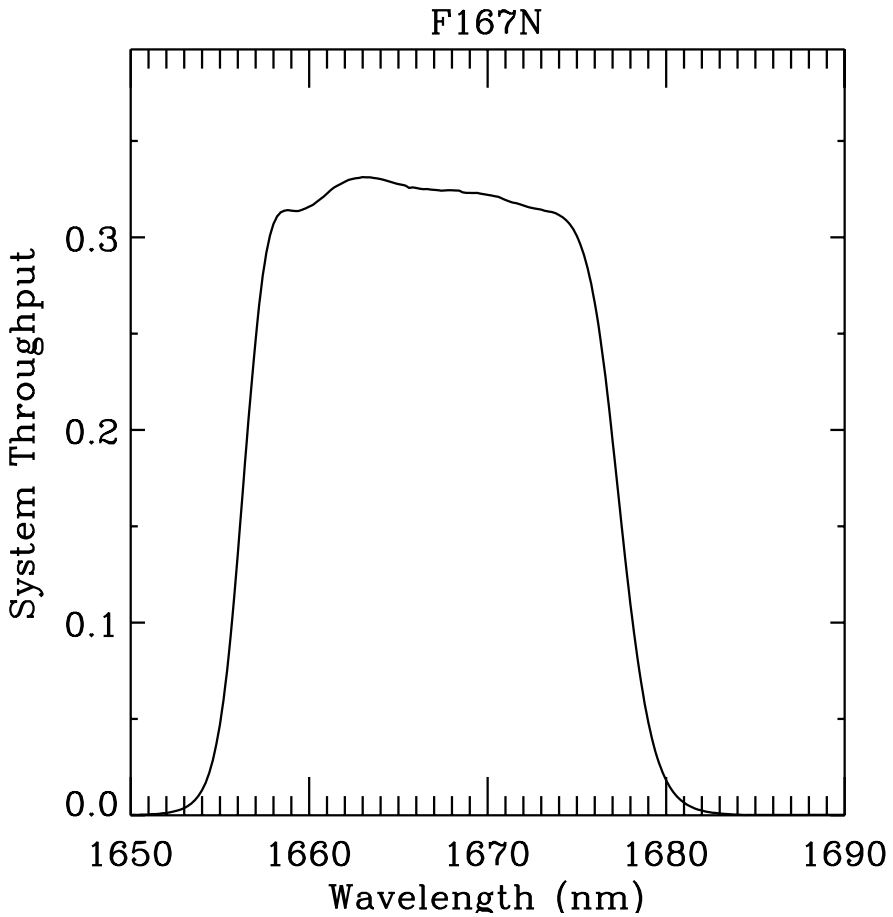

Figure A.230: Point source S/N vs. V+ABν for the F167N filter, assuming high sky backgrounds and a 3×3 pixel aperture.

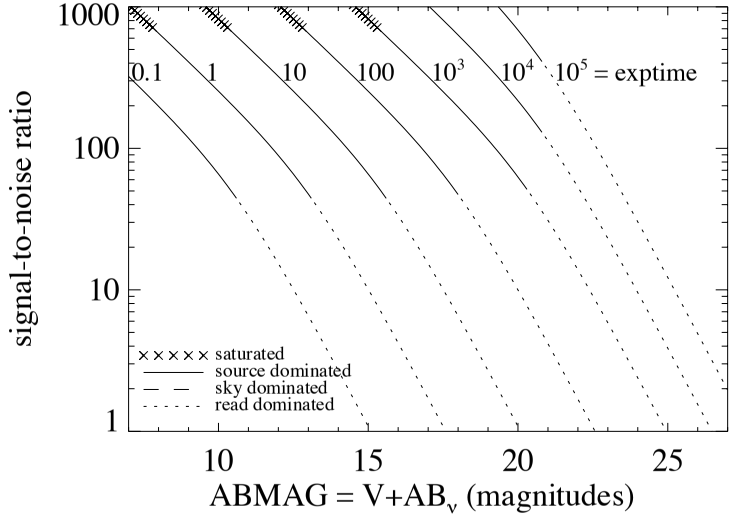

Figure A.231: Extended source S/N vs. V+ABν for the F167N filter, assuming high sky backgrounds and a source uniformly filling a 1 arcsec^2 aperture.

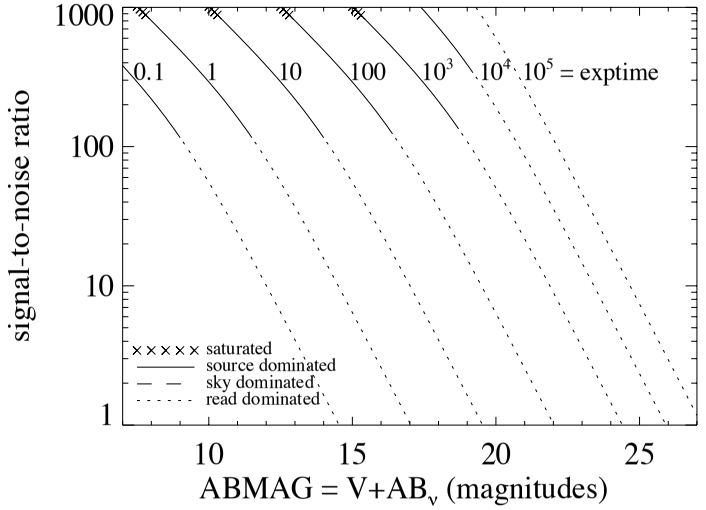

Table A.1: Color corrections AB_V to go from Johnson V magnitude to AB magnitude for WFC3 as a function of stellar effective temperature.

	T_{eff}							
Mode	**2500K**	**5000K**	**7500K**	**10000K**	**15000K**	**20000K**	**30000K**	**50000K**
UVIS/F200LP	-2.22	0.45	0.48	0.40	0.08	-0.12	-0.40	-0.57
UVIS/F218W	7.21	7.82	2.95	1.51	0.09	-0.53	-1.22	-1.55
UVIS/F225W	6.07	7.22	2.84	1.51	0.12	-0.49	-1.15	-1.46
UVIS/F275W	7.30	5.30	2.27	1.35	0.10	-0.42	-0.96	-1.24
UVIS/F280N	3.29	4.49	2.50	1.44	0.13	-0.40	-0.90	-1.17
UVIS/F300X	5.96	4.05	1.98	1.26	0.10	-0.39	-0.91	-1.19
UVIS/F336W	4.98	2.71	1.31	1.00	0.10	-0.26	-0.64	-0.86
UVIS/F343N	4.74	2.62	1.24	0.97	0.11	-0.24	-0.60	-0.82
UVIS/F350LP	-2.64	0.07	0.18	0.18	0.09	0.04	-0.02	-0.07
UVIS/F373N	7.03	2.53	1.10	0.94	0.21	-0.09	-0.43	-0.65
UVIS/F390M	4.25	2.08	0.67	0.25	-0.20	-0.33	-0.48	-0.60
UVIS/F390W	3.80	1.63	0.59	0.26	-0.14	-0.29	-0.47	-0.60
UVIS/F395N	3.91	1.92	0.67	0.15	-0.27	-0.37	-0.49	-0.58
UVIS/F410M	2.96	1.16	0.29	-0.10	-0.32	-0.39	-0.46	-0.52
UVIS/F438W	2.28	0.86	0.18	-0.12	-0.28	-0.33	-0.39	-0.43
UVIS/F467M	1.74	0.34	0.02	-0.15	-0.22	-0.24	-0.26	-0.27
UVIS/F469N	1.64	0.33	0.03	-0.14	-0.21	-0.24	-0.26	-0.26
UVIS/F475W	1.23	0.44	0.09	-0.07	-0.17	-0.20	-0.24	-0.26
UVIS/F475X	0.61	0.35	0.12	-0.01	-0.12	-0.15	-0.19	-0.23
UVIS/F487N	1.47	0.29	0.20	0.28	0.06	-0.02	-0.11	-0.17
UVIS/F502N	2.32	0.32	0.02	-0.07	-0.11	-0.12	-0.14	-0.15
UVIS/FQ508N	1.07	0.32	0.01	-0.06	-0.08	-0.10	-0.11	-0.12
UVIS/F547M	0.08	0.03	0.02	0.01	0.01	0.01	0.01	0.02
UVIS/F555W	0.15	0.09	0.03	-0.01	-0.03	-0.04	-0.05	-0.06
UVIS/F600LP	-3.71	-0.42	0.09	0.34	0.47	0.52	0.57	0.60
UVIS/F606W	-0.83	-0.11	0.04	0.10	0.12	0.12	0.13	0.13
UVIS/F621M	-1.23	-0.26	0.03	0.16	0.22	0.25	0.27	0.28
UVIS/F625W	-1.17	-0.25	0.04	0.16	0.22	0.24	0.26	0.27

Table A.1: Color corrections AB_V to go from Johnson V magnitude to AB magnitude for WFC3 as a function of stellar effective temperature.

	T_{eff}							
Mode	**2500K**	**5000K**	**7500K**	**10000K**	**15000K**	**20000K**	**30000K**	**50000K**
UVIS/F631N	-0.33	-0.28	0.03	0.17	0.24	0.27	0.30	0.31
UVIS/F645N	-2.20	-0.29	0.04	0.20	0.28	0.31	0.35	0.35
UVIS/F656N	-1.99	-0.26	0.36	0.63	0.56	0.54	0.52	0.45
UVIS/F657N	-2.31	-0.31	0.14	0.37	0.39	0.41	0.42	0.41
UVIS/F658N	-2.04	-0.31	0.18	0.42	0.42	0.43	0.44	0.41
UVIS/F665N	-1.30	-0.35	0.06	0.26	0.34	0.38	0.42	0.42
UVIS/F673N	-0.69	-0.37	0.04	0.24	0.35	0.39	0.44	0.45
UVIS/F680N	-1.61	-0.38	0.05	0.26	0.38	0.42	0.47	0.48
UVIS/F689M	-1.69	-0.37	0.06	0.28	0.39	0.43	0.47	0.48
UVIS/F763M	-3.09	-0.45	0.09	0.37	0.53	0.59	0.65	0.69
UVIS/F775W	-3.60	-0.45	0.09	0.38	0.54	0.59	0.65	0.70
UVIS/F814W	-4.14	-0.48	0.12	0.43	0.60	0.67	0.74	0.79
UVIS/F845M	-4.56	-0.51	0.16	0.51	0.70	0.77	0.84	0.91
UVIS/F850LP	-5.03	-0.56	0.21	0.56	0.79	0.89	0.98	1.06
UVIS/F953N	-5.52	-0.59	0.27	0.68	0.91	1.00	1.10	1.16
UVIS/FQ232N	2.15	4.54	2.68	1.53	0.20	-0.43	-1.12	-1.46
UVIS/FQ243N	2.84	5.10	2.76	1.52	0.18	-0.44	-1.11	-1.40
UVIS/FQ378N	4.90	2.32	0.86	0.61	0.01	-0.20	-0.44	-0.62
UVIS/FQ387N	6.34	2.42	0.61	0.25	-0.21	-0.34	-0.49	-0.61
UVIS/FQ422M	5.05	1.17	0.18	-0.22	-0.36	-0.41	-0.46	-0.48
UVIS/FQ436N	2.64	0.84	0.23	0.08	-0.16	-0.24	-0.31	-0.39
UVIS/FQ437N	2.59	0.83	0.18	0.00	-0.21	-0.28	-0.34	-0.40
UVIS/FQ492N	0.91	0.27	0.04	-0.02	-0.10	-0.13	-0.16	-0.17
UVIS/FQ575N	-0.58	-0.18	0.01	0.07	0.10	0.11	0.13	0.13
UVIS/FQ619N	0.72	-0.25	0.03	0.15	0.22	0.24	0.27	0.27
UVIS/FQ634N	-0.96	-0.28	0.03	0.18	0.26	0.29	0.32	0.32
UVIS/FQ672N	-0.77	-0.35	0.04	0.23	0.34	0.38	0.42	0.44
UVIS/FQ674N	-0.39	-0.37	0.04	0.24	0.35	0.39	0.43	0.44
UVIS/FQ727N	-2.81	-0.41	0.07	0.32	0.46	0.52	0.57	0.60

Table A.1: Color corrections AB_V to go from Johnson *V* magnitude to AB magnitude for WFC3 as a function of stellar effective temperature.

	T_{eff}							
Mode	**2500K**	**5000K**	**7500K**	**10000K**	**15000K**	**20000K**	**30000K**	**50000K**
UVIS/FQ750N	-3.06	-0.44	0.08	0.36	0.51	0.57	0.63	0.66
UVIS/FQ889N	-4.98	-0.55	0.20	0.57	0.78	0.86	0.95	1.01
UVIS/FQ906N	-5.15	-0.56	0.21	0.57	0.79	0.88	0.98	1.05
UVIS/FQ924N	-4.89	-0.57	0.26	0.66	0.87	0.95	1.04	1.10
UVIS/FQ937N	-5.19	-0.58	0.19	0.48	0.77	0.89	1.01	1.11
IR/F098M	-5.40	-0.60	0.25	0.60	0.88	1.00	1.12	1.21
IR/F105W	-5.68	-0.62	0.31	0.69	0.98	1.11	1.24	1.34
IR/F110W	-5.77	-0.64	0.39	0.80	1.12	1.25	1.39	1.49
IR/F125W	-5.91	-0.67	0.48	0.94	1.28	1.43	1.58	1.69
IR/F126N	-5.99	-0.67	0.49	0.96	1.31	1.46	1.61	1.72
IR/F127M	-6.04	-0.67	0.52	1.01	1.35	1.49	1.65	1.75
IR/F128N	-6.08	-0.67	0.59	1.11	1.41	1.55	1.69	1.78
IR/F130N	-6.13	-0.68	0.53	1.02	1.37	1.52	1.68	1.79
IR/F132N	-6.04	-0.67	0.54	1.03	1.39	1.55	1.71	1.82
IR/F139M	-5.64	-0.69	0.60	1.11	1.49	1.64	1.81	1.92
IR/F140W	-5.89	-0.69	0.61	1.12	1.49	1.64	1.80	1.92
IR/F153M	-6.03	-0.71	0.73	1.29	1.69	1.85	2.02	2.14
IR/F160W	-6.05	-0.70	0.74	1.30	1.69	1.85	2.02	2.15
IR/F164N	-6.39	-0.70	0.84	1.42	1.82	1.99	2.16	2.28
IR/F167N	-6.32	-0.69	0.84	1.41	1.83	2.00	2.18	2.31

Table A.2: Color corrections AB_V to go from Johnson *V* magnitude to AB magnitude for WFC3 as a function of age in an instantaneous burst population.

	Age				
Mode	**10 Gyr**	**1 Gyr**	**100 Myr**	**10 Myr**	**1 Myr**
UVIS/F200LP	0.27	0.38	0.24	0.00	-0.41
UVIS/F218W	6.05	3.87	1.06	0.15	-1.23
UVIS/F225W	5.78	3.74	1.02	0.16	-1.15

Table A.2: Color corrections AB_V to go from Johnson *V* magnitude to AB magnitude for WFC3 as a function of age in an instantaneous burst population.

	Age				
Mode	**10 Gyr**	**1 Gyr**	**100 Myr**	**10 Myr**	**1 Myr**
UVIS/F275W	4.73	3.13	0.92	0.19	-0.98
UVIS/F280N	4.21	2.98	0.88	0.21	-0.93
UVIS/F300X	3.87	2.75	0.88	0.20	-0.93
UVIS/F336W	2.68	1.97	0.76	0.27	-0.68
UVIS/F343N	2.55	1.89	0.75	0.28	-0.64
UVIS/F350LP	-0.12	0.03	0.05	-0.07	-0.04
UVIS/F373N	2.28	1.57	0.66	0.34	-0.50
UVIS/F390M	2.03	1.12	0.21	0.13	-0.51
UVIS/F390W	1.63	1.00	0.26	0.15	-0.50
UVIS/F395N	1.89	1.04	0.14	0.10	-0.50
UVIS/F410M	1.23	0.64	0.01	0.02	-0.48
UVIS/F438W	0.90	0.48	0.00	0.02	-0.40
UVIS/F467M	0.44	0.22	-0.03	-0.01	-0.27
UVIS/F469N	0.47	0.23	-0.02	-0.01	-0.26
UVIS/F475W	0.48	0.27	0.01	0.04	-0.24
UVIS/F475X	0.37	0.23	0.03	0.03	-0.20
UVIS/F487N	0.36	0.27	0.12	0.10	-0.15
UVIS/F502N	0.33	0.17	0.01	0.08	-0.13
UVIS/FQ508N	0.31	0.16	0.03	0.12	-0.10
UVIS/F547M	0.04	0.03	0.02	0.03	0.02
UVIS/F555W	0.10	0.07	0.01	0.01	-0.06
UVIS/F600LP	-0.74	-0.39	-0.05	-0.28	0.54
UVIS/F606W	-0.17	-0.08	0.01	-0.05	0.12
UVIS/F621M	-0.32	-0.18	-0.00	-0.10	0.25
UVIS/F625W	-0.33	-0.17	-0.00	-0.10	0.24
UVIS/F631N	-0.33	-0.19	0.00	-0.10	0.28
UVIS/F645N	-0.42	-0.23	-0.02	-0.15	0.32
UVIS/F656N	-0.45	-0.18	0.06	-0.16	0.36
UVIS/F657N	-0.47	-0.23	-0.00	-0.18	0.36

Table A.2: Color corrections AB_ν to go from Johnson V magnitude to AB magnitude for WFC3 as a function of age in an instantaneous burst population.

	Age				
Mode	**10 Gyr**	**1 Gyr**	**100 Myr**	**10 Myr**	**1 Myr**
UVIS/F658N	-0.47	-0.22	-0.00	-0.19	0.36
UVIS/F665N	-0.48	-0.26	-0.03	-0.19	0.38
UVIS/F673N	-0.49	-0.29	-0.03	-0.15	0.41
UVIS/F680N	-0.54	-0.31	-0.03	-0.17	0.44
UVIS/F689M	-0.53	-0.29	-0.02	-0.19	0.44
UVIS/F763M	-0.77	-0.40	-0.05	-0.32	0.63
UVIS/F775W	-0.78	-0.41	-0.05	-0.32	0.63
UVIS/F814W	-0.89	-0.48	-0.07	-0.36	0.71
UVIS/F845M	-1.00	-0.54	-0.10	-0.42	0.81
UVIS/F850LP	-1.18	-0.65	-0.13	-0.47	0.95
UVIS/F953N	-1.26	-0.71	-0.12	-0.50	1.06
UVIS/FQ232N	4.21	3.31	1.02	0.16	-1.14
UVIS/FQ243N	4.65	3.53	0.97	0.14	-1.11
UVIS/FQ378N	2.24	1.37	0.42	0.22	-0.52
UVIS/FQ387N	2.27	1.16	0.22	0.14	-0.52
UVIS/FQ422M	1.16	0.55	-0.03	0.01	-0.45
UVIS/FQ436N	0.87	0.49	0.04	0.05	-0.37
UVIS/FQ437N	0.86	0.46	-0.00	0.02	-0.38
UVIS/FQ492N	0.31	0.17	0.01	0.05	-0.16
UVIS/FQ575N	-0.18	-0.08	-0.00	-0.07	0.12
UVIS/FQ619N	-0.28	-0.16	0.01	-0.06	0.25
UVIS/FQ634N	-0.37	-0.21	-0.01	-0.12	0.29
UVIS/FQ672N	-0.47	-0.27	-0.03	-0.17	0.40
UVIS/FQ674N	-0.47	-0.27	-0.03	-0.16	0.40
UVIS/FQ727N	-0.64	-0.34	-0.02	-0.26	0.55
UVIS/FQ750N	-0.81	-0.43	-0.07	-0.33	0.60
UVIS/FQ889N	-1.11	-0.61	-0.14	-0.46	0.90
UVIS/FQ906N	-1.22	-0.68	-0.16	-0.49	0.93
UVIS/FQ924N	-1.21	-0.65	-0.12	-0.48	0.99

Table A.2: Color corrections AB_V to go from Johnson *V* magnitude to AB magnitude for WFC3 as a function of age in an instantaneous burst population.

	Age				
Mode	**10 Gyr**	**1 Gyr**	**100 Myr**	**10 Myr**	**1 Myr**
UVIS/FQ937N	-1.16	-0.65	-0.12	-0.47	0.99
IR/F098M	-1.35	-0.75	-0.15	-0.52	1.09
IR/F105W	-1.39	-0.74	-0.14	-0.55	1.22
IR/F110W	-1.38	-0.70	-0.11	-0.57	1.37
IR/F125W	-1.39	-0.67	-0.09	-0.61	1.56
IR/F126N	-1.37	-0.65	-0.07	-0.62	1.59
IR/F127M	-1.38	-0.65	-0.07	-0.63	1.62
IR/F128N	-1.39	-0.64	-0.07	-0.63	1.63
IR/F130N	-1.40	-0.65	-0.07	-0.63	1.65
IR/F132N	-1.40	-0.64	-0.07	-0.62	1.68
IR/F139M	-1.37	-0.62	-0.05	-0.60	1.77
IR/F140W	-1.41	-0.65	-0.07	-0.64	1.77
IR/F153M	-1.49	-0.69	-0.08	-0.70	1.97
IR/F160W	-1.49	-0.69	-0.08	-0.71	1.97
IR/F164N	-1.58	-0.75	-0.12	-0.79	2.09
IR/F167N	-1.58	-0.74	-0.11	-0.78	2.12

Table A.3: Color corrections AB_V to go from Johnson *V* magnitude to AB magnitude for WFC3 as a function of age in a population with constant star formation.

	Age				
Mode	**10 Gyr**	**1 Gyr**	**100 Myr**	**10 Myr**	**1 Myr**
UVIS/F200LP	0.24	0.19	0.02	-0.13	-0.41
UVIS/F218W	1.39	0.78	0.07	-0.48	-1.23
UVIS/F225W	1.39	0.79	0.09	-0.45	-1.15
UVIS/F275W	1.35	0.78	0.12	-0.37	-0.98
UVIS/F280N	1.33	0.77	0.13	-0.34	-0.92
UVIS/F300X	1.30	0.75	0.13	-0.34	-0.93
UVIS/F336W	1.15	0.71	0.19	-0.21	-0.67

Table A.3: Color corrections AB_V to go from Johnson V magnitude to AB magnitude for WFC3 as a function of age in a population with constant star formation.

	Age				
Mode	**10 Gyr**	**1 Gyr**	**100 Myr**	**10 Myr**	**1 Myr**
UVIS/F343N	1.13	0.71	0.20	-0.19	-0.63
UVIS/F350LP	-0.02	0.02	-0.02	-0.01	-0.04
UVIS/F373N	1.03	0.65	0.23	-0.12	-0.50
UVIS/F390M	0.67	0.28	-0.00	-0.26	-0.51
UVIS/F390W	0.64	0.30	0.02	-0.23	-0.50
UVIS/F395N	0.61	0.21	-0.04	-0.27	-0.50
UVIS/F410M	0.37	0.06	-0.12	-0.31	-0.48
UVIS/F438W	0.29	0.05	-0.09	-0.26	-0.40
UVIS/F467M	0.14	-0.01	-0.08	-0.18	-0.27
UVIS/F469N	0.15	-0.00	-0.08	-0.18	-0.26
UVIS/F475W	0.18	0.04	-0.04	-0.15	-0.24
UVIS/F475X	0.16	0.05	-0.03	-0.12	-0.20
UVIS/F487N	0.21	0.14	0.05	-0.05	-0.15
UVIS/F502N	0.13	0.04	0.00	-0.07	-0.13
UVIS/FQ508N	0.14	0.06	0.04	-0.03	-0.10
UVIS/F547M	0.03	0.03	0.02	0.02	0.02
UVIS/F555W	0.05	0.02	-0.01	-0.03	-0.06
UVIS/F600LP	-0.37	-0.14	-0.06	0.21	0.54
UVIS/F606W	-0.06	-0.01	0.01	0.06	0.12
UVIS/F621M	-0.14	-0.03	0.00	0.12	0.25
UVIS/F625W	-0.14	-0.03	0.00	0.12	0.24
UVIS/F631N	-0.15	-0.03	0.01	0.13	0.28
UVIS/F645N	-0.20	-0.06	-0.01	0.14	0.32
UVIS/F656N	-0.17	0.01	0.02	0.18	0.36
UVIS/F657N	-0.20	-0.04	-0.02	0.15	0.36
UVIS/F658N	-0.20	-0.04	-0.02	0.15	0.36
UVIS/F665N	-0.23	-0.07	-0.03	0.16	0.38
UVIS/F673N	-0.24	-0.07	0.00	0.19	0.41
UVIS/F680N	-0.26	-0.08	-0.00	0.20	0.44

Table A.3: Color corrections AB_V to go from Johnson *V* magnitude to AB magnitude for WFC3 as a function of age in a population with constant star formation.

	Age				
Mode	**10 Gyr**	**1 Gyr**	**100 Myr**	**10 Myr**	**1 Myr**
UVIS/F689M	-0.25	-0.07	-0.01	0.19	0.44
UVIS/F763M	-0.39	-0.14	-0.07	0.24	0.63
UVIS/F775W	-0.39	-0.14	-0.07	0.24	0.63
UVIS/F814W	-0.47	-0.19	-0.09	0.26	0.71
UVIS/F845M	-0.54	-0.23	-0.12	0.27	0.81
UVIS/F850LP	-0.66	-0.31	-0.15	0.29	0.95
UVIS/F953N	-0.72	-0.34	-0.15	0.31	1.06
UVIS/FQ232N	1.36	0.78	0.10	-0.44	-1.14
UVIS/FQ243N	1.36	0.77	0.08	-0.44	-1.11
UVIS/FQ378N	0.85	0.45	0.10	-0.21	-0.51
UVIS/FQ387N	0.70	0.28	-0.00	-0.26	-0.52
UVIS/FQ422M	0.32	0.02	-0.13	-0.30	-0.45
UVIS/FQ436N	0.31	0.08	-0.07	-0.23	-0.37
UVIS/FQ437N	0.28	0.05	-0.09	-0.25	-0.38
UVIS/FQ492N	0.12	0.03	-0.02	-0.10	-0.16
UVIS/FQ575N	-0.07	-0.02	-0.01	0.06	0.12
UVIS/FQ619N	-0.12	-0.02	0.03	0.13	0.25
UVIS/FQ634N	-0.17	-0.04	-0.00	0.13	0.29
UVIS/FQ672N	-0.22	-0.06	-0.01	0.17	0.40
UVIS/FQ674N	-0.23	-0.06	-0.00	0.18	0.40
UVIS/FQ727N	-0.31	-0.09	-0.04	0.22	0.55
UVIS/FQ750N	-0.42	-0.17	-0.08	0.22	0.60
UVIS/FQ889N	-0.62	-0.28	-0.15	0.27	0.90
UVIS/FQ906N	-0.69	-0.34	-0.17	0.27	0.93
UVIS/FQ924N	-0.67	-0.31	-0.15	0.31	0.99
UVIS/FQ937N	-0.65	-0.31	-0.14	0.30	0.99
IR/F098M	-0.77	-0.38	-0.17	0.32	1.09
IR/F105W	-0.78	-0.37	-0.18	0.35	1.22
IR/F110W	-0.76	-0.34	-0.17	0.39	1.36

Table A.3: Color corrections AB_V to go from Johnson V magnitude to AB magnitude for WFC3 as a function of age in a population with constant star formation.

	Age				
Mode	**10 Gyr**	**1 Gyr**	**100 Myr**	**10 Myr**	**1 Myr**
IR/F125W	-0.74	-0.30	-0.17	0.43	1.56
IR/F126N	-0.73	-0.29	-0.18	0.44	1.59
IR/F127M	-0.73	-0.29	-0.18	0.44	1.61
IR/F128N	-0.74	-0.29	-0.18	0.44	1.63
IR/F130N	-0.74	-0.30	-0.18	0.45	1.65
IR/F132N	-0.74	-0.29	-0.17	0.46	1.68
IR/F139M	-0.71	-0.25	-0.14	0.49	1.77
IR/F140W	-0.75	-0.29	-0.18	0.46	1.77
IR/F153M	-0.81	-0.32	-0.21	0.46	1.96
IR/F160W	-0.81	-0.32	-0.21	0.46	1.97
IR/F164N	-0.89	-0.39	-0.28	0.42	2.09
IR/F167N	-0.88	-0.38	-0.27	0.43	2.12

APPENDIX B:

Geometric Distortion

In this appendix . . .

B.1 Overview

WFC3 images will exhibit significant geometric distortion, similar to that seen in ACS images. The required folding, with powered optics, of the light paths in both channels to fit within the instrument's optical-bench envelope results in substantial tilts of the focal surfaces with respect to the chief rays. The WFC3 UVIS detector is tilted at ~21° about one of its diagonals, producing a rhomboidal elongation of ~7%. The IR detector has a ~24° tilt about its *x*-axis, creating a rectangular elongation of ~10%.

If these were the only distortions they would not present much difficulty: their impacts on photometry, mosaicking, or dithering could be computed simply. More problematic, however, is the variation of plate scale across each detector. For the WFC3 UVIS and IR channels, this variation in plate scale amounts to a change of 3.5% and 2%, respectively, over the full field. Hence the area on the sky covered by an UVIS pixel varies by about 7% from corner to corner, and about 8% for the IR channel. Allowance for this change in plate scale must be made in photometric reductions of WFC3 data.

Dithering and mosaicking are complicated by the fact that an integer pixel shift near the center of the detector will translate into a non-integer displacement for pixels near the edges. Even this is not a fundamental difficulty, but will imply some computational complexity in registering and correcting images. All of these considerations make it necessary to obtain accurate measurements of the distortions. The orientations of the WFC3 detector edges for both detectors are at approximately 45° with respect to the V2 and V3 coordinate axes of the telescope. Figure 2.2 shows

the WFC3 apertures in the telescope's V2,V3 reference frame. For a telescope roll angle of zero this would correspond to an on-sky view with the V3 axis aligned with north and the V2 axis with east.

The information presented here is derived from the optical model of the instrument, and thus must be regarded as preliminary. After installation of WFC3 into *HST* this information will be revised on the basis of astrometry in rich stellar fields, as has been done previously for the ACS. For the ACS, the residuals in the distortion corrections in the data pipeline are now at the 0.01 pixel level.

B.2 UVIS Channel

Figure B.1 illustrates the shape of the UVIS channel field of view as projected onto the sky. As noted above, its rhomboidal shape is due primarily to the diagonal tilt of the CCD focal plane with respect to the chief ray (see the schematic mechanical drawing of the instrument in Figure 2.1). The angle between the *x*- and *y*-axes is ~86.1°. The field diagonals are tilted slightly from the V2 and V3 axes.

The UVIS distortion is illustrated in Figure B.1, a vector-displacement diagram that shows the contribution of the non-linear part of a quadratic fit to the data. The vectors represent the displacements, and have been scaled up by a factor of 10 for display. In the diagrams in this appendix, the square points indicate the actual location and the other end of the line shows where the image would be located without non-linear distortion.

The corner displacements are about 30 pixels, corresponding to 1.3 arcsec. The principal effect is the diagonal variation of scale. At the center of UVIS1 (CCD Chip 1), the scale in the *x*-direction is 0.0396 arcsec/pixel, and 0.0393 arcsec/pixel in the *y*-direction. For UVIS2 (CCD Chip 2), these scales are 0.0400 arcsec/pixel, and 0.0398 arcsec/pixel, respectively. Between the corner of the UVIS image nearest to the V1 axis and the diagonally opposite corner, the overall scale increases by 3.5%. UVIS1 forms a slightly distorted rectangle 162×81 arcsec in size, while UVIS2 subtends 164×81 arcsec.

Figure B.1: Non-linear component of the WFC3/UVIS channel distortion.

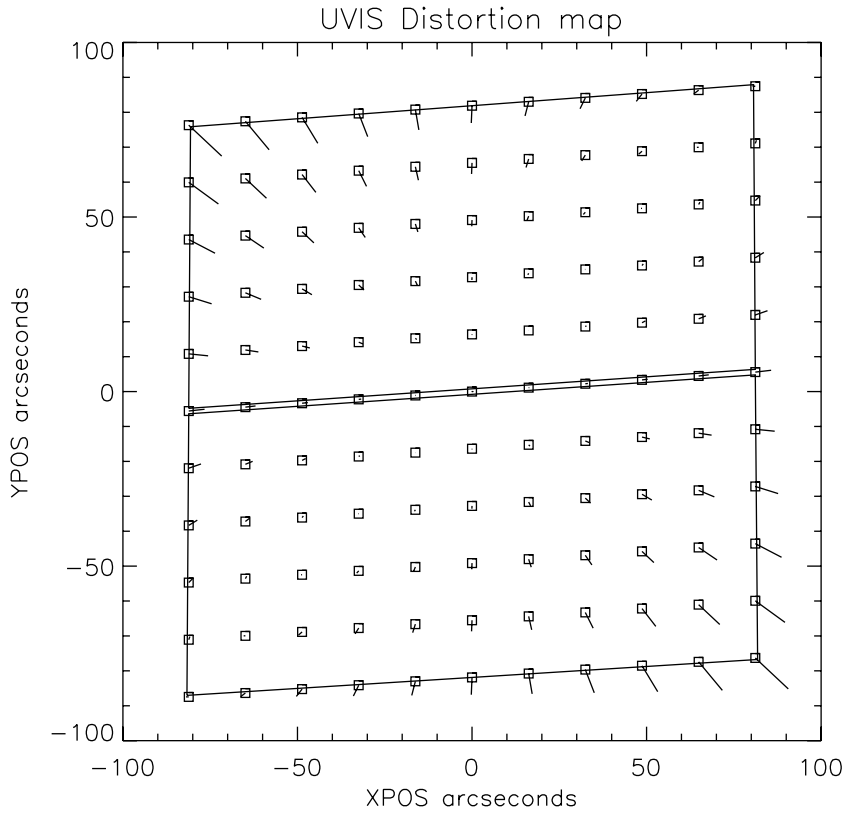

There is an approximately 1.4 arcsec gap between the two chips. The resulting variation of the projected pixel area on the sky requires corrections to photometry of point sources using geometrically corrected images. A contour plot of relative pixel size across the UVIS image, normalized to the central pixel, is shown in Figure B.2. The range of pixel area is from 0.965 to 1.035 times the central value.

Figure B.2: Variation of the UVIS channel effective pixel area with position in detector coordinates.

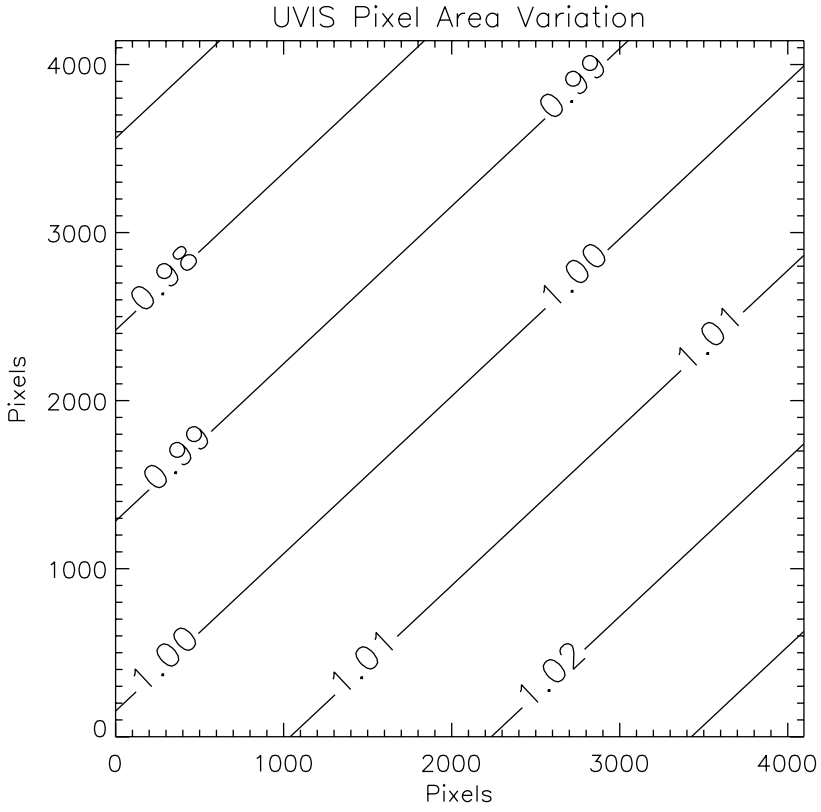

B.3 IR Channel

The IR channel field of view is nominally concentric with the UVIS field, but subtends a somewhat smaller area on the sky, 136×123 arcsec. The detector tilt is about the *x*-axis (USER1), so the projected aperture shape is nearly an elongated rectangle, with the angle between the *x*- and *y*-axes on the sky nearly 90°, as shown by the outline in Figure B.3. At field center, the *x*- and *y*-scales are 0.135 and 0.121 arcsec/pixel, respectively. A vector plot of the deviation from linearity is given in Figure B.3, in which the deviations have been magnified by a factor of 10 for illustrative purposes. The largest deviation is 10 pixels, corresponding to about 1.4 arcsec.

Figure B.3: Non-linear component of the WFC3/IR channel distortion.

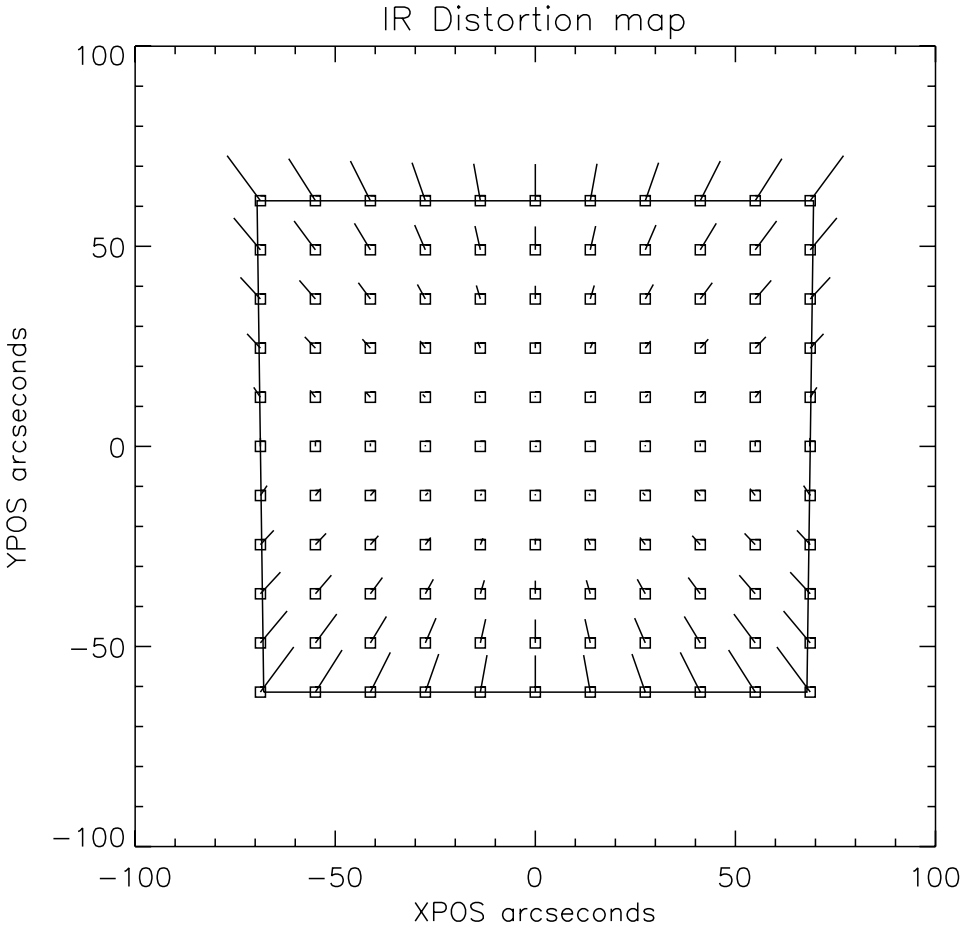

The variation of pixel area across the IR channel to be used for correction of point-source photometry from distortion-corrected images is shown in Figure B.4. The maximum deviation from the central value is 4.1%.

Figure B.4: Variation of the IR channel effective pixel area with position in detector coordinates.

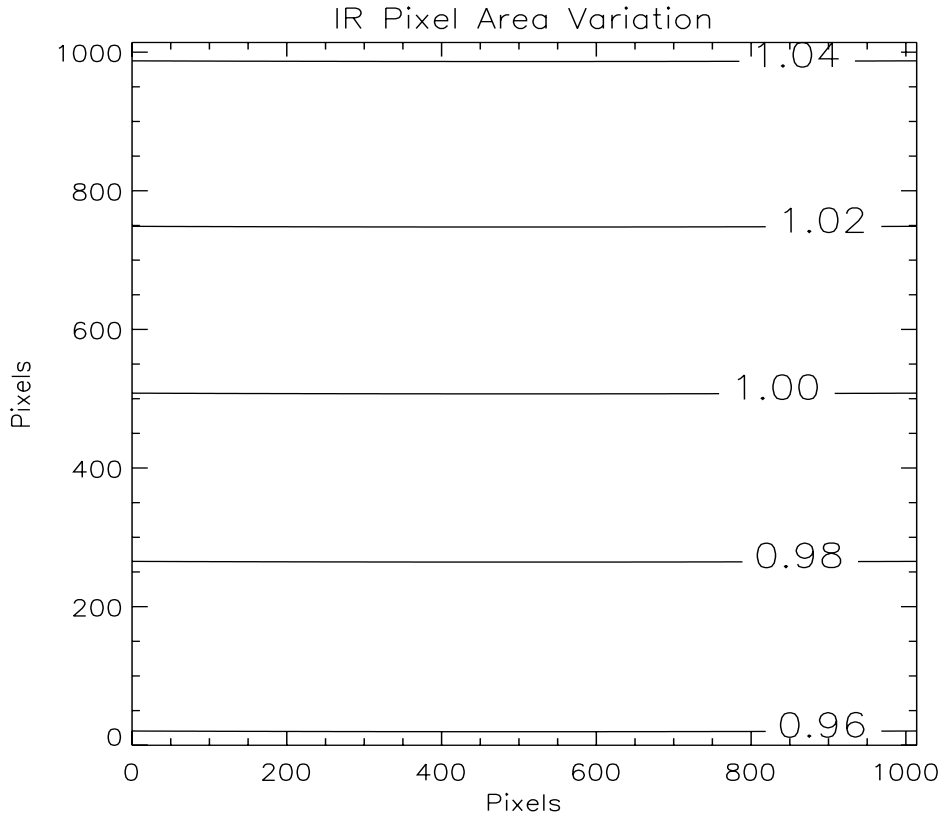

B.4 Summary

Images produced by both WFC3 channels will be affected by considerable geometric distortion, dominated by a linear anamorphism introduced by the tilt of the image surface with respect to the chief ray. This is compounded by non-linear terms that produce changes across the field of view in both plate scale and area subtended by the pixels.

All values presented here are based on optical modeling of the instrument, and corroborated with measurements using a telescope simulator in ground thermal-vacuum tests. We expect that on-orbit measurements of the distortion scale factors will deviate by less than 1% from those presented here.

APPENDIX C:

Dithering and Mosaicking

In this appendix . . .

C.1 Why Mosaicking and Dithering are Needed

It is frequently desirable to shift the telescope pointing between successive exposures. The sizes of these offsets can be very different, depending on the purpose of changing the pointing.

It is useful to distinguish between "**mosaicking**" and "**dithering**." Mosaicking is done with the aim of increasing the area of sky covered by a particular set of exposures, usually with the goal of providing a seamless joining of contiguous frames. The angular offsets used when mosaicking are generally large, comparable to the size of the field of view.

Dithering generally involves much smaller telescope offsets, often just a few pixels in size. It is done for a variety of reasons, including:

- removal of hot pixels and other detector blemishes
- improving sampling of the PSF
- improving photometric accuracy by averaging over flat-fielding errors
- bridging over the gap between the chips in the UVIS channel.

C.2 WFC3 Patterns

A number of different types of patterns are available to support dithered and mosaicked WFC3 observations. Use of these patterns has the advantage that it allows exposures to be associated automatically during ***calwfc3*** pipeline processing. However, the following restrictions apply: only pattern exposures obtained within a single visit, and those patterns where the cumulative offset is smaller than the ~100 arcsecond guide-star limitation, can be associated.

The current set of available patterns is summarized in Table C.1. The parameters of these patterns (e.g., the sizes of the offsets and their directions) can be adjusted by the observer. These patterns have not been finalized at the time of writing, but they will be described in detail on a future Dither Web page linked on the main WFC3 Web Site.

As described in Appendix B, the plate scales for both WFC3 channels vary significantly over the field of view, such that an integer-pixel dither near the center of the field will not be an integer-pixel dither in the corners. For this reason, dither patterns attempt to strike a balance between having offsets large enough to reject detector artifacts, but as small as possible to maintain the integrity of the pattern over the entire field of view. Larger displacements will have varying sub-pixel properties across the image.

Table C.1:Dithering and Mosaicking Patterns for WFC3.

Pattern Name	Description
WFC3 UVIS Patterns	
WFC3-UVIS-DITHER-LINE	Provides linear offsets useful for better UVIS PSF sampling
WFC3-UVIS-DITHER-BOX	A UVIS sub-pixel dither box, with minimum sub-pixel steps placed to miss diffraction spikes.
WFC3-UVIS-MOS-DITH-LINE	A combination mosaic primary pattern with a 2-point dither at each primary position.
WFC3-UVIS-MOS-BOX-LRG	A 4-point box that results in the largest areal coverage with the UVIS detector.
WFC3-UVIS-MOS-BOX-GAP	A pattern that combines large areal coverage while sampling the UVIS inter-chip gap.
WFC3-UVIS-MOS-BOX-IR	A pattern useful for covering the same field of view with both channels.
WFC3-UVIS-MOSAIC-LINE	A pattern useful for WFC3 UVIS observations with ACS WFC in parallel.
WFC3 IR Patterns	
WFC3-IR-DITHER-LINE	Provides linear offsets useful for better IR PSF sampling.
WFC3-IR-DITHER-BOX-MIN	An IR sub-pixel dither box, with minimum sub-pixel steps placed to miss diffraction spikes.
WFC3-IR-DITHER-BOX-GAP	Covers the UVIS inter-chip gap when imaging one field with both channels.
WFC3-IR-DITHER-BOX-MED	Dithers over steps larger than the IR detector defects, for higher photometric accuracy.
WFC3-IR-DITHER-BOX-UVIS	Dithers the IR detector to cover the same area as the UVIS detector.

In addition to the plate-scale variation associated with the significant WFC3 geometric distortion, there can also be a temporal variation of overall image

alignment. Some CR-SPLIT images taken during ACS SMOV testing, in which the two components were separated by the scheduling system across orbital occultations (about a one-hour gap), showed registration differences of about 0.5 pixels corner-to-corner. Thus, to combine multiple images to create oversampled images at the resolution WFC3 is capable of providing, the user may need to allow for the general problem of combining distorted, misregistered images. A variety of tools are being made available within STSDAS and ***PyRAF*** to assist with these tasks, including ***PyDrizzle*** and ***MultiDrizzle***. The issues for WFC3 are similar to those for ACS, so users should see the ACS Drizzle Web page and the *ACS Data Handbook* for more discussion at this time. Analogous resources are being developed for WFC3.

Further discussion of image-alignment stability is given in WFC3 ISR 2007-18.

Additional information on dithering, and processing drizzled data using ***MultiDrizzle*** can be obtained from the *Dither Handbook*

APPENDIX D:

Bright-Object Constraints and Image Persistence

In this appendix . . .

D.1 UVIS Channel

The UVIS channel's CCDs have no known bright-object constraints. It is not anticipated that overexposures on very bright targets will have any adverse health and safety issues, nor should they affect subsequent exposures.

D.2 IR Channel

The IR channel likewise has no bright-object constraints that are imposed due to instrument safety concerns. However, observers should bear in mind that there is a potential for image-persistence effects that could compromise observations made immediately following an exposure on a very bright target. Such observations could potentially contain an "afterglow" image at the location of the overexposed object, which would gradually fade away over an interval of several hours.

The WFC IR channel will be at least as sensitive as NICMOS, but have a field of view seven times larger than NICMOS Camera 3. This combination of high sensitivity and large field size means that WFC3/IR images will often contain saturated stellar images. These can impact subsequent observations if the WFC3/IR detector exhibits

significant persistence. At the time of this writing, it is not yet known how much persistence there will be with the IR detector selected for flight, and we are still developing procedures for dealing with potential severe overexposures that might affect subsequent observations from a different program.

If you are planning a sequence of IR observations that may contain severely overexposed images, you may wish to estimate the degree of overexposure. An IR observer might expect that the Two Micron All Sky Survey (2MASS) would be the appropriate catalog for examining the frequency of WFC3/IR saturations, but in fact the 2MASS catalog is generally not deep enough for this purpose. Although the depth of the survey varies across the sky, the faint limit is typically near 15th mag in *J*, *H*, and *Ks* (the formal Level 1 requirements on limiting magnitudes of the 2MASS catalog are $J = 15.8$, $H = 15.1$, and $Ks = 14.3$). Stars near this faint limit will saturate the WFC3/IR detector in a relatively short time (of order 100 s in some of the wide IR bandpasses). The STScI Guide Star Catalog (GSC), currently at version 2.3, generally goes much fainter (down to 22nd mag in *V*), but the extrapolation from the optical into the infrared depends on the accuracy of the spectral type implied by the optical colors and the assumed extinction (which will be a large source of systematic errors along sightlines of high extinction).

Thus, neither the 2MASS nor the GSC catalog is particularly well suited to predicting the number of saturated stars in WFC3/IR images. However, if persistence proves to be a problem for the WFC3/IR channel, it will likely only arise when the detector is over-saturated by a factor of 100 or more; in this case, the 2MASS catalog should be sufficiently deep for screening observations against extreme saturations.

As described in Chapter 9, the WFC3 Exposure Time Calculator (ETC) can be used to estimate the count rate in the central pixel for a given astronomical source. However, as a rough guideline, below we present tables of the count rates for two cases: a "hot star" with $T_{eff} = 50{,}000$ K, [Fe/H] = −2, and $\log g = 5$; and a "cool star" with $T_{eff} = 2{,}500$ K, [Fe/H] = 0, and $\log g = 3$.

Tables D.1, D.2, D.3, and D.4 give the results for the cases where one normalizes to 2MASS *J*, *H*, and *Ks* magnitudes, and to Johnson *V,* respectively. In each case a magnitude of 15 in the respective bandpass is assumed. The count rates are given in electrons/s for the central pixel of a star centered in a WFC3 IR pixel. To interpret these numbers, one should note that there is more than 5% departure from linearity at a pixel signal of 95,000 electrons (see Section 5.7.5). These tables give the most reliable results when normalizing to a ground-based bandpass that overlaps with the WFC3 bandpass, regardless of the assumed spectral energy distribution. However, when normalizing to Johnson *V,* one must know the underlying spectral energy distribution to high accuracy in order to predict the count rate in the WFC3/IR bandpasses.

The Bright Object Tool (BOT) in the Astronomer's Proposal Tool (APT) can provide a list of saturated objects for a potential WFC3/IR observation, given a Phase II proposal. Because the 2MASS survey is sufficiently deep for objects that would severely oversaturate the detector (by more than a factor of 100), the BOT uses 2MASS data where they are available, and the GSC2 where no 2MASS data are available.

Table D.1: Count Rates (e-/s) for source with J = 15.

WFC3 IR filter	Cool star[1]	Hot star[1]
F098M	1717.7	3701.6
F105W	3228.0	5485.9
F110W	5306.0	7584.9
F125W	3177.0	3356.9
F126N	164.0	150.4
F127M	823.8	704.5
F128N	185.7	151.8
F130N	188.4	147.5
F132N	162.4	137.7
F139M	418.8	490.7
F140W	3479.9	3066.7
F153M	589.9	365.6
F160W	2313.2	1437.2
F164N	200.2	72.8
F167N	182.0	68.6

1. See text for definition of “cool” and “hot” star.

Table D.2: Count Rates (e-/s) for source with H = 15.

WFC3 IR filter	Cool star[1]	Hot star[1]
F098M	870.2	4203.1
F105W	1635.3	6229.1
F110W	2687.9	8612.4
F125W	1609.4	3811.6
F126N	83.1	170.7
F127M	417.3	799.9
F128N	94.1	172.3
F130N	95.4	167.5
F132N	82.3	156.3
F139M	212.2	557.2
F140W	1762.9	3482.1
F153M	298.8	415.2

WFC3 IR filter	Cool star[1]	Hot star[1]
F160W	1171.8	1631.9
F164N	101.4	82.6
F167N	92.2	77.8

Table D.3: Count Rates (e-/s) for source with Ks = 15.

WFC3 IR filter	Cool star[1]	Hot star[1]
F098M	634.9	4497.7
F105W	1193.2	6665.8
F110W	1961.2	9216.2
F125W	1174.3	4078.9
F126N	60.6	182.7
F127M	304.5	856.0
F128N	68.6	184.4
F130N	69.6	179.2
F132N	60.0	167.3
F139M	154.8	596.2
F140W	1286.3	3726.2
F153M	218.0	444.3
F160W	855.0	1746.3
F164N	74.0	88.4
F167N	67.3	83.3

Table D.4: Count Rates (e-/s) for source with V = 15.

WFC3 IR filter	Cool star[1]	Hot star[1]
F098M	473356.0	1835.7
F105W	889581.0	2720.6
F110W	1462211.6	3761.6
F125W	875518.6	1664.8
F126N	45206.0	74.6
F127M	227010.4	349.4
F128N	51183.0	75.3
F130N	51919.3	73.2

WFC3 IR filter	Cool star[1]	Hot star[1]
F132N	44760.0	68.3
F139M	115417.6	243.4
F140W	958999.0	1520.8
F153M	162569.9	181.3
F160W	637460.3	712.7
F164N	55157.8	36.1
F167N	50145.8	34.0

APPENDIX E:

Reduction and Calibration of WFC3 Data

In this appendix . . .

E.1 The STScI Reduction and Calibration Pipeline

In this appendix, we summarize the basic reductions and calibrations that are performed in the STScI WFC3 pipeline. The material in this appendix is intended to provide only enough background to develop robust observing proposals. The forthcoming WFC3 Data Handbook will provide more detailed information needed for analyzing your data.

Science data taken by WFC3 are received from the Space Telescope Data Capture Facility and sent to the STScI OPUS pipeline, where the data are unpacked, keyword values are extracted from the telemetry stream, and the science data reformatted and repackaged into raw (uncalibrated) FITS files by the generic conversion process. All WFC3 science data products are two-dimensional images that are stored in FITS image-extension files.

Like ACS and STIS images, WFC3 UVIS channel exposures are stored as triplets of FITS image extensions, consisting of science (SCI), error (ERR), and data quality (DQ) arrays. There will be one triplet of image extensions for each CCD chip used in an exposure. Full-frame exposures, using both chips, will therefore have two triplets of SCI, ERR, and DQ extensions in a single FITS file. UVIS subarray exposures, which use only one CCD chip, will have a single triplet of extensions in their FITS files.

WFC3 IR channel exposures use the NICMOS file structure, which are quintuplets of FITS image extensions, consisting of science (SCI), error (ERR), data quality (DQ), number of samples (SAMP), and integration time (TIME) arrays. There is one quintuplet of extensions for each of the non-destructive detector readouts that make up an IR exposure. Using the maximum number of readouts (16) in an IR exposure therefore results in a single FITS file containing a total of 80 image extensions.

The raw, uncalibrated FITS files are processed through ***calwf3***, the software code that calibrates the data for individual exposures, producing calibrated FITS files. Exposures that are obtained as part of an associated set, such as dithered images, will have ***calwf3*** calibration applied to the individual exposures before being processed as a set for the purpose of image combination. All calibrated images will be processed further with the STScI ***MultiDrizzle*** software, for the purpose of removing geometric distortions from individual exposures and for combining associated exposures.

The file name suffixes given to WFC3 raw and calibrated data products are described in Table E.1 and closely mimic the suffixes used by ACS and NICMOS. The initial input files to ***calwf3*** are the raw (RAW) files from generic conversion and the association (ASN) table, if applicable, for the complete observation set. For WFC3/UVIS images, a temporary file, with the suffix "BLV_TMP," is created once bias levels are subtracted and the overscan regions are trimmed. This file is renamed to the "FLT" suffix after the standard calibrations (dark subtraction, flat fielding, etc.) are complete. The FLT files serve as input for cosmic ray rejection, if required. For UVIS CR-SPLIT and REPEAT-OBS exposures, a temporary CR-combined image (CRJ_TMP) is created and then renamed to the CRJ suffix once basic calibrations are complete.

Table E.1: WFC3 File Name Suffixes.

File Suffix	Description	Units
_RAW	Raw data	DN
_ASN	Association file for observation set	
_SPT	Telemetry and engineering data	
_TRL	Trailer file with processing log	
_BLV_TMP	Overscan-trimmed individual UVIS exposure	DN
_CRJ_TMP	Uncalibrated, CR-rejected combined UVIS image	DN
_IMA	Calibrated intermediate IR exposure	DN
_FLT	Calibrated, flat-fielded individual exposure	e^- (UVIS) e^-/s (IR)
_CRJ	Calibrated, CR-rejected, combined UVIS image	e^-
_DRZ	Calibrated, Geometrically-corrected, dither-combined image	e^-/s

Processing of WFC3/IR exposures results in an intermediate MULTIACCUM (IMA) file, which is a file that has had all calibrations applied (dark subtraction,

linearity correction, flat fielding, etc.) to all of the individual readouts of the IR exposure. A final step in ***calwf3*** processing of WFC3/IR exposures produces a combined image from the individual readouts, which is stored in an FLT output product file.

The UVIS processing portion of ***calwf3*** is based on ***calacs*** calibrations of ACS/WFC CCD images, while the ***calwf3*** IR processing is very similar to ***calnica*** processing of NICMOS images. ***Calwf3*** performs the following basic science data calibrations:

- Bad pixel flagging
- Bias level subtraction (UVIS); Reference pixel subtraction (IR)
- Bias image subtraction (UVIS); Zero-read subtraction (IR)
- Dark current subtraction
- Non-linearity correction
- Flat field correction
- Shutter shading correction (UVIS only)
- Up-the-ramp fitting (IR only)
- Photometric calibration (keyword updates only)
- CR-SPLIT/REPEAT-OBS image combination

As noted in the list above, the details of some calibration steps differ for UVIS and IR exposures, while others do not apply at all. The process of bias subtraction, in particular, differs for UVIS and IR exposures. The UVIS channel CCDs include regions of overscan, which are used for measuring and subtracting the overall bias level from each CCD exposure. A bias reference image is also subtracted from each science exposure to remove spatial variations in the bias. For IR exposures, the reference pixels located around the perimeter of the detector are used to track and remove changes in the overall bias level between readouts, while the image from the initial ("zeroth") readout of the exposure is subtracted from all subsequent readouts to remove spatial bias structure.

Shutter shading correction is only necessary for very short-duration UVIS exposures (the IR channel does not have a shutter mechanism).

Up-the-ramp fitting is applied to IR exposures to determine a final count-rate for each pixel in the image. This process not only determines the best-fit count-rate from the individual readouts of the exposure, but also detects and removes effects due to cosmic-ray hits and is also capable of recovering a useful signal for pixels that go into saturation during the exposure by using only the non-saturated readouts.

WFC3 grism observations will be handled in a special way by the pipeline. ***Calwf3*** will only process grism observations up to the point immediately preceding flat fielding of the two-dimensional images. A separate software package, **aXe**, which was developed at ST-ECF and previously used for processing NICMOS and ACS spectral observations, will also be used to extract and calibrate one-dimensional spectra from WFC3 grism exposures. The **aXe** software is available in STSDAS via **PyRAF**. The

aXe software is used to locate and extract individual spectra from calibrated images, and performs wavelength calibration, background subtraction, flat fielding, and absolute flux calibration for extracted spectra.

Table E.2 shows the values assigned to pixels in the DQ array. If more than one data-quality condition applies to a pixel, the sum of the values is used.

Table E.2: WFC3 Data Quality Flags.

FLAG Value	Data Quality Condition
0	OK
1	Reed-Solomon decoding error
2	Data replaced by fill value
4	Bad detector pixel
8	(Reserved)
16	Hot pixel
32	Large blemish
64	IR zero-read signal correction
128	UVIS overscan or IR reference pixel
256	Full-well or A-to-D saturation
512	Bad pixel in reference file
1024	Small blemish
2048	A-to-D saturation
4096	Cosmic ray rejected by MultiDrizzle
8192	Cosmic ray rejected during up-the-ramp fitting (IR) or combination of CR-SPLITS (UVIS)
16384	(Reserved)
32768	(Reserved)

E.2 The SMOV Calibration Plan

A detailed plan for calibrating the various imaging and spectroscopic modes of WFC3 during the Servicing Mission Orbital Verification (SMOV) phase following installation of the camera into *HST* is not available at this writing.

We plan to provide the calibration plan on the WFC3 Web site (http://www.stsci.edu/hst/wfc3) early in 2008.

Glossary

The following terms and acronyms are used in this Handbook.

ADU: Analog-to-digital Unit

ADC: Analog to digital Converter

ABMAG: –2.5 log (F_ν) – 48.60 where F_ν is the flux from the source in erg cm^{-2} sec^{-1} Hz^{-1}

AB$_\nu$: Correction to ABMAG to account for the fact that the source spectrum is not constant in F_ν (ABMAG=V+AB_ν)

ACS: Advanced Camera for Surveys

APT: Astronomer's Proposal Tool

aXe: Spectroscopic Data Extraction Software

BOP: Bright Object Protection

calwfc3: WFC3 calibration pipeline software

CCD: Charge Coupled Device. Solid-state, light detecting device

COS: Cosmet Origins Spectrograph

CP: Call for Proposals

CR: Cosmic ray

CR-SPLIT: Division of a CCD exposure into shorter exposures to be used for cosmic ray rejection

CSM: Channel select mechanism

CTE: Charge transfer efficiency

CVZ: Continuous viewing zone

DCL: Detector Characterization Laboratory

DN: Data number

EE: Encircled energy

ETC: Exposure Time Calculator. ETCs are Web-based tools which can be accessed through the WFC3 Web pages.

FET: Field-effect Transistor

FGS: Fine Guidance Sensors

FITS: Flexible Image Transport System

FOV: Field of view

FPA: Focal-Plane Array

FSM: Filter selection mechanism

FWHM: Full width at half maximum

GO: General Observer

GSC: Guide Star Catalog

GSFC: NASA's Goddard Space Flight Center

Help Desk: Facility for getting help on HST related topics via email. help@stsci.edu.

HRC: High Resolution Channel

HST: Hubble Space Telescope

IPT: Integrated Product Team

IR: Infrared

IRAF: Image Reduction and Analysis System. The environment in which STSDAS operates.

ISR: Instrument Science Report. Available at the SFC3 Web site.

K: Degree Kelvin

MBE: Molecular-beam Epitaxial

MPP: Multi Pinned Phased, a CCD mode that reduces dark current rate

MTF: Modulation Transfer Function

MUX: Multiplexer

NICMOS: Near-Infrared Camera and Multi-Object Spectrograph

NUV: Near ultraviolet (~2000 to 4000 Å)

OTA: Optical Telescope Assembly

PASP: Publications of the Astronomical Society of the Pacific

Phase I proposal: A proposal for observing time on HST

Phase II program: An approved HST program; includes precise detail of how program is to be executed

PI: Principal investigator

POM: Pick- off Mirror

PRF: Pixel Response Function

PSF: Point-spread function.

PyRAF: version of IRAF implemented in the Python language

QE: Quantum Efficiency

rms: Root mean square

SAA: South Atlantic Anomaly

SBC: Solar-Blind Channel of ACS

SDSS: Sloan Digital Sky Survey

SED: Spectral-energy Distribution

SLIM: Slitless Spectroscopy Simulator

SM4: Servicing Mission 4

SMOV: Servicing Mission Observatory Verification

S/N: signal-to-noise ratio

SOFA: Selectable Optical Filter Assembly

SOC: Scientific Oversight Committee

ST-ECF: Space Telescope European Coordinating Facility

STIS: Space Telescope Imaging Spectrograph

STScI: Space Telescope Science Institute

STSDAS: Space Telescope Science Data Analysis System. The complete suite of IRAF data analysis and calibration routines used to process HST data.

synphot: STSDAS synthetic photometry (IRAF) software package

TAC: Telescope Allocation Committee

TEC: Thermal Electric Coolers

UV: Ultraviolet

UVIS: Ultraviolet and Visual (CCD channel of WFC3)

WFC: Wide-Field Channel of ACS

WFC3: Wide Field Camera 3

WF/PC-1: Wide Field Planetary Camera-1. Original on-axis HST camera.

WFPC2: Wide Field Planetary Camera 2. Replacement for WF/PC-1 installed during first servicing mission of December 1993.

Index

F

G

H

I

L

M

O

P

Q

R

S

T

U

W